The Atomistic Modelling Approach to Designing New Metal-Boride Superconductors



Sheena Shah
Mansfield College

D.Phil. Thesis

Hilary Term
2013

The Atomistic Modelling Approach to Designing New Metal-Boride Superconductors

Sheena Shah
Mansfield College

Abstract of DPhil Thesis, Hilary Term 2013

A series of metal-boride compounds have been studied using density functional theory with the goal of discovering and designing new superconductors with the highest possible superconducting critical temperature (T_c). The materials design process involves predicting crystal structures using an evolutionary algorithm followed by the calculation of the T_c for any metallic structures using the Migdal-Eliashberg theory. The reasons for superconductivity are rationalised through examining the electronic and vibrational features of the system. Finally, the stability of metal-boride compounds is studied to find hints to speed up the superconductor design process.

An ambient pressure, ground state structure of oP10-FeB_4 is proposed as being one of the rare iron-based BCS-type superconductors, with a T_c of 15 - 20 K. Unlike MgB_2 where the Fermi level is composed of boron electronic states, here 2/3 of the states at the Fermi level originate from the iron atom and only 1/3 from the boron atom. An extensive study has been done to show that the structure is neither ferro- nor antiferromagnetic. CrB_4 is also predicted to form same oP10 structure as FeB_4 but is not expected to be superconducting. Experiments have recently confirmed the predicted oP10 FeB_4 and CrB_4 structures, with superconductivity being observed in FeB_4.

The whole Ca_xB_{1-x} composition range has been studied at ambient and gigapascal pressures, proposing stable high pressure superconducting compounds for CaB, CaB_2 and $CaB_{6.125}$. The highest T_c predicted is 5 K for CaB at 30 GPa. The rest of the compounds have T_c's on the order of 1 K showing that whilst may be possible to predict very stable structures, this is not so good for discovering a superconductor with a high T_c. Stable high pressure forms of CaB_4 and CaB_6 are also discussed where their pressure induced crystallographic phase transitions are explained through comparing with alkaline earth analogues. The stability of a particular boron network at any pressure is shown to be heavily dependent on the metallic ion size.

Acknowledgments

I would like to thank my DPhil supervisor Dr. Aleksey Kolmogorov for all his support, advice and patience throughout my doctoral studies. He has taught me how to use the density functional theory, how to program, parts of the theory of quantum mechanics and much more. Most of all he taught me how to be a good scientist. I know that the skills I have learned from Aleksey over the past few years will be invaluable for the rest of my life.

I would also like to thank Dr. Elena Roxana Margine who taught me how to use Quantum ESPRESSO and about the theories of superconductivity. Without her advice I would not have been able to run the many phonon and electron-phonon calculations that have formed part of this thesis.

Finally I thank Jignesh Radia for reading and commenting on my thesis, reports, research articles and presentations throughout my doctoral studies.

Contents

1 Designing New Superconductors **5**

1.1 Superconducting materials 10

1.1.1 Elemental phases 10

1.1.2 Compounds and alloys 13

1.1.3 Metal borides 16

1.1.4 Hypothetical materials 24

1.2 The computational approach 28

1.3 Density Functional Theory (DFT) 30

1.3.1 The Thomas-Fermi approximation 30

1.3.2 The Hohenberg-Kohn theorems 31

1.3.3 Kohn-Sham theory 32

1.3.4 Exchange-correlation functionals 35

1.3.5 Implementation of DFT 37

1.3.6 Crystal structure search 38

1.4 Theory of superconductivity 41

1.4.1 The BCS theory 43

1.4.2 The Migdal-Eliashberg theory 48

1.5 Calculation of superconductivity properties 54

1.5.1 Phonon properties 54

1.5.2 Electron-phonon interaction 57

1.6 Computational details and nomenclature 58

1.6.1 The Pearson symbol 59

2 Iron Tetraboride **61**

2.1 Determining the most stable crystal structure 62

2.2 Electronic properties 66

2.3 Superconducting properties 69

2.3.1 Convergence of the electron-phonon calculations 70

2.3.2 The isotope effect 73

2.3.3 Magnetic properties 76

2.3.4 CrB_4 81

2.3.5 Synthesis of FeB_4 83

3 Calcium boride under pressure **84**

3.1 Evolutionary crystal structure search 87

3.2 Calcium hexaboride: CaB_6 89

3.2.1 Structural properties of CaB_6 91

3.2.2 X-ray diffraction experiments 107

3.2.3 Electronic properties of CaB_6 109

3.2.4 Superconducting properties of CaB_6 112

3.3 Calcium tetraboride: CaB_4 116

3.3.1 Structural stability of CaB_4 117

3.3.2 Electronic properties of CaB_4 129

3.3.3 Superconducting properties of CaB_4 132

3.4 Calcium diboride 134

3.4.1 Structural properties of CaB_2 135

3.4.2 Electronic properties of CaB_2 . . . 137
3.4.3 Superconducting properties of CaB_2 . . . 138
3.5 Calcium monoboride: CaB . . . 142
3.5.1 Structural properties of CaB . . . 142
3.5.2 Electronic properties of CaB . . . 144
3.5.3 Superconducting properties of CaB . . . 147
3.5.4 Comparison of CaB with isoelectronic LiC . . . 147
3.6 LiC superconductivity calculations . . . 148
3.7 Other Ca-B compositions considered . . . 151

4 Conclusions and Outlook **153**

5 Appendix **159**

5.1 FeB_4 appendix . . . 159
5.2 Ca-B appendix . . . 162

Bibliography **171**

1 Designing New Superconductors

Superconductivity is the vanishing of electrical resistance in a metal as it is cooled below a critical temperature, T_c. Superconducting materials can carry large currents and generate large magnetic fields. These properties are being exploited in a number of fields such as medicine (MRI), power transmission and transportation (Maglev) [1]. Specifically, the particle accelerator, the Large Hadron Collider at CERN, uses niobium-titanium wires to generate magnetic fields (8T) that are sixteen hundred times as strong as the fields from the common fridge magnet. To maintain the low temperatures required for the wire's superconductivity, 130 tonnes of liquid helium is used per year [2]. The enormous expense ($\sim$£5 per litre [3]) of helium and future scarcity due to large-scale use is of major concern to the scientific community. Therefore the discovery of new materials which are superconductors above 77K would be a technological breakthrough as this would permit the use of cheaper ($\sim$£0.05 per litre [4]), more abundant liquid nitrogen as a coolant. An example of such materials are the high-T_c cuprates discovered in 1987, however these are brittle and are required to be in a single crystal form for optimal performance. Therefore, the desirable mechanical properties of low-T_c alloys such as being able to be drawn into wires explains why these materials still dominate the superconductors market.

New superconductors have mostly been discovered by accident, and through this they often violated rules existing at the time, defining what a good superconductor needs. Due to this, the task of predicting the superconducting T_c of a material is difficult because of the complexity of the mechanism behind the superconducting state.

The Bardeen, Cooper and Schrieffer (BCS) theory [5] rationalises superconductivity as the pairing of electrons through interactions with lattice vibrations (phonons). An extension of this formalism, the Migdal-Eliashberg theory [6, 7] together with density functional theory [8] enables a reasonable estimate of the T_c to be made through calculations of the strength of the electron-phonon coupling. Since there is currently no viable theory of the mechanism of high T_c superconductors (e.g. copper oxides and iron-based), the prediction of similar superconductors is outside of the scope of the Migdal-Eliashberg theory.

Using the modelling approach to discover new BCS superconductors could save time and effort compared with experimental techniques. High throughput screening still presents a challenge as accurate evaluation of the T_c incurs high computational cost. However, currently it is feasible to study periodic systems with around ten atoms per unit cell. Coupled with advanced crystal structure prediction methods, the modelling approach could become an essential starting point in the search for new superconductors.

The steps for superconductor design that were used in this thesis will be described before the background theory is explained.

The steps for superconductor design

1. Choose a compound to study

The first step in superconductor design is to find out as much as possible about why known superconductors are superconducting. This would involve analysing their elemental composition, electronic, vibrational and electron-phonon properties. It is essential to understand why these materials are superconducting so that we can either find similar properties in related materials or design new materials by combining the features of known ones. Section 1.1 will go through key classes of superconductors that we currently know of and how our understanding of them could form the basis for designing better superconductors. A focus will be placed on the metal-boron class as it contains the highest T_c BCS superconductor, magnesium diboride and the class forms the basis of the research presented here. As it is impractical to study every single combination of elements in the periodic table we will use the knowledge gained about known superconductors to choose a compound to study. In this thesis the two sets of compounds chosen are iron and calcium boride. The reasons for their choice are explained in the relevant chapters.

2. Determine the most stable crystal structure of the chosen compound

The computational method chosen to determine the most stable crystal structure is the quantum mechanical modelling approach known as the density functional theory (DFT). The developments leading up to the current form of DFT will be described in Section 1.2. DFT allows us to calculate the thermodynamic properties of a given periodic arrangement of elements, known as the crystal structure. Given an elemental stoichiometry, e.g. FeB_4, state-of-the-art computational algorithms are able to determine the most stable crystal structure of this chosen compound. The algorithm used in this study is based on evolution and will be described in Subsection 1.3.6. When a lowest enthalpy structure is proposed,

one must make sure that it is thermodynamically stable. Thermodynamic stability means that the structure is unable to lower its energy by either transforming into another structure or decomposing into other products. For the two compounds described in this thesis, the whole composition range of M_xB_{1-x} has been explored using an evolutionary algorithm to make sure that proposed ground state crystal structures are thermodynamically stable. A final check for stability of a crystal structure is to calculate its phonon dispersion, where the absence of imaginary phonon frequencies will signal dynamic stability. An imaginary frequency indicates that there is no activation barrier for the structure to transform into a nearby minima in the configuration space. An extension of DFT called density functional perturbation theory with linear response methods are used to calculate phonon properties and will be described in subsection 1.5.1. Stability analysis is essential as we would like to propose superconductors which could be synthesised. Many hypothetical materials with desirable superconducting properties have been previously proposed but as described in subsection 1.1.4 none of these have been synthesised.

3. Calculate superconducting properties of proposed stable crystal structure

If the proposed lowest energy crystal structure of the compound is metallic then the superconducting T_c is calculated using the Migdal-Eliashberg theory. The development of superconductivity theories are described in section 1.4. Electronic and vibrational properties are also analysed to understand why the compound is or is not superconducting. The information gained here can be fed back into step one to propose other compounds to study.

4. Analysis of non-metallic structures

Many of the most stable structures have a low T_c or are semi-conducting and so cannot

be superconducting. It is important to understand the stability of these structures so that guidelines can be created to speed up compound prediction (Step 2). For example, a boron network may prefer a specific sized metal ion to sit within it. An understanding of why a compound is not superconducting can also be just as helpful to designing higher T_c materials as we will know which electronic or structural properties to avoid. Stability analysis has been performed on the calcium borides through comparison with their alkaline earth analogues, explaining various pressure induced phase transitions. The conclusions formed in this step are fed back into step one to discover better superconducting compounds.

1.1 Superconducting materials

The first stage of superconductor materials design is to study known superconductors to find traits that can be emulated in other materials. The goal is to either combine or enhance these traits which can result in both the highest possible T_c and desirable mechanical properties such as strength and ability to be drawn into a wire. The tunable factor that is important is the elemental composition of the compound and its resulting electronic and vibrational features. An analysis is performed to see why these features result in superconductivity. The chemical bonding of a compound and thus its ability to transport electrons is also a factor to take into consideration. This section will discuss the properties of known superconductors and give hints towards new materials design.

1.1.1 Elemental phases

The relative simplicity of elemental phases and the variety of ways to induce their superconductivity gives reason for their study (Figure 1.1). Interestingly, the group V elements vanadium, niobium and tantalum display the highest critical temperatures. In fact, niobium has the highest T_c (9.25K) of any element at atmospheric pressure (Fig. 1.2). A relationship between the number valence electrons and the T_c was described by Matthias in the 1950s [10], who proposed that the T_c is at its maximum for structures containing five or seven electrons per atom. This could therefore be used as a guide for the design of new superconductors.

Figure 1.2 shows that when applying pressure to the transition metals different trends in their critical temperatures are observed. For example, for zirconium, a pressure induced crystallographic phase transition (hcp$\rightarrow$bcc) occurs at 30 GPa, resulting in a rapid

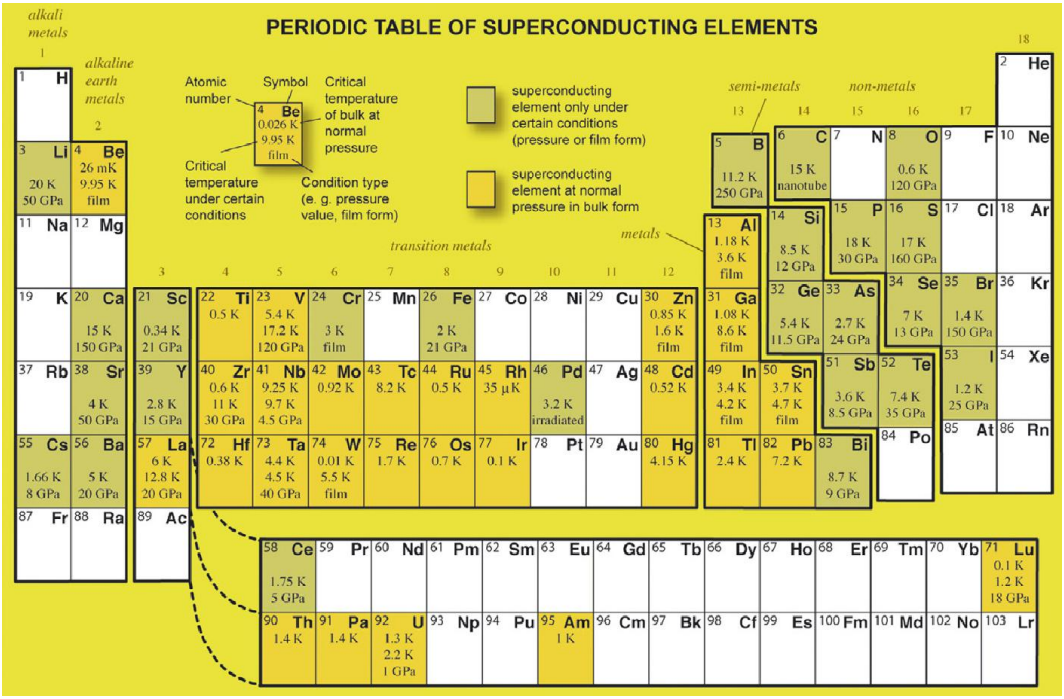


Figure 1.1: Periodic table of superconducting elements. Most metallic elements are superconductors, with most transition metals being superconductors at atmospheric pressure. The figure is reproduced from Ref. [9], doi:10.1088/0953-2048/18/1/R01. © IOP Publishing. Reproduced by permission of IOP Publishing. All rights reserved.

increase in the T_c. In vanadium, the T_c increases linearly with pressure and this is thought to be because of the suppression of the fluctuation of electron spins through the broadening of the d-band [11, 12].

For elements other than the transition metals, superconducting phases mainly exist at high pressure. This is because applying pressure changes their electronic properties and in some cases induce a transformation to a metallic phase, which could be a superconductor. Due to developments of diamond anvil cell technology, it has become possible to explore the superconductivity properties of substances under ever increasing pressures (up to ∼320 GPa). As a result, calcium in its simple cubic phase has the highest experimentally measured T_c of any element (29 K at 216 GPa) [13]. Similarly, lithium under pressure has a T_c of 20K at 50GPa, with recent calculations predicting a drop in the T_c at higher pressures [14] due to a structural phase transition around 80GPa. Experiments have not

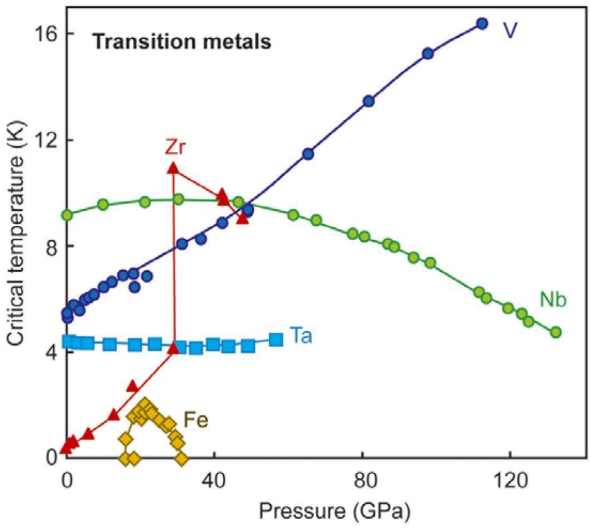


Figure 1.2: Variation of the critical temperature with pressure for transition metal elements. No general trends can be observed across the periodic table. For example, vanadium, niobium and tantalum all with a valence of 5 show no similarities in their pressure-T_c dependence. The figure is reproduced from Ref. [9], doi:10.1088/0953-2048/18/1/R01. © IOP Publishing. Reproduced by permission of IOP Publishing. All rights reserved.

yet been able to identify the new phase [15].

The potential superconductivity of metallic hydrogen has been a hotly debated topic since 1968 when Ashcroft [16] predicted that it would be superconducting at almost room temperature. From the BCS theory (Section 1.4.1), one may say that the use of light elements in superconductors is desirable as they have high phonon frequencies, which will lead to strong electron-phonon interactions. Metallisation of hydrogen was originally predicted to occur at 25 GPa by Wigner in 1935 [17]. Over the years a wide variety of alternative predictions have been made ([18] and references therein), with the most extreme stating that 2000 GPa would be required for metallisation to occur. Currently, many believe that pressures between 400 and 600 GPa are required for the transition [19], and recently it was claimed that the metallic phase had been observed [20], however to this date no one has been able to prove its predicted superconductivity. The main reason being that hydrogen's high diffusivity and chemical reactivity result in it being difficult to contain under pressure.

The examples described in this section demonstrate that applying pressure to an element can change its electronic and vibrational properties which can improve the T_c, or induce metallisation to a phase which is superconducting. It is not feasible to use superconducting high pressure phases for industrial applications, however, the studies help to understand the physics behind the superconductivity of that particular material and therefore can guide the search for new superconductors.

1.1.2 Compounds and alloys

Combining elements to form stable compounds is another way of creating superconductors, from simple binaries (magnesium diboride) to more complex structures such as yttrium-barium-copper-oxides. The search space for possible superconductors is dramatically increased since combining elements which on their own are not superconducting may potentially form a new material that is.

Copper Oxides

Amongst the class known as high T_c superconductors ($T_c > 30$K) there are the copper oxides, also known as the cuprates. Discovered in 1986 by Bednorz and Müller [21], the Ba-La-Cu-O system had the highest T_c value of any known superconductor at the time. Replacing the lanthanum ions with yttrium, shot the superconducting T_c up to 90K for $YBa_2Cu_3O_{7-x}$ (YBCO).

The crystal structure of YBCO consists of CuO_2 layers sandwiching metal ions (Fig. 1.3). Dominating views are that the CuO_2 acts as a charge reservoir providing charge to the rest of the crystal, eventually to form Cooper pairs [23]. There have also been suggestions that a magnetic interaction is responsible for superconductivity, however the

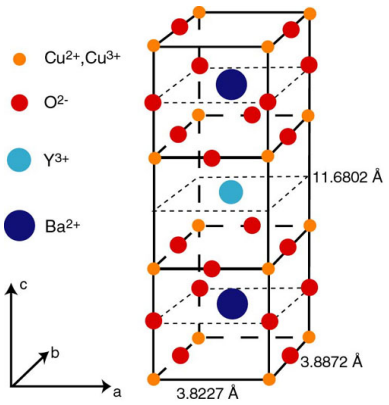


Figure 1.3: The layered crystal structure of yttrium-barium-copper-oxide (YBCO) taken from Ref. [22].

condensed matter physics community has not come to any consensus to explain the superconducting state [23].

Importantly, the yttrium-barium-copper-oxides (YBCO) have a T_c above the boiling point of liquid nitrogen. Unfortunately these materials are brittle and require a single crystal form for their optimum performance as a superconductor [24]. For this reason, the graininess of YBCO has been the focus of much research [25], to enable the best contact angle between grains and thus allow efficient electrical flow across grain boundaries.

The copper oxide class of materials holds the current record for the highest measured T_c. Claims have been made for a thallium-barium-calcium-copper oxide compound having a T_c of 254 K [26]. These observations were however not peer reviewed and as of yet have not been reproduced.

Iron-Based

2008 brought the unexpected discovery of the iron-based layered superconductor $La[O_{1-x}F_x]FeAs$ [27]. Traditionally, researchers avoided using magnetic elements as it was thought that magnetism destroyed superconductivity [28], therefore no one would have predicted superconductivity in this system. Like copper oxides, the iron supercon-

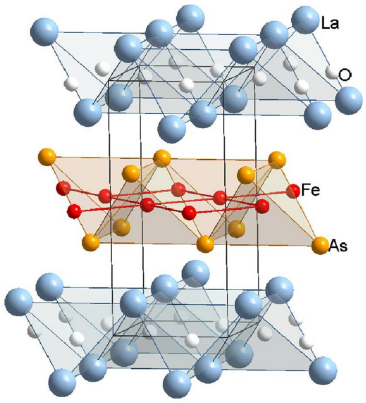


Figure 1.4: The layered crystal structure of iron-based superconductors. Reprinted Fig. 1 with permission from Ref. [29], http://link.aps.org/doi/10.1103/PhysRevLett.101.026403. Copyright (2008) by the American Physical Society.

ductors are layered compounds, however their differing elemental compositions show that more classes of high T_c layered structures could still be discovered. The mechanism of superconductivity in iron-based compounds is still under debate but currently it is thought that long-range magnetic correlations are the cause [23, 28]. The electron-phonon interaction alone cannot account for the high T_c as demonstrated by theoretical calculations which predict a T_c that is five times smaller than experimentally observed [29].

Carbon-Based

A variety of organic superconductors exist [30, 31, 32] but one of the most interesting is the fullerene-based compound Cs_3C_{60}, which has a T_c of 38 K [33]. Comparing with derivatives of this face-centered cubic compound, it is found that the larger the metal ion is, the higher the T_c becomes due to the increase in density of states at the Fermi level [34]. There are no fully developed theories behind the superconductivity in fullerides however it is currently thought that strong electronic correlations and Jahn-Teller electron-phonon coupling lead to local electron pairing [30].

The graphite intercalation compounds (GIC) CaC_6 (T_c = 6.5K) and YbC_6 (T_c =

11.5K) [35] have been well studied as they are structurally similar to MgB_2. Despite the similarities, the mechanism of superconductivity in GICs is very different from that in MgB_2. The vibrational component of the electron-phonon interaction consists of bond-bending of the graphene sheet and movement of the metal intercalant [36]. The electron component is from electronic states lying between the graphene layers [37, 38]. It is thought to be unlikely that higher transition temperatures can be obtained in MC_6 graphite intercalation compounds of other metals, due to incipient lattice instabilities associated with the intercalant phonon modes [39, 36].

1.1.3 Metal borides

The metal borides are particularly interesting to study because of the diverse range of bonding and structures available. Boron can form a variety of morphologies, ranging from linear chains and layered networks to interconnected polyhedra [40, 41]. Covalent boron-boron and metal-boron bonds together with a high density of states (DOS) at the Fermi level give the metal borides desirable characteristics for potential superconductors. This subsection will give an overview of the metal-boron class, showing that due to there being many combinations of metal and boron available, future superconductivity discoveries could be from this class.

Magnesium diboride

The material magnesium diboride (MgB_2) was first synthesised in the mid 1950s [42]. Almost half a century later, then with the material being widely and commercially available, researchers in Japan discovered that the compound was a superconductor with a surprisingly high T_c of 39K [43]. In the six months following this discovery, over two

hundred and fifty studies related to the superconductivity properties of MgB_2 had been reported, with over eighty appearing in peer-reviewed journals [44]. The vast effort of researchers was directed at understanding the electronic features responsible for superconductivity, testing synthesis conditions and investigating similar compounds with the hope of discovering a better superconductor. This section will explain why MgB_2 is so unique and describe some of the scientific efforts aimed at increasing the T_c, including experiments but focusing on theoretical studies.

Almost immediately after the discovery was published in Nature, two theoretical papers offered insightful observations to explain the mechanism of superconductivity in MgB_2 [45, 46]. The compound has an AlB_2 type structure consisting of hexagonal rings of boron, sandwiching magnesium atoms as shown in Figure 1.5. The structure is partially

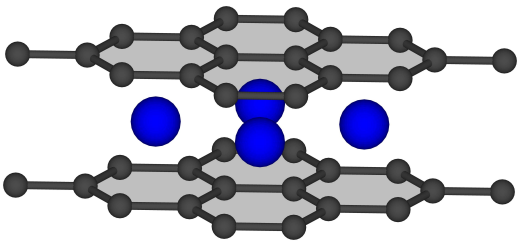


Figure 1.5: AlB_2 structure of MgB_2 and other diborides. Dark grey spheres represent boron atoms and blue spheres metal atoms.

ionic with strong B-B covalent bonds and a large density of states (DOS) at the Fermi level. The band structure of MgB_2 can be used to explain some key electronic features of this material (Fig. 1.6). The DOS at the Fermi level is dominated by boron p states. p_z orbitals which are perpendicular to the boron plane form two π bands (bonding and anti-bonding) due to hybridisation. The B $p_{x,y}$ states which cross the Fermi level are σ bands formed through sp^2 hybridsation within the boron layer. Superconductivity is caused by the incomplete filling or hole doping of these bands. Mg^{2+} attracts π electrons to it more strongly than σ electrons, resulting in σ-π charge transfer and an incompletely

filled σ band.

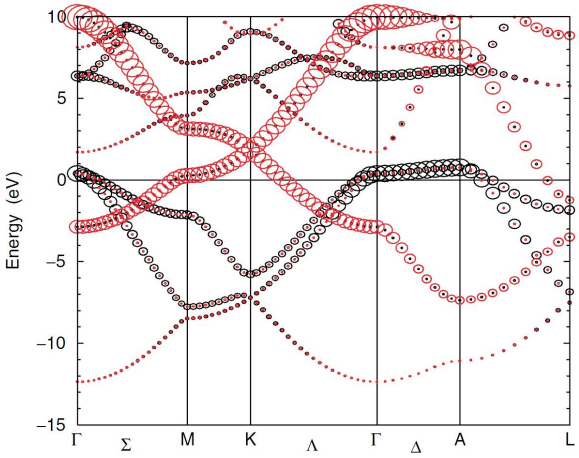


Figure 1.6: The electronic band structure of MgB_2. The radii of the circles represent boron p character: red - B p_z, black - B $p_{x,y}$. Reprinted Fig. 1 with permission from Ref. [46], http://prl.aps.org/abstract/PRL/v86/i20/p4656_1. Copyright (2001) by the American Physical Society.

The density of states at the Fermi level [$n(\varepsilon_F)$] defines which electronic states can couple with the phonon, resulting in the superconductivity. Calculations show that if the system were to be electron-doped there would be a rapid drop in the DOS at the moment when doping has increased the Fermi level by 0.4eV (Fig. 1.7). It is this feature which has meant that most atomic substitutions into the MgB_2 lattice has led to a lowering of the T_c and will be discussed in Section 1.1.3.

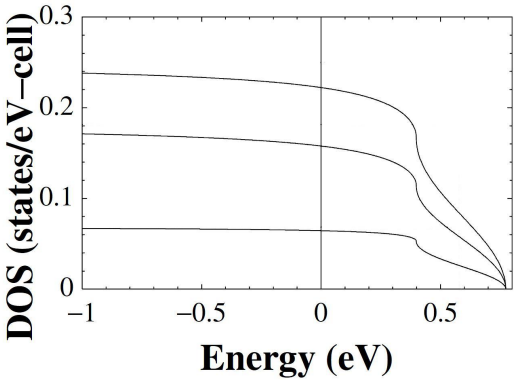


Figure 1.7: The density of states (solid lines) of the light hole band, heavy hole band and total for MgB_2. Reprinted Fig. 2 with permission from Ref. [45], http://prl.aps.org/abstract/PRL/v86/i19/p4366_1. Copyright (2001) by the American Physical Society.

Analysis of the electron-phonon coupling for particular phonon modes of MgB_2 shows that the doubly degenerate E_{2g} mode of in-plane boron movement couples most strongly with electrons in MgB_2. This property can be observed by studying the effect of the vibration on the band structure, where splitting of the σ band occurs along the Γ-A part of the Brillouin zone (Figure 1.8).

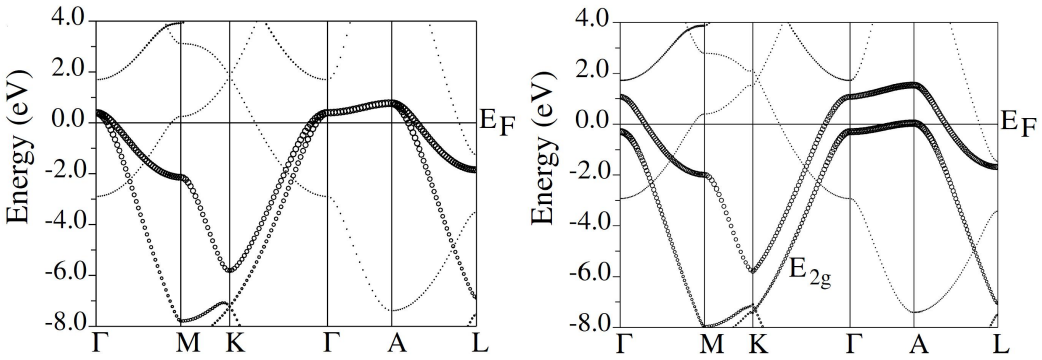


Figure 1.8: Left: The band structure of magnesium diboride. Right: The effect of the E_{2g} phonon mode on the band structure of MgB_2, showing the splitting of the σ band along the Γ-A part of the Brillouin Zone. This is the main phonon mode responsible for superconductivity in MgB_2. Reprinted Fig. 1 and 3 with permission from Ref. [45], http://prl.aps.org/abstract/PRL/v86/i19/p4366_1. Copyright (2001) by the American Physical Society.

One of the theoretical investigations described here, estimated the T_c of MgB_2 to be 22K [46]. The discrepancy with experiment is due to effects created by having two superconducting gaps (multigap nature described in [47]) in MgB_2, which were not taken into account in the calculations.

Finally, an interesting observation of MgB_2 [48, 49] is that its T_c decreases with increasing pressure since the B $p_{x,y}$ bands shift downwards, eventually falling below the Fermi level along the Γ-A direction. This results in a reduction of the B $p_{x,y}$ holes, which drive superconductivity.

Doping of MgB_2

Substitution at the boron and magnesium sites of MgB_2 have been studied heavily using both theory and experiment. It was hoped that this would increase the density of states (DOS) at the Fermi level or make other electronic states available for phonon interactions.

Aluminium doping introduces electrons into the system, which results in a drop in the DOS at the Fermi level (Fig. 1.7). It has been shown that the T_c of $Mg_{1-x}Al_xB_2$ drops smoothly as the aluminium content is increased from x = 0 to x = 0.1 [50]. When the σ bands become nearly filled at x = 0.25, the compound is suddenly no longer superconducting. One would therefore expect substitutions of atoms to the right of magnesium on the periodic table not to improve the T_c of an AlB_2 type structure.

Electron doping substitutions at the boron site are however still being studied because the upper critical magnetic field (H_{c2}) created in doped structures could be higher than that of the undoped structure, at a detriment to the critical temperature. An example is carbon doping which has increased H_{c2} from 16 to 32.5T [51]. Silicon substitution of the boron site has been shown to increase the critical current density (J_c) three-fold [52].

Other metal lattice substitutions tested have included the transition metals scandium [53], titanium [54], copper [55], zirconium [56], gold [57] and lanthanum [58]. The advantage of having metal substitution defects [59] is that they introduce flux pinning sites, which allow the trapping of magnetic flux and thus improve superconductivity properties such as the J_c.

Hole doping of MgB_2 will slightly increase its DOS at the Fermi level (Fig. 1.7). Various hole-doped boride systems have been studied [44], most notably lithium and sodium substitutions of the magnesium site [60]. Theoretical investigations have shown the difficulty of introducing lithium defects into MgB_2 [61], however some successful experimental

studies do exist. For example, 7% lithium doping has been shown not to affect the T_c and improves on the J_c [62]. More recently, it has been shown that even at 30% lithium doping, there is little drop in the T_c [63]. To my knowledge there are no experimental studies displaying the effects of sodium substitution on MgB_2.

Attempts have been made to synthesise calcium doped MgB_2 but this has proven to be difficult. Those reporting experimental procedures yielding calcium doped MgB_2 also show that disorder created in the crystal structure by the dopant decreases the T_c [64]. Due to unfavourable thermodynamic factors impeding calcium substitution, it seems unlikely that this is a promising way to proceed.

AlB_2 type compounds

Though the metal atom is not directly involved in the superconductivity of MgB_2, it can affect the properties of boron electronic states and produce a higher DOS at the Fermi level, thus the superconductivity of many other AlB_2 type borides have been investigated ([44] and references therein).

Much earlier, in the 1970s, Cooper [65] and Leyarovska [66] had already tested various transition metal diborides: yttrium, titanium, zirconium, hafnium, vanadium, niobium, tantalum, chromium and molybdenum. Only NbB_2 was found to be superconducting however this fact has been the subject of much debate [67, 68, 69, 70, 71, 72, 73] so one may say that none of these compounds are in fact superconductors.

In 2001 it was reported in a preprint archive that tantalum diboride exhibited superconductivity at 9.5K [74]. The unusually high T_c brought about much excitement but subsequently different groups reported a range of superconducting temperatures, including 4.4K [75], and many stated a lack of superconductivity altogether [76, 77].

Gasparov *et. al.* [75] reported a T_c of 4.4K but x-ray diffraction measurements showed

the presence of metallic tantalum impurities in their sample. His study also showed that pure samples of TaB_2 displayed no superconducting transition down to 0.37K, agreeing with many recent studies. Those reporting the higher T_c used the oxide Ta_2O_5 as a starting material which could have meant that the superconductivity measurement was actually being made for a reduced oxide compound with intercalated boron atoms. It was generally inferred that the T_c of TaB_2 was highly dependent on the sample and its preparation. With conflicting results from experiment one could turn to theoretical studies to assess the superconducting properties of a compound.

Calculations by Rosner et. al. [76] show many differences between TaB_2 and MgB_2. Some differences include: the tantalum 5d states contributing 70% of the DOS for TaB_2 and essential MgB_2 bonding states being filled for the tantalum compounds, leading to the lack of characteristic nearly 2D Fermi sheets. As a result, there is lower electron-phonon coupling for TaB_2 compared with MgB_2. Rosner's study calculated the electron-phonon coupling constant (λ), and subsequently a T_c, using only zone centre phonon modes. A lack of Brillouin zone sampling could have led to the contradiction of this T_c value with the earlier experimental results (9.5K T_c). To establish if this was the case, one may turn to a further study by Singh [78] who calculated λ by using a high density of k and q vectors across the Brillouin zone. Using linear response methods (described in Section 1.5) to assess the electron-phonon interaction, he predicted a T_c of 12K.

Since the described theoretical articles were published, only two experimental studies [67, 69] have examined the superconducting properties of TaB_2. As there is no conclusive evidence that TaB_2 is a superconductor, this compound requires further experimental and theoretical study for a consensus to be reached.

Non-centrosymmetric compounds

A well accepted requirement for a BCS superconductor used to be that its structure has to have a centre of inversion, which allows the formation of a Cooper pair of electrons with opposing momentum. However it was discovered that inversion symmetry rules could be violated at interfaces or in thin films [79]. Despite this interesting property, these system environments received little attention until he discovery of the first bulk non-centrosymmetric heavy Fermion superconductor ($CePt_3Si$) in 2004 [80].

Notably two non-centrosymmetric borides were subsequently found. Li_2Pd_3B, with a rather high T_c of 8K [81], and its analogue Li_2Pt_3B [82], with the lower T_c of 2.8K, have been compared using electronic structure calculations [83]. When increasing x in the pseudo-binary solid solution $Li_2B(Pd_{1-x}Pt_x)$, one finds an almost linear decrease in T_c as it turns from a palladium rich to a platinum rich compound [82].

However it is still not fully clear why the critical temperatures of Li_2Pd_3B and Li_2Pt_3B differ. The higher mass of platinum, resulting in lower phonon frequencies, only accounts for half of the drop in the T_c. The reason for the rest of the drop is thought to be related to the shape of the Fermi surface, however this is still the subject of debate [83].

In Li_2Pd_3B, B-Pd tetrahedra are involved in most of the electron-phonon coupling, with negligible contribution from the lithium atom. This indicates that substitutions of the lithium atom may have little effect on the T_c. However it would affect the overall crystal structure and disrupt the network of lithium ions. The arrangement of lithium atoms aids the superconductivity to some extent as efficient charge transfer occurs from it to the B-Pd units [84].

Another insight into the superconductivity in this set of compounds could be gained by substituting the palladium/platinum for the isovalent nickel atom. One experimental

study has shown that the T_c decreases with nickel substitution [85]. However no further theoretical investigations have been done to clarify the reason.

Overall, the mechanism of superconductivity in these two compounds is not fully understood and is still being explored [86, 87]. Few studies have focused on improving the T_c through substitution or finding related noncentrosymmetric boride structures, which would be a step forward in the discovery of new superconducting materials.

Recently there has been renewed interest in the non-centrosymmetric boride Ru_7B_3, which has a T_c of 3.3K [88]. Although not topping the T_c of the palladium compound, its study has still enabled relationships between crystal structure/electronic properties and superconductivity to be established. The DOS for this compound is not smooth and contains many singularities, similar to the DOS observed in another non-centrosymmetric boride, $Mg_{10}Ir_{19}B_{16}$ ($T_c = 5$K, [89]). As in the palladium compound, 4d-ruthenium states dominate the DOS and there is little contribution from the boron. Ru_7B_3 is a single band superconductor with weak electron-phonon coupling, explaining the low T_c.

The superconductors discussed here all fall under the category of weakly correlated electron systems and are often explained through the effects created by inversion symmetry breaking. The four borides mentioned here, Li_2Pd_3B, Li_2Pt_3B, Ru_7B_3 and $Mg_{10}Ir_{19}B_{16}$, are the only known non-centrosymmetric boride superconductors, leaving opportunity for the discovery of new ones.

1.1.4 Hypothetical materials

Theoretical calculations of hypothetical materials could give indications of what a good superconductor should be made of.

Amongst studies of the graphite-like material BC_3 [90, 91] there have been some

interesting superconductivity predictions [92]. It is thought that hypothetical hole doping with 0.2-0.3 holes per unit cell could achieve a superconducting transition temperature of 22K [92]. Electron-phonon coupling in the doped system involves high frequency in-plane bond stretching, similar to the dominant E_{2g} mode in MgB_2. So far, there are no published experimental studies which back up or contradict the prediction. Reasons could be due to the difficulty in making substitutions to such a rigid structure. In addition, the electron-phonon coupling interaction was calculated at one point in the Brillouin zone, therefore may not represent the true picture. The authors of the theoretical study did acknowledge this point and said that if there is a peak in the e-ph coupling at the point sampled, then the T_c would be overestimated. More recently, it has been suggested that applying pressure could remove the need for hole doping, with calculations (which sampled the whole Brillouin zone) predicting a T_c of 20 K at 5 GPa and 17.5K at 10 GPa [93]. The decrease in the transition temperature with pressure is attributed to the decrease in the density of states at the Fermi level. Experimental studies are required to verify the prediction.

One of the most ambitious predictions, attracting much experimental research interest [94, 95, 96, 97, 98, 99, 100, 101] is that the hole doped system $Li_{0.5}BC$ could have a T_c of 100K [102]. LiBC which is isoelectronic and structurally similar to MgB_2 is an insulator. The theoretical prediction attempted to make the system metallic and thus potentially be a superconductor. Further theoretical investigations which sampled the whole Brillouin zone, yielded a T_c of 65 K [103]. Although lower than the original estimate, it is still much higher than that of MgB_2, giving hope for the superconductivity potential of this compound. The similar hole doped NaBC was also proposed to be a superconductor with a comparable T_c [104]. To this date, no experimental evidence exists to show that either

compounds are superconductors down to 2 K [105].

Various explanations have been given to understand why the predicted T_c has not been achieved. Hole doping of LiBC can be achieved through removal of lithium atoms. An experimental study which showed synthesis of the hole doped structure, reported that no superconducting transition is observed down to 4 K, attributed to the presence of disorder in B-C stacking [94]. Others claim that standard experimental techniques have only been able to remove small amounts of lithium from the surface which leaves the bulk of the material non metallic and most importantly not a superconductor [105].
X-ray scattering experiments [105] show that there could be incomplete hybridisation between boron and carbon states, which was not displayed by the theoretical calculations.

An alternative method to induce an insulator-metal transition in LiBC is to apply pressure [105, 95]. Unfortunately metallisation occurs at pressures above 345 GPa. The electronic structure of LiBC becomes less like MgB_2 with increasing pressure as σ bands separate, drop below the Fermi level and lose their flatness along Γ-A. Given contradictory experimental data on the possibility of superconductivity in $Li_{0.5}BC$, one may expect more exciting work related to this compound in the future.

Following the discovery of MgB_2 the hypothetical isoelectronic structures CaB_2 [60, 106, 107, 108, 109] and BeB_2 [110, 60, 106] were investigated for their possible superconducting properties. Neither structures are stable in the hexagonal AlB_2 configuration and therefore no one has been able to synthesise them. However the superconductivity community did learn about electronic features of the calcium and beryllium compounds which could serve as a guide towards developing new superconductors. Specifically, if there were a way to stabilize CaB_2 then as predicted by Choi [111], the T_c could be much higher than that of MgB_2 ($\sim$50 K). This higher predicted T_c was attributed to a higher

superconducting gap ($\Delta(\mathbf{k})$) on the σ bands, but slightly a smaller gap for the π bands. This indicated an enhanced two-gap nature for CaB_2 compared to MgB_2. This final example shows that much can be gained from studies of hypothetical materials as we can learn about which electronic features could lead to a good superconductor.

1.2 The computational approach

The development of quantum mechanics, our understanding of interactions at the atomic scale, now allows us to study materials using a theoretical, ab initio approach. Quantum mechanics describes particles as waves through a wavefunction, $\psi(\mathbf{r}, \mathbf{t})$. If this function is known for the ground state of a system a variety of experimental observables can be predicted. This is done through solution of the Schrödinger equation, which takes into account kinetic and potential energy of particles within a system:

$$\left[-\frac{\hbar^2}{2m}\nabla^2(\mathbf{r}) + V(\mathbf{r})\right]\psi(\mathbf{r}, t) = i\hbar\frac{\partial}{\partial t}\psi(\mathbf{r}, t). \tag{1.1}$$

In an ideal situation this equation could be solved for any system, however it becomes complicated for systems with more electrons than the hydrogen atom due to the many body nature of the problem. Therefore approximations are required to solve and subsequently predict properties of materials.

The Schrödinger Equation

A central equation of quantum mechanics is the Schrödinger equation, which was formulated by Erwin Schrödinger in 1926 [112]. The time-independent, non-relativistic form of the equation is:

$$\hat{H}\psi\left(\mathbf{r_1}, ...\mathbf{r_N}\right) = E\psi\left(\mathbf{r_1}, ...\mathbf{r_N}\right), \tag{1.2}$$

where $\hat{H}$ is the Hamiltonian operator acting on $\psi\left(\mathbf{r_1}, ...\mathbf{r_N}\right)$ which is the many-body wavefunction for a system of particles (electrons and nuclei) at positions $\mathbf{r_i}$ and E is an energy eigenvalue.

The first step towards solving this complicated equation is to decouple the electronic

and vibrational components (Born-Oppenheimer approximation). The decoupling is justified by considering the large difference in mass between protons and electrons. Due to this difference, it is possible to assume that nuclei are stationary, which simplifies the calculation of the electronic component of ψ.

The Hamiltonian is a differential operator which represents the total energy as a sum of potential and kinetic energies:

$$\hat{H} = \hat{T}_e + \hat{V}_{ne} + \hat{V}_{ee}. \tag{1.3}$$

Defined in terms of atomic units where fundamental physical constants are set to unity, $\hat{T}_e$ is the kinetic energy operator which sums over i electrons:

$$\hat{T}_e = -\frac{1}{2}\sum_i \nabla^2. \tag{1.4}$$

$\hat{V}_{ne}$ is the potential energy operator for electron-ion interactions:

$$\hat{V}_{ne} = -\sum_i \sum_I \frac{Z_I}{|\mathbf{r_i} - \mathbf{R_I}|}, \tag{1.5}$$

where Z_I is the charge on the I^{th} ion and $\mathbf{r_i}$ and $\mathbf{R_I}$ are the positions of electrons and ions (nuclei) respectively. V_{ee} represents the interaction between electrons:

$$V_{ee} = \frac{1}{2}\sum_{i \neq j} \frac{1}{|\mathbf{r_i} - \mathbf{r_j}|}. \tag{1.6}$$

The exact solution of the Schrödinger equation becomes problematic for systems larger than the hydrogen atom because it then becomes a many body problem. Approximated solutions are used to predict properties of materials, with one of the most successful ways being the use of the density functional theory (DFT). Research developments leading up to the current form of DFT are explained below.

1.3 Density Functional Theory (DFT)

One of the most widely used approximations for solving the Schrödinger equation is the density functional theory (DFT). The theory describes the total energy of a system as a functional of a single function, the charge density n($\mathbf{r}$). Research developments leading up to the current form of DFT will be explained below.

1.3.1 The Thomas-Fermi approximation

In the late 1920's Llewellyn Thomas and Enrico Fermi used electronic density, not wave-functions, to study atoms and molecules. The Thomas-Fermi (TF) model treated only the kinetic energy of electrons quantum mechanically whilst nuclear-electron and electron-electron interactions were treated classically. Their approach was to assume the system to be a homogeneous gas of non-interacting electrons. The TF equation then gives the energy of a system in terms of the electron density, $n(\mathbf{r})$.

The TF theory has been successful at calculating the equations of state for elements [113] but the theory fails to describe key chemical properties such as the shell structures of atoms and binding of molecules. In particular, Teller [114] showed that the TF method incorrectly indicates that it is energetically favourable for a nitrogen dimer to remain as two separate atoms. The problem can be traced back to the crude estimation of the kinetic energy and the treatment of the electron-electron interactions in a classical way, ignoring quantum mechanical effects such as the exchange interaction. There was therefore a need for a different approach which treated these interactions quantum mechanically. Steps towards achieving this goal were made with the formulation of the Hohenberg-Kohn Theorem and subsequently development of the Kohn-Sham theory.

1.3.2 The Hohenberg-Kohn theorems

The first formulation of density functional theory as it is known today came from Hohenberg and Kohn (H-K) in 1964 [115]. They modelled the system as a gas of interacting electrons under the influence of an external potential $\upsilon_{ext}(\mathbf{r})$.

The first H-K theorem states that the external potential and therefore the total energy is a unique functional of the electron density $n(\mathbf{r})$. Since the external potential is a unique property of a specific system, this theorem implies that so is the ground state electron density. The second H-K theorem shows that for N electrons in a potential $\upsilon(\mathbf{r})$, the density functional is at its minimum value, that is the system is in its ground state, when the wavefunction yields the ground state density. Hohenberg and Kohn were thus able to describe the ground state energy (E) of a unique system in terms of its ground state electron density $n(\mathbf{r})$.

The Hamiltonian (Eqn. 1.3) is fully described by the external potential and the total number of electrons, which in turn can be calculated by integrating the electron density over all space. Therefore if external potential and the charge density are known, the Hamiltonian operator can be determined. Hohenberg and Kohn thus described the ground state energy of a system as:

$$E[n(\mathbf{r})] = \int n(\mathbf{r})\upsilon_{ext}(\mathbf{r})d\mathbf{r} + F[n(\mathbf{r})]. \tag{1.7}$$

$F[n(\mathbf{r})]$ is a universal functional of the electron density but is unknown. Approximations for it will be described in section 1.3.4.

1.3.3 Kohn-Sham theory

There are no known ways of calculating F[n(**r**)] exactly, however an approach to solving it was provided by Kohn and Sham in 1965 [116]. The starting point for Kohn and Sham's approximation to it was to set up a system of N non-interacting electrons in an effective potential $V_S(\mathbf{r})$, with a Hamiltonian ($\hat{f}^{KS}$) as a sum of the kinetic energy of the electrons and this effective potential:

$$\hat{f}^{KS} = -\frac{1}{2}\nabla^2 + V_S(\mathbf{r}), \tag{1.8}$$

Such as system's ground state wavefunction Θ_S (an approximation to the real wavefunction) is exactly represented by:

$$\Theta_S = \frac{1}{\sqrt{N}} \begin{vmatrix} \varphi_1(\vec{x_1}) & \varphi_2(\vec{x_1}) & \dots & \varphi_N(\vec{x_1}) \\ \varphi_1(\vec{x_2}) & \varphi_2(\vec{x_2}) & \dots & \varphi_N(\vec{x_2}) \\ \vdots & \vdots & \ddots & \vdots \\ \varphi_1(\vec{x_N}) & \varphi_2(\vec{x_N}) & \dots & \varphi_N(\vec{x_N}) \end{vmatrix}, \tag{1.9}$$

where $\varphi_i(\vec{x_i})$ is the wavefunction describing the ith electron, at position $\vec{x_i}$. The wavefunction of the system is defined in terms of the individual wavefunctions of each of the electrons that make the system up and can be determined using the following eigenvalue equation:

$$\hat{f}^{KS}\varphi_i = \varepsilon_i\varphi_i. \tag{1.10}$$

The ground state wavefunction (Eqn. 1.9) is a Slater determinant, which is an approximation to the real N-electron wavefunction. An effective potential $V_S(\mathbf{r})$ is applied to the fictitious system so that this system can represent the real one. To choose a $V_S(\mathbf{r})$ the

following condition must apply: the density of the fictitious system $n_{_S}(\mathbf{r})$ would equal that of the ground state density of the real (interacting) system ($n_{_0}(\mathbf{r})$). The condition is achieved by choosing a $V_S(\mathbf{r})$, which produces single electron wavefunctions (at position $\mathbf{r}$ and of spin s) that satisfy:

$$n_{_S}(\mathbf{r}) = \sum_{i}^{N} \sum_{s} |\varphi_i(\mathbf{r}, s)|^2 = n_{_0}(\mathbf{r}). \tag{1.11}$$

In the Kohn-Sham approach, as much of the true kinetic energy as possible is calculated exactly and approximations are used for the rest. The exact kinetic energy of a system of non-interacting electrons (with the same electron density as the real interacting system) is:

$$T_{_S} = -\frac{1}{2} \sum_{1}^{N} \left\langle \varphi_i \left| \nabla^2 \right| \varphi_i \right\rangle . \tag{1.12}$$

The true kinetic energy of an interacting system ($T[n(\mathbf{r})]$) is not described here so a correction is introduced to the universal functional $F[n(\mathbf{r})]$:

$$F[n(\mathbf{r})] = T[n(\mathbf{r})] + J[n(\mathbf{r})] + E_{XC}[n(\mathbf{r})], \tag{1.13}$$

where $J[n(\mathbf{r})]$ is the electron-electron interaction as a function of the electron density. The correction, the exchange correlation energy $E_{XC}[n(\mathbf{r})]$ represents the parts of the universal functional that are unknown:

$$\begin{aligned} E_{XC}[n(\mathbf{r})] &\equiv (T[n(\mathbf{r})] - T_S[n(\mathbf{r})]) + (E_{ee}[n(\mathbf{r})] - J[n(\mathbf{r})]) \\ &= T_c[n(\mathbf{r})] + E_{ncl}[n(\mathbf{r})]. \end{aligned} \tag{1.14}$$

E_{XC} is a sum of the excess of the true kinetic energy over the fictitious one ($T_c[n(\mathbf{r})]$) and the energy of the non-classical electrostatic contributions ($E_{ncl}[n(\mathbf{r})]$). The latter covers

the correction due to self-interaction and exchange and correlation effects between the electrons.

Kohn-Sham equations for an interacting system are attained by applying the variational principle and seeing how the orbitals φ_i can minimise the energy (assuming orthogonality of two orbitals), resulting in:

$$\begin{aligned} &\left(-\frac{1}{2}\nabla^2 + \left[\int \frac{n(\mathbf{r_2})}{r_{12}} d\mathbf{r_2} + V_{XC}(\mathbf{r_1}) - \sum_I^M \frac{Z_I}{r_{1I}}\right]\right)\varphi_i \\ &= \left(-\frac{1}{2}\nabla^2 + V_{eff}(\mathbf{r_1})\right)\varphi_i \\ &= \varepsilon_i \varphi_i \end{aligned} \tag{1.15}$$

The equation is a sum of the kinetic energy of the electrons, the electron-electron interaction, the exchange-correlation potential $V_{XC}(\mathbf{r_1})$ and the electron-nuclear interaction. The expression in the square brackets is equal to the effective potential and is equivalent to the non-interacting potential $V_S(\mathbf{r})$. Since $V_{XC}(\mathbf{r_1})$ is unknown, it is defined as a derivative of the energy with respect to the density:

$$V_{XC}(\mathbf{r_1}) \equiv \frac{\delta E_{XC}}{\delta n(\mathbf{r})}. \tag{1.16}$$

As V_{eff} is a function of the density, the Kohn-Sham single-electron equations (1.15) need to be solved iteratively until self-consistency is reached. Knowing V_{eff}, the orbitals φ_i and thus the ground state density (Eqn 1.11) and energy can be determined.

Kohn-Sham eigenstates do not represent any measurable quantities as they describe single-electron wavefunctions for a non-interacting gas. It is only the total energy and electron density derived from the Kohn-Sham equations that do have a physical meaning. However, the Kohn-Sham energy levels give adequate description of the band structure

for the occupied states of a real (interacting) crystal and capture the essential physics of the system.

1.3.4 Exchange-correlation functionals

The accuracy of DFT results is dependent upon the approximation of the exchange correlation functional. Many flavours of functional are available and are constantly under development, with their choice depending on the type of system being studied [8].

The most commonly used functionals are developed from the idea of a homogeneous electron gas, where exchange and correlation effects are local. This allowed the proposal of the local density approximation or LDA by Kohn and Sham [116]. The LDA treats the exchange-correlation energy as an integral over a local function of the electron density. This is a reasonable approximation for solids due to their fairly uniform charge distribution that is periodic in space, however it does not describe atoms and molecules well due to their rapidly varying charge densities. The exchange-correlation density at each point in space is assumed to be equal to that in a homogeneous electron gas with the same density. The energy functional is defined as:

$$E_{XC}^{LDA} = \int n(\mathbf{r}) \varepsilon_{XC}(n(\mathbf{r})) d\mathbf{r}, \tag{1.17}$$

where $\varepsilon_{XC}(n(\mathbf{r}))$ is the exchange-correlation energy per particle in a uniform electron gas with density $n(\mathbf{r})$. The energy can be split into its exchange and correlation components. There is no explicit expression for the correlation but the exchange, known as the Slater exchange can be defined as:

$$E_X = -\frac{3}{4} \sqrt[3]{\frac{3n(\mathbf{r})}{\pi}}. \tag{1.18}$$

Analytic expressions for the correlation energy have been developed based on simulations of the homogeneous electron gas [117, 118, 119].

Properties calculated using the LDA such as equilibrium structures, vibrational frequencies, phase stability and elastic moduli are comparable with experiment. However when calculating binding energies, the LDA can overestimate by 20-30%. The LDA also slightly underestimates bond lengths by 1-2% [8].

To account for non-homogeneity in the real electron density an extension of the LDA was proposed to include information about the gradient of the charge density $\nabla n(\mathbf{r})$. Named the generalized gradient approximation or the GGA, it has the following form for its energy functional:

$$E_{XC}^{GGA} = \int n(\mathbf{r})\varepsilon_{_{XC}}(n(\mathbf{r}), \nabla n(\mathbf{r}))d\mathbf{r}. \tag{1.19}$$

The GGA improves on the LDA calculation of binding energies in molecules and solids, yet it often over-estimates properties that rely on the equilibrium lattice constant. Efforts have been made to create functionals which improve lattice constants and cohesive energies, however there have been some troubles. Introducing more gradient dependence into the functional improves the total energies. Reducing gradient dependence improves the lattice constants but at a detriment to the calculated energies. Overall the LDA and GGA are thought to be good approximations for most solid state systems. However it still needs to be noted that the GGA exchange-correlation functional is often called semi-local even though it depends on a single point in space and does not provide any information about nonlocal effects.

In this thesis we will use the GGA for evaluating the thermodynamic, electronic and superconducting properties of compounds. To confirm the thermodynamic stability of

one particular structure over another, the GGA enthalpies are sometimes compared with various flavours of the GGA and LDA.

1.3.5 Implementation of DFT

The method of implementing DFT depends on the system being studied. For periodic crystals, Bloch's theorem can be used to describe the single electron wavefunctions ($\varphi_i(\vec{x_i})$) required by the Kohn-Sham theory. As the electron will be within a periodic potential, the wavefunction can be written as a product of the lattice periodicity $u_{n\mathbf{k}}(\mathbf{r})$ and a wave-like part $e^{ik\cdot\mathbf{r}}$:

$$\psi_{n\mathbf{k}}(\mathbf{r}) = u_{n\mathbf{k}}(\mathbf{r})e^{i\mathbf{k}\cdot\mathbf{r}}, \tag{1.20}$$

where n represents the band index and $\mathbf{k}$, the wavevector. As $u_{n\mathbf{k}}(\mathbf{r})$ follows the periodicity of the real lattice it can be written in terms of a plane-wave basis set:

$$u_n(\mathbf{r}) = \sum_G c_{n,\mathbf{G}} e^{i\mathbf{G}\cdot\mathbf{r}}. \tag{1.21}$$

$\mathbf{G}$ represents the wavevectors which are the reciprocal lattice vectors of the crystal and $c_{n,\mathbf{G}}$ the plane-wave coefficients. The electronic wavefunction can be expanded in terms of a linear combination of these plane-waves:

$$\psi_{n,\mathbf{k}}(\mathbf{r}) = \sum_G c_{n,\mathbf{k}+\mathbf{G}} e^{i\mathbf{k}+\mathbf{G}\cdot\mathbf{r}}. \tag{1.22}$$

For a true wavefunction the expression would need to be expanded at each $\mathbf{k}$-point with an infinite number of plane-waves. As this is not practical and only small kinetic energy terms representing the valence electrons are important, an energy cut off is imposed:

$$\frac{1}{2}\left|\mathbf{k}+\mathbf{G}\right|^2 < E_{cut}. \tag{1.23}$$

Using this constraint makes it easy to check the convergence of the energy with respect to accuracy, which is not to easy to do when using localised atomic basis sets. Other advantages of plane waves include ease of switching between real and reciprocal space due advanced FFT (Fast Fourier Transform) algorithms and having no bias towards atomic positions.

Wavefunctions of electrons close to the nuclear core oscillate rapidly for heavy elements, requiring a very large number of plane waves to represent them. As the core electrons do not participate in binding, it is possible to replace core electron wavefunctions and the strong Coulomb potential of the nucleus with a pseudopotential. This saves significant computational costs.

1.3.6 Crystal structure search

Traditionally, the search for new superconducting materials has involved combining chemical elements in the laboratory at varying compositions with the intent of discovering new compounds. The trial and error approach, known as combinatorial chemistry, is expensive and time consuming. Due to advancements in the availability of supercomputing power it is now possible to use the combinatorial approach with computational experiments.

A variety of computational *ab initio* crystal structure prediction tools have been developed by the material science community over the past decade [120, 121, 122, 123, 124,]. All the tools have the goal of determining the lowest energy configuration of atoms within a unit cell, defined as the ground state crystal structure. Whilst many of the tools use DFT they differ in the way (algorithms) they arrive at the proposed lowest energy structure. Predictions of new superconductors in particular have been dominated by the use of evolutionary algorithms, for example FeB_4, T_c = 15-20K [125] (described in section 2)

and $CaLi_2$ at 45 GPa, $T_c = 15$K [126]. Particle-swarm optimisation methods (BC_7, $T_c =$ 11 K [127]), random sampling (PtH at 80 GPa, $T_c = 20$ K [128]) and the minima hopping method (Si_2H_6 at 100 GPa, $T_c = 20$ K [129]) are also becoming more common.

Structure prediction is used to study variety of materials and compounds other than superconductors. For example, the simulated annealing approach has been used successfuly to solve inorganic crystal structures from experimental results. The method uses a Monte Carlo scheme or molecular dynamics to perturb random atoms in the crystal at high temperatures. The process is repeated whilst lowering the temperature with the aim of mapping out the potential energy surface and finding the global minimum. The higher temperatures used for similuated annealing over evolutionary search methods allows the system to overcome energy barriers between local minima more easily. The method generally requires some unit cell parameters which are not an input for evolutionary searches [130].

The pharmaceutical industry requires accurate determination of a medicine's crystal structure due to problems associated with different crystal polymorphs resulting in different medicinal side effects. The structure prediction of organic molecular crystals is thus an active field of research. Molecular dynamics simulations are often used to study the packing of molecules in a unit cell and theoretical studies are often coupled with experiments. The methods for prediction of the structures of molecular crystals are advancing rapidly as demonstrated by the success achieved in blind tests to determine the structures of new (unpublished) compounds [130].

The work described in this thesis has used an evolutionary algorithm implemented by Dr Aleksey Kolmogorov into a tool called the Module for Ab Initio Structure Evolution (MAISE) [120]. All structure searches have been performed by Aleksey Kolmogorov.

I have taken the resulting structures from the search and analysed their electronic, vibrational, superconducting and stability properties related to geometry. From stability analysis I have provided some input as to which searches should be run. A short description of MAISE will be given here.

All the crystal structure searches begin with using DFT to calculate the formation enthalpy of the metal boride compound in known structures listed in the inorganic crystal structure database (ICSD). This is followed by an unconstrained search to find the lowest energy structure using the evolutionary algorithm tool, MAISE. To begin, a 'population' of structures are generated given only the stoichiometry of the compound. The structures are created by placing atoms randomly in a unit cell with variable cell parameters (vectors and angles). DFT as implemented in VASP is used to calculate the enthalpy of each structure in the population. The structures are then left to 'mate' and 'mutate' to generate offspring or the new population. The probability of a structure's survival to the next population is set to be nearly proportional to the enthalpy of that structure, the lowest enthalpy being most likely to survive. The generation of offspring involves a combination of operations. A crossover operation merges approximately half of two parents selected at random. The mutation operation involves distortion of the lattice vectors and the distortion or swapping of atomic positions. An inversion operation results in a parent structure being selected at random, half of it being removed and filled with an inversion (with respect to the origin) of the half that is left. A combination of all these operations (as set by the user) are used to generate the next population. The process of creating new populations is repeated until the lowest energy structure in a series of populations remains the same.

1.4 Theory of superconductivity

In the early 1900's H. Kamerlingh Onnes [131] was the first scientist to liquefy helium and thus reach temperatures of only a few kelvin. It was this achievement that led to the discovery of superconductivity. The aim was then to understand how the electrons and ions behaved when a material went from a normal conducting state to a superconducting one. The major question was how the two states differed. Many famous physicists of the time attempted to answer the question including Einstein and Heisenberg [132]. However it was not until the late 1950s that a now widely accepted, microscopic theory was proposed.

Onnes noted the disappearance of electrical resistance in metals such as mercury, lead and tin below specific critical temperatures, T_c, which is the first benchmark for showing that a material is a superconductor. Early attempts were made to explain the phenomenon by describing interactions between fundamental particles using the recently developed ideas of quantum mechanics. However no theory had predicted the second benchmark in superconductivity history. In 1933, Meissner and Ochsenfeld (original - [133], translated - [134]) demonstrated that a superconductor excludes the magnetic field from entering the material. They also showed that as a superconductor is cooled below its T_c, the magnetic field present in the normal state is expelled from the material as shown in Figure 1.9. Most importantly, as the expulsion of a field is a reversible process, it demonstrated that the superconducting state is truly thermodynamic. The lack of magnetic field inside the superconductor also indicated perfect diamagnetism but showed that superconductors are not perfect conductors as this would require the magnetic field to remain fixed inside the material. It was later found that the magnetic field is not

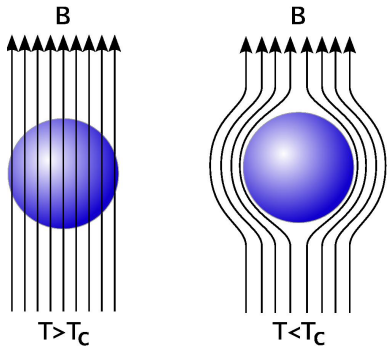


Figure 1.9: At temperatures above T_c, magnetic field lines are able to pass through the material. Below the T_c magnetic field is expelled, displaying the Meissner and Oschenfeld effect. The image is taken from Reference [135].

completely excluded from an ideal superconductor but exists within a small layer at the surface. This layer, known as the penetration depth (λ), is about five hundred angstroms thick and was described by F. and H. London in 1935 [136].

London and London proposed equations for the microscopic electric and magnetic fields within a superconductor. One of their equations showed that applying an electric field to a superconductor accelerates the superconducting electrons, unlike electrons in a normal conductor which would move at a velocity determined by collisions with the ionic lattice, resulting in electrical resistance.

In the nineteen thirties and forties a few attempts were made at developing superconductivity theories [137, 138] however none of these were successful. The goal was to find the interaction between the conducting electrons that cause the total energy of the system to be lowered when entering a superconducting state. The next major development came in 1950 when two independent groups showed that the T_c is dependent on the mass of the isotope present in the superconductor [139, 140]. Their work on mercury was a primary indication that the lattice is involved with the superconducting transition, possibly through an electron-phonon interaction. At the same time Fröhlich [141] was developing a superconductivity theory which would predict the isotope effect. He showed through

second-order perturbation theory that electrons are attracted to each other through interactions with phonons. His theory was not complete as the Meissner effect could not be described but it formed a new way of thinking for future attempts [138] at explaining the superconducting state. In 1956 Cooper described a part of the mechanism as we know it today, with electrons forming bound pairs [142]. These Cooper pairs formed the basis of the full BCS theory published the following year.

1.4.1 The BCS theory

In 1957 John Bardeen, Leon Cooper and John Robert Schrieffer published a monumental paper with their theory of superconductivity [5]. The BCS theory assumes a lattice of atomic ions surrounded by electrons that can be described as a Fermi gas. Introducing just one electron into this system, ignoring all other electrons, the electron distorts the lattice by attracting positive ions to it. The electron has now polarised the lattice and led to an accumulation of positive charge around its path. A second electron is introduced and feels the polarization due to the first electron, resulting in the second electron being attracted to the first, forming a pair of electrons known as the Cooper pair. The situation just described is the electron-phonon coupling mechanism, whose strength determines the T_c of a material.

To formulate BCS theory, one must first establish some properties of the Cooper pair [143]. A Fermi gas of electrons is unstable with respect to the formation of at least one bound pair of electrons, so long as there is an attractive interaction between them. When two electrons are added to a Fermi sea at 0K they interact with each other but not with the sea as a whole, apart from via the Pauli exclusion principle. For a description of the system a two-particle wavefunction needs to be established. Using Bloch's theory and the

fact that the lowest energy state requires the two electrons to have equal and opposite spin, the following orbital wavefunction is obtained:

$$\psi_0(\mathbf{r_1}, \mathbf{r_1}) = \sum_{\mathbf{k}} \mathbf{g_k} \mathbf{e}^{\mathbf{ik \cdot r_1}} \mathbf{e}^{-\mathbf{ik \cdot r_2}}. \tag{1.24}$$

Taking into account the antisymmetry of the total wavefunction with respect to exchange of the two electrons and inserting the Schrödinger equation, the result is an energy eigenvalue problem:

$$(E - 2\varepsilon_{\mathbf{k}}) g_{\mathbf{k}} = \sum_{k>k_f} V_{\mathbf{kk'}} g_{\mathbf{k'}}, \tag{1.25}$$

with weighting coefficients $g_{\mathbf{k}}$ and plane-wave energies $\varepsilon_{\mathbf{k}}$. $V_{\mathbf{kk'}}$ are the matrix elements for the interaction potential between two electrons, representing the strength for scattering a pair of electrons with momenta $(\mathbf{k'}, -\mathbf{k'})$ to $(\mathbf{k}, -\mathbf{k})$. A bound-pair exists when a set of $g_{\mathbf{k}}$ is found with $E < 2E_F$. The difficulty comes when describing the situation for any general $V_{\mathbf{kk'}}$. For this reason, Cooper introduced an approximation (Figure 1.10): for all states out to a cutoff energy $\hbar\omega_c$ away from E_F, $V_{\mathbf{kk'}} = -V$, $V_{\mathbf{kk'}} = 0$ for all states beyond $\hbar\omega_c$.

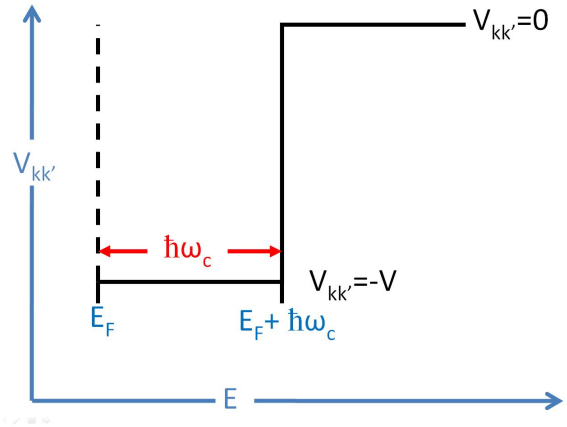


Figure 1.10: Cooper's approximation to the interaction potential $V_{\mathbf{kk'}}$.

Using Cooper's approximation yields an equation which integrates only over energy

states whose potential depends on **k** and introduce N(0) which is the density of states at the Fermi level per unit spin:

$$\frac{1}{V} = N(0) \int_{E_F}^{E_F+\hbar\omega_c} \frac{d\varepsilon}{2\varepsilon - E} = \frac{1}{2} N(0) ln \frac{2E_F - E + 2\hbar\omega_c}{2E_F - E}. \tag{1.26}$$

N(0)V is usually < 0.3 for BCS superconductors, so the equation can be written as:

$$E \approx 2E_F - 2\hbar\omega_c e^{-2/N(0)V}. \tag{1.27}$$

The result is a bound state of electrons which have an energy lower than the Fermi surface and $\mathbf{k} > \mathbf{k}_f$. The kinetic energy of the electrons is higher than E_F, but the attractive potential contributes more to the total energy of the system, leading to binding no matter how small V is.

Going back to the idea of electrons polarising the lattice leading to an attraction between two electrons, one would assume that the fundamental phonon frequencies of the lattice would affect this attraction. For example, if an electron is scattered from **k** to **k'**, the associated phonon would carry a momentum of $\mathbf{q} = \mathbf{k}\text{-}\mathbf{k'}$, with a phonon frequency $\omega_{\mathbf{q}}$. If the difference in energies between the two electrons is greater than $\hbar\omega_{\mathbf{q}}$, that results in a repulsive interaction and therefore bound pairs of electrons will not form. Subsequently the cutoff energy $\hbar\omega_c$ of the matrix element -V is assumed as being of the order of the Debye energy $\hbar\omega_D = \mathbf{k}\theta_D$, which also characterises the cutoff of the phonon spectrum.

A description of the superconducting system is made simpler, through the definition of the BCS wavefunction. For the wavefunction, Slater determinants representing antisymmetrized product functions of N electrons are written in terms of the occupancy of states. A compact way of representing the many-body quasi-particle excitations of the system is through the process of second quantisation. For this, there is a creation operator

$c^*_{\mathbf{k}\uparrow}$, which creates a spin up electron with momentum $\mathbf{k}$. An analogous annihilation operator $c_{\mathbf{k}\uparrow}$ removes the electron from this state, resulting in the following ground state function using operators acting on the Fermi sea $|F\rangle$:

$$|\psi_0\rangle = \sum_{k>k_F} g_{\mathbf{k}} c^*_{\mathbf{k}\uparrow} c^*_{-\mathbf{k}\downarrow} |F\rangle \,. \tag{1.28}$$

A particle number operator $n_{\mathbf{k}\sigma}$ is defined. It has has an eigenvalue of one for an occupied state and zero for an unoccupied state:

$$n_{\mathbf{k}\sigma} = c^*_{-\mathbf{k}\sigma} c_{\mathbf{k}\sigma}. \tag{1.29}$$

The BCS wavefunction is an N-electron wavefunction in terms of momentum eigenfunctions:

$$|\psi_N\rangle = \sum g(\mathbf{k_i}, ..., \mathbf{k_l}) \mathbf{c}^*_{\mathbf{k_i}\uparrow} \mathbf{c}^*_{-\mathbf{k_i}\downarrow} \cdots \mathbf{c}^*_{\mathbf{k_l}\uparrow} \mathbf{c}^*_{-\mathbf{k_l}\downarrow} |\phi_{\mathbf{0}}\rangle \,, \tag{1.30}$$

where the operators act on the vacuum state $|\phi_0\rangle$ containing no particles. $\mathbf{k_i}$ and $\mathbf{k_l}$ are the $\mathbf{k}$ values for the initial and final parts of the occupied band. g is the weight of that particular product of creation operators. As the sum is over all $\mathbf{k}$ values in the band, there are more combinations of occupancies than can be handled. To simplify, the Hartree self-consistent field approach is used, where the occupancy of each state $\mathbf{k}$ depends only on the average occupancy of all other states, defining the BCS ground state as:

$$|\psi_G\rangle = \prod_{\mathbf{k}=\mathbf{k_1},...,\mathbf{k_M}} (u_{\mathbf{k}} + \nu_{\mathbf{k}} c^*_{\mathbf{k}\uparrow} c^*_{-\mathbf{k}\downarrow}) |\phi_0\rangle \,, \tag{1.31}$$

where $|u_{\mathbf{k}}|^2 + |\nu_{\mathbf{k}}|^2 = 1$. $|\nu_{\mathbf{k}}|^2$ is the probability that the pair $(\mathbf{k}\uparrow, -\mathbf{k}\downarrow)$ is occupied and $|u_{\mathbf{k}}|^2$ the probability that it is unoccupied. Therefore the state is solely determined by $u_{\mathbf{k}}$ and $\nu_{\mathbf{k}}$. A pairing or reduced Hamiltonian is defined involving only paired states

as unpaired states have zero expectation values:

$$H_{red} = \sum_{\mathbf{k}\sigma} \epsilon_{\mathbf{k}} n_{\mathbf{k}\sigma} + \sum_{\mathbf{kl}} c^*_{\mathbf{k}\uparrow} c^*_{-\mathbf{k}\downarrow} c_{-l\downarrow} c_{l\uparrow}. \tag{1.32}$$

Minimizing the ground state energy using the proposed ansatz for the wavefunction (Eqn. 1.31) and the reduced Hamiltonian, the result is:

$$\Delta_{\mathbf{k}} = -\sum_{\mathbf{k}'} V_{\mathbf{k}\mathbf{k}'} \frac{\Delta_{\mathbf{k}'}}{2E_{\mathbf{k}'}} tanh \frac{E_{\mathbf{k}'}}{2k_B T}, \tag{1.33}$$

where $E_{\mathbf{k}}$ is the quasiparticle excitation energy and is equal to $\sqrt{\varepsilon^2_{\mathbf{k}} + \Delta_{\mathbf{k}^2}}$. At the Fermi level, the excitation energy tends towards a value $\Delta_{\mathbf{k}}$, the energy gap. The gap can be defined as the energy required to pull apart the Cooper pair, thus destroying superconductivity. Giving reason for the gap to tend towards zero at the T_c, defining:

$$k_B T_c = 1.14\omega_c e^{-\frac{1}{N(0)V}}. \tag{1.34}$$

The product N(0)V is equal to λ, the electron-phonon coupling constant. Taking into account coulomb repulsions between the electrons an equation including μ the coulomb pseudopotential is defined, which will be described in the next section.

The BCS theory yielded many universal numbers including the most important relationship between the energy gap and the T_c:

$$\frac{2\Delta(0)}{T_c} = 3.54. \tag{1.35}$$

Unfortunately the BCS theory was not able to predict the T_c of so called strong coupling superconductors (lead, mercury) - those with high λ values, leading to the developments of the Eliashberg theory, which will be described in the following section.

1.4.2 The Migdal-Eliashberg theory

The main problem with Frohlich's theory of superconductivity was the failure of perturbation theory to properly describe the state. In 1958 Migdal [6] overcame this with a Green's function approach to the problem [144, 145], which allowed the study of the electronic excitation spectrum for any electron-phonon coupling strength for the normal state of a metal. Migdal stated that as the BCS theory used a time-independent interaction between electrons, not enough of the electron-phonon effects were described properly. Eliashberg used the Migdal theorem for the normal state and applied it to the superconducting state, introducing a pair of equations which relate the energy gap function $\Delta(\omega)$ for the superconducting state to the electron-electron and electron-phonon interactions in the normal state. Both theories have been well described in many reviews and books [146, 147, 148, 149, 138]

Many-body interactions in a superconductor cannot be assumed to be weak, therefore it is difficult to evaluate macroscopic properties accurately without considering infinite sequences in a perturbation theory series [144]. To overcome this problem, the Green's function approach as used in quantum field theory was employed by Gor'kov. Knowledge of the form of the Green's functions for electrons in a solid, allowed properties related to quasiparticles and the elementary excitations to be calculated. Gor'kov showed that the superconducting state can be described by two Green's functions: one for the normal state of a metal and the other, an anomalous function, for the condensate of Cooper pairs. Therefore the superconducting state can be represented as a generalised Green's function which is a 2x2 matrix:

$$\hat{G}(k,\tau) = -\begin{pmatrix} \langle T_\tau c_{k\uparrow}(\tau) c^+_{k\uparrow}(0)\rangle & \langle T_\tau c_{k\uparrow}(\tau) c_{-k\downarrow}(0)\rangle \\ \langle T_\tau c^+_{-k\downarrow}(\tau) c^+_{k\uparrow}(0)\rangle & \langle T_\tau c^+_{-k\downarrow}(\tau) c_{-k\downarrow}(0)\rangle \end{pmatrix}. \tag{1.36}$$

The top left element of the matrix is the normal state single particle Green's function. The top right and bottom left, off diagonal elements are Gor'kov's anomalous functions. For a non-interacting system of electrons, the off-diagonal elements vanish. This leaves the (1,1) element of the form (iω_n-ε_k)$^{-1}$, where $i\omega_n$ is the Fermion Matsubara frequency and ε_k the quasiparticle excitation energy. The equations of motion (Eqns. 1.37, 1.38) for anomalous Green's functions yields a pair of coupled nonlinear differential equations, which return the BCS theory when solved.

$$\left(-\frac{d}{d\tau} - \varepsilon_k\right) G(k,\tau) = \delta(\tau) - \sum_{k'} V_{kk'} F(k',0) \overline{F}(k,\tau), \tag{1.37}$$

$$\left(-\frac{d}{d\tau} - \varepsilon_k\right) \overline{F}(k,\tau) = -\sum_{k'} V_{kk'} \overline{F}(k',0) G(k,\tau). \tag{1.38}$$

Extracting the BCS gap $\Delta_k = \sum_{k'} V_{kk'} F(k',0)$ and applying a Fourier transform yields the matrix:

$$\begin{pmatrix} i\omega_n - \varepsilon_k & \Delta_k \\ \Delta_k^* & i\omega_n + \varepsilon_k \end{pmatrix} \begin{pmatrix} G(k,i\omega_n) \\ \overline{F}(k,i\omega_n) \end{pmatrix} = \begin{pmatrix} 1 \\ 0 \end{pmatrix}. \tag{1.39}$$

In the limit of $\Delta_k \to 0$, the normal state solution is retrieved.

In order to include all interactions, a corresponding phonon Green's function needs to be introduced:

$$D_{\alpha\beta}(\mathbf{q},\tau) = -\langle T_\tau u_{\mathbf{q}\alpha}(\tau) u_{-\mathbf{q}\beta}(0)\rangle, \tag{1.40}$$

where u is the displacement operator, T_τ is the Wick time ordering operator and $\mathbf{q}$ is

the wave vector. To calculate the Green's functions for a system of interacting electrons and phonons, the functions can be expressed in terms of their respective self-energies Σ and Π, giving Dyson's equations (Eqns. 1.41,1.42). The self-energy is the contribution to particle's energy due to interactions between the particle and its surrounding system.

$$G^{-1}(\mathbf{k}, i\omega_n) = [G_0^{-1}(\mathbf{k}, i\omega_n) - \Sigma(\mathbf{k}, i\omega_\nu)], \tag{1.41}$$

$$D^{-1}(\mathbf{q}, i\omega_\nu) = [D_0^{-1}(\mathbf{q}, i\omega_\nu) - \Pi(\mathbf{q}, i\omega_n)], \tag{1.42}$$

where G_0 and D_0 are the bare, non interacting functions which equal:

$$G_0(\mathbf{k}, i\omega_n) = [i\omega_n - \varepsilon_k]^{-1} \tag{1.43}$$

for the electron and

$$D_0(\mathbf{q}, i\omega_\nu) = [-M(\omega^2(\mathbf{q}) + \omega_\nu^2)]^{-1} \tag{1.44}$$

for the phonon. $\omega(\mathbf{q})$ is the phonon dispersion and ε_k the single electron dispersion. It is relatively simple to compute the bare functions compared to the self-energies, which are more difficult to compute.

Using the Migdal theory, the electronic self-energy is defined as a product of the electron Green's function, phonon Green's function and the square of a coupling function g:

$$\Sigma(\mathbf{k}, i\omega_m) = -\frac{1}{N\beta} \sum_{\mathbf{k}', m'} |g_{\mathbf{k},\mathbf{k}'}|^2 \times D(\mathbf{k} - \mathbf{k}', i\omega_m - i\omega_{m'}) \times G(\mathbf{k}', i\omega_{m'}). \tag{1.45}$$

The simplicity of using Migdal theory comes from the fact that only the lowest order Feynmann diagrams, or perturbations are used to calculate the self-energy of the electron (1.45). With this in mind, the self-energy can still be calculated to within an accuracy

of order $(m/M)^{1/2}$ (m = electron mass, M = ionic mass), which is approximately 10^{-2}. The result demonstrates the success and universality of Migdal's theory as it does not depend on the electron-phonon coupling strength, but only on a small parameter $(m/M)^{1/2}$, resulting in analogous equations to 1.45 and 1.41 being developed by Eliashberg for the superconducting state which will be discussed later in this section.

To evaluate the expression for the electronic self-energy due to the electron-phonon interaction (1.45), the phonon Green's function needs to be written in terms of its spectral representation:

$$\Sigma(\mathbf{k}, i\omega_m) = T\sum_{\mathbf{k}',\nu}\int_0^\infty d\Omega \frac{\alpha^2F(\mathbf{k},\mathbf{k}',\Omega)}{N(0)}\left(\frac{2\Omega}{\omega_\nu^2+\Omega^2}\right)G(\mathbf{k}', i\omega_n-\omega_\nu). \tag{1.46}$$

The important electron-phonon spectral function α^2F has now been introduced and is defined by the product of the density of states at the Fermi level N(0), the square of the coupling function g and the phonon density of states B:

$$\alpha^2_{\mathbf{k},\mathbf{k}'}F(\mathbf{k},\mathbf{k}',\Omega) \equiv N(0)\left|g_{\mathbf{k},\mathbf{k}'}\right|^2 B(\mathbf{k}-\mathbf{k}',\Omega). \tag{1.47}$$

This particular form describes the ability of phonons with frequency Ω to scatter electrons from **k** to **k'** on the Fermi surface. The form which will be used by the Migdal-Eliashberg theory is the ability of a phonon to scatter electrons from any state to any other state on the Fermi surface and is defined by:

$$\begin{aligned}\alpha^2F(\Omega) \quad &= \tfrac{1}{N(0)^2}\textstyle\sum_{\mathbf{k},\mathbf{k}'}\alpha^2F(\mathbf{k},\mathbf{k}',\Omega)\delta(\varepsilon_{\mathbf{k}})\delta(\varepsilon_{\mathbf{k}'}) \\ &\equiv \langle\alpha^2F(\mathbf{k},\Omega)\rangle_{FS} = \langle\langle\alpha^2F(\mathbf{k},\mathbf{k}',\Omega)\rangle\rangle_{FS}\end{aligned} \tag{1.48}$$

where the total density of states is calculated by summing the delta functions over all **k**

points.

Based on the theories presented by Migdal, Nambu and Gor'kov, Eliashberg developed a pair of coupled integral equations relating the superconducting gap to interactions in the normal state. The energy gap function $\Delta(\omega)$ at T = 0 K is defined as:

$$\Delta(\omega) = \frac{1}{Z_s(\omega)} \int_0^{\omega_c} d\nu Re \left\{ \frac{\Delta(\nu)}{[\nu^2 - \Delta^2(\nu)]^{1/2}} \right\} \{K_+(\nu, \omega) - N(0)U_C\}, \tag{1.49}$$

where $Z_s(\omega)$, the renormalization parameter is:

$$[1 - Z_s(\omega)]\omega = \int_0^{\infty} d\nu Re \left\{ \frac{\nu}{[\nu^2 - \Delta^2(\nu)]^{1/2}} \right\} K_-(\nu, \omega), \tag{1.50}$$

and the functions $K_\pm(\nu, \omega)$ are:

$$K_\pm(\nu, \omega) = \int_0^{\omega_{max}} d\omega' \alpha^2 F(\omega') \left(\frac{1}{\omega + \omega' + \nu + i\delta} \mp \frac{1}{\omega - \omega' - \nu + i\delta} \right). \tag{1.51}$$

$\alpha^2 F(\omega')$, the electron-phonon coupling function is the same as for the normal state. U_C, the Coulomb pseudopotential, represents the the Coulomb interaction between the electrons. ω_c, the cutoff frequency is often chosen to be around ten times the Debye frequency and δ is a positive infinitesimal number. Isotropy has been assumed, therefore the magnitude of $\Delta(\omega)$ and $Z_s(\omega)$ does not depend on the wavevector.

A number of of empirical formulae to calculate the T_c from the Eliashberg equations, were proposed and are reviewed by Allen and Mitrović [148] and Grimvall [146]. The most popular form was developed by McMillan in 1968 [150]. His equation was derived from experimental results, which defined the T_c in terms of the phonon spectrum, electron-phonon interaction and Coulomb electron-electron interactions. The McMillan equation was successful because it could be applied for a larger range of coupling constants than

the equations resulting from the BCS theory. McMillan assumed that the Eliashberg spectral $\alpha^2F(\omega)$ function had the same shape as the phonon density of states $F(\omega)$ for niobium. The value of $\alpha^2F(\omega)$ was then adjusted to give values for the coupling constant λ ranging between 0.1 and 1.5. Electron-electron interactions were represented by a Coulomb pseudopotential μ^* first described by Morel and Anderson [151], which is defined by:

$$\mu^* = \frac{N(0)V_c}{1 + N(0)V_c ln(E_B/\omega_0)}. \tag{1.52}$$

μ^* was taken to be a constant between 0 and 0.25. Finally McMillan found the best fit between λ and μ^* for a particular T_c.

Many improvements on the McMillan formula have been proposed [146]. The Allen-Dynes form is the most commonly used in present calculations:

$$T_c = \frac{\langle\omega\rangle_{log}}{1.20} exp\left(-\frac{1.04(1+\lambda)}{\lambda - \mu^*(1+0.62\lambda)}\right). \tag{1.53}$$

λ is a dimensionless measure of the strength of the spectral coupling function $\alpha^2F(\omega)$:

$$\lambda \equiv 2\int_0^\infty \frac{\alpha^2F(\omega)}{\omega} d\omega. \tag{1.54}$$

$\langle\omega\rangle_{log}$ is the logarithmic averaged phonon frequency and is calculated using:

$$\langle\omega\rangle_{log} = exp\left[\left(\frac{2}{\lambda}\right)\int_0^\infty \frac{\alpha^2F(\omega)log(\omega)}{\omega} d\omega\right]. \tag{1.55}$$

Finally to calculate the T_c, all the components of the Allen-Dynes equation need to be determined. The phonon frequency and lambda are calculated using density functional perturbation theory as described in section 1.5. μ^* is often taken as a value between 0.1 and 0.15 as this ensures good agreement with experiment, typically to within a factor of 2.

1.5 Calculation of superconductivity properties

The Migdal-Eliashberg theory can provide a practical estimate of the T_c. One of the methods of implementation is through the use of the Allen-Dynes equation (Eqn. 1.53). Two quantities are required for its calculation: $\langle\omega\rangle_{log}$, the logarithmic averaged phonon frequency and λ, the strength of the electron-phonon interaction, which is itself an integral of the Eliashberg spectral function $\alpha^2F(\Omega)$ (Eqn. 1.47). The following section will describe how individual components of the Allen-Dynes equation can be calculated through computation of electronic and vibrational properties. It will also show how linear response is used to obtain these, allowing the fast assessment of the superconductivity potential of any stable compound.

The Eliashberg function can be evaluated as a product of three components (Eqn. 1.47). The electronic density of states at the Fermi level, N(0) can be found directly using density functional theory. Density functional perturbation theory is required to calculate the vibrational properties, the phonon density of states (PHDOS) and the electron-phonon matrix element. Originally researchers would take vibrational information from experimental inelastic neutron scattering data but it is now more convenient to calculate this from first principles.

1.5.1 Phonon properties

Developments of the linear-response theory of lattice vibrations together with density functional perturbation theory (DFPT) now allow straightforward assessment of the vibrational properties of a crystal [152], limited only by the computational resources available. DFPT applies standard equations of motion to the ions present in a solid. Considering

a periodic solid at its equilibrium position $\mathbf{R_I}$ and making a small displacement $\mathbf{u_I}$ from it, the total energy of the system can be expanded as a Taylor series with respect to this displacement:

$$E_{tot}(\mathbf{R}_I + \mathbf{u}_I) = E_{tot}(\mathbf{R}_I) + \sum_{I\alpha} \frac{\partial E_{tot}}{\partial \mathbf{u}_{I\alpha}} \mathbf{u}_{I\alpha} + \frac{1}{2} \sum_{\mathbf{I}\alpha, J\beta} \frac{\partial^2 E_{tot}}{\partial \mathbf{u}_{I\alpha} \partial \mathbf{u}_{J\beta}} \mathbf{u}_{I\alpha} \mathbf{u}_{J\beta} + ..., \tag{1.56}$$

with atoms I and J and their cartesian coordinates α and β. At the equilibrium position, the derivative of the total energy with respect to displacement is zero. To calculate the vibrational frequencies of the system it is assumed that the solution of the equations of motion have the form of that of a phonon:

$$\omega^2_{\mathbf{q}} \mathbf{u}_{s\alpha}(\mathbf{q}) = \sum_{s'\beta} D_{s\alpha s'\beta}(\mathbf{q}) \mathbf{u}_{s'\beta}(\mathbf{q}). \tag{1.57}$$

$D_{s\alpha s'\beta}(\mathbf{q})$ represents the dynamical matrix of the solid and is defined as:

$$D_{s\alpha s'\beta}(\mathbf{q}) = \frac{1}{\sqrt{M_s M_{s'}}} \sum_{\nu} \frac{\partial^2 E_{tot}}{\partial \mathbf{u}_{\mu \mathbf{S}\alpha} \partial \mathbf{u}_{\nu \mathbf{S}'\beta}} e^{i\mathbf{q}(\mathbf{R}_\nu - \mathbf{R}_\mu)}. \tag{1.58}$$

Computing the dynamical matrix requires the derivative of the total energy with respect to displacement. Perturbation theory is used to assess the effect of these displacements (perturbations) on the charge density as calculated from DFT. This results in a set of self-consistent equations for 3 X N_{at} perturbations for a fixed vector $\mathbf{q}$. Solving the equations for a particular $\mathbf{q}$ will give the dynamical matrix for this vector. Diagonalising the matrix yields 3 X N_{at} frequencies $\omega_{\mathbf{q}}$. By repeating for several $\mathbf{q}$ it is possible to plot $\omega_{\mathbf{q}}$ as a function of $\mathbf{q}$. It is however more convenient to approach the problem in a different way by calculating the dynamical matrix on a small uniform mesh of $\mathbf{q}$ vectors.

The dynamical matrix is a periodic function of $\mathbf{q}$ with $D_{s\alpha s'\beta}(\mathbf{q} + \mathbf{G}) = D_{s\alpha s'\beta}(\mathbf{q})$ for

any reciprocal lattice vector $\mathbf{G}$. Also, due to the translational invariance of the solid, the function does not depend on μ. The Fourier expansion of a three dimensional periodic function for this system contains Fourier components only at discrete values $\mathbf{R}_\nu$ of the Bravais lattice:

$$\frac{1}{\sqrt{M_s M_{s'}}} \frac{\partial^2 E_{tot}}{\partial \mathbf{u}_{\mu \mathbf{S}\alpha} \partial \mathbf{u}_{\nu \mathbf{S}'\beta}} = \frac{\Omega}{(2\pi)^3} \int d^3\mathbf{q} D_{s\alpha s'\beta}(\mathbf{q}) e^{-i\mathbf{q}(\mathbf{R}_\nu - \mathbf{R}_\mu)}, \tag{1.59}$$

where Ω is the unit cell volume. Discritising the integral onto the uniform mesh of $\mathbf{q}_i$ vectors yields:

$$\frac{\partial^2 E_{tot}}{\partial \mathbf{u}_{\mu \mathbf{S}\alpha} \partial \mathbf{u}_{\nu \mathbf{S}'\beta}} = \frac{1}{N_q} \sum_{i=1}^{N_q} C_{\mathbf{S}\alpha \mathbf{S}'\beta}(\mathbf{q}_i) e^{-i\mathbf{q}_i(\mathbf{R}_\nu - \mathbf{R}_\mu)}, \tag{1.60}$$

where $C_{\mathbf{S}\alpha \mathbf{S}'\beta}(\mathbf{q}_i) = \sqrt{M_s M_{s'}} D_{s\alpha s'\beta}(\mathbf{q})$. As the second derivative of the energy depends only on the vector $\mathbf{R} = \mathbf{R}_\mu - \mathbf{R}_\nu$, then it is possible to say:

$$C_{\mathbf{S}\alpha \mathbf{S}'\beta}(\mathbf{R}) = \frac{\partial^2 E_{tot}}{\partial \mathbf{u}_{\mu \mathbf{S}\alpha} \partial \mathbf{u}_{\nu \mathbf{S}'\beta}} \tag{1.61}$$

and write the following relationship:

$$C_{\mathbf{S}\alpha \mathbf{S}'\beta}(\mathbf{R}) = \frac{1}{N_q} \sum_{i=1}^{N_q} C_{\mathbf{S}\alpha \mathbf{S}'\beta}(\mathbf{q}_i) e^{-i\mathbf{q}_i \mathbf{R}}. \tag{1.62}$$

Using this equation and the dynamical matrices for the mesh of $\mathbf{q}$ points, the inter-atomic force constants for some neighbours of the point $\mathbf{R} = 0$ are calculated. If the dynamical matrix is a sufficiently smooth function of $\mathbf{q}$ in reciprocal space, the inter-atomic force constants will decay rapidly in real space. This permits limiting the sum in Equation 1.58 over ν to the few neighbours around the equilibrium $\mathbf{R}_\mu$. Using only a few inter-atomic force constants and the following relationship, it is possible to interpolate the dynamical matrix at an arbitrary $\mathbf{q}$:

$$C_{\mathbf{S}\alpha\mathbf{S}'\beta}(\mathbf{R}) = \sum_{i=1}^{N_q} C_{\mathbf{S}\alpha\mathbf{S}'\beta}(\mathbf{R}) e^{-i\mathbf{q}_i\mathbf{R}}, \tag{1.63}$$

obtaining an accurate phonon dispersion as shown in Figures 5.1 to 5.10 in the appendix.

In practice, parallelisation of the calculations across several computers allows the computation of each **q** point simultaneously. The time to compute the frequencies at each **q** depends on the symmetry of the vector. Low symmetry **q** vectors take the longest to compute and thus incur the greatest cost.

1.5.2 Electron-phonon interaction

Knowledge of the Eliashberg spectral functional (Eqn. 1.48) allows assessment of the strength of the electron-phonon interaction. Using DFPT, electron-phonon matrix elements (g) are calculated from the first order derivative of the self-consistent Kohn-Sham potential with respect to atomic displacements from their equilibrium lattice position:

$$g^{\mathbf{q}\nu,mn}_{\mathbf{k}+\mathbf{q},\mathbf{k}} = \left(\frac{\hbar}{2\omega_{\mathbf{q}\nu}}\right)^{\frac{1}{2}} \langle \psi_{\mathbf{k}+\mathbf{q},m} | \Delta V^{\mathbf{q}\nu}_{KS} | \psi_{\mathbf{k},n} \rangle . \tag{1.64}$$

$\psi_{\mathbf{k},n}$ is the n-th valence Kohn-Sham orbital of wavevector **k**. The matrix elements are entered into Equation 1.47, which is subsequently put into Equation 1.48. Calculating the spectral function requires a lot of computer power because integration of the double delta over the whole Fermi surface requires great accuracy. This can be achieved through very dense sampling of electron **k** and phonon **q** grids. This can also be achieved through the use of Wannier functions [153], but this is outside the scope of this review. The method described here and in the previous subsection are currently implemented in the open-source software package Quantum ESPRESSO [154].

1.6 Computational details and nomenclature

Thermodynamic stability calculations have been run using the DFT as implemented in VASP, the Vienna Ab initio Simulation Package [155]. VASP adopts the projector augmented waves method [156]. For high accuracy we have used an energy cutoff of 500 eV and dense Monkhorst-Pack k-meshes [157, 158]. We employ the Perdew-Burke-Ernzerhof (PBE) exchange-correlation functional [159] within the generalized gradient approximation (GGA).

Phonon dispersion and electron-phonon coupling calculations are performed with the Quantum ESPRESSO package [154] using ultrasoft pseudopotentials. The PBE exchange correlation functional is also adopted for these calculations. Dense k and q-point meshes as listed in Table 5.6 in the appendix ensure that phonon frequencies converged with respect to the k- and q-mesh to within 10 cm^{-1}. Energy cutoffs of 40 and 320 Ry are used for the wave functions and charge density respectively. The pseudopotentials used for B, Fe and Ca were taken from the Quantum ESPRESSO database. Unless specifically stated these are B.pbe-n-van.UPF, Fe.pbe-sp-van_ak.UPF and Ca.pbe-nsp-van.UPF.

Most calculations have been run on high performance computing clusters owned by the research group and some using the Oxford Supercomputing Centre. Each simulation was split up so that eight simultaneous calculations could occur on eight computer cores. This process is known as parallelisation. The computer code compiled the individual results throughout and at the end of the simulation. Splitting up of the simulation into the eight individual calcululations is determined by the specific code used such as VASP or Quantum ESPRESSO.

All crystal structure diagrams have been adapted from those generated using VESTA

[160]. All fermi surface plots have been generated using XCrySDen [161].

1.6.1 The Pearson symbol

Throughout this document crystal structures are labelled according to their Pearson symbol [162]. The symbol is composed of two letters followed by a number, e.g. cP7. The first letter corresponds to the Bravais lattice, the second letter the lattice type and the number is the number of atoms in the conventional unit cell. For ease of understanding the document the nomenclature is defined in the following table.

First letter	
Symbol	**Bravais lattice**
a	Triclinic
m	Monoclinic
o	Orthorhombic
t	Tetragonal
h	Hexagonal and rhombohedral
c	Cubic

Second letter	
Symbol	**Lattice type**
S	Side face centred
F	All face centred
I	Body centred
R	Rhombohedral
P	Primitive

Table 1.1: Pearson Symbol notation

2 Iron Tetraboride

Many new iron-based superconductors have been discovered over the past few years and, although it is still not clear what the physical mechanism of superconductivity is in these compounds, it is known that they are unconventional meaning they not do not follow the phonon-mediated BCS mechanism (see Section 1.1.2). A well understood property of BCS superconductors is that it is not possible for them to simultaneously be in a superconducting and magnetic state. According to the BCS theory, the superconducting state involves electrons of opposite spins pairing up. For a ferromagnetic state however all the spins align the same direction. Note that while some rare earth alloys have been found to contain contain localised magnetic moments, this study is concerned only with an ordered bulk magnetic state [163].

All the known unconventional iron-based superconductors are magnetic and as far as we are aware, there have only been two reported iron-based BCS-type superconductors (Th_7Fe_3 [164] and $LaFe_4P_{12}$ [165]), both of which have relatively low T_cs. This chapter will describe the properties of a new stable and therefore synthesizable non-magnetic iron-based BCS superconductor. We chose to study iron-borides as they had formed the basis for much experimental research due to their ability to increase the hardness of steel. At ambient pressure and temperature, FeB and Fe_2B are the only known iron boride phases. Even though both are metallic structures with a fairly high DOS at E_F of around 1 state/(spin eV f.u.), the compounds cannot be considered as candidate BCS superconductors since they are ferromagnetic. This study reexamined the whole Fe-B

system using an evolutionary crystal structure search in order to discover new metallic Fe-B structures that were expected to be non-magnetic as a result of the boron suppressing any magnetic moment on the iron atoms. My work focussed on one composition only, iron tetraboride (FeB_4), but the relative stability of structures described herein has been checked against nearby Fe-B compositions. The work described in this section has been published in two articles (Refs [125] and [166]).

2.1 Determining the most stable crystal structure

The first stage in discovering new metal-boride superconductors is to determine the lowest energy crystal structure at a particular stoichiometry, in this case FeB_4. To do this, the formation enthalpy for crystal structures of known metal borides and related compounds at that stoichiometry within the Inorganic Crystal Structure Database [167] was calculated. Before this study was done, the known transition metal tetraboride structures were: tP20-ThB_4, oI10-CrB_4 and mS10-MnB_4. Of these, oI10-CrB_4 type was the lowest energy form of FeB_4. oI10-FeB_4 is metastable with respect to FeB and Fe_2B, lying 8 meV/atom above the tie-line at 0 K (Figure 2.1). oI10-CrB_4 is also composed of rectangular units of boron which lie in the plane. The planes are ABA stacked, where the next layer is composed of shifted rectangular units. Each rectangular unit is joined to its adjacent one in the planes on either side, resulting in a distorted hexagonal pattern as you look down the plane (see Figure 2.2).

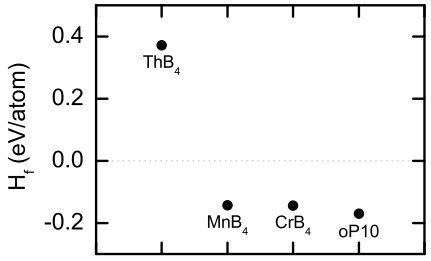


Figure 2.1: Formation enthalpy of FeB_4 phases of ThB_4, MnB_4 and CrB_4 structure types with proposed oP10.

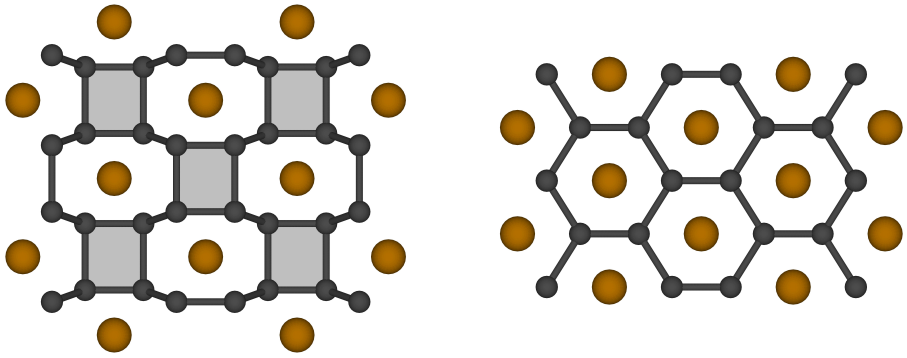


Figure 2.2: The CrB_4 structure type of FeB_4 where brown circles represent iron atoms and black circles boron atoms. Left: A top down view of the boron layer where the grey shading is used to highlight the rectangular unit that is formed. Right: side view of the FeB_4 structure where distorted hexagons are formed through joining up the rectangular units.

To determine if the structure was dynamically stable, a phonon dispersion curve of the primitive unit cell (5 atoms) was calculated using a mesh of 8 q-points (3 x 3 x 3) and a k-mesh of 12 x 12 x 12. The dispersion curve revealed one branch becoming imaginary at various points in the Brillouin zone. Imaginary phonon frequencies indicate that the structure is not the lowest energy one since the movement of atoms (a phonon displacement) results in a lowering of the total energy of the structure. As it is unusual for a structure to become dynamically unstable through the substitution of an element that is close in size and nearby in the periodic table (Cr→Fe), it was not clear at this stage if the structure was indeed dynamically unstable or if the imaginary mode was an artifact of the calculation. As a result, further tests were performed to confirm whether the structure was unstable.

Three of the eight sampled q-vectors were calculated to have imaginary phonon frequencies. The phonon calculation was repeated for one of these three q-vectors, replacing the iron pseudopotential with two further pseudopotentials with varying occupations of the 3d, 4s and 4p orbitals. As the calculated frequencies using all three pseudopotentials did not vary by more than 17 cm^{-1} (see Table 5.1) it was deemed that the original phonon

calculation was reliable. More importantly, varying the pseudopotential still resulted in the calculation of an imaginary phonon frequency at this specific q-vector.

For further clarification that the structure was indeed dynamically unstable, the convergence of Γ point and the imaginary mode q-vector phonon frequencies with respect to k-mesh was tested using the original pseudopotential (1st in Table 5.1). N x N x N k-meshes where N = 12, 16, 20, 24, 28 and 32 for the Γ point and N = 12, 16, 20, 24 and 28 for the other q-vector were used. At both the Γ and other q-vector the phonon frequencies were converged at 12 x 12 x 12 to within 3 cm^{-1}.

A final test calculated the phonon dispersion for the conventional unit cell of Fe_2B_8. It revealed that the imaginary band of frequency -208cm^{-1} at the Γ point was the only imaginary mode in the whole Brillouin zone. As it is at the Γ point, the eigenvector for the imaginary mode can simply be used to displace the atoms into a lower energy structure. The mode involves movement of only the boron atoms in the plane of the rectangle as shown by the red arrows in Figure 2.3. The movement causes the rectangle to distort into a diamond like shape. The energy change with respect to oI10 of structures created by applying the eigenvector to oI10 is plotted in Figure 2.3. The minimum energy structure was achieved at 15% movement along the eigenvector, where the boron atoms were displaced by 1.55-1.65Å. oP10-FeB_4 is 25 meV/atom lower in enthalpy than oI10-FeB_4 and lies just below the α-boron-FeB tie line.

Finally, an evolutionary crystal structure search was run using unit cells of 1:4, 2:8 and 3:12, Fe:B. The structure search would determine if it is credible to propose oP10 as the lowest energy structure of FeB_4. oP10-FeB_4 was the lowest energy structure in the 2:8 search. From now on, oP10-FeB_4 will represented in writing as FeB_4.

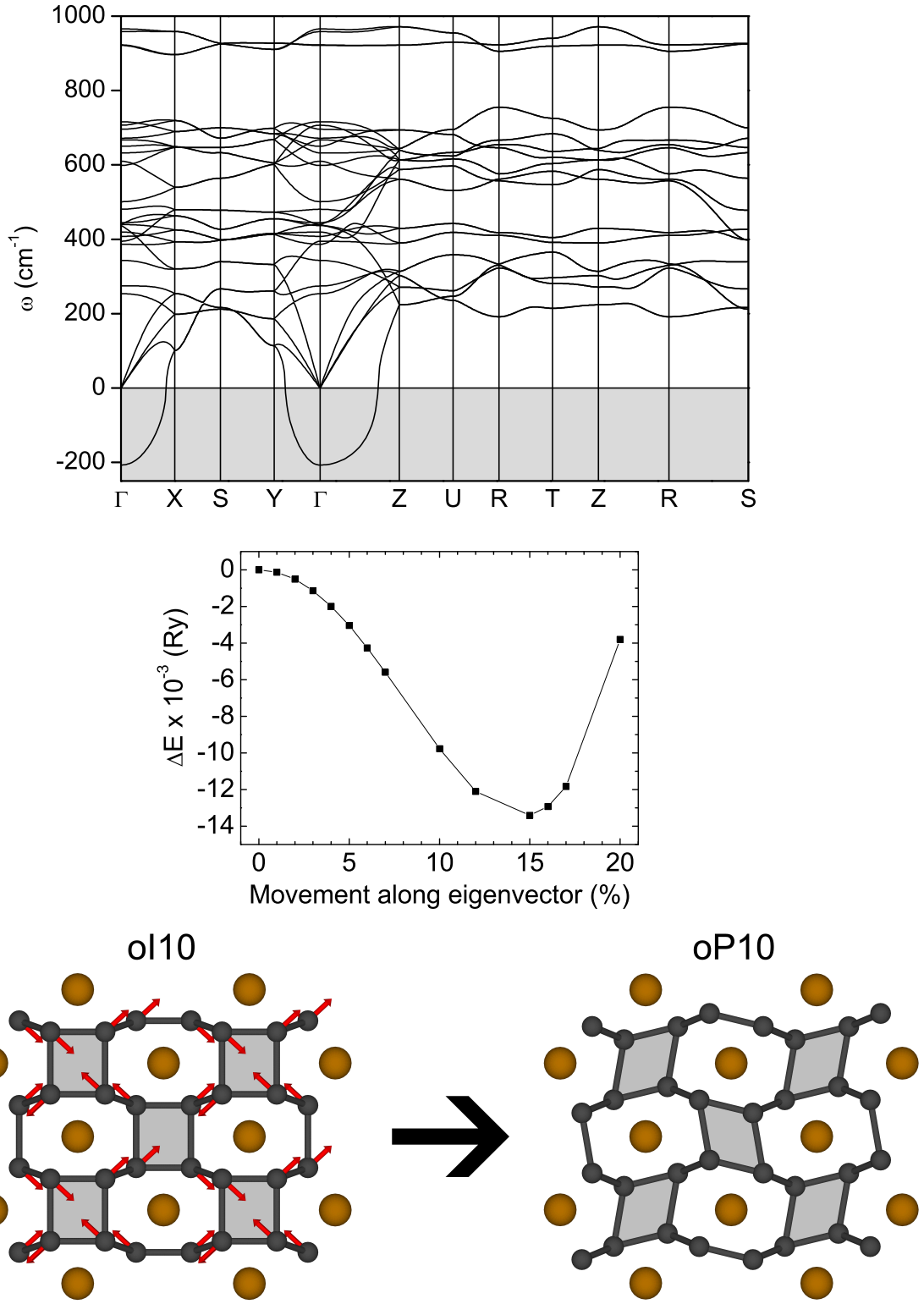


Figure 2.3: Top: A phonon dispersion curve for the conventional unit cell of oI10-FeB_4. The grey shaded region indicates where one branch has imaginary frequencies. Middle: The energy change with respect to oI10-FeB_4 of FeB_4 crystal structures created by moving atoms with the imaginary frequency eigenvector. Bottom: The crystal structure of oI10 with the eigenvectors of the imaginary mode shown as red arrows that transform oI10 into oP10.

2.2 Electronic properties

Now that the lowest energy structure had been proposed an electronic density of states (DOS) calculation was run to see if it was metallic. FeB_4 was found to be a metallic structure and so could be considered as a candidate superconductor. When designing new superconductors, the electron-phonon properties of the compound are usually determined before further analysis of the electronic structure is performed. Here the electronic properties will be described first followed by superconducting properties in the next section.

FeB_4 has desirable electronic properties for a BCS type superconductor because of its high density of states at the Fermi level of 1.0 state/(eV spin f.u.) (Figure 2.4). The Fermi level lies on a peak, which is unusual for stable compounds. 2/3 of the states at E_F are from the iron atom and 1/3 from the boron atom. It is interesting to observe that iron plays the dominant role in electronic states at the Fermi level as the metal atom in MgB_2 has a negligible contribution. For future superconductor design, therefore, strongly bonded covalent boride systems may not necessarily contribute to the electronic states at the Fermi level when combined with certain metallic elements. In this case, boron is important for the stability of the crystal structure and when synthesised, the strength of the material.

The Fermi level is at the edge of the antibonding $p_{x,y}$-$d_{x^2-y^2}$ peak as shown in the band structure plots in Figure 2.6. The boron states contributing to the Fermi level are mainly p_y (56%), with roughly equal p_z (20%) and p_x (24%). The iron states are mainly $d_{x^2-y^2}$, that lie in the boron plane. The Fe d_{z^2} component contributes least to states at the Fermi level which is not suprising as these lie perpendicular to the boron plane. The

three-dimensional Fermi surface is described in the next section more greatly in relation to the superconducting properties.

The superconducting properties of FeB_4 may be strongly affected by the presence of vacancies or impurities due to the large gradient of the DOS near the Fermi level. Removal of just 0.1 electrons per FeB_4 would result in a halving of the DOS at E_F, which would result in a dramatic reduction of the T_c. Given trends of the DOS and T_c observed in the calcium borides (Chapter 3) one could approximate that hypothetical removal of 0.1 electrons would result in a reduction of the T_c down to 5 K.

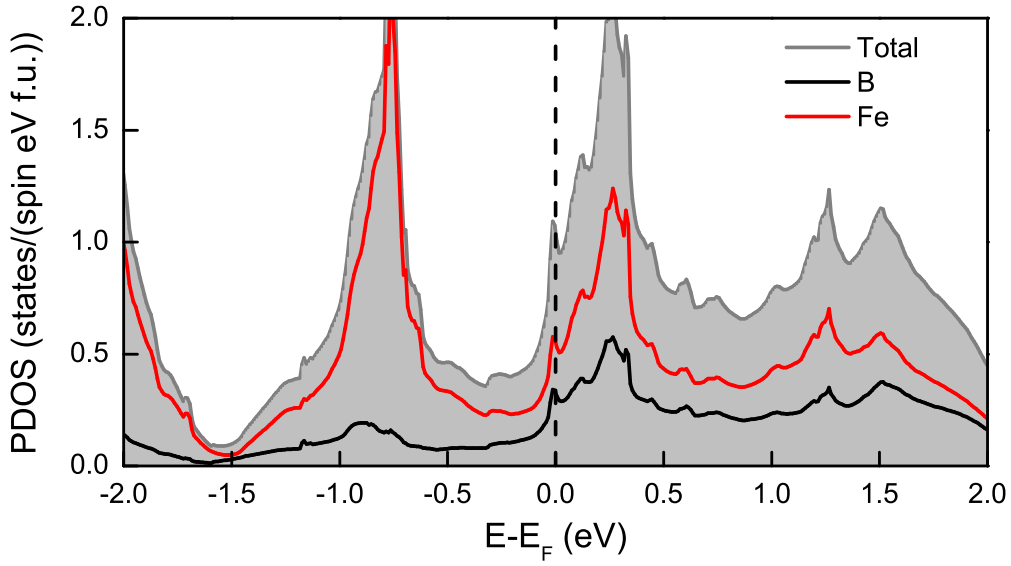


Figure 2.4: Projected electronic density of states for oP10-FeB_4.

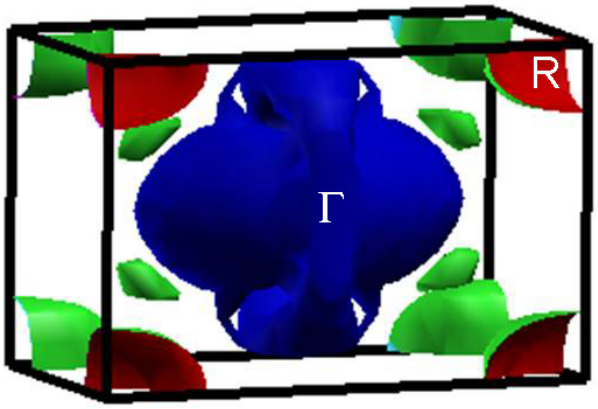


Figure 2.5: Fermi surface for oP10-FeB_4.

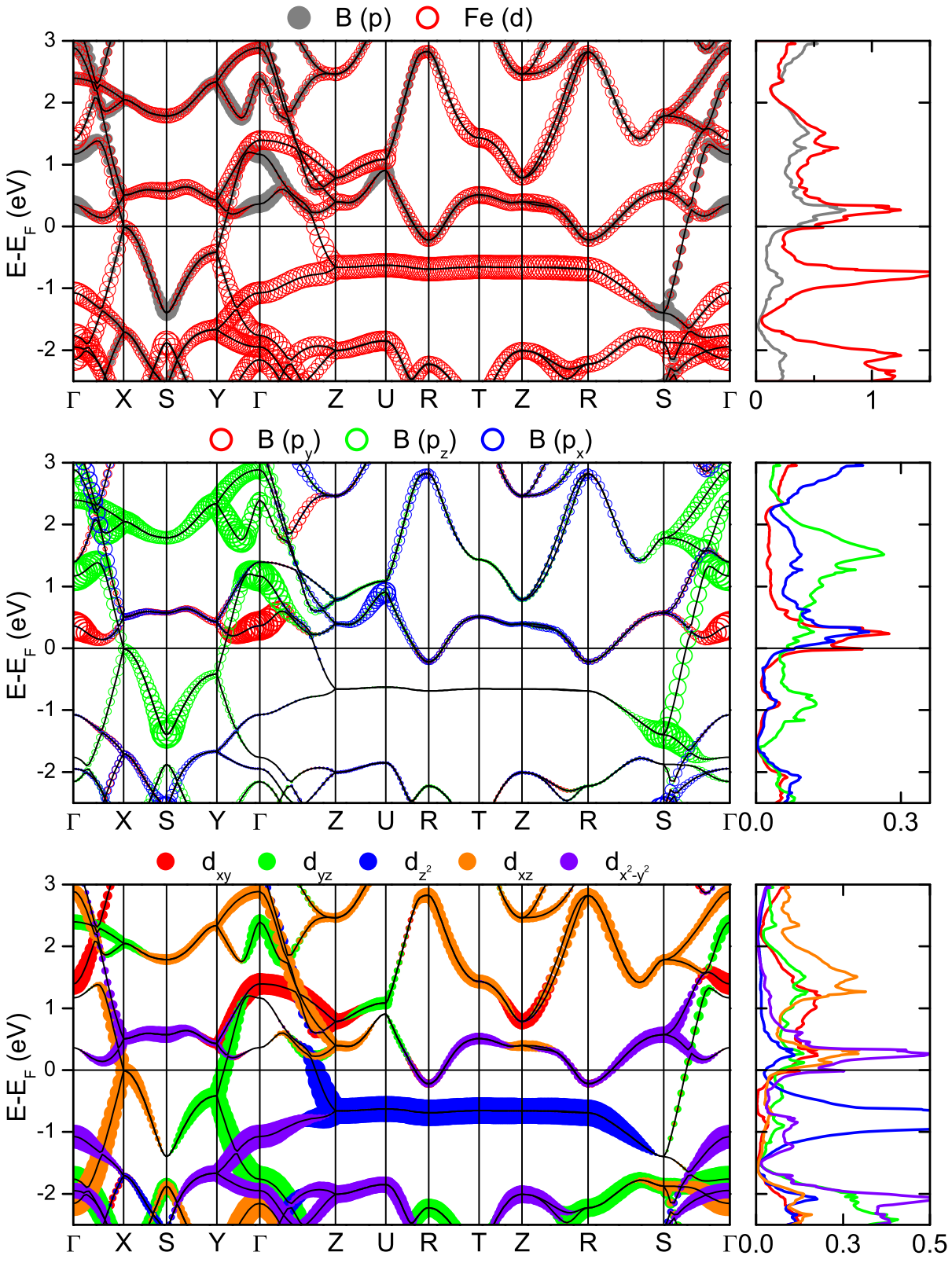


Figure 2.6: BAND structure of oP10-FeB_4 with circles whose size represents the weight of specific orbitals as labelled in the plot. The plots on the right are the projected density of states (in units of states/(e.V. spin f.u.)) for those orbitals.

2.3 Superconducting properties

The superconducting features of the FeB_4 candidate superconducting material were then analysed. FeB_4 can be considered to be a naturally electron-doped material with a high DOS at E_F. The vibrational modes responsible for the superconducting properties can be seen in the phonon spectrum in Figure 2.7. The spectrum can be divided into three regions: mixed Fe-B modes (0-320 cm^{-1}), B modes with a relatively flat PHDOS (320-740 cm^{-1}) and B modes involving in-plane optical distortions of B parallelograms (860-920 cm^{-1}). The Eliashberg function integrates to a large total λ of 0.80 and gives the logarithmic average $\langle\omega_{ln}\rangle = 430$ cm^{-1}. The main contributions to the superconductivity of other BCS type superconductors with similar total λ come from a single atom. In CaC_6 the low-frequency Ca modes ($\omega < 150$ cm^{-1}) contribute most and in MgB_2 the high-frequency B modes (500 $cm^{-1} < \omega <$ 560 cm^{-1}) [36] contribute most. In contrast, nearly 60% of λ_{tot} in FeB_4 is generated by the mixed Fe-B modes in the 160-300 cm^{-1} range. $\langle\omega_{ln}\rangle$ in FeB_4 is much closer to the MgB_2 value of ~ 450 cm^{-1} [36], as opposed to ~ 200 cm^{-1} in CaC_6 (cite). Using the Allen-Dynes formula and typical μ^* of 0.14-0.10 we estimate the T_c in oP10-FeB_4 to be 15-20 K.

Figure 2.5 shows the Fermi surface of FeB_4. There are two surfaces which are centered at the Γ and R points, meaning that the T_c may be further enhanced by the multiband effect which is where two or more sets of bands contribute to the superconductivity in a compound as is observed in MgB_2 which has quasi-2D σ-bands and weakly superconducting 3D π-bands.

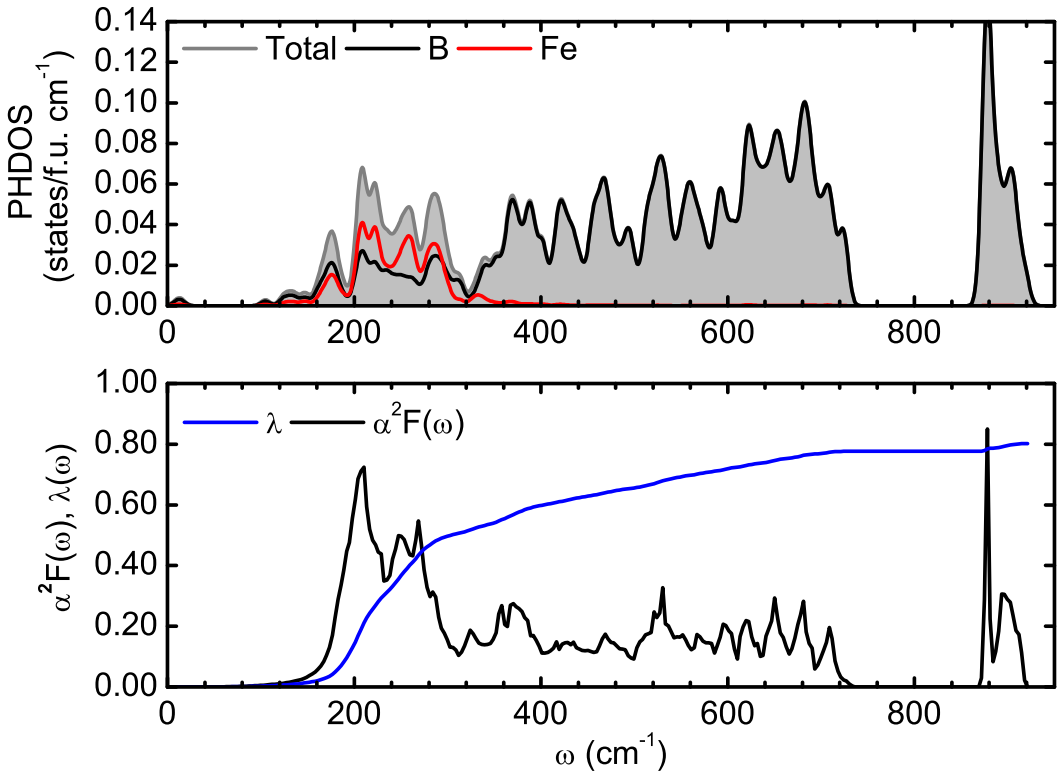


Figure 2.7: Top: total and projected phonon density of states (PHDOS), bottom: Eliashberg function and the strength of the electron-phonon coupling (λ) of oP10-FeB_4.

2.3.1 Convergence of the electron-phonon calculations

In order to check that the calculated T_c did not change when we increased the accuracy of the electron or phonon grids, we measured the convergence of λ for calculations performed with two sets of grids: (i) the 2 x 2 x 4 q- and 6 x 6 x 12 k-meshes for the dynamical matrix and the 12 x 12 x 24 k-mesh for the e-ph coupling (ii) the 3 x 3 x 6 q- and 9 x 9 x 18 k-meshes for the dynamical matrix and the 18 x 18 x 36 k-mesh for the e-ph coupling. For the 0.02 Ry smearing in the k-point integration we find nearly identical values of λ = 0.80 (note that in these calculations the smearing leads to a lower value of n(EF) $\approx$ 0.8 states/(eV spin f.u.) due to a large gradient of the DOS near the Fermi level). We also find negligible changes (below 0.4 cm^{-1}) in Γ-point frequencies when the k-mesh is increased from 9 x 9 x 18 to 12 x 12 x 24 and 15 x 15 x 30.

Table 2.1 shows the calculated superconductivity parameters for the three sets of grids used for convergence tests. To calculate lambda at the 12 x 12 x 24 k-mesh grid, 4 of the lowest symmetry q-points had to be run at the lower 9 x 9 x 18 k-mesh because the calculation did not complete. λ and $\langle\omega_{ln}\rangle$ did not change between the 9 x 9 x 18 and 12 x 12 x 24 grid. μ^* is estimated to be between 0.10 and 0.15. The T_c does not change much when increasing the q-mesh or the k-mesh, leading to the conclusion that the 3 x 3 x 6 and 9 x 9 x 18 grids were appropriate to use. λ and $\alpha^2F(\omega)$ for the two k- and q-meshes considered are plotted in Figure 2.8. The main difference is in $\alpha^2F(\omega)$ around 260 cm^{-1} which is reduced from 0.78 to 0.5 when increasing the k- and q-mesh. λ_{tot} however remains unaffected by the increase in the meshes. All the superconducting properties given in Table 2.1 assume a smearing of 0.02 Ry for the k-point integration. λ and the T_c are calculated for a range of smearing values as plotted in Figure 2.9. A smearing, or Gaussian broadening, value is chosen when both λ and the T_c are considered to be converged, typically at 0.02 Ry.

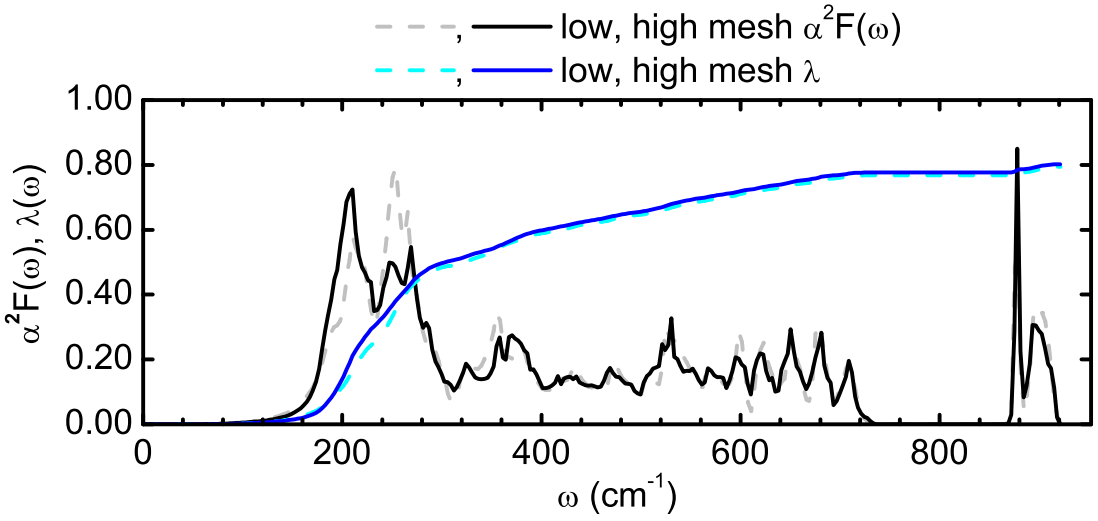


Figure 2.8: Convergence of electron phonon calculations. Low mesh is q-2 x 2 x 4 and k-6 x 6 x 12 (for phonons), high mesh is q-3 x 3 x 6 and k-9 x 9 x 18 (for phonons)

q-mesh	2 x 2 x 4	3 x 3 x 6	3 x 3 x 6
number of q-points	12	16	16 (-4 (low))
k-mesh (ph)	6 x 6 x 12	9 x 9 x 18	12 x 12 x 24
k-points (ph)	112	250	637
k-mesh (e-ph)	12 x 12 x 24	18 x 18 x 36	24 x 24 x 48
number of k-points (e-ph)	637	1900	4225
Γ ph frequency error (w.r.t. 15x15x15 mesh) (cm^{-1})	± 2.26806	± 0.38965	± 0.30313
$\boldsymbol{\lambda}$	0.7939	0.8021	0.8028
$\langle \omega_{ln} \rangle$ (cm^{-1})	437	430	430
$\boldsymbol{T_c}$ **($\mu^* = 0.10$) (K)**	20.18	20.24	20.30
$\boldsymbol{T_c}$ **($\mu^* = 0.11$) (K)**	18.84	18.50	18.52
$\boldsymbol{T_c}$ **($\mu^* = 0.12$) (K)**	17.54	17.22	17.24
$\boldsymbol{T_c}$ **($\mu^* = 0.13$) (K)**	16.26	15.97	15.98
$\boldsymbol{T_c}$ **($\mu^* = 0.14$) (K)**	15.02	14.75	14.77
$\boldsymbol{T_c}$ **($\mu^* = 0.15$) (K)**	13.82	13.57	13.58

Table 2.1: Convergence tests with the meshes and number of k- and q-points used for phonon (ph) and electron-phonon (e-ph). The calculated superconducting properties, lambda, and the logarithmic average phonon frequency are given for these meshes. As mentioned in the text, the k-12x12x24 calculation did not complete for 4 low symmetry q-points so the 9x9x18 data was used to calulate the superconducting parameters. The T_c is calculated for different μ^*.

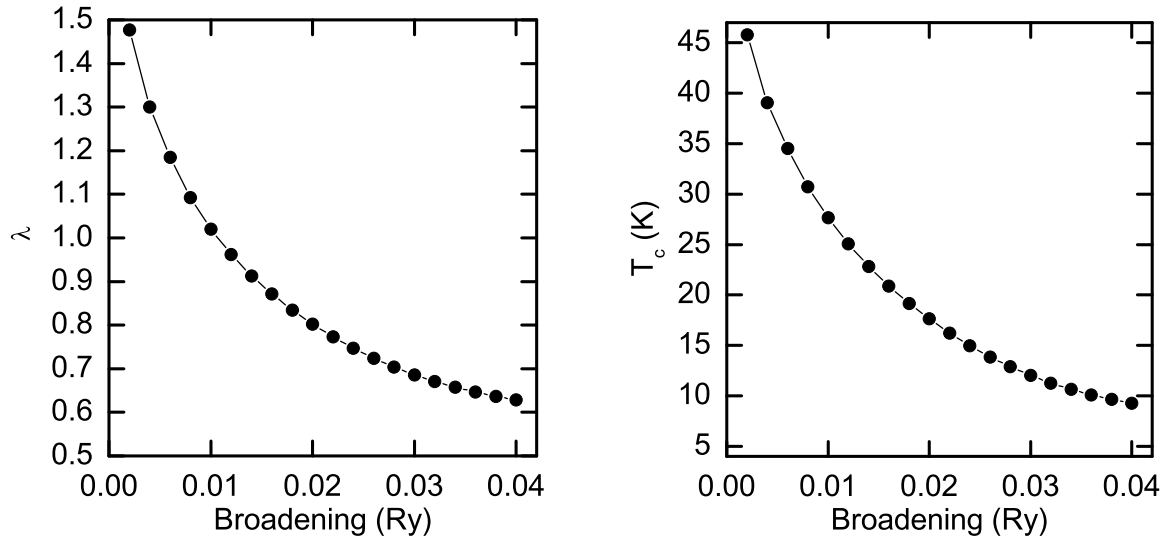


Figure 2.9: Variation of λ and the T_c with respect to the Gaussian broadening (smearing) used for the k-point integration.

2.3.2 The isotope effect

One of the experiments used to confirm the existence of a BCS superconductor is the observation of the "isotope effect". Replacing an atom in a superconducting compound with its isotope of a different mass results in a change in the T_c that is proportional to the mass change [139, 140]. This early experimental observation in superconducting materials was important for the understanding that phonons play a crucial role in what is now called phonon-mediated superconductivity. The isotope effect, labelled as α, is defined in equation 2.1 as a sum over the isotope effect of each atom (i) in the compound, with mass M_i.

$$\alpha_{tot} = \sum_{0}^{N} -\frac{\partial ln T_c}{\partial ln M_i} \tag{2.1}$$

We have replaced the boron atom of standard atomic mass 10.811 amu (denoted by ^{11}B) with its isotope ^{10}B of mass 10.013 amu (denoted by ^{10}B). Using μ^* of 0.12, the T_c changed from 17.6 K to 18.0 K, with an $\alpha_{tot} = 0.28$. The calculation of α and the superconducting properties are shown in Table 2.2. For μ^* between 0.10 and 0.15, α is around 0.3, lying between 0.275 and 0.286 (to 3 d.p.). By comparison, the experimental isotope effect measured in MgB_2 on substituting ^{10}B for ^{11}B is 0.26 [168]. The isotope effect in FeB_4 would be noticeable if experimental studies try to check the prediction.

The Eliashberg spectral function and phonon density of states are shown in Figure 2.10. Decreasing the atomic mass increases the boron phonon frequencies. For example, the peak at 878 cm^{-1} is increased by 33 cm^{-1} to 911 cm^{-1}. There is no change in the Eliashberg function below 320 cm^{-1} which is the frequency region with mostly Fe modes. Above 320 cm^{-1} there are slight shifts in the Eliashberg function to higher frequencies, corresponding to the higher frequency boron phonon modes.

Applying the eigenvector of a phonon mode of FeB_4 to its relaxed structure results in a change in the bandstructure close to the Fermi level. This further indicates that there is strong electron-phonon coupling. Along the direction of X-S, the valence (predominantly d_xz) and conduction (predominantly ($d_{x^2-y^2}$) bands split. The conduction bands along Γ-Z, that are also mainly d_xz demonstrate that the phonons responsible for superconductivity interact mainly with electronic iron states.

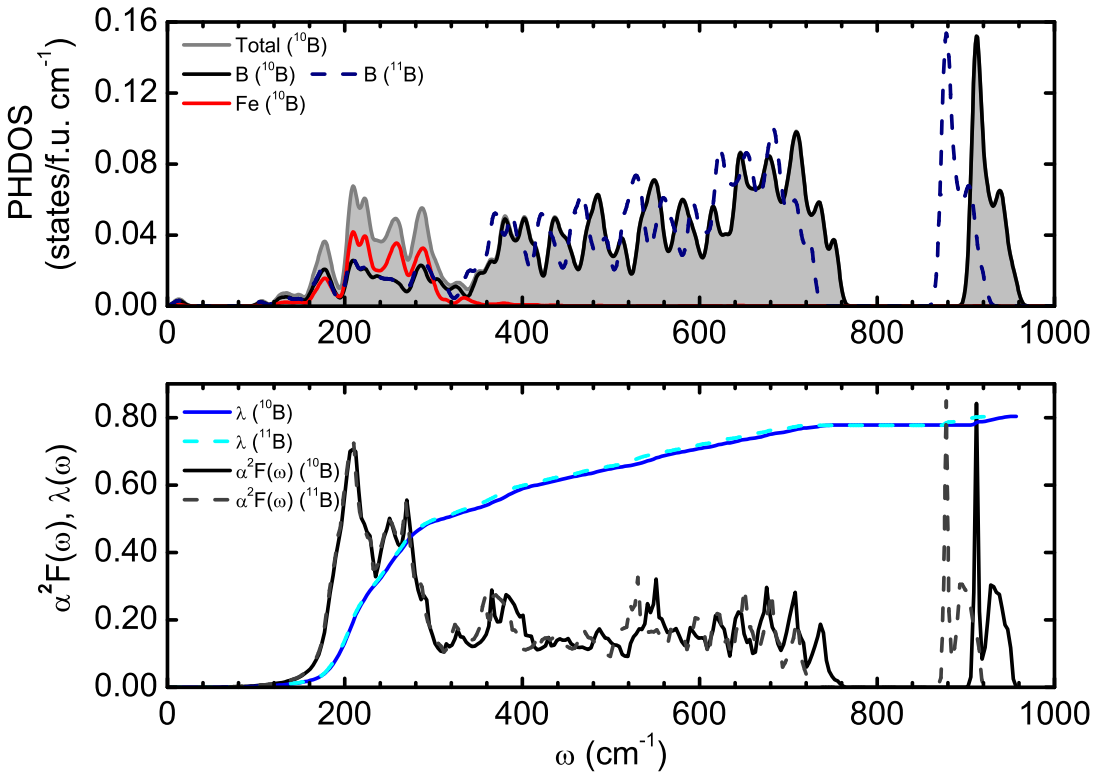


Figure 2.10: The phonon density of states, Eliashberg function and lambda for oP10-FeB_4 with two isotopes of boron (^{10}B and ^{11}B).

B isotope name	^{11}**B**	^{10}**B**	
B isotope mass (amu)	10.811	10.013	
$\boldsymbol{\lambda}$	0.8021	0.8033	
$\langle \boldsymbol{\omega_{ln}} \rangle$ **(cm^{-1})**	429.605	437.414	
$\boldsymbol{\mu^*}$	$\boldsymbol{T_c}$ **(K)**	$\boldsymbol{T_c}$ **(K)**	$\boldsymbol{\alpha}$
0.10	20.240	20.671	0.275
0.11	18.919	19.325	0.277
0.12	17.627	18.008	0.279
0.13	16.366	16.723	0.281
0.14	15.139	15.471	0.284
0.15	13.947	14.256	0.286

Table 2.2: Calculated superconducting properties for the two isotopic masses of boron - lambda, and the logarithmic average phonon frequency. The T_c and the isotope effect α are calculated for different μ^*.

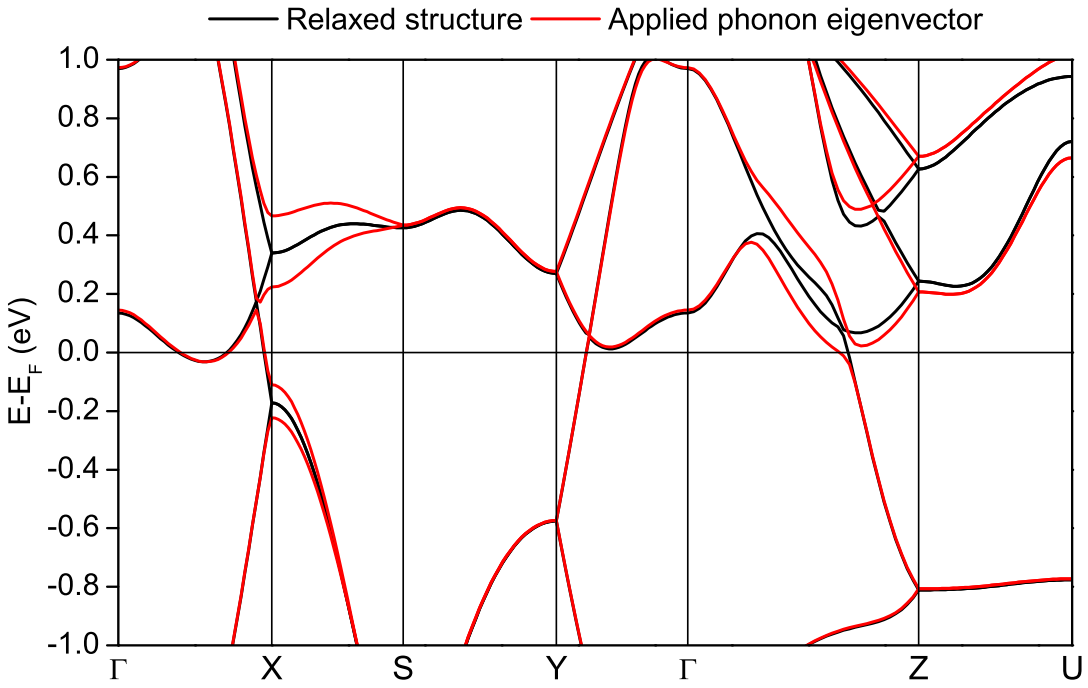


Figure 2.11: The electronic band structure of the relaxed structure of oP10-FeB_4 and the structure with an eigenvector of a phonon mode applied to the structure.

2.3.3 Magnetic properties

When theoretically proposing a BCS superconductor containing magnetic elements it is important to make sure that the material is not magnetic. If the material is found to be magnetic when synthesised, it cannot be a BCS superconductor.

A non-magnetic state is where the number of spin up electrons ($N_\uparrow$) equals the number of spin down ($N_\downarrow$). A ferromagnetic state occurs where the number of electrons with a certain spin (e.g. $N_\uparrow$) is greater than the number of electrons with the opposite spin (e.g. $N_\downarrow$). The magnetic moment is the difference between the numbers of electrons in the two spin states, e.g. $N_\uparrow$ - $N_\downarrow$. A magnetic state will be lower energy than the non-magnetic form if it is energetically favourable for spins to align. If the gain in exchange energy due to alignment of spins is greater than the loss of kinetic energy then a magnetic state will be favoured. Relative to atomic systems, solids have delocalised electrons which generally results in a large loss of kinetic energy, where the loss is greater than the gain of exchange energy, resulting in non-magnetic structures. A solid will be magnetic if the electrons are sufficiently localised. A variety of tests will now be described which show that the electrons are sufficiently delocalised in oP10-FeB_4 meaning that it is neither a ferro- nor antiferromagnetic.

Firstly, a spin-polarised relaxation of the crystal structure using Quantum ESPRESSO and VASP resulted in structures with zero magnetisation. An antiferromagnetic structure was forced using the lambda flag in Quantum ESPRESSO. A magnetization is set for each of the iron atoms at the beginning of the calculation. The lambda flag adds a penalty to the total energy of the system that is proportional to lambda and the square of the deviation in magnetization away from the set atomic magnetization to a set value. Figure 2.12 shows that the lowest energy structure was not antiferromagnetic.

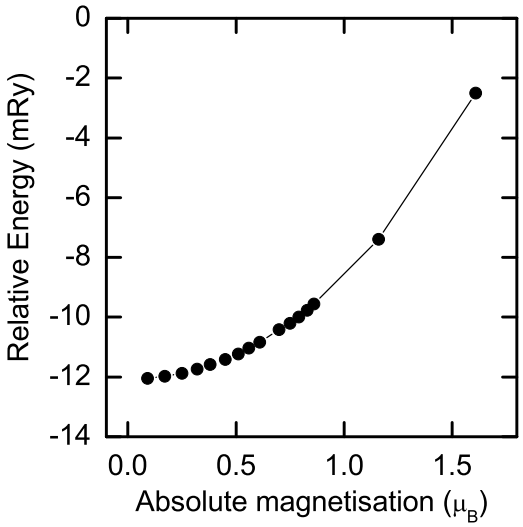


Figure 2.12: The antiferromagnetic structure of FeB_4 forced using lambda. The lowest energy structure is at zero absolute magnetization. The graph depicts energy relative to -556.486 Ry for ease of reading.

Next, the structure was shown to not fulfill the Stoner criterion for ferromagnetism (Equation 2.2) [169], which defines whether a structure will be ferromagnetic based on its electronic properties. Ferromagnetism occurs if:

$$IN(E_F) > 1, \tag{2.2}$$

where $N(E_F)$ is the DOS at E_F of the non-magnetic structure (in states/(eV spin f.u.)) and I is the Stoner parameter. The criterion can be applied easily to any system as it is independent of the structure. In a ferromagnetic state, the spin up and spin down electronic eigenvalues are shifted relative to each other due to the exchange interaction between spins. A larger magnetic moment (M) results in a larger shift relative to the non-magnetic case (ϵ^{NM}), which is proportional to I:

$$\epsilon^{\pm} = \epsilon^{NM} \mp \frac{1}{2} IM \tag{2.3}$$

Spin polarised projected density of states calculations were run on forced ferromagnetic structures using VASP. The energy of one peak was followed with increasing magnetization and thus used to determine the Stoner parameter (I). Similar results were obtained when using eigenvalues for specific bands. $IN(E_F)$ for FeB_4 is 0.701 showing that it is far away from being ferromagnetic. The same methodology for calculating the Stoner parameter was applied to bcc Fe and the result was comparable with experiment.

Finally, a hypothetical test was run to see how close the relaxed structure was to a magnetic transition. Applying pressure to magnetic solids results in a suppression of the magnetic moment. An expansion of the crystal lattice would thus induce either a ferromagnetic or antiferromagnetic moment on the system. To determine how close FeB_4 is to a magnetic state we found out how much you had to expand the lattice in order to induce an antiferromagnetic state. The lattice parameters were expanded, equally in a and c, to 115% of their relaxed size. Figure 2.13 shows that a non-zero magnetisation appears at 6% expansion in volume. 26% lattice volume expansion is required for a significant antiferromagnetic moment. Assuming a linear increase in magnetisation with expansion, a 75% increase in volume would be required to induce a ferromagnetic moment equal to that in bcc Fe.

The flag NUPDOWN in VASP was also varied. NUPDOWN represents the difference between the number of electrons in up spin and down spin. Figure 2.14 shows that at 13-15% lattice constant expansion, the most stable state has an NUPDOWN of 4. The most stable state has a magnetisation of 2-2.1μ_B per Fe and this corresponds to the same magnetisation as on each Fe atom in bcc Fe.

Finally, the Stoner parameter, I, was determined for cells of the increased lattice volumes (see Table 2.3). A ferromagnetic state is induced between 33 and 52 % increase

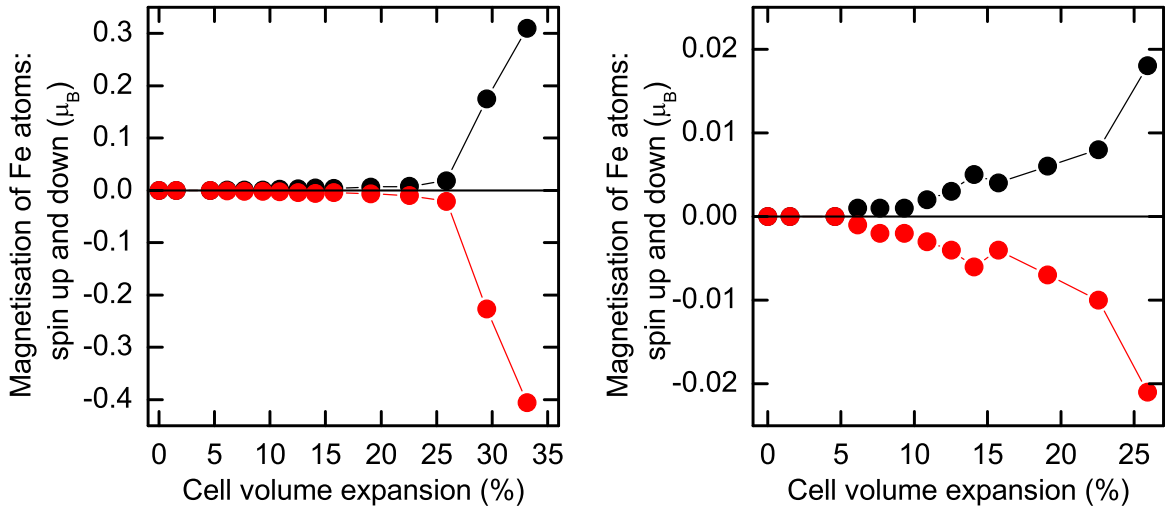


Figure 2.13: Left: The magnetization of Fe atoms with expansion of the FeB_4 lattice until it becomes antiferromagnetic. Right: The left plot zoomed in to 0-26% cell volume expansion.

in the lattice volume (or 10-15% increase in lattice parameters).

Lattice volume expansion (%)	I	n(E_F) (states/(spin eV f.u.))	I n(E_F)
0	0.701	1.00	0.70
16	0.711	0.81	0.57
33	0.692	0.96	0.66
52	0.766	2.11	1.61
73	0.791	1.47	1.16
95	0.776	3.00	2.33

Table 2.3: The calculated Stoner parameter for expanded lattices of oP10-FeB_4.

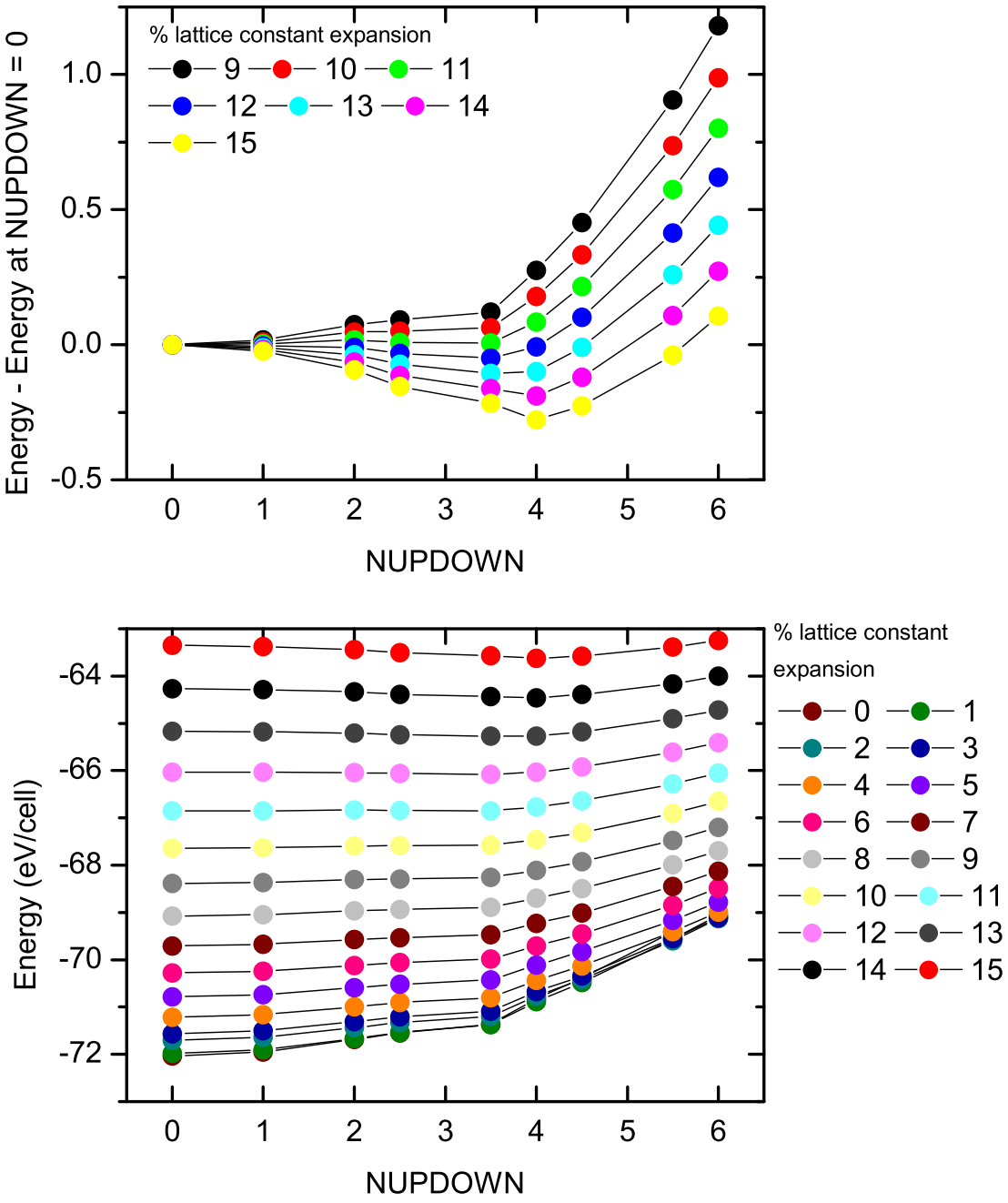


Figure 2.14: Top: For lattice constant expansions of 9-15% we plot the energy of FeB_4 with respect to the energy of these structures with no magnetization. The energy difference is plotted against varying magnetization achieved through the NUPDOWN flag. Bottom: The energy of FeB_4 for lattice constant expansions of 0-15% at varying magnetization achieved through the NUPDOWN flag.

2.3.4 CrB_4

The first structure of FeB_4 studied was of the CrB_4 structure type. Section 2.1 showed that FeB_4 in this configuration was dynamically unstable. A phonon dispersion curve of of CrB_4 showed that it too was dynamically unstable: oI10 transforms into oP10. The structure may have originally been incorrectly characterised as the X-ray diffraction patterns of both oI10 and oP10 are indistinguishable (see supplementary material in Ref. [166]).

The superconducting properties of oP10-CrB_4 were investigated, finding that it has a negligible superconducting T_c of $\ll$1 K. The low T_c is thought to be related to the low density of states at the Fermi level (Figure 2.15). The group investigated the effect of the substitution of Fe into the CrB_4 lattice as a possible means for synthesising FeB_4 from the already experimentally known CrB_4. We found that maximum stability was achieved at the two ends of the $Fe_xCr_{1-x}B_4$ composition scale, in addition to a structure where x = 0.5. The introduction of only a small amount of chromium results in a dramatic reduction in the DOS and therefore probably the T_c. If Fe substituted CrB_4 at x = 0.5 could be synthesised its superconducting properties would not be desirable.

The research on CrB_4 described here was published in Reference [166]. Since then, the proposed structure of CrB_4 has been experimentally confirmed by two research groups [170, 171]. The confirmation shows that computational methods are a viable option for predicting ground state crystal structures.

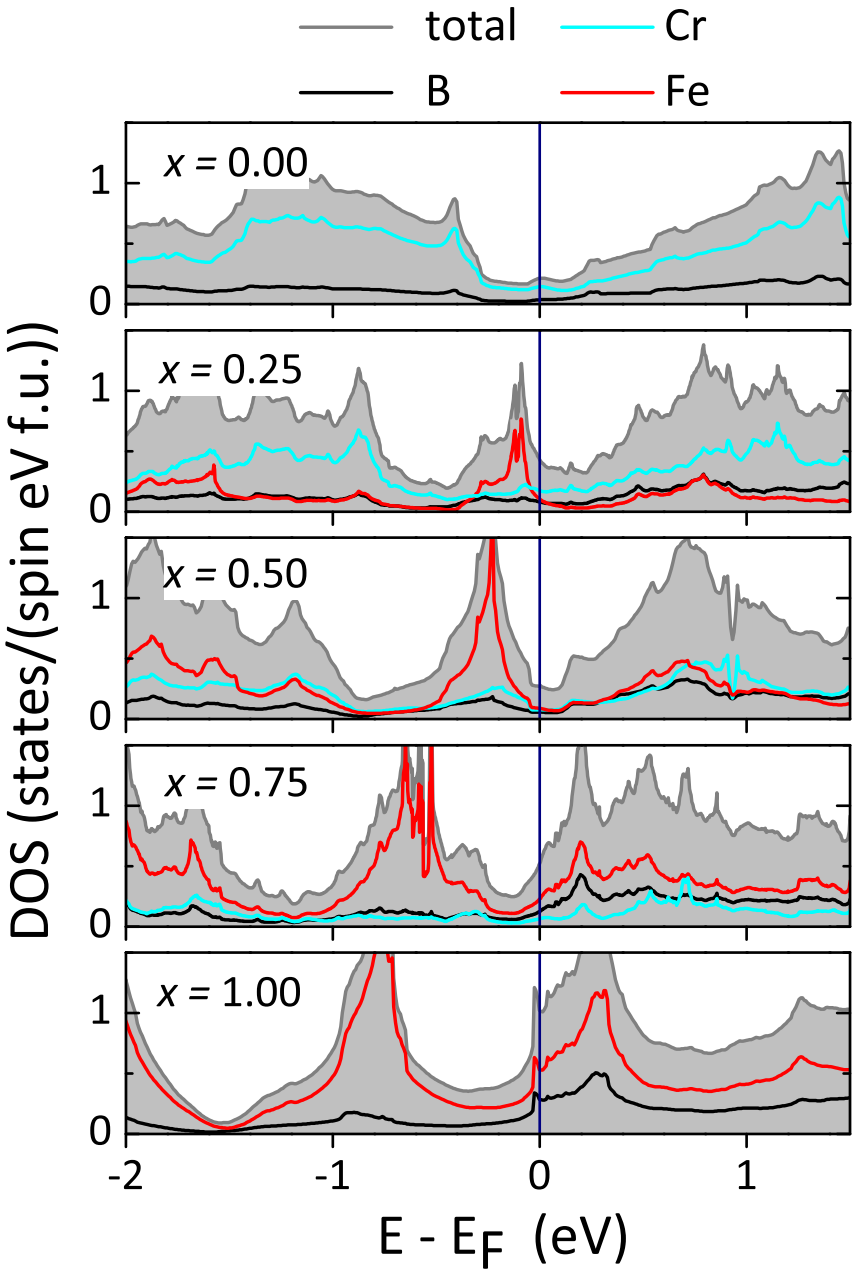


Figure 2.15: The projected density of states for Cr substitution of FeB_4. Reprinted Fig. 2 with permission from Ref. [166], http://dx.doi.org/10.1063/1.3556564. Copyright [2011], American Institute of Physics.

2.3.5 Synthesis of FeB_4

Around the time of the submission of this thesis, two articles have been published in a pre-print archive reporting the synthesis of FeB_4 [172, 173]. Gou et al. have synthesised oP10-FeB_4 under 8 GPa of pressure and high temperatures. The structure has been determined using single-crystal X-ray diffraction and the lattice parameters and atomic positions are in good agreement with the prediction. Magnetic susceptibility measurements have demonstrated bulk superconductivity and diamagnetism below 2.9 K. The lower than expected T_c is possibly due to the presence of impurites and thus the DOS at E_F is lower than in the pure form (see Section 2.2). Observation of the isotope effect upon substitution of ^{11}B boron with ^{10}B indicates that the predicted material is indeed a phonon-mediated superconductor. Suprisingly the study also proposes FeB_4 as being a superhard material. The synthesis of the predicted structure and the observation of superconductivity further suggests that the prediction methods used in this study are of sufficient reliability. The second study by Jin et al. fabricated thin film spreads of the Fe-B system. They observe a resistance drop and thus superconductivity at 4 K. A weak diamagnetic signal was observed at 9 K. The authors were unable to identify the composition of the Fe-B compound however conclude that since no other Fe-B compound is known to be a superconductor they must have synthesised the predicted FeB_4. In light of these new observations, one would expect to see further work examining the superconducting properties of FeB_4. Even though many new superconducting crystal structures are regularly being predicted using evolutionary algorithms, as far as I am aware, FeB_4 is the first of these predictions to be confirmed with experiments.

3 Calcium boride under pressure

When designing new superconductors, whether it be in the lab or on a computer, it is impossible to study all chemical systems using a combinatorial, trial and error method. Instead, scientists narrow their study with ideas from known superconducting materials. Calcium boride was chosen to be studied as it is isoelectronic to the best BCS superconductor magnesium boride [43]. The hypothetical structure of CaB_2 is predicted to have a T_c of 50 K [111]. This is due to its higher electronic DOS at the Fermi level than MgB_2 and the presence of multiple superconducting gaps. Unfortunately the structure is thermodynamically unstable at ambient pressure. Pure calcium under pressure however currently holds the record for the highest T_c amongst the elements, with a T_c of 25 K [174].

The calcium borides are studied here at gigapascal pressures as it was thought that new covalent boron networks could stabilise under these extreme condictions. In addition, various high pressure complex phases of calcium (see Ref [175] and references within) and boron (review [176]) have been predicted and experimentally shown to form so,- it was thought that their combination would result in interesting new networks. High pressure would just be used a method for synthesis of these new boron structures and once the pressure is released it is hoped that the new crystal phases remain metastable states. In this chapter, predicted stable crystal structures across the whole composition range of Ca_xB_{1-x} at ambient and high pressure (0-50 GPa) will be given and the superconducting properties of any metallic structures. Designing new superconductors is a balance

between stability and T_c as can be seen in the calcium boride system where very stable structures are found but these are poor superconductors. Medium concentrations of calcium (0.33-0.50) seem to be required for stable superconducting compounds with higher concentrations of calcium resulting in unstable structures. An evolutionary ground state crystal structure search has identified four new high-pressure superconducting structures: oI8-CaB ($T_c = 5$ K), oI12-CaB_2 ($T_c \sim 1$ K), mS12-CaB_2 ($T_c \sim 1$ K) and $CaB_{6.25}$ ($T_c \approx 2$ K). All pressure induced crystallographic phase transitions are explained, mainly through comparison with their alkaline earth analogues as metallic ion size plays a large role in stability. Understanding the reasons for the stability of boron structures can be used as a guide for boride superconductor discovery thus this part of the study was important to do even for non and poor superconducting structures. Figure 3 gives a summary of all predicted structures, the pressures they are stable over and the calculated T = 0 K formation energies.

This chapter is split up into 4 sections about each stable Ca:B composition: CaB_6, CaB_4, CaB_2 and CaB. The final section will consider other Ca:B compositions that did not have stable ground states. Each section will cover the analysis of stability of the ground state, the electronic (DOS and band structures) and vibrational properties (phonon) and if metallic the superconducting properties. Some of the research described in this chapter has been published in a collaborative study [177]. The rest of the research presented here relating CaB_6 and all other all the other calcium boride compounds has been published in a separate article [178].

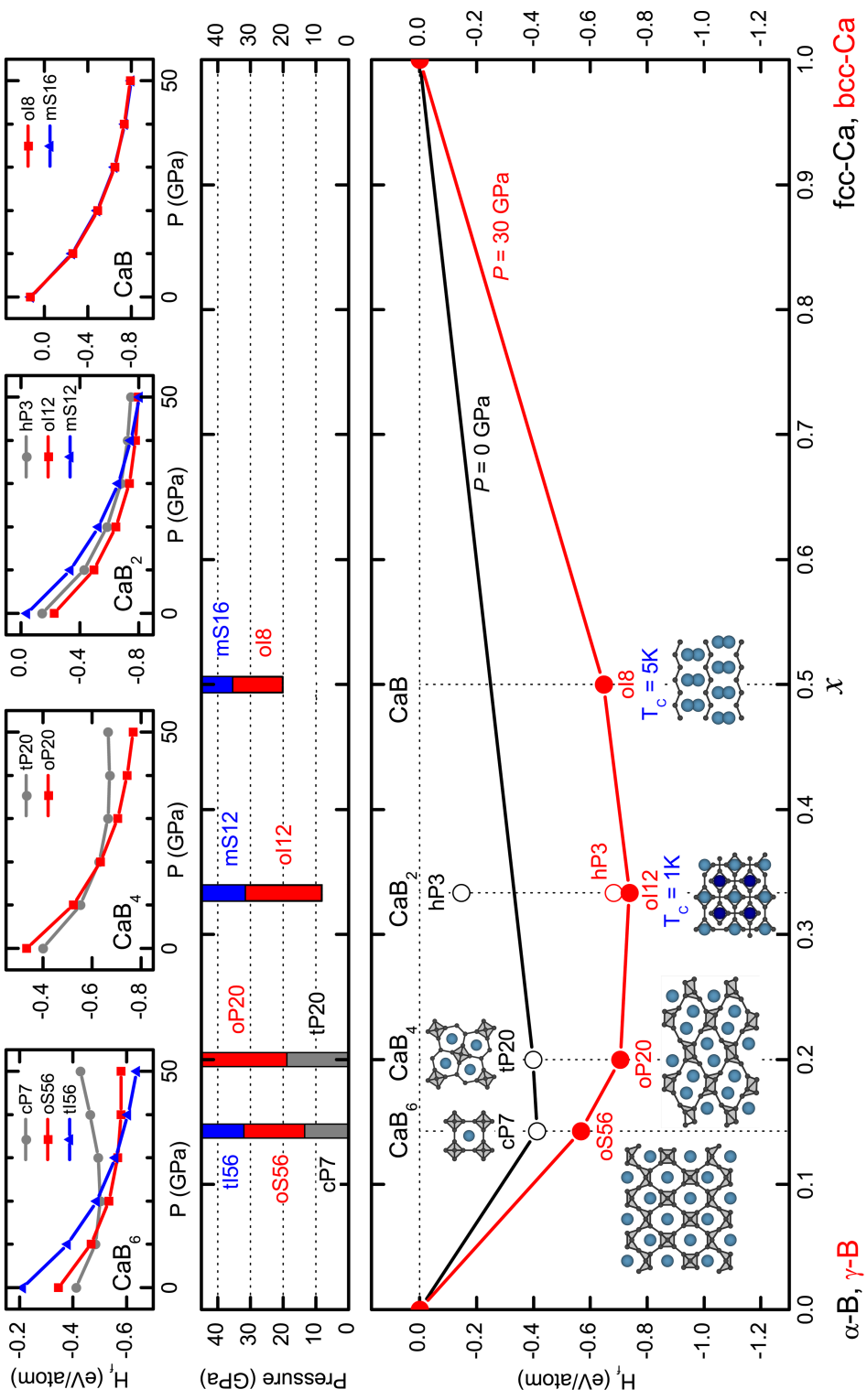


Figure 3.1: Top: The formation enthalpy of proposed structures of CaB_6, CaB_4, CaB_2 and CaB with the colours corresponding to those labelled in the middle plot. Unstable hP3-CaB_2 is given in grey for comparison. mS16-CaB cannot be seen as it lies directly beneath oI8-CaB. Middle: The pressure ranges that the proposed ground state structures are stable with Pearson symbols as labels. Bottom: Calculated formation enthalpies of Ca_xB_{1-x} compounds at 0 (black) and 30 GPa (red) with their crystal structures and proposed superconducting T_c.

3.1 Evolutionary crystal structure search

An evolutionary structure search was run at 30 GPa for each of the unit cells and stoichiometries listed in Table 3.1. Proposed ground states were compared with metal boride structures listed in the ICSD [167]. Table 3.1 also lists the relative enthalpy (H_{rel}) for each composition. H_{rel} is the ordinate distance between the point corresponding to the most stable structure at a given composition and the line connecting two nearest ground states in the formation enthalpy plot (Fig. 3).

Compound	Unit cells Ca:B	H_{rel} (meV/atom)
CaB_{12}	1:12	32
CaB_7	2:14	60
CaB_6	1:6, 2:12, 3:18, 4:24	0
CaB_5	1:5, 2:10	81
CaB_4	1:14, 2:8, 3:16, 4:16	0
CaB_3	2:6, 3:9, 4:12	114
CaB_2	3:6, 4:8, 6:12	0
Ca_2B_3	2:3, 6:9	136
Ca_5B_6	5:6	153
CaB	3:3, 4:4, 5:5, 6:6, 8:8	0
Ca_2B	4:2, 8:4, 12:6	44

Table 3.1: List of unit cells used for the evolutionary search across the Ca_xB_{1-x} composition range and the relative enthalpy, H_{rel}, (described in the text) of the lowest enthalpy structure at that composition at 30 GPa.

With no available experimental information at high pressure, a focus was put on the most likely to occur compositions found in metal borides. A study of intermetallics for example, showed that binary compounds prefer the simple stoichiometries of 1:1, 1:2, 1:3, 2:3 and 3:5 [179]. We have studied most of these and, for example, 1:6 and 1:4 as their ambient pressure Ca-B structures are known. 1:7 and 1:12 were studied since ambient pressure structures of MgB_7 and MgB_12 are known. 1:5 was studied to make sure that proposed high pressure ground states structures of CaB_6 and CaB_4 were stable relative

to decomposition into nearby stoichiometries. Similarly, a search of Ca_5B_6 gave further evidence for the stability of CaB. A search for Ca_2B_3 was run to sample as much of the composition space of calcium borides as possible. Also, another boride, Cr_2B_3, is known to exist at ambient pressure so although the metal ion is of a different size, it was still worth investigating. Finally, a search for Ca_2B was done since Be_2B is known. The known structures described here are listed in the ICSD [167].

All proposed ground states have been tested for thermodynamic stability relative to other Ca_xB_{1-x} compositions. It should be noted that an evolutionary search has only been performed at 30 GPa (apart from for CaB_6) and therefore at other pressures is possible that structures that have not been considered could stabilise. We use relative thermodynamic stabilities of structures considered at 30 GPa to assess what could be the ground state at other pressures.

3.2 Calcium hexaboride: CaB_6

At ambient pressure, a large variety of hexaborides all adopt the same simple cubic CaB_6 prototype structure (cP7) of boron octahedra surrounding the metal ion (Fig. 3.8). These are the alkali metals: KB_6; alkali earth metals: CaB_6, BaB_6 and SrB_6; transition metals: LaB_6 and YB_6; lanthanides: CeB_6, PrB_6, NdB_6, SmB_6, EuB_6, GdB_6, TbB_6, DyB_6, HoB_6, ErB_6, TmB_6, YbB_6 and LuB_6 and the actinides, ThB_6, NpB_6, PuB_6 and AmB_6. To our knowledge, no other crystal structure is known for any hexaboride.

Calcium hexaboride was first synthesised in 1897 by Moissan and Williams [180], however it was not until 1932 when its crystal structure (Fig. 3.2) was determined [181].

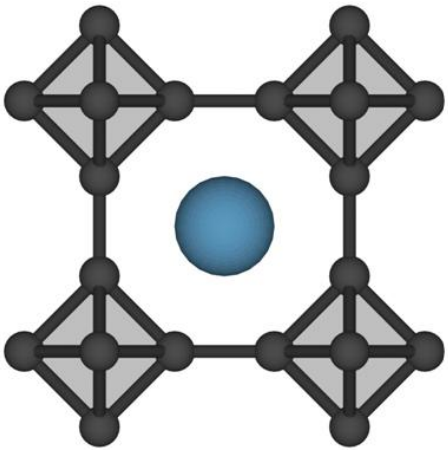


Figure 3.2: Crystal structure of cP7-CaB_6. Boron atoms are in dark grey and the calcium atom in blue.

CaB_6 gained great interest around 1999 when it was reported that the compound became weakly ferromagnetic when electron doped with lanthanum [182]. This was surprising as it does not have partially filled d or f orbitals, a requirement for ferromagnetism [183]. However, later this was demonstrated not to be the case and that the ferromagnetic behaviour was observed when the CaB_6 was synthesised using low purity boron [184]. More recently much theoretical modelling work has focussed on proving if calcium hexa-

boride is a semimetal or semiconductor [183, 83, 185]. It has been concluded that it is a semiconductor with a band gap around 0.8 eV [185].

Calcium hexaboride is chemically very stable with a high melting point of 2373 K and has a high hardness (27 GPa) [186] making it interesting to study from a materials perspective. Hexaborides as a whole are of interest for their valence-fluctuation (SmB_6), Kondo effects (CeB_6) [187], superconducting properties (YB_6, T_c = 7 K) and use as thermionic emitters (LaB_6) [187].

The stability of CaB_6 has been investigated by studying its electronic structure, finding that twenty electrons per boron octahedron ($B_6{}^{2-}$) are required for the stability of cP7-MB_6 [188]. Longuet-Higgins and Roberts showed that if the metal has a valency of greater than two then the crystal will be metallic. This explains the semi-conductivity of calcium hexaboride and shows that to find a superconductor one would need to induce metallicity in this structure. One method would be through electronic doping which in turn could destabilise the structure. The alternative is to apply pressure resulting in a structural phase transition to a different boron network which would be metallic with only two electrons transferred to it. The latter will be explored in this section.

CaB_6 has previously been studied at high pressure through X-ray diffraction (XRD) experiments which indicated a cubic to orthorhombic phase transition around 12 GPa [189] but the observation was not confirmed in follow up experiments [190, 177]. Theoretical calculations led Wei et al. [191] to conclude that CaB_6 does not undergo a phase transition up to 100 GPa. They however only considered two possible crystal structures of CaB_6, the cP7 and an orthorhombic Pban structure which was previously proposed as a high pressure form of LaB_6 [192]. The study missed other possible arrangements of CaB_6, which were found in the work presented in this section, exemplifying the need

to examine considerably more candidate structures at a particular elemental composition before making conclusions about stability.

High pressure phase transitions observed in other metal hexaborides include LaB_6 and YB_6. The LaB_6 structure was indexed as Pban [192] but was not observed in subsequent experiments [193]. Our phonon calculations also indicate no reason for the cP7 structure of LaB_6 to distort up to 60 GPa and that its proposed Pban structure [192] relaxes back to cP7 at 15 GPa. More relevant for this study, YB_6 is superconducting with a T_c of 7.1K [194]. The T_c has been predicted to drop with pressure [195] and a high pressure phase transition has been theoretically proposed but the structure has not yet been characterised [195].

It is clear from the literature that there is a pressure induced phase transition in the hexaborides away from the cubic structure but it is yet to be characterised. We will try to address the question in this section and propose high pressure phases for calcium hexaboride.

3.2.1 Structural properties of CaB_6

cP7 and derivative structures

cP7-CaB_6 is thermodynamically and dynamically stable under ambient conditions, but calculation of its phonon dispersion under 30 GPa of pressure (Figure 3.3) revealed that a whole branch along the M-R direction becomes imaginary above 24 GPa *, immediately indicating that this was not the lowest energy state.

To determine the lower energy structure, the phonon dispersion of cP7-CaB_6 was first calculated as a function of pressure to find out which phonon mode, or displacement of

*Phonons became imaginary at critical pressures of 24 GPa (for $q = R$) and 26 GPa (for $q = M$) found in our ultrasoft pseudopotential calculations and these compare well against the corresponding values of 23 GPa and 25 GPa found in our projector-augmented wave (PAW) VASP calculations.

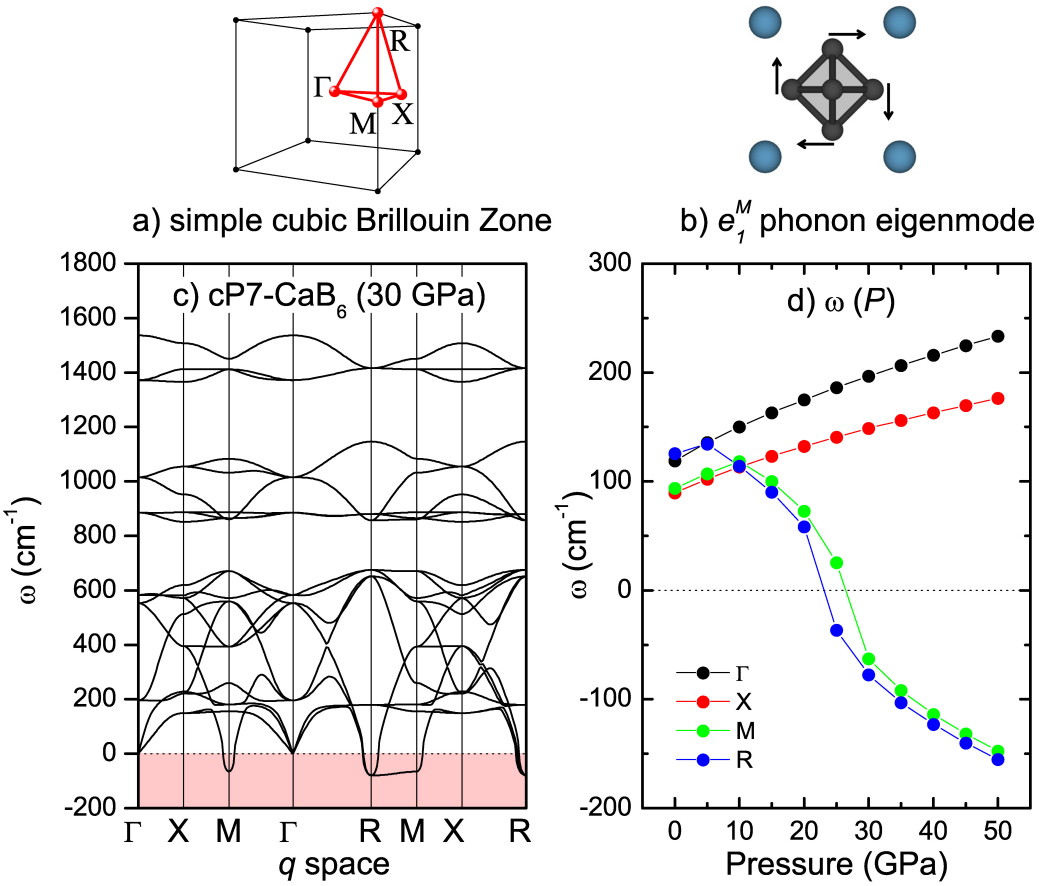


Figure 3.3: a) High symmetry points defining the irreducible wedge in the simple cubic Brillouin zone. b) Displacements of boron positions in real space viewed along [100] corresponding to the M-point phonon. c) Calculated phonon dispersion for cP7-CaB_6 at 30 GPa showing multiple imaginary modes. d) Calculated variation of R and M phonon frequencies with pressure.

atoms, and what applied pressure was responsible for instability. Frequencies of selected phonon modes at the Γ (0, 0, 0), X (0, $\frac{1}{2}$, 0), M ($\frac{1}{2}$, $\frac{1}{2}$, 0), and R ($\frac{1}{2}$, $\frac{1}{2}$, $\frac{1}{2}$) high-symmetry points were plotted (Fig. 3.3d) showing that R and M are the only modes that become imaginary and thus can be used to distort cP7 into its lower energy state [†]. Similarly, the R and M phonon modes of superconducting YB_6 have also been demonstrated to become imaginary at high pressures (55 and 63 GPa respectively) but the new crystal structure has not yet been determined [195].

[†]The phonon frequencies plotted were calculated using a 16 x 16 x 16 k-mesh and are converged to within 0.5 cm^{-1} with respect to a 12 x 12 x 12 k-mesh.

The imaginary mode at R is triply degenerate and the imaginary mode at M is singly degenerate with both modes causing rotation of the boron octahedra. All non-equivalent combinations of the imaginary frequency eigenvectors (listed in Table 3.2) were applied to a 2 x 2 x 2 supercell of the cP7 structure relaxed to 50 GPa. The 50 GPa structure was used as there are larger differences in enthalpy between distorted structures than at 30 GPa, enabling a more accurate determination of the lowest energy state. Based on the equations describing the phonon properties in Subsection 1.5.1, the atoms are displaced by the eigenvector to create the distorted structures using Equation 3.1.

$$u^a_{I\alpha} = \eta_{\mathbf{q}}(I\alpha)e^{i\mathbf{q}\mathbf{R}_a} \tag{3.1}$$

The displacement u for atom I which is in unit cell a is equal to the product of the eigenvector η for that particular q-vector ($\mathbf{q}$) and the exponent of the q-vector and a vector ($\mathbf{R}$) defining the position of the unit cell. The displacement is defined for a particular cartesian direction α. Normalised combinations of the four eigenvectors were used to generate the distorted structures in Table 3.2.

The resulting distorted unit cells were carefully relaxed by making sure that the residual forces were below 0.001 eV/atom. The cells were found to converge to several distinct configurations judging by their space group, enthalpy, atomic volume, simulated XRD pattern and radial distribution functions (see Ref. [177]) [‡]. For example, the most general distortion $e^R_1 + e^R_2 + e^R_3 + e^M_1$ led to the same oP28 structure as the $e^R_2 + e^R_3 + e^M_1$ distortion. A phonon dispersion calculation (Figures 5.2, 5.3 and 5.4) was run for each distinct structure, finding that the oP28, hR42 and tI28 structures of CaB_6 (Figure 3.4) are dynamically stable.

At this stage, one could propose oP28 as a high pressure ground state of CaB_6. It could

[‡]The judging criteria analysis and relaxation was performed by Dr Aleksey Kolmogorov.

number	eigenvector combination	starting SG#	final SG#	Pearson symbol	H-H_{cP7} [meV/atom]	dynamical stability
1	$e_1^R + e_2^R + e_3^R + e_1^M$	14	62	oP28	-10.12	yes
2	$e_2^R + e_3^R + e_1^M$	62	62	oP28	-10.12	yes
3	$e_1^R + e_2^R + e_3^R$	167	167	hR42	-8.85	yes
4	$e_1^R + e_1^M$	127	140	tP28	-9.96	yes
5	e_1^R	140	140	tI28	-9.96	yes
6	e_1^M	127	127	tP14	-8.49	no
7	$e_1^R + e_2^R$	74	74	oI28	-9.07	no
8	$e_1^R + e_2^R + e_1^M$	12	12	mS56	-9.99	no
9	$e_2^R + e_1^M$	63	63	oS56	-9.99	no

Table 3.2: Structure and stability of 9 possible distorted structures for a 2×2×2 cP7-CaB_6 supercell using combinations of 4 eigenvectors and fully relaxed at 50 GPa. The table gives the starting and final space group symmetry, Pearson symbol, enthalpy gain and the dynamical stability for the proposed structures. Structure 9 is not the same structure as the proposed oS56 high pressure ground state.

explain the orthorhombic distortions observed in other hexaboride compounds. However, our group ran some high pressure experiments which led us to investigate the compound further. Calcium hexaboride was compressed in a diamond anvil cell to gigapascal pressures and the structures were probed using X-ray diffraction. The results are shown in section 3.2.2 but there was difficulty in solving the 30+ GPa structure so it was clear that input from theory was required. An evolutionary structure search was run at 30 and 50 GPa using larger unit cells of Ca_4B_{24}. A new structure (oS56) was found from the 30 GPa search. oS56-CaB_6 was 74 meV/atom lower in enthalpy than both cP7 and oP28, stabilizing over cP7 at 13 GPa. The distorted cP7 structures are thus local minima around the parent cP7 structure.

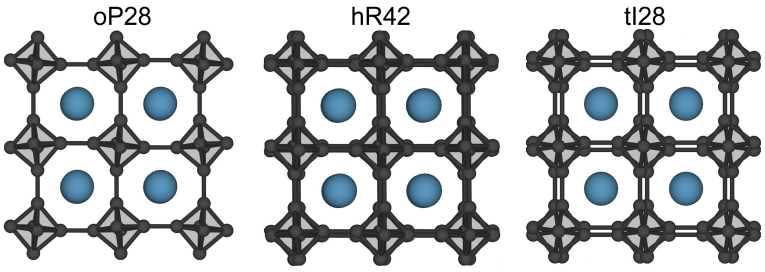


Figure 3.4: The oP28, hR42 and tI28 crystal structures of CaB_6. Boron atoms are in dark grey and calcium atoms in blue.

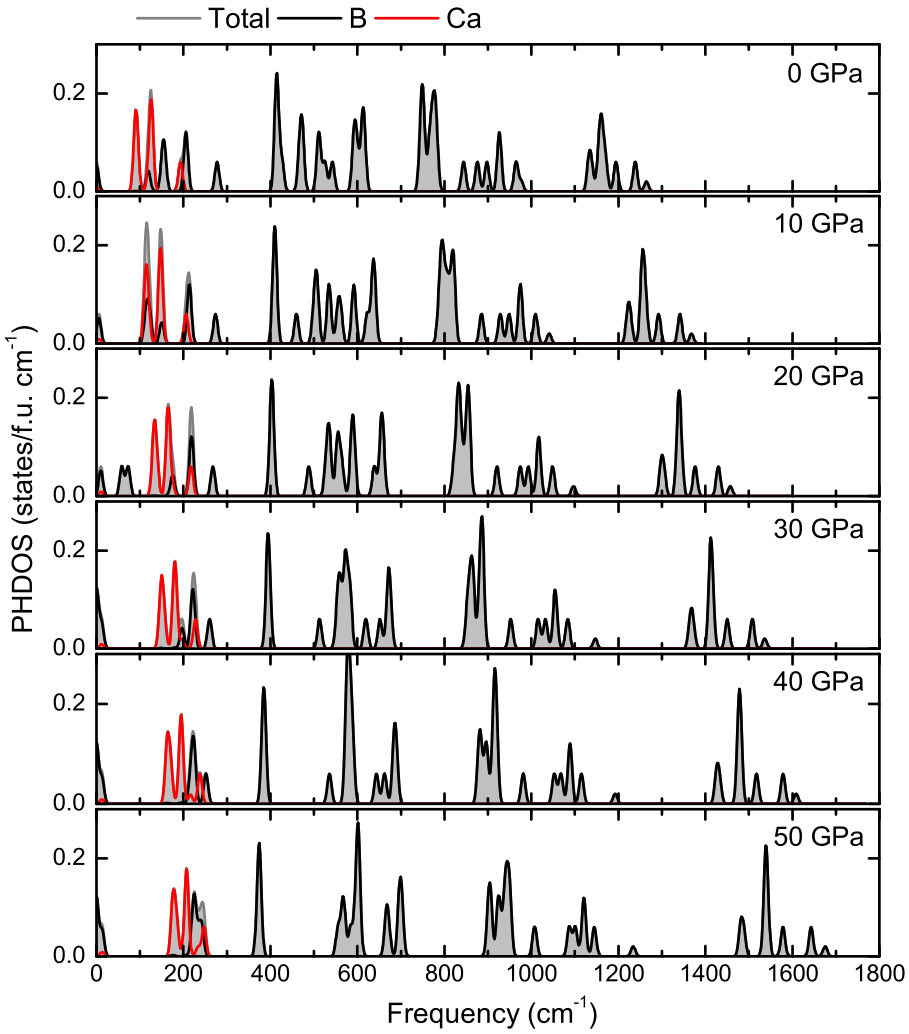


Figure 3.5: The phonon density of states of cP7-CaB_6 with pressure with labelled projections onto the calcium and boron atoms.

Studying the phonon density of states of cP7 with pressure (Figure 3.5) may help to rationalize the structural distortion. A major change occurs between 20 and 30 GPa with the merging of boron peaks around 570 cm^{-1} forming a strong narrow peak at 575 cm^{-1} at 40 GPa. The other two sets of boron peaks (735-1000 and 1120-1280 cm^{-1}) just move to higher frequencies with pressure. At 20 GPa the doublet centered at 65 cm^{-1} corresponds to the R and M frequencies which become imaginary and so do not appear in the 30 GPa plot.

Muetterties [196] has stated that the length of the external boron bond (b_e), which is

between the octahedra, is related to the length of the bond within the octahedron (b_i) through equation 3.2.

$$\frac{\sqrt{2b_e} + b_i}{a} = 1 \tag{3.2}$$

Using calculated bond lengths we find that between 0 and 50 GPa the Muetterties parameter for CaB_6 ranges between 0.855 and 0.870, slightly lower than the prediction of 1.000, with all other alkaline earth metals having values similar to that of CaB_6 (Figure 3.6a).

By studying the M phonon mode up to 60 GPa of applied pressure, for all the alkaline earth hexaborides, we found that BeB_6 and MgB_6 were dynamically unstable as the metal ions are too small and Ba and Sr remain stable as their ions are large enough to keep the boron network from collapsing [177]. Investigating this further, Figure 3.6b shows that the percentage volume taken up by the metal ion in the cP7 structure is correlated with the stability of the structure. In general, cP7 is dynamically stable if metal filling is >29% and thermodynamically stable if it is <40%, the only exception to these rules is calcium, showing that the size of the metal ion in a shrinking boron framework is not the main reason for dynamic instability.

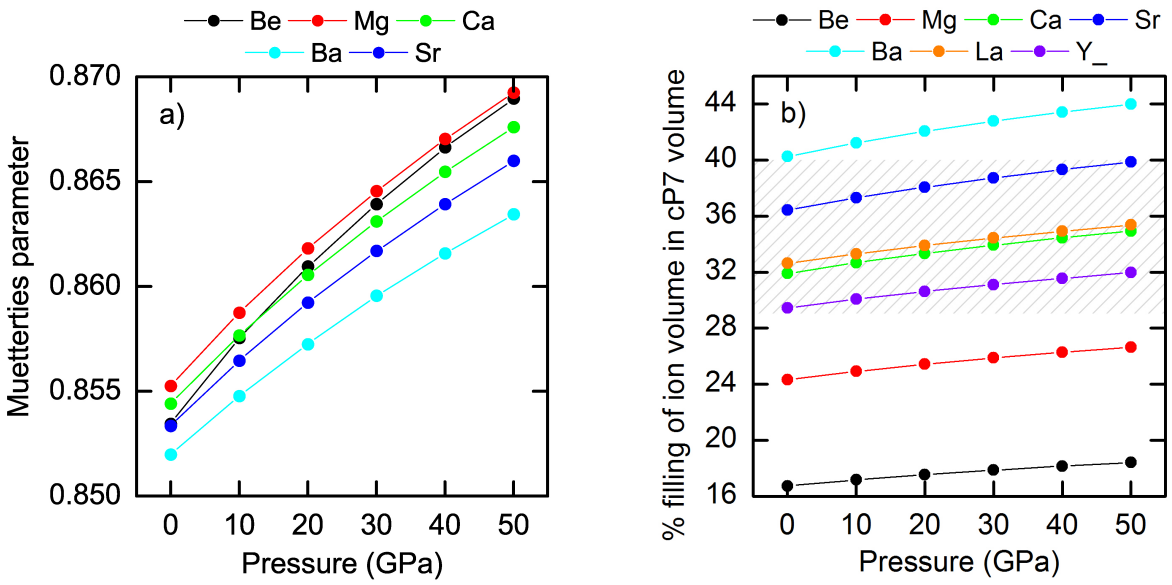


Figure 3.6: Left: Muetterties parameter (Equation 3.2) for alkaline earth hexaborides with pressure. Right: Percentage filling of the metal ion volume in the cP7 unit cell for alkaline earth, lanthanium and ytrium hexaborides with pressure. The percentage filling for stable compounds is shown by the grey shaded region.

Without proper analysis of the stability of a particular crystal structure it is easy to discover interesting properties of unstable hypothetical materials. For example, it was recently suggested that cubic MgB_6 could exhibit magnetic and antiferroelectric properties [197]. Considering only one distortion of the cP7 crystal structure, the authors suggested that MgB_6 would stabilise as the cubic structure with the magnesium ion sitting closer to the face of the cube [197]. We repeated their calculation to find the minimum energy position of the alkaline earth metal ions in the cube and also found that magnesium would prefer to sit closer to the edge and beryllium sits at the edge (Figure 3.7).

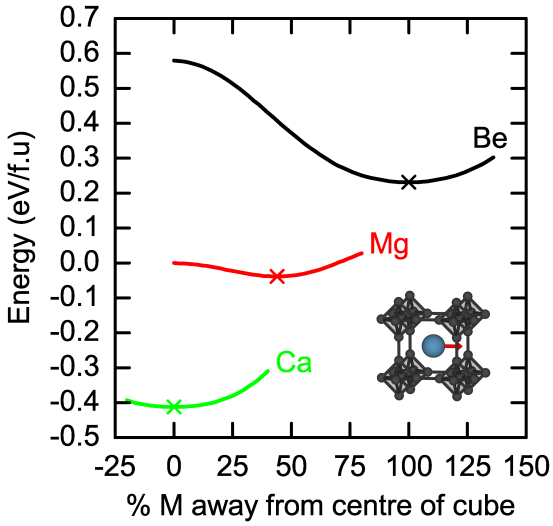


Figure 3.7: The energy of a hypothetical structure of MB_6 created by moving the metal ion away from the equilibrium position in cP7 structure. The minimum energy positions for Ca, Mg and Be, labelled with an X are at 0, 44 and 100% away from the centre respectively.

Unfortunately we found the proposed magnesium structure to be unstable relative to decomposition into experimentally known MgB_7 and MgB_4, lying 95 meV/atom above this tie-line. We have also found more stable configurations for MgB_6: the proposed orthorhombic (oS56) ground state of CaB_6 and local minima around cP7-CaB_6 of oP28, hR42 and tI28. The lowest energy, oS56, is 37 meV/atom lower in enthalpy than the proposed magnetic cubic structure but is still unstable as it is 59 meV/atom above the $MgB_7 \leftrightarrow MgB_4$ tie-line.

oS56-CaB_6

oS56-CaB_6 is thermodynamically more stable than cP7-CaB_6 at 13 GPa. oS56 is formed from cP7 through half of the boron octahedra opening up, fusing and sharing a bond in between. The fused octahedra form zig-zag strips running in one direction down the unit cell resulting in alternating layers of fused and unfused octahedra. From now on, unfused octahedra will be referenced simply as octahedra. The origin of the phase transition from cP7 to oS56 was determined by studying the structural parameters of their MB_6 compounds of the alkaline earth metals with pressure. Parameters such as bond angles, boron-boron (B-B) bond lengths, cell volumes and metal-metal (M-M) distances were compared.

To understand a phase transition it is wise to begin with comparing the parts of the structure that remain the same, in this case, it is the boron octahedra. Applying pressure to cP7-CaB_6 reduces the B-B bond (red in Figure 3.8) between octahedra (1.673 Å at 0 GPa, 1.571 Å at 30 GPa). The shortened bond breaks resulting in half of the octahedra opening up, fusing and sharing a bond. For all alkaline earth hexaborides at 0 - 50 GPa, oS56 is found to be more stable when B-B bonds between octahedra are longer than in cP7 (Figure 3.9).

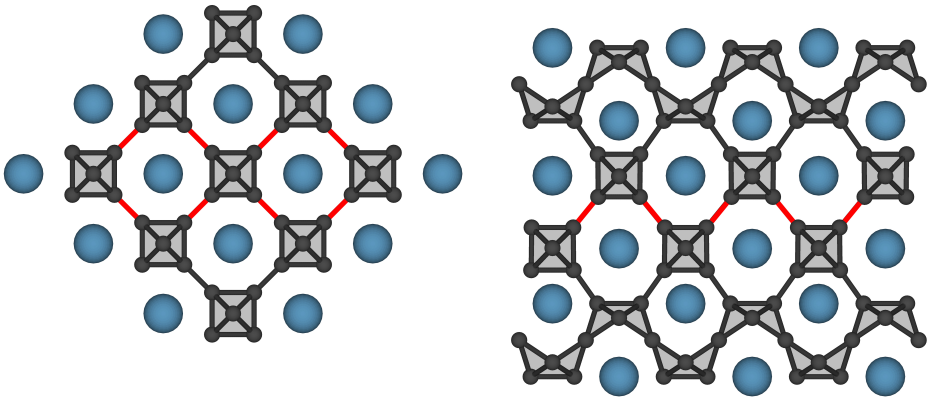


Figure 3.8: Crystal structures of cP7 (left) and oS56 (right) CaB_6 relaxed to 30 GPa. Boron atoms are in dark grey and calcium atoms in blue. The bonds between octahedra as described in the text and in Fig. 3.9 are shown in red.

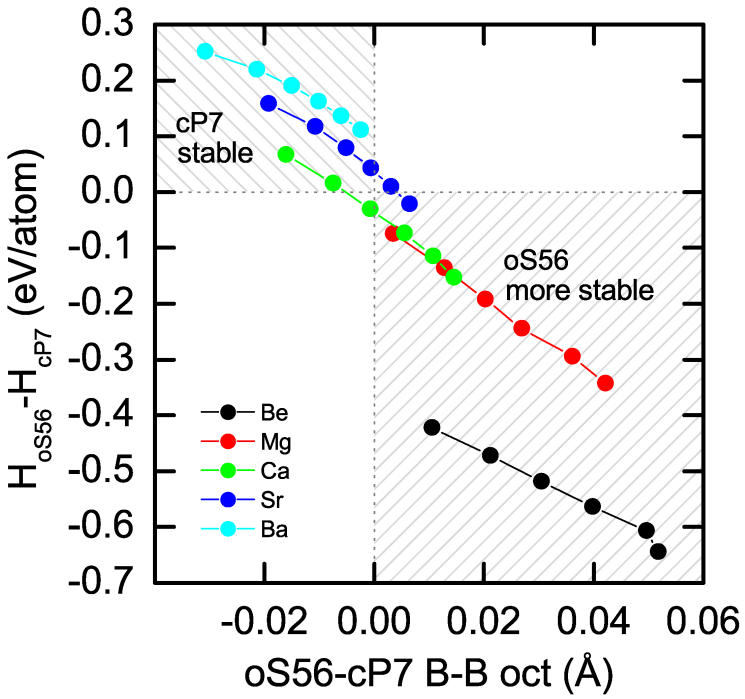


Figure 3.9: Difference between the boron-boron (B-B) bond length between octahedra in oS56 and cP7 against the difference in their formation enthalpies for all alkaline earth metals at increasing pressures from left to right of 0, 10, 20, 30, 40 and 50 GPa. The B-B bond is shown in red in Figure 3.8. The kink at 50 GPa for the Be point is thought to be due to BeB_6 being highly unstable at all pressures.

cP7-BaB_6 is more stable than oS56 at 0 to 50 GPa as the distance between octahedra is larger in cP7. cP7-SrB_6 is stable up to 43 GPa as around this pressure the distance between octahedra becomes greater for oS56 thus causing a phase transition. At all pressures, MgB_6 and BeB_6 are more stable in oS56 however neither metals have hexaboride ground states and are known to be dynamically unstable in the cP7 structure [177, 196].

The length of the B-B bond between octahedra was found to be the main factor causing the phase transition in cP7. The change of other structural parameters are still thought to have a small influence. The second most important factor affecting stability is the distance between planes. Figure 3.10 shows that oS56 is more stable than cP7 when the distance between planes is shorter, i.e. stable structures prefer to be more compact. The volume per atom for oS56 (8.080 $Å^3$) is less than than cP7 (8.751 $Å^3$) at 30 GPa.

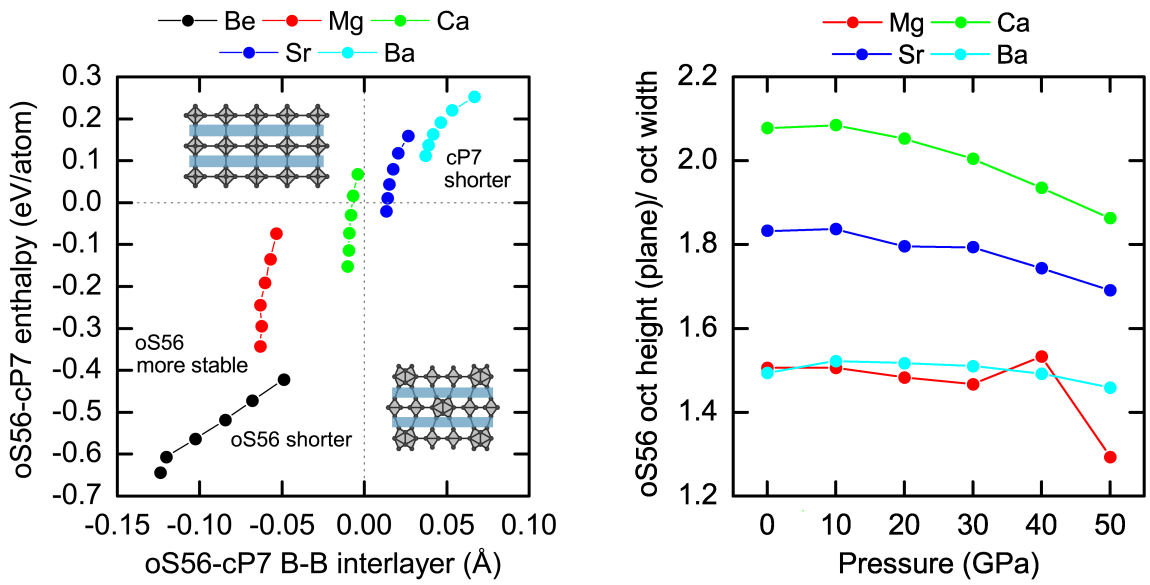


Figure 3.10: Left: The difference between the distance between planes in oS56 and cP7 against the difference in their formation enthalpies for all alkaline earth metals at 0, 10, 20, 30, 40 and 50 GPa. The interlayer distance for cP7 and oS56 is shown by the blue strip in the crystal structure diagrams (which show boron only). Right: Ratio of the height to the width of the octahedron in oS56-MB_6 for M = Ba, Ca, Sr and Mg, with increasing pressure.

The cP7 structure is symmetric in all directions. Applying pressure to cP7-CaB_6 reduces the symmetry through the formation of a strip only in one direction of oS56. The distance between octahedra in oS56, elongates perpendicular to the strip (Fig. 3.11b) and narrows parallel to it (Fig. 3.11a). The octahedra themselves are also no longer symmetric as in cP7, elongated perpendicular to the plane and squashed in the plane. Figure 3.10 shows that comparing the alkaline earth metals, there is greatest distortion of the octahedron for Ca, Sr is less distorted and Be and Mg are only slightly distorted. Finally, metal ions in oS56 are not equidistant from the octahedron as in cP7. In the direction of the strip, metal ions get closer to the octahedra. Perpendicular to the strip, the ion next to the strip gets closer to the octahedron whilst the metal on the other side of the octahedron moves further away.

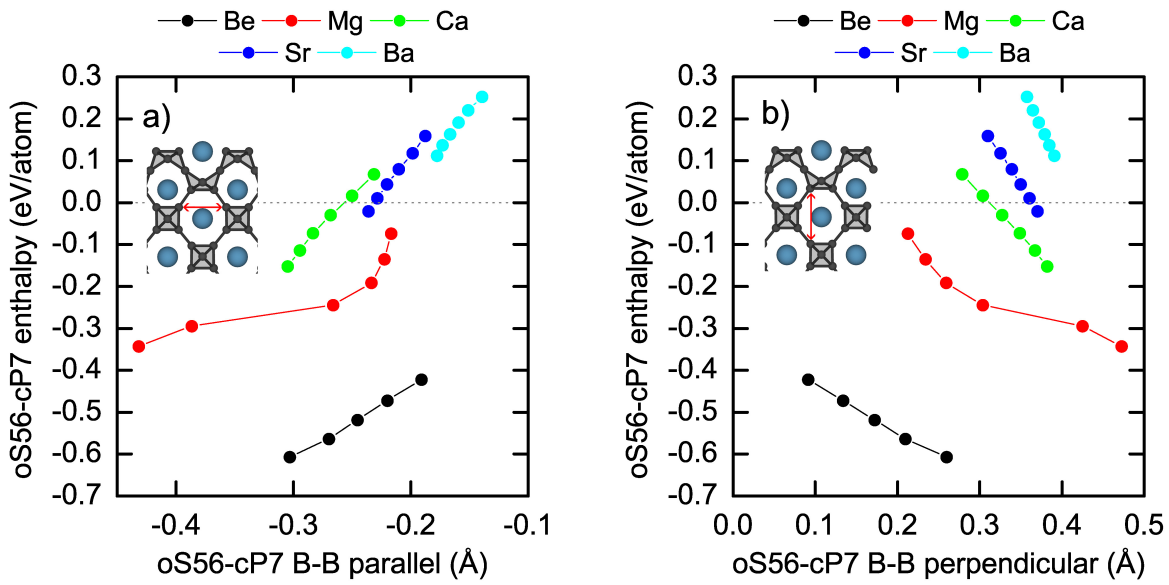


Figure 3.11: a) The shortening of the distance between octahedra parallel to the fused strip and b) the lengthening of the distance between octahedra perpendicular to the fused strip against the relative stability of oS56 versus cP7 for alkaline earth hexaborides at 0, 10, 20, 30, 40 and 50 GPa [a) right to left, b) left to right].

tI56 and derivatives

As described above, experimental observations of CaB_6 under pressure led us to run an evolutionary structure search of CaB_6 at 50 GPa using large unit cells of Ca_4B_{24}. The search revealed a tetragonal unit cell (tI56) which stabilizes over oS56 at 32 GPa. The formation of tI56-CaB_6 is more easily seen by comparing with cP7, from which all the octahedra open up and fuse with 7 others to form a 24-atom boron unit.

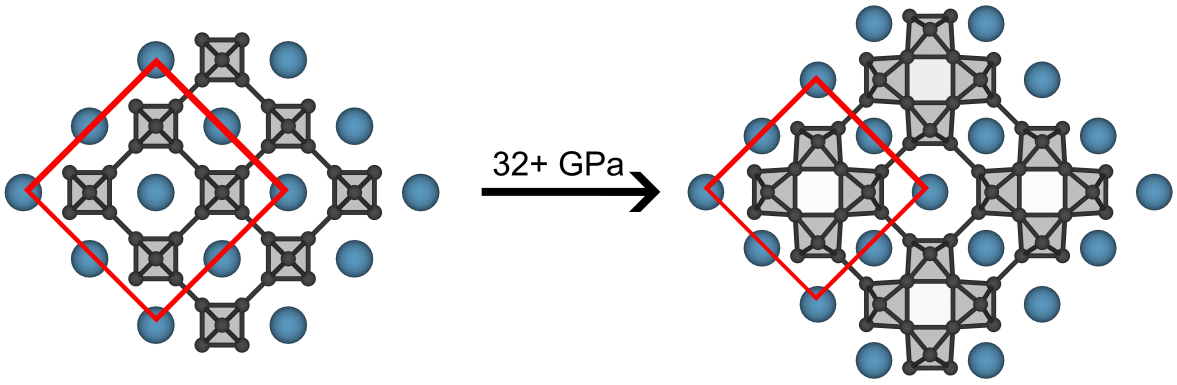


Figure 3.12: Structural transformation of cP7 to tI56 CaB_6 with pressure. The red box shows how the 24-atom boron unit is formed from cP7. The diagram is shown to look down onto one plane so only half of the boron octahedra units which fuse can been seen.

Based on preliminary comparison of the formation enthalpies of the discussed MB_6 structures, we find CaB_6 is the only alkaline earth hexaboride to stabilise as tI56. This is thought to be because the fusion of octahdedra forms a small enough cuboid in the center of the B_{24} unit to hold the whole unit together. The volume of the cuboid needs to be below 6.2 $Å^3$ for stability (Figure 3.13). tI56 is also found to be more stable than cP7 when the central cuboid takes up a high percentage of the unit cell volume ($> 1.2\%$) relative to the other alkaline earth metal hexaborides.

The metal ion plays a large role in the stabilization of tI56 at high pressures. The M-M distance between ions sitting on one side of the B_{24} unit sit closer together as you increase pressure and go down the group II elements. A parameter defined as the normalised M-M, which is [(2 x ionic radius)/M-M], is used to determine how close the metal ions are

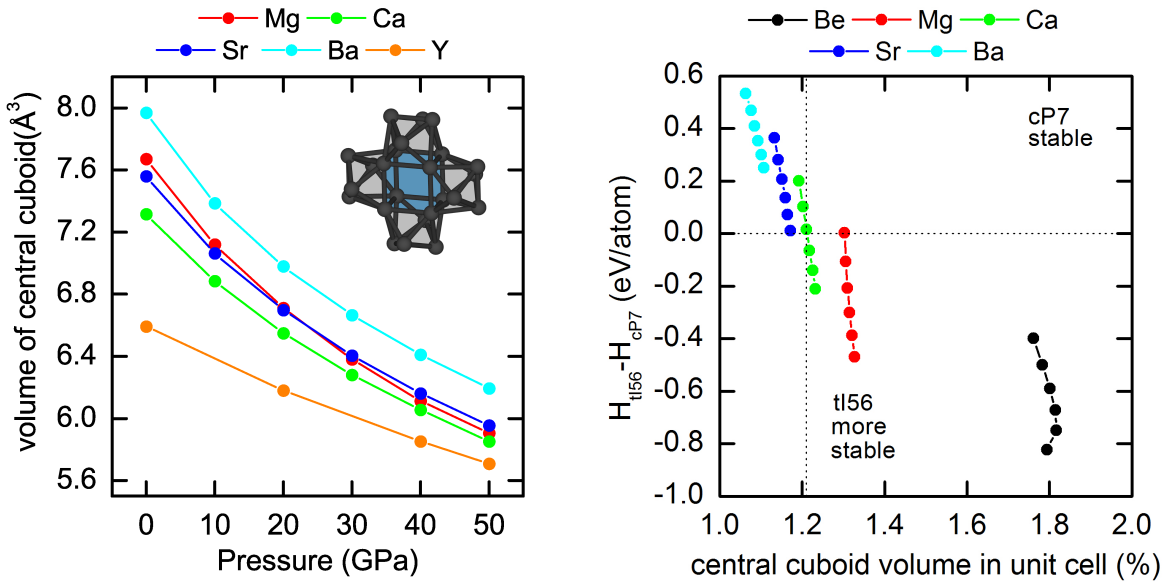


Figure 3.13: Left: Volume of the central cuboid in the B_{24} unit in tI56-MB_6 coloured in blue on the structure diagram. Right: Percentage space taking up by the central cuboid in the tI56 unit cell against the relative stability of tI56 with respect to cP7. The points are plotted for structures relaxed to 0, 10, 20, 30, 40 and 50 GPa, running left to right.

together. Figure 3.14 shows that for stability of tI56, the normalised M-M parallel to the unit needs to be between 0.65 and 0.70 (shown in Figure 3.14). Using these boundaries, a prediction can be made that tI56-CaB_6 would destabilise at around 95 GPa.

No relationship between B-B bond lengths between the B_{24} units and stability was found. The B-B bond length between units decreases with pressure by a similar % in both directions (in line and perpendicular to the plane).

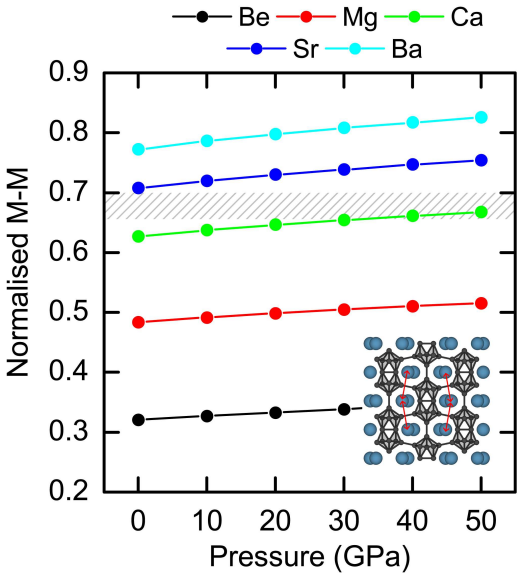


Figure 3.14: The normalised M-M (described in the text) of metal ions along one side of the B_{24} unit, the distance is shown by the red arrows on the crystal structure diagram. The shaded region shows the normalised M-M range for stable tI56 structures.

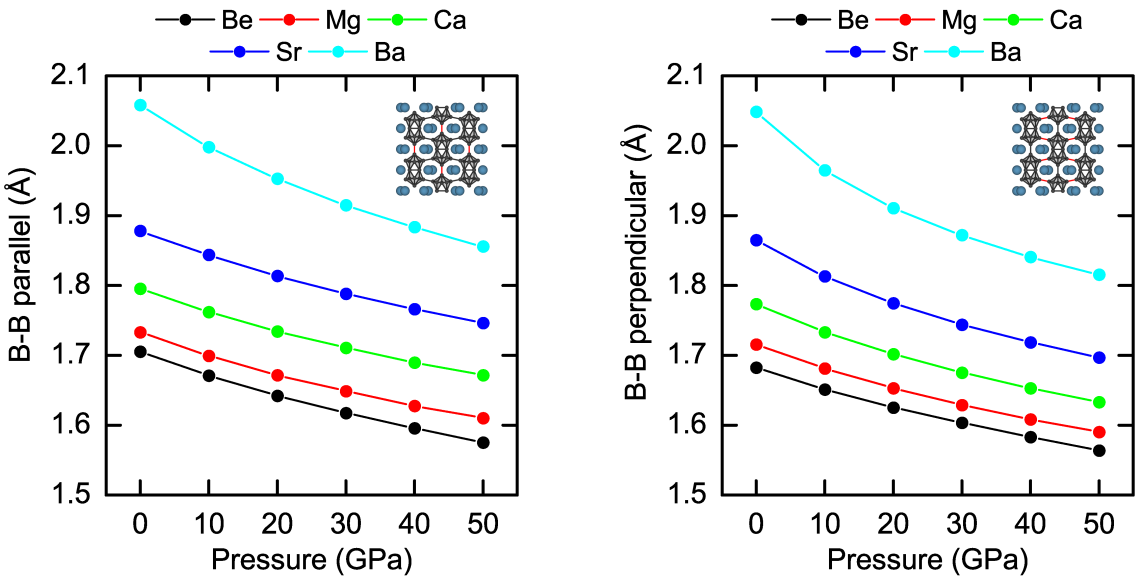


Figure 3.15: Boron-boron bond lengths between the B_{24} units in tI56-MB_6 with pressure. The specific bond length is labelled in red on the crystal structure diagrams.

Insertion of extra boron atoms into tI56

The evolutionary search revealed a metastable state where the one boron atom had migrated to the centre of the B_{24} unit. As there is enough space in the middle for an extra boron atom we constructed unit cells with extra boron atoms in the centre of half and all of the B_{24} units. The resulting structures are shown in Figure 3.17. The relative enthalpy of half-filled tP57-$CaB_{6.125}$ is 5 meV/atom lower than unfilled tI56, whilst the fully filled tI58-$CaB_{6.25}$ is 4meV/atom higher [§]. We only tested the three most ordered configurations of boron atoms inside the units and it is possible that others could result in a lower energy structure. Out of all alkaline earth metal hexaborides, the calcium structure is stable as it provides the smallest cuboid volume in the B_{24} unit for a boron atom to sit (Figure 3.16). tP57-$CaB_{6.125}$ is the most stable of the three structures as it has the smallest cuboid size as shown in Figure 3.16.

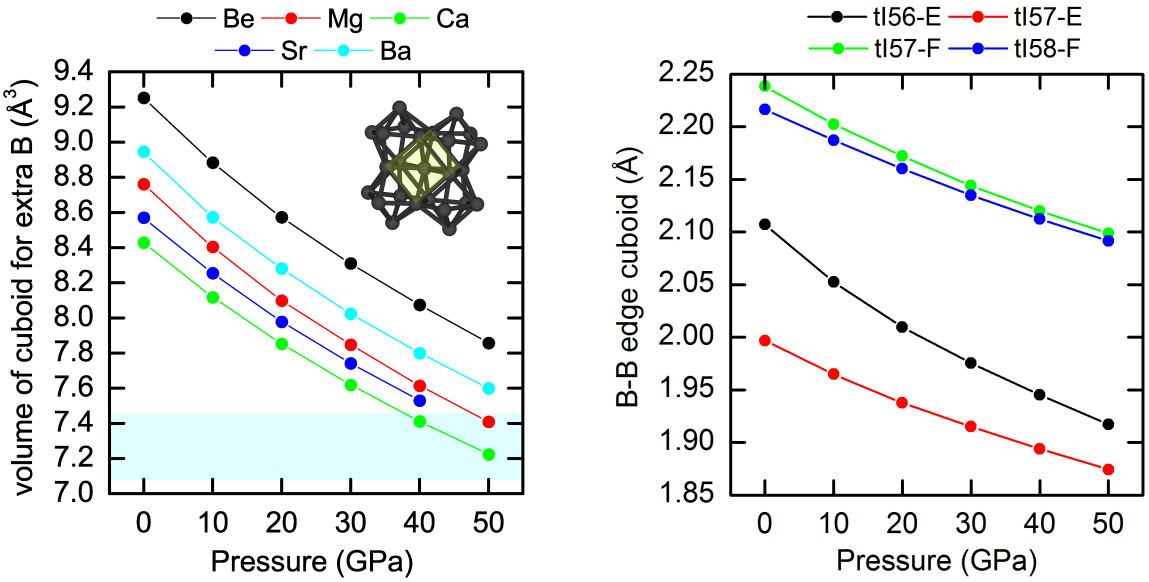


Figure 3.16: Left: Volume of the cuboid that holds the extra boron atom in tI58-$CaB_{6.25}$. The cuboid is shown in yellow on the boron unit structure diagram. The blue shaded region indicates the volumes for which stable structures are found. Right: B-B bond length of the edge of the cuboid in filled (F) and empty (E) B_{24} units in tI56, tP57 and tI58 CaB_6 derivatives with pressure.

[§]The cells were constructed by Dr Aleksey Kolmogorov.

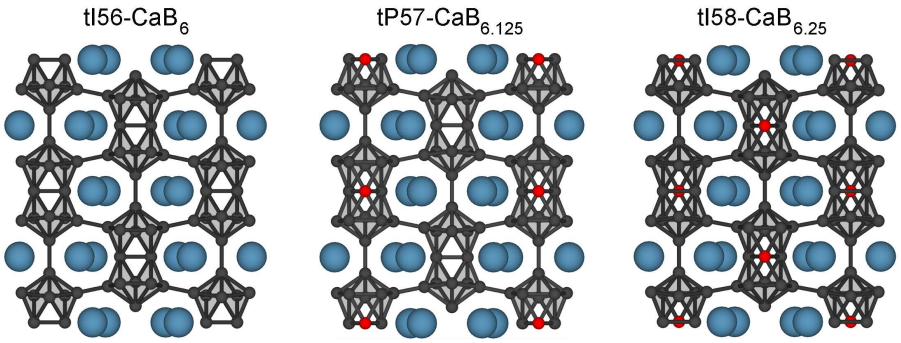


Figure 3.17: Structures of tI56-CaB_6, tP57-$CaB_{6.125}$ and tI58-$CaB_{6.25}$, where the red atom is the extra boron atom in this structure relative to CaB_6.

3.2.2 X-ray diffraction experiments

In a series of experiments, CaB_6 was squeezed in a diamond anvil cell to gigapascal pressures and laser heated to around 2000 K. The crystal structure changes were observed with powder X-ray diffraction (XRD).

The work described in this section has been done in collaboration with a team of scientists in Oxford. The diamond anvil cells were set up and loaded with samples by Andrew Jephcoat and Annette Kleppe from the Department of Earth Sciences and Diamond Light Source in Oxfordshire. XRD measurements were taken at the I15 beamline at the Diamond Light Source in Oxfordshire by myself, Aleksey Kolmogorov and Roxana Margine. The samples were laser heated by Andrew Jephcoat. Initial analysis of the data was done by myself and the Le Bail fitting by Aleksey Kolmogorov. As the work was done as part of a collaboration, I will only give an overview of the results in this section and any further details can be found in the supplementary material of reference [177].

When the dynamic instability of CaB_6 under pressure was predicted we decided to run some experiments to confirm the observation. Nine loadings of CaB_6 in a diamond anvil cell with a variety of sample amounts and pressure regulating media (argon, argon-helium

or methanol-ethanol) were run. For each loading, XRD patterns were measured during the compression to around 30-50 GPa, after laser heating (if done for that loading) and during decompression back to ambient pressure.

A previous study had suggested that around 12 GPa there would be splitting of the [200] peak indicating a cubic to orthorhombic phase transition [190]. Our experiments showed no splitting of the [200] peak up to at least 28 GPa. We did however observe a reduction in intensity of the [111] peak. At higher pressures, samples at 31, 34 and 44 GPa were laser heated to promote the rebonding of the strong covalent boron network. This resulted in a change of the XRD pattern relative to the cP7 pattern indicating that a phase transition had occurred. The XRD patterns contained many wide peaks which overlapped each other and showed that there were multi-phase products present. Resolving the complex crystal structure therefore was deemed as being practically impossible and clearly showed that input from theory was required.

The lowest energy structure from our evolutionary crystal structure search containing two formula units of CaB_6 however did not match the new XRD pattern. Various settings (described in Ref. [177]) were used for the structure searches including relaxing to 30 and 50 GPa. 50,000 structures with 14 atoms in the unit cell were generated but as there was no match to the experimental XRD pattern it was clear that in order to resolve the structure, one needed to investigate a larger unit cell. An oS56 structure (stable 13-32 GPa) and tI56 structure (stable over 32 GPa) were revealed from the larger 28-atom unit cell search. All the peaks in the simulated XRD pattern for tI56-CaB_6 matched the experimental XRD patterns. Some extra peaks are still unresolved in the experimental pattern showing that the laser heating resulted in multi-phase products. All the tI56 peaks remained upon decompression down to ambient pressure meaning that high pressure and

temperature can be used as a method of synthesis of this crystal structure which can then be utilised at ambient pressure.

The observation of an XRD pattern that matches that of the simulated tI56 pattern is encouraging that the predicted ground state structure could indeed be correct. Further experiments are required to understand the CaB_6 phase at medium pressures. The predicted oS56-CaB_6 is thermodynamically more stable than tI56 and cP7 between 23 and 32 GPa but may also require high temperature to promote its formation.

3.2.3 Electronic properties of CaB_6

The electronic properties of known cP7 and proposed structures of CaB_6 (oS56, tI56) and tP57-$CaB_{6.125}$ were calculated within the GGA (Figure 3.18). cP7-CaB_6 is semiconducting but because of the known limitations of the standard DFT approximations to describe bandgaps [83] the tests were meant only for preliminary analysis of the electronic states in this compound. However, the observation of no significant change in the electronic density of states (DOS) and band structure of cP7 with pressure does add to the conclusion in the previous section (3.2.1) that a phase transition from cP7 to oS56 occurs mainly for structural reasons. As there are multiple bands that cross the Fermi level in the high pressure structures, all are assumed to be metallic meaning that there is a potential for superconductivity here.

The decomposed band structure plots in Fig. 3.18 show orbital contribution to specific bands close to the Fermi level. The valence bands close to and below the Fermi level are dominated by boron p states in all three structures. The conduction band for the cP7 structure across Γ-X-M is composed of a hybrid between B (p) and Ca (d_{z^2}) and Ca ($d_{x^2-y^2}$). In the oS56 structure, it is the nearly free-electron Ca (d_{yz}) states that

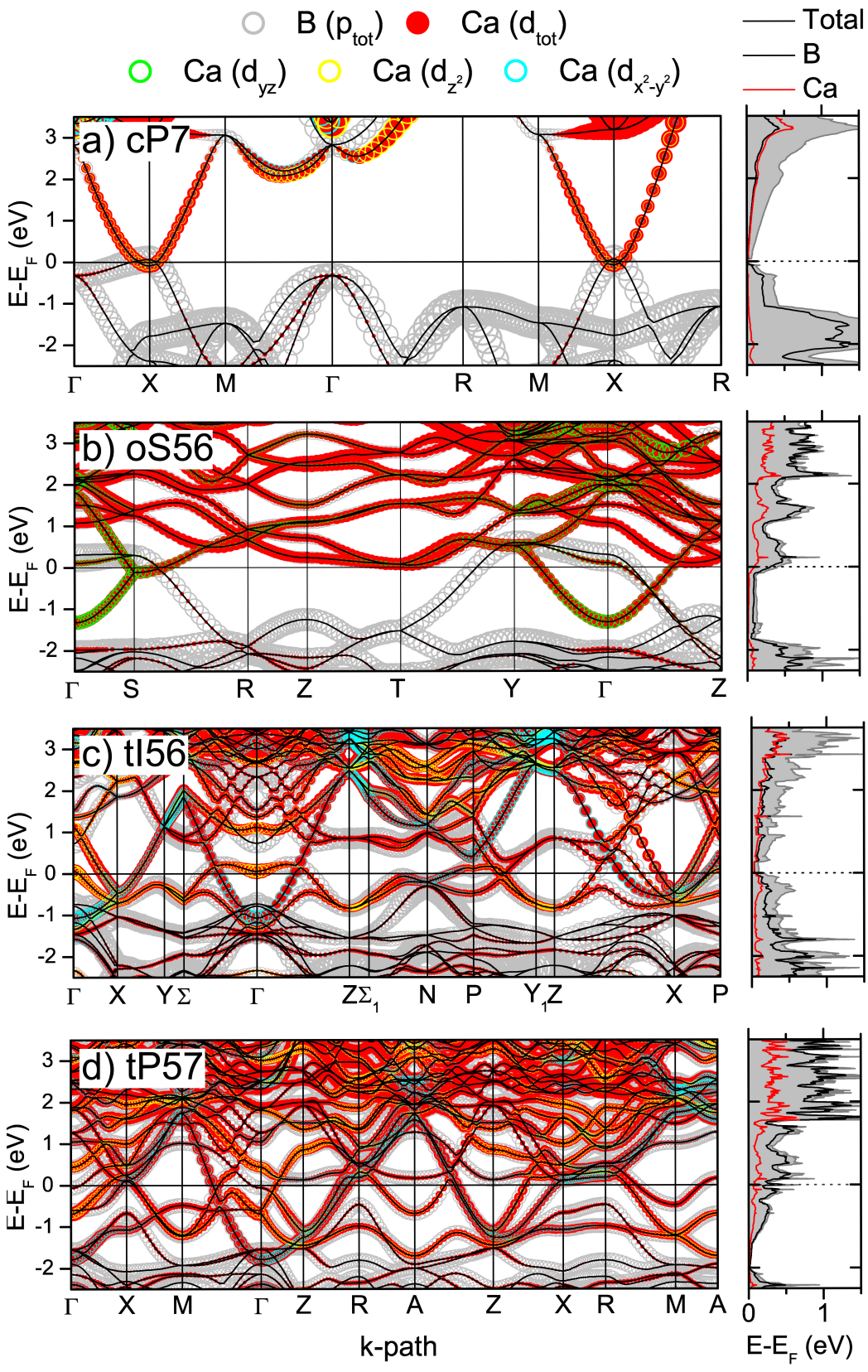


Figure 3.18: Calculated band structure and density of states (DOS) plots of of known (cP7-CaB_6) and predicted (oS56-CaB_6, tI56-CaB_6 and tP57-$CaB_{6.125}$) structures relaxed under 30 GPa of pressure. The size of the coloured circles indicates the orbital contributions to the bands. The decomposition was done within the default PAW radius. The k-paths have been generated using Ref.[198, 199] and [200].

hybridize with the B-p states near the Fermi level and produce a nearly constant DOS in the pseudogap region from -2 to 0 eV. The Fermi level lies on the slope of a DOS peak further suggesting that this is a suboptimal configuration and a more stable related structure might be found by considering larger unit cells. In the tI56 structure, just as in cP7, the Ca (d) states close to the Fermi level are from Ca (d_{z^2}) and Ca ($d_{x^2-y^2}$). The bottom of the Ca d bands in both oS56 and tI56 structures now lies well below the Fermi level (by $\sim$ 1 eV) while the top of the predominantly B p bands lies above the Fermi level (by $\sim$ 0.5 eV). These observations suggest that the predicted polymorphs should be metallic with multiple Fermi surfaces of mixed Ca-d/B-p or predominantly B-p character but more accurate methods, such as GW or time-dependent DFT, should be used to determine the exact position of these electronic states and whether the band gap in cP7 closes at high pressures.

The insertion of an extra boron atom into half of tI56-CaB_6 boron units results in mostly boron states at E_F. These states are mainly B(p_y) which lie in the direction of the filled boron unit layers. The Ca($d_{x^2-y^2}$) band crossing gamma around -1 eV in tI56 is moved down by 0.7 eV in tP57 due to the filling of hybrid B(p) and Ca(d_{z^2}) band close to Γ.

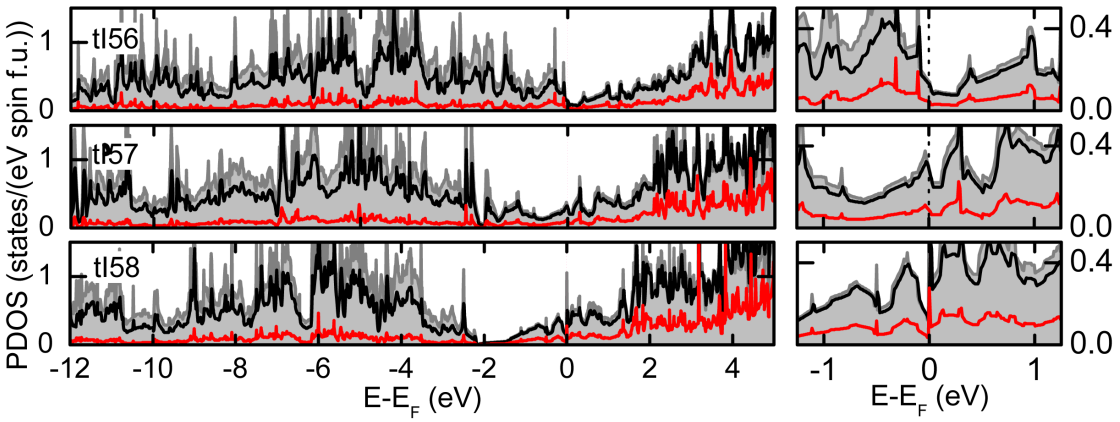


Figure 3.19: Projected DOS of tI56-CaB_6, tP67-$CaB_{6.125}$ and tI58-$CaB_{6.25}$. PDOS is stated in units of states per eV per spin per formula unit (f.u.) against the energy relative to the Fermi energy (E_F). To the right is a zoomed in portion of the DOS close to the Fermi level.

The DOS of dynamically stable distorted cP7 structures is given in Figure 3.20. The shape and composition of the DOS around the Fermi level is similar for all structures where boron states dominate and all are assumed to be semiconducting as in cP7.

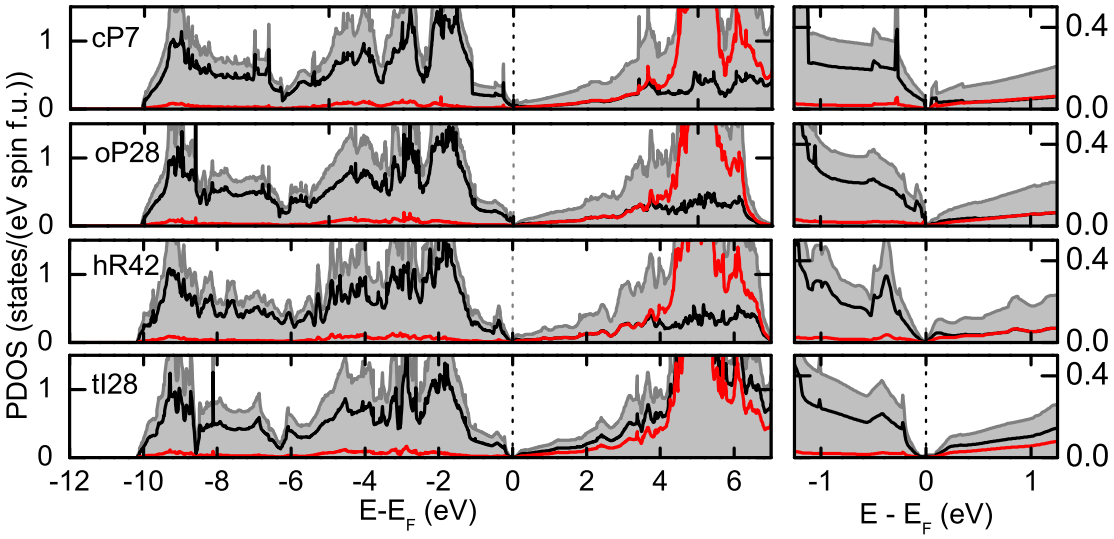


Figure 3.20: Projected density of states of the resulting structures (relaxed to 30 GPa) from combinations of phonon eigenvectors as listed in Table 3.2. PDOS is stated in units of states per eV per spin per formula unit (f.u.) against the energy relative to the Fermi energy (E_F). To the right is a zoomed in portion of the DOS close to the Fermi level. To the right is a zoomed in portion of the DOS close to the Fermi level.

3.2.4 Superconducting properties of CaB_6

Figure 3.21 shows the Eliashberg function calculated for oS56-CaB_6 at 30 GPa at the Γ q-vector. This preliminary calculation indicated that the structure would not be superconducting if a full mesh of q-points was used so the large calculation was not run. The plot is given for comparison with the higher pressure structures and to indicate the reason for the lack of superconductivity. The plot is not deemed to be reliable and should not be taken as the final result. Total lambda is around 0.3, with the majority of phonon contributions coming from boron modes. All the superconducting calcium borides presented in this chapter have a large proportion of lambda resulting from low frequency mixed

calcium and boron modes. Less than one third of lambda is from these modes in oS56 so this may be a reason for the lack of superconductivity. The phonon density of states shows that the calcium frequencies are up to around 240 cm^{-1}, whilst in superconducting oI8-CaB the calcium frequency range is higher, ending around 360 cm^{-1}. Lower frequency calcium phonon modes in oS56-CaB_6 may be another reason for its lack of superconductivity. Similarly the peak of calcium phonon modes in non-superconducting tI56-CaB_6 ends around 360 cm^{-1} but this is for a 50 GPa structure, which would be reduced at 30 GPa.

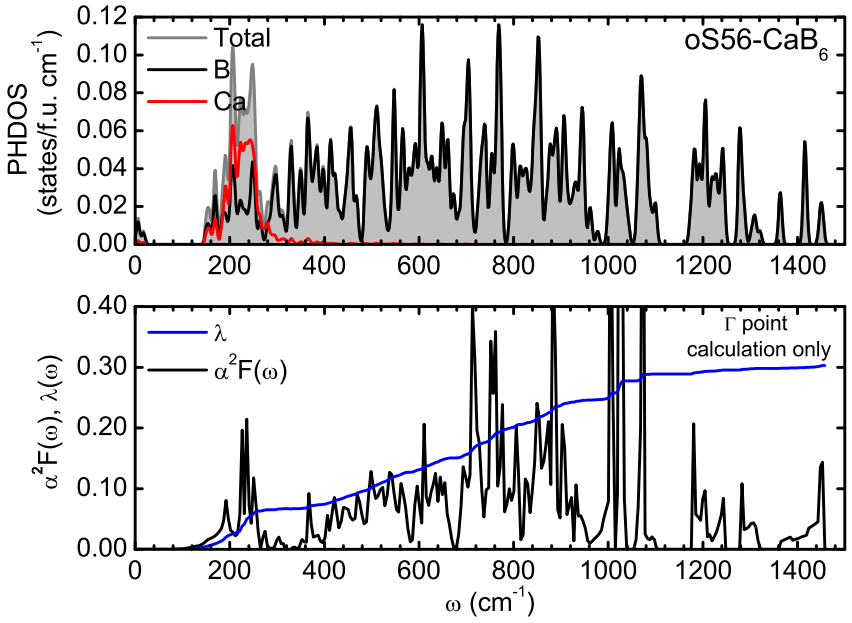


Figure 3.21: Top: Total and projected phonon density of states (PHDOS) of oS56-CaB_6 calculated using a mesh of q-points. Bottom: Eliashberg function and the strength of the electron-phonon coupling (λ) of oS56-CaB_6 relaxed to 30 GPa. The electron-phonon calculation was run using the Γ q-vector only.

The metastable tI58-$CaB_{6.25}$ is predicted to be superconducting at 50 GPa with a T_c of 1.9 K, total lambda of 0.41, ω_{log} of 653.9 when using a value of 0.12 for μ^*. Approximately 80% of the total lambda results from modes between 160 and 700 cm^{-1} which are mixed modes from movement of both calcium and boron atoms (Figure 3.22). This can be split into two regions: the first 45% of total lambda from mixed modes dominated by calcium

atoms and the rest from boron modes.

Using a mesh of 6 q-points (q- 3 x 3 x 3), tI56-CaB_6 is found to be non-superconducting. Whilst the structure has a higher ω_{log} than the tI58 structure of 712 cm^{-1}, it has a lower total lambda of 0.24. The Eliashberg function shown in Figure 3.22 shows that like in tI58-$CaB_{6.25}$, the majority of modes contributing to lambda in tI56-CaB_6 come from those below around 600 cm^{-1}. The prediction of superconductivity in the boron doped structure may be attributed to the calcium phonon peaks at generally higher frequencies than the undoped structure. tI58-$CaB_{6.25}$ has a small calcium peak centered at 400 cm^{-1} that is not present in tI56-CaB_6. The combination of these phonon properties and lack of electronic density of states at the Fermi level make tI56-CaB_6 a non-superconducting structure.

We were unable to complete the calculation of the Eliashberg function for the more stable tP57-$CaB_{6.125}$ as the number of atoms in its unit cell is too large. Judging by the slightly lower DOS at E_F than tI56 but slightly higher DOS than tI58 (Figure 3.19), we expect tP57-$CaB_{6.125}$ to be superconducting with T_c of $\sim$1 K.

Boron-doped structures of tP57-$CaB_{6.125}$ and tI58-$CaB_{6.25}$ are expected to be superconducting. The DOS of undoped tI56-CaB_6 is however too low for this metastable state to be superconducting. The tI58 Eliashberg function shown in Figure 3.22 can be split into two regions: the first 35% of total lambda from mixed modes dominated by calcium atoms and the second 45% of total lambda from mixed modes dominated by boron atom movement.

Applying pressure to semiconducting calcium hexaboride results in phase transitions to metallic structures. As the high pressure phases are very stable, their electronic density of states at the Fermi level is low resulting in poor or non-superconducting structures.

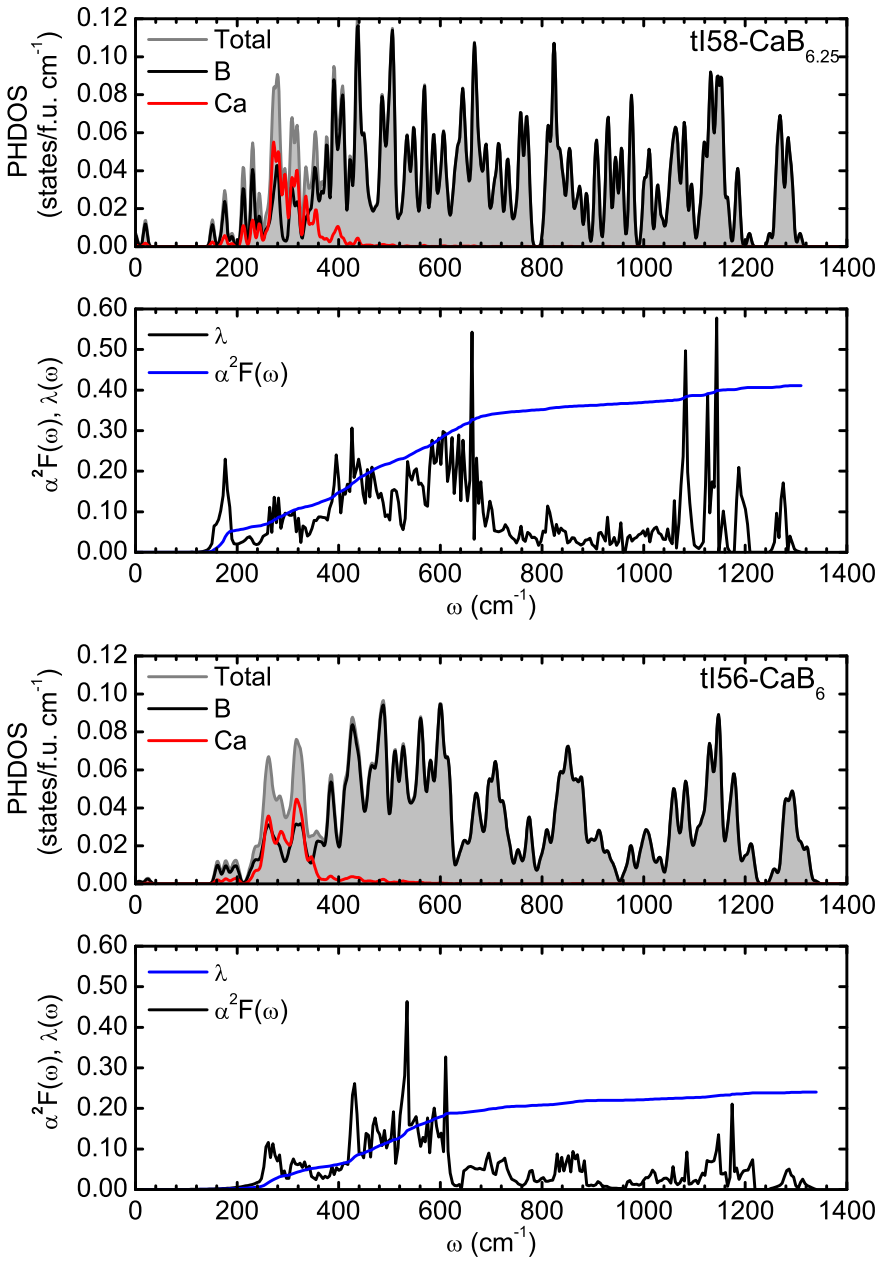


Figure 3.22: Top: total and projected phonon density of states (PHDOS), bottom: Eliashberg function and the strength of the electron-phonon coupling (λ) of $CaB_{6.25}$ in the first two plots and tI56-CaB_6 in the second two plots. Both structures are relaxed to 50 GPa.

In addition, the calcium phonon modes are bunched around the low frequency region, depressing the T_c further. A small addition of boron to calcium hexaboride is found result in a low T_c material as the phonon and electronic properties become slightly more desirable for superconductivity.

3.3 Calcium tetraboride: CaB_4

Twenty metal tetraborides are known to have a common structure, the tetragonal ThB_4 type tP20 structure (Figure 3.23), first determined by Zalkin and Templeton [201] in 1952. Tetraborides are of interest for their electronic and magnetic properties. Nd, Sm, Gd, Tb, Dy and Ho borides are antiferromagnetic, Pr boride is ferromagnetic and Er and Yb are thought to be metamagnetic. Like LaB_6, LaB_4 is also a good thermionic electron emitter allowing it to be used as a cathode in electron microscopy [202].

Calcium tetraboride is the only alkaline earth metal thought to form the tP20 structure and although it was first synthesised in 1961 [203], the compound has regained some interest recently [204, 205, 206, 207]. Liu et. al. [207] reported the synthesis of CaB_4 under low pressure but stated that their calculations showed this to be a metastable state as it is unstable with respect to CaB_6 and elemental calcium. It is therefore clear that some questions about the stability and electronic structure of CaB_4 still remain unanswered. Also, to our knowledge there have been no studies on the effect of pressure on calcium tetraboride and none that have observed a phase transition of ThB_4 type tetraborides under pressure.

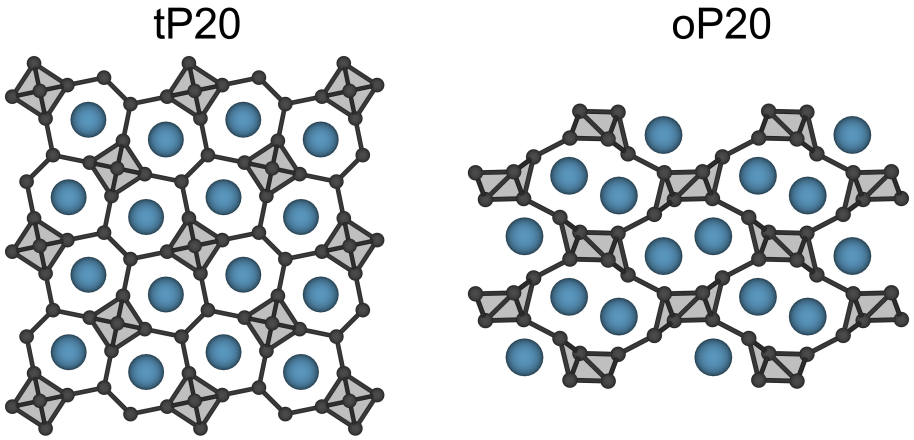


Figure 3.23: Looking down at the layered structure of the tP20 ground state at 0 GPa and a side on view of the oP20 MgB_4 type structure.

3.3.1 Structural stability of CaB_4

The ThB_4 type structure contains 4 formula units (f.u.) of CaB_4 and consists of a boron layer with B_6 octahedra joined by B_2 dimers (Fig. 3.23). Muetterties [196] suggested that the structure is a combination of the B_6 octahedra observed in CaB_6 type MB_6 compounds and the B_2 dimers that form hexagons in AlB_2 type MB_2 compounds. Metal atoms sit above and below the boron layer in between the 7 membered ring formed by links between B_6 and B_2 units. B-B bonds join the layers of octahedra forming a three dimensional covalent boron network as can been seen in the crystal structure part of Figure 3.25.

The stability of ThB_4 type CaB_4 has been questioned by groups studying its electronic structure. Initially, Lipscomb and Britton [208] took earlier analysis of the electronic structure of hexaborides [188] and applied it to the tetraborides. In addition to 20 electrons required for stability of each B_6 unit, they suggested that each B_2 unit requires 8 electrons, 6 of which would come from the boron atoms and the extra 2 provided by the metal. 4 of the 8 electrons for the B_2 unit would form a double-like bond as in ethylene and the other 4 electrons used for external bonds to the octahedra. Per unit cell the total of 56 electrons would be nicely provided by 16 boron atoms and 4 M^{2+} ions. The new and unusual chemistry suggested here was that boron could form a double bond in the solid state.

The idea of a double bond was supported by further theoretical investigation [209] but when an experimental study was performed [204] the stability of pure CaB_4 with a double bonded dimer came into question. Schmitt et al. [204] were only able to synthesise CaB_4 with the presence of a small amount of carbon. Unfortunately their X-ray diffraction analysis was unable to determine the positions of the carbon atom substitutions into

the boron network. Further Hückel based electronic structure calculations on doped and undoped CaB_4 supported a double bonded dimer [204].

Yahia et al. [205] however concluded from theoretical calculations that CaB_4 requires electron doping (maybe from carbon as experiments would suggest) as insufficient electrons are transferred from the calcium atom to stabilise the boron network. Their analysis assumed localized 2-center-2-electron bonding around the dimer and examined three possible electron arrangements shown in Figure 3.24.

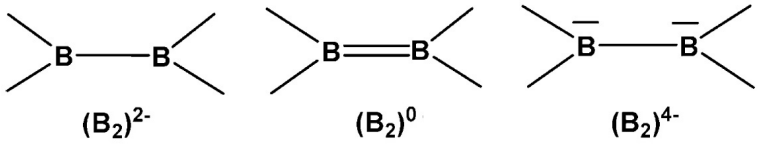


Figure 3.24: The three Lewis formulas for possible bonding configurations of the boron dimer in CaB_4 described in Reference [205]

The first situation was described as satisfactory as the boron atoms are in a trigonal planar configuration and obey the sextet rule but have an unnatural charge balance between metal and boron of $(M^+)_2(B_6^{2-})(B_2^{2-})$. In this situation a trivalent metal would be forced into a very low oxidation state. The second situation is more realistic for the metal ion but B-B dimer bond lengths in any of the experimentally determined tetraboride structures do not indicate multiple bonding. The final situation containing a trivalent metal ion does not seem reasonable. It is unlikely that electron rich B^{2-} atoms each with a nonbonding lone-pair would sit close to electron-poor ${B_6}^{2-}$. The conclusion from this study was that none of the three situations were chemically plausible and thus CaB_4 could not exist without electron doping.

In this thesis section we will show that CaB_4 is thermodynamically stable because of the size of its metal ion. In addition, enough charge is transferred to the boron network as it has been shown in lanthanide and actinide tetraborides that semi-filled bonding bands

are sufficient for stability [206]. Here we will explain why ThB_4 type CaB_4 is stable at ambient pressure and give a general rule for the stability of all ThB_4 type tetraborides with pressure. Stability is shown to be a balance between the size restrictions posed by the metal ion within the boron lattice and the distribution of charge between B_6 and B_2 units.

To begin determining the ground state structure of CaB_4 at ambient pressure, the formation enthalpy of known tetraboride structures in the ICSD was calculated. The ThB_4 type tP20-CaB_4 was found to be the lowest enthalpy structure. Transition metal tetraboride structures of CrB_4 and WB_4 [125, 166] are both highly unfavourable configurations for both CaB_4 and the other alkaline earth metals. Using an evolutionary search of we found that at 19 GPa the semi-conducting oP20 MgB_4 type structure becomes energetically favourable relative to the low pressure metallic phase of ThB_4 type tP20-CaB_4 (Fig. 3.23). oP20-CaB_4 is composed of a chain of pentagonal pyramids with metal atoms sitting in channels running in one direction. At 30 GPa, the tP20 structure is 39 meV/atom higher in enthalpy than the proposed oP20 ground state (Fig. 3). Two higher pressure (50 GPa) semi-conducting metastable states (mP20 and hR10) were also revealed in the search whose properties will be described later.

In an attempt to understand why the tP20 structure becomes unstable with applied pressure, various structural parameters were examined and compared with experimentally known tP20 structures (lanthanides, actinides and Y). The stability was found to be most greatly affected by how close the metal ions are between the planes. These ions sit directly on top of each other and are closer in distance than those within the plane and so automatically indicate that they would have a greater affect on stability. Figure 3.25 shows how the percentage space filled up by the divalent metal ion perpendicular to the

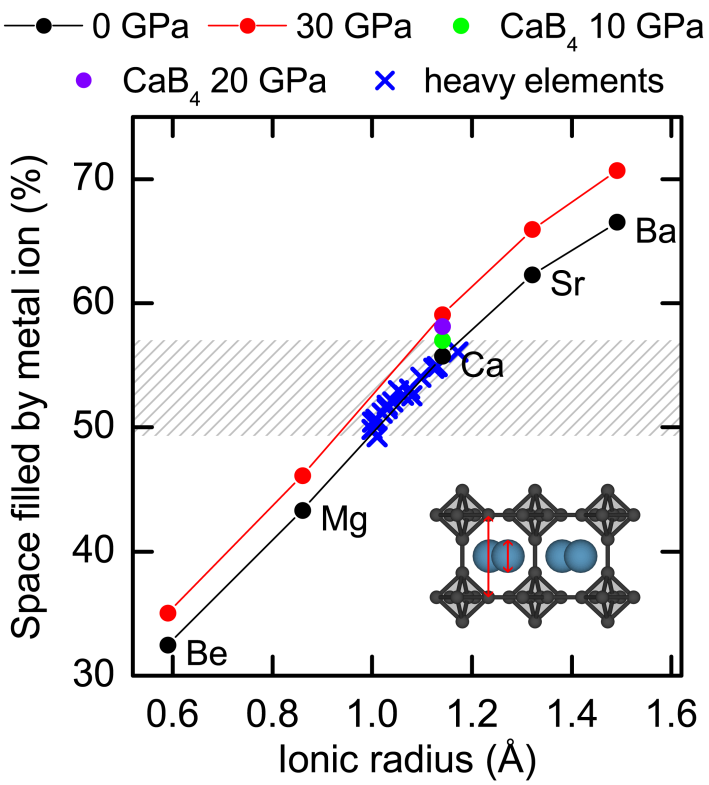


Figure 3.25: The space filled by the metal ion in the c axis plotted against the ionic radius, for the tP20 structure of MB_4. Alkaline earth metals are assumed to be divalent. Heavy elements here are these lanthanides and actinides: Th, Lu, Ce, Nd, Y, Gd, Sm, Tb, Er, Pr, Dy, La, Pu, Ho, U and Tm. Lanthanides are assumed to be trivalent as known in the literature.

boron plane varies with ionic radius and pressure for the alkaline earth metal borides.

Going down the group, the interplanar separation (lattice vector c) does not increase greatly to accommodate the larger ionic radius so the space filled up by the ion increases almost linearly. As expected, applying pressure slightly increases the fraction of the space filled by the ion as the rigid boron lattice is restricted by the B-B bond between the layers (Figure 3.26) and this can be correlated to the stability of the tP20 structure. All known metal tetraborides with the tP20 structure fit neatly over a small range where 49-57% of the interplanar distance can be filled with the metal ion. At both 0 and 30 GPa, MgB_4 falls below this range which is the reason for the tP20 structure being 105 and 293 meV/atom higher in enthalpy than the ground state at these two pressures. The heavy

elements, lanthanides and actinides, plotted here all fall within this percentage range. CaB_4 is stable in the tP20 structure up to 19 GPa before becoming thermodynamically unstable relative to the oP20 structure. tP20-CaB_4 at 20 GPa lies outside the percentage filling range. At high percentage space filling direct metal-metal repulsion makes this configuration thermodynamically unfavourable.

At ambient pressure, tetraborides with metallic ions of radii 0.99-1.18 Å are predicted to form the tP20 structure and can be applied to explain the formation of tetraborides for all metals. Muetterties [196] defined an atomic radius range over which tetraborides were stable (1.97 - 1.68 Å, center - 1.82 Å) but we have defined it in terms of an ionic radius. The trend between atomic radius and the space filling was not as strong as when the ionic radius was used and some experimentally known tetraborides did not fit on the trend line. The ionic radius fit the data better and as it is known that electron transfer occurs between metal and boron network it was deemed more accurate to use the ionic radius. The choice of ionic radius and the correlation coefficient between ionic radius and space filling is shown in table 3.3. The ionic radii used to form the conclusions in the next few paragraphs are from reference [210].

At ambient pressure, monovalent sodium is the only alkali metal that falls within the defined tP20 stability range. Two electrons are not available to be transferred to the boron network so tP20-NaB_4 does not form a stable structure, lying 120 meV/atom above the Na_3B_{20}-Na tie-line.

Across row 1 of the transition metals, only one ion (1+, 2+, 3+, 4+ or 5+), Ti^{2+} fits within the range. Since titanium prefers to be in the 3+ or 4+ state, tP20-TiB_4 does not form. 2nd row transition metals are more complicated. YB_4, with an ionic radius of 1.04 Å falls within the window and is stable in the tP20 configuration. Divalent

palladium, silver and cadmium have ionic radii of 1.00, 1.08 and 1.09 Å respectively so fall within the stability window. The tP20 structure is not stable for these borides as the metals are thought to prefer to be in other valence states (for example silver prefers to be monovalent). No cadmium borides are known and palladium only forms metal rich borides.

Praseodymium and europium tetraborides are the only lanthanide tetraborides that are not stable at ambient pressure [206]. Trivalent praseodymium has an ionic radius of 1.13 Å so theoretically we would expect this to form a tP20 structure, however we are unlikely to see any experimental studies to prove this due to the low abundance of the element. Trivalent europium has an ionic radius of 1.09 Å, however it is thought that the element prefers to be in a 2+ state which would make the ion too large (1.31 Å) to form the tP20 tetraboride structure. All the known actinide tetraborides fall within the window (Th, U, Np, Pu, Am). The trivalent ions of Pa, Cm, Bk and Cf are of an appropriate size to fit into the window however the rarity of these elements makes it difficult to form a sound conclusion as to whether we would expect to see the experimental observation of these compounds or not.

Here are some more structural details relating to the stability of the tP20-MB_4 structure. The interplanar B-B bond should be between 1.56 Å (as for DyB_4) and 1.75 Å (as for LaB_4 and SmB_4). At 0 GPa, Be and Mg have appropriate B-B but as described above their ions are too small. Studying the ratio between the interplanar B-B and the height of the octahedron reveals some interesting properties. The largest and smallest group II ions behave in opposite manners with pressure (Figure 3.26. The size of the octahedra in BaB_4 remain fairly constant whilst the interplanar distance collapses dramatically. For CaB_4, the ratio drops dramatically (by 1%) from 0 - 20 GPa then only falls by half as

much to 50 GPa, playing a role in the destabilisation of the structure. Despite the ratio being between 0.65 and 0.70 for all MB_4 compounds (including heavy elements), it is not possible to exactly define a boundary for instability as CaB_4 at high pressure falls within these values.

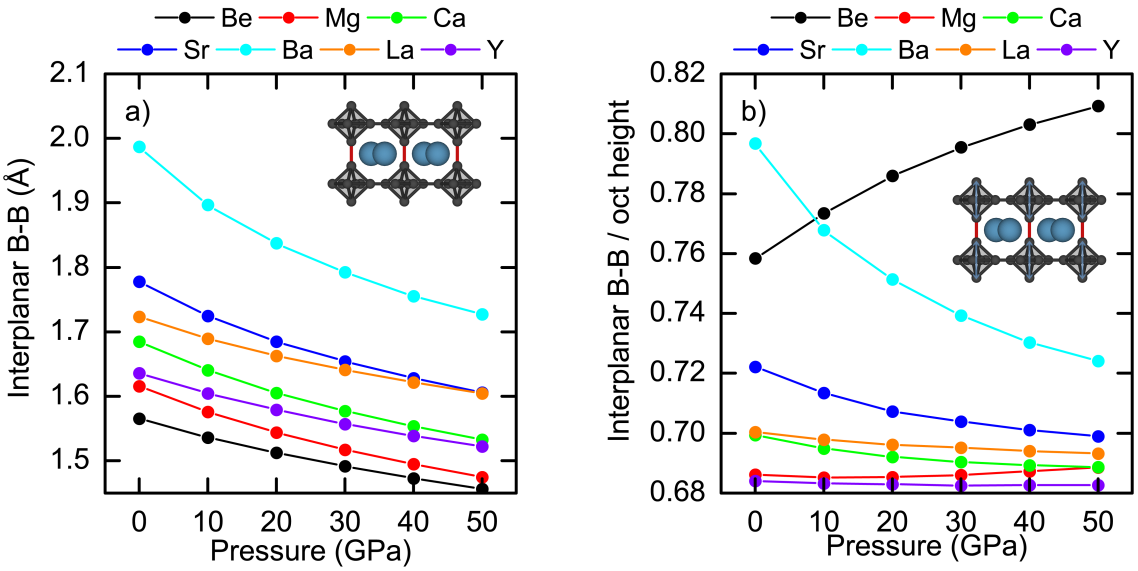


Figure 3.26: a) Interplanar B-B bond length (labelled in red) and b) ratio of interplanar B-B to octahedron height (blue arrow) for alkaline earth metals, lanthanium and ytrium with pressure.

The metal-boron distance between each of the dimer boron atoms and the metal ion are compared in Figure 3.27. The metal ion is closer to B_{dimer1} than B_{dimer2}. In addition, B_{dimer2} for Ca is shortest amongst all the alkaline earth metals, which may be a factor contributing to high pressure instability but again no clear boundary is found.

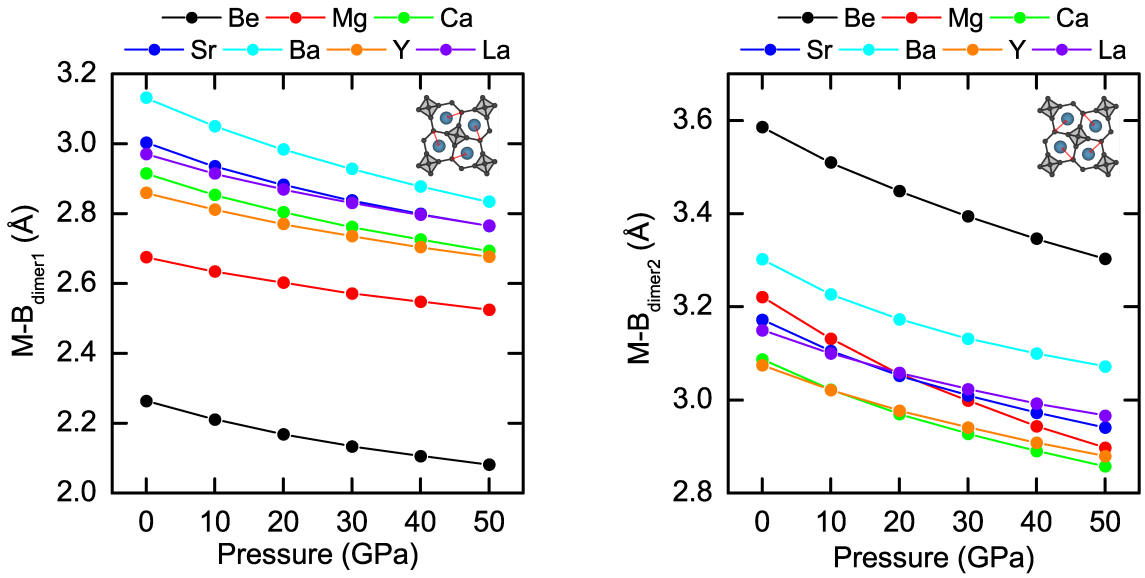


Figure 3.27: The length of the two metal-boron distances to the dimer in tP20-MB_4 with pressure, where M = alkaline earth metals, lanthanium and ytrium. The red arrows show which bond is shown in the plots.

To understand the CaB_4 structure as a whole one must compare its octahedra with those in cP7-CaB_6 and its dimer with that in hypothetical hP3-CaB_2. At pressures up to 50 GPa, the dimer unit in CaB_4 is shorter than in CaB_2 whilst the octahedron is larger than in CaB_6.

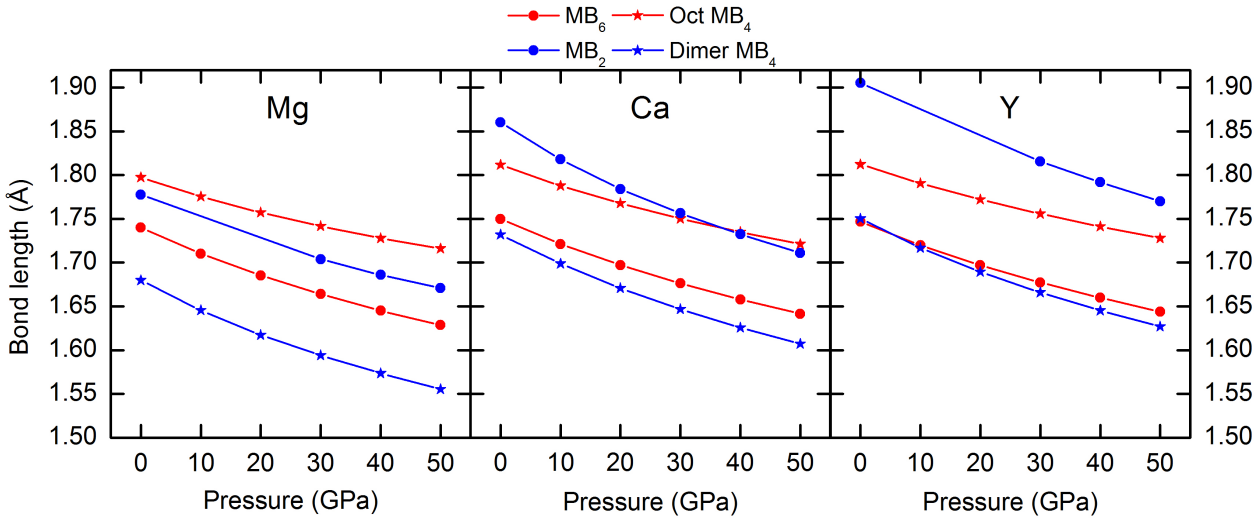


Figure 3.28: The B-B bond length of the dimer and octahedron in tP20-MB_4 with pressure, compared with the octahedron in cP7-MB_6 and dimer in hP3-MB_2, where M = Mg, Ca and Y.

Element	c (Å)	Radii (Å)			Space filled (%)		
		Crystal ionic [210]	Effective ionic [210]	Atomic [211]	Crystal ionic	Effective ionic	Atomic
Be	3.6301	0.590	0.450	1.050	32.5	57.8	57.8
Mg	3.9708	0.860	0.720	1.500	43.3	36.3	75.6
Ca	4.0941	1.140	1.000	1.800	55.7	48.9	87.9
Sr	4.2395	1.320	1.180	2.000	62.3	55.7	94.4
Ba	4.4795	1.490	1.350	2.150	66.5	60.3	96.0
Y	4.0280	1.040	0.900	1.800	51.6	44.7	89.4
La	4.1811	1.172	1.032	1.950	56.1	49.4	93.3
Ce	4.1006	1.010	0.870	1.850	49.3	42.4	90.2
Pr	4.1160	1.130	0.990	1.850	54.9	48.1	89.9
Nd	4.1016	1.123	0.983	1.850	54.8	47.9	90.2
Sm	4.0642	1.098	0.958	1.850	54.0	47.1	91.0
Gd	4.0505	1.078	0.935	1.800	53.2	46.2	88.9
Tb	4.0422	1.063	0.923	1.750	52.6	45.7	86.6
Dy	3.9721	1.052	0.912	1.750	53.0	45.9	88.1
Ho	4.0003	1.041	0.901	1.750	52.0	45.0	87.5
Er	4.0000	1.030	0.890	1.750	51.5	44.5	87.5
Tm	3.9900	1.020	0.880	1.750	51.1	44.1	87.7
Yb	3.9820	1.008	0.868	1.750	50.6	43.6	87.9
Lu	3.9710	1.001	0.861	1.750	50.4	43.4	88.1
Th	4.1118	1.080	0.940	1.800	52.5	45.7	87.6
U	3.9792	1.030	0.890	1.750	51.8	44.7	88.0
Pu	4.0145	1.000	0.860	1.750	49.8	42.8	87.2
				R^2	**0.984**	**0.138**	**0.953**

Table 3.3: Ionic and atomic radii (given in Angstrom) used for calculation of % space filled by the metal in tP20-MB_4. % space filled by the metal in the tP20-MB_4 structure at 0 GPa using different atomic and ionic radii as listed in the previous table. c is the lattice constant taken either from experiment in the ICSD [167] or calculated values for the hypothetical alkaline earth metal tetraborides. The correlation between the radius and the % space taken by the metal is given by the R^2 or correlation coefficient. This is largest for the crystal ionic radii and so has been used for analysis. Atomic radii also has a large correlation but it is known that the the metal atoms are ions so it is more chemically intuitive to use the ionic radius.

At 19 GPa, the oP20 MgB_4 structure type of CaB_4 is themodynamically more stable than tP20. oP20 is quite different from tP20 as can be seen in Figure 3.29. oP20 is composed of chains of pentagonal pyramids that layer up with metal ions sitting over the centre of each pyramid. The distances and structural parameters shown in Figure 3.29 will be used to explain the stability of CaB_4 at high pressure.

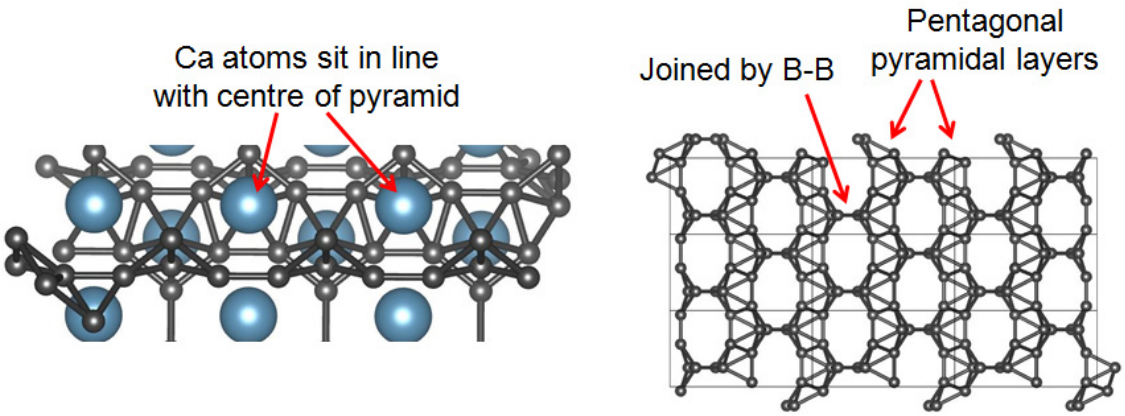


Figure 3.29: Pentagonal pyramid layered structure of oP20-CaB_4, where boron atoms are dark grey and calcium blue spheres. The diagram on the right is just of the boron framework.

Applying pressure to oP20-CaB_4 reduces the distance between metal ions sitting in the channel. Interestingly, the distance between the metal ions in oP20-MgB_4, which is stable up to at least 25 GPa, does not change with pressure, remaining around 3.03 Å (Figure 3.30). One could then conclude that CaB_4 stabilises as the MgB_4, oP20 structure above 19 GPa as as its metal ions get closer to this possibly optimal distance. The size of the ion does not seem to correlate to stability as it did with tP20. The distance between metal ions in adjacent channels also does not correlate with stability.

The distance between metal ions and the centre of the pentagonal pyramid (M-B) affects the stability of oP20. Amongst the alkaline earth metals, oP20 is stable when M-B is between 2.34 and 2.54 Å (Figure 3.30). These boundaries have been defined from initial relative stability calculations (without an evolutionary search) which indicate that

oP20-MgB_4 should destabilise above 25 GPa, whilst oP20-SrB_4 stabilises above 31 GPa.

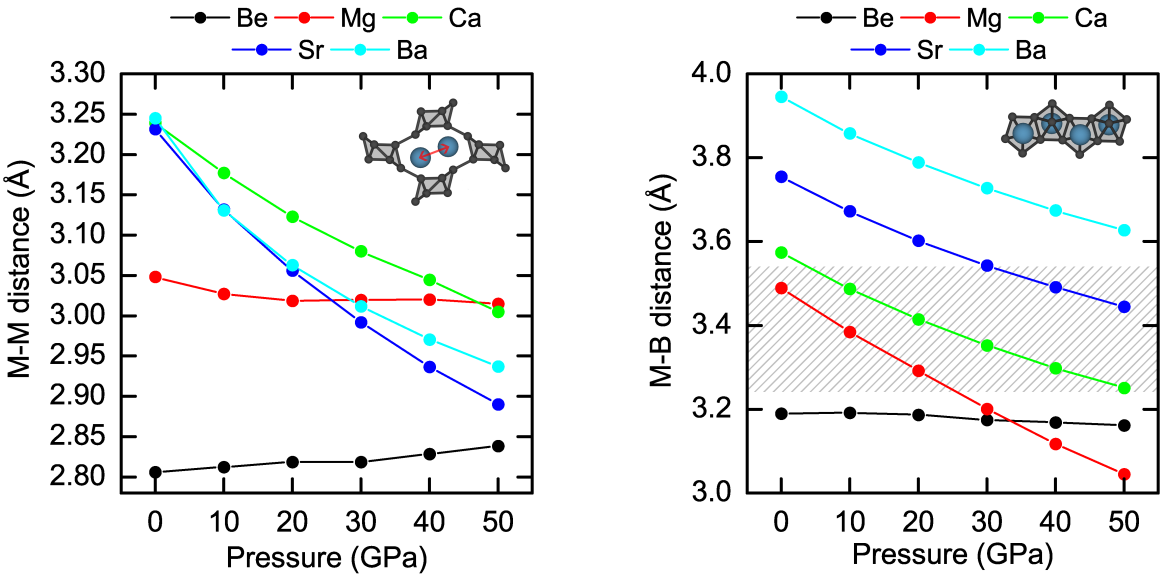


Figure 3.30: Structural parameters of oP20-MB_4 with pressure, where M = Be, Mg, Ca, Sr, Ba. Left: The distance between alkaline earth metal ions that sit in the channel (red arrow). Right: The distance between the metal ions and the centre of the pentagonal pyramid. The shaded region shows the M-B boundaries for stable oP20 structures with pressure.

Applying pressure to CaB_4 makes it more compact. At 30 GPa the volume per ion for oP20 is 8.45 Å, whilst for tP20 it is 8.97 Å. Naslain et. al [212] studied the structure of magnesium tetraboride and explained that larger ions prefer to be in the tP20 structure whilst the smaller magnesium ion prefers the oP20 structure. We extend this idea to include the effect of externally applied pressure and to explain why the oP20 structure destabilises at high pressures for all alkaline earths. We find that there is an ideal volume for the oP20 structure to be stable, 7.78 - 9.1 $Å^3$ per atom (Figure 3.31).

Our evolutionary structure search also revealed two tetraboride polymorphs that are metastable states at 50 GPa, lying 13 meV/atom above oP20. These hR10 and mP20 structures are shown in Figure 3.32). Our database of tetraboride structures contains those taken from the ICSD and the structures described here, found in evolutionary structure searches. We calculated the formation enthalpy and relaxed atomic positions of

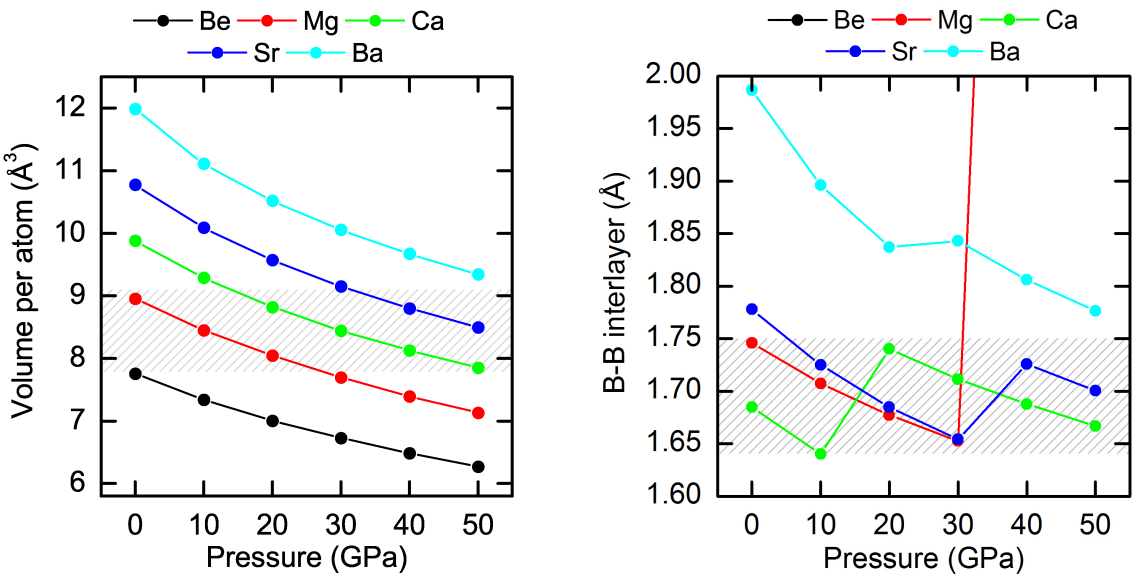


Figure 3.31: Left: The volume per atom for oP20-MB_4 compounds of the alkaline earth metals with pressure. oP20-MB_4 is stable if the volume is 7.78 - 9.1 Å^3, shown by the shaded region. Right: Interlayer B-B distance for the lowest energy MB_4 structure in our database of considered structures. The shaded region indicates the B-B for stable tetraboride structures. The lines joining the data points are to make the graph easier to read and do not indicate a change of B-B over that pressure. MgB_4 at pressures over 30 GPa is more stable as a structure with a large interlayer B-B distance so the red line linking 30 and 40 GPa points goes outside of the range of the graph. BeB_4 is not shown as its B-B distances are longer than the range of the graph.

all these tetraboride structures at 0 - 50 GPa for all alkaline earth metals. We found that at each pressure up to 50 GPa, the lowest energy structure is the one with the lowest B-B bond length between layers as plotted in Figure 3.31. Identified ground state structures fall into a band of B-B lengths 1.64 - 1.75 Å. The proposed high pressure ground state of oP20-CaB_4 stabilises around 20 GPa as the interlayer distance falls within the boundary. The structure becomes thermodynamically unstable at pressures above 50 GPa as the interlayer distance becomes too short. Our initial analysis shows that mP20-CaB_4 should become thermodynamically stable relative to oP20 at these pressures as its interlayer distance is 1.69 Å at 60 GPa compared to 1.64 Å for oP20. oP20-SrB_4 for example is found to be unstable below 20 GPa as its interlayer B-B is too long. BaB_4 and BeB_4 do not stabilise at any pressure as their interlayer B-B is too long. At high pressures,

oP20-MgB_4 is found to become thermodynamically unstable relative to a structure in our database which does not have B-B bond between layers, resulting in MgB_4 decomposing into MgB_2 and MgB_7.

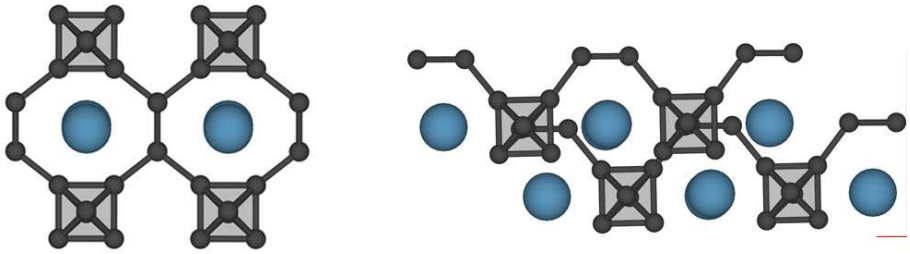


Figure 3.32: Metastable states of CaB_4. Left: one layer of ABA stacked hR10 where the next layer is shifted from what is shown. Right: mP20 - repeating unit that forms alternating ABA layers.

3.3.2 Electronic properties of CaB_4

The electronic structure of ambient pressure tP20-CaB_4 has been the subject of many studies with suggestions that the dimer in CaB_4 does not have sufficient electrons transferred to it from the calcium atom [204, 205, 206]. Our theoretical band structure calculations, those already in the literature [207, 205, 206] and resistance measurements [207] confirm that the tP20 is metallic as contrary to this, Hückel calculations showed that this structure was a semiconductor with a small indirect band gap (0.2 eV) [204].

The valence bands in tP20-CaB_4 are mainly from the boron dimer unit. The dimer bands are semi-filled which is not optimal but leads to stability in lanthanide and actinide tetraborides [206] so can also be used to explain stability of CaB_4.

Bader charge decomposition has been used previously to study charge distribution within structures [213]. We have used the highest accuracy (dense k-meshes and high cutoff energies) to calculate the Bader charge decomposition for tP20-CaB_4 with pressure. The results differed from the integrated projected density of states so we couldn't draw any conclusive ideas from them. We observed that at pressures above 20 GPa, the excess

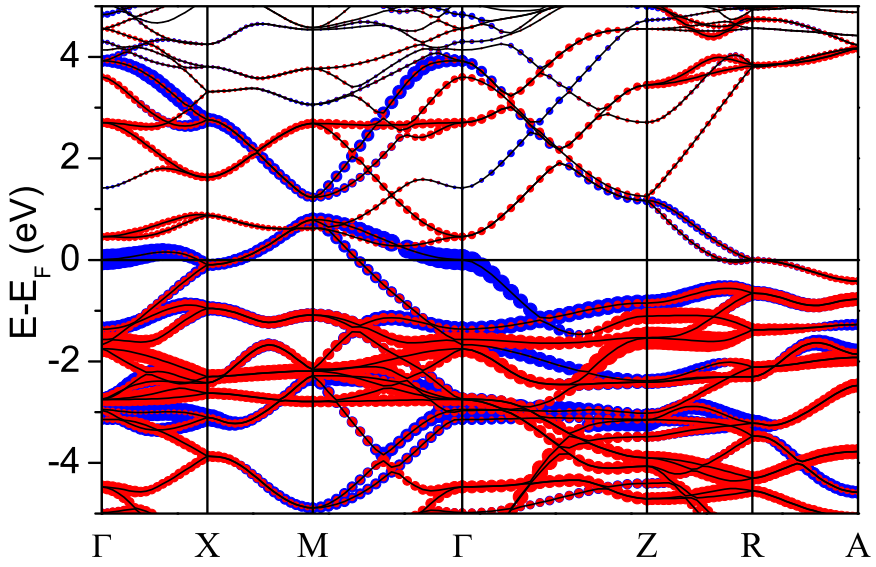


Figure 3.33: Electronic band structure of tP20 CaB_4 at 0 GPa. The contribution of B_2 and B_6 to the bands are represented by the size of the blue and red circles, respectively.

Bader charge on the dimer (relative to 3 electrons per boron) falls below 0.4 electrons (Figure 3.34). This is thought to lead to instability of the B_2 unit and thus the whole tP20 framework. The excess charge on the octahedron does not change much with pressure so one could assume that lower charge around the dimer in tP20-CaB_4 causes destabilisation. Using this information one could also predict destabilisation of YB_4 and LaB_4 above 50 GPa as excess charge on the dimer falls below 0.4 electrons. We wanted to run a high pressure evolutionary search for YB_4 but with 20 atoms per unit cell the search too difficult with the limited computing power we had access to.

Above 19 GPa, the metallic tP20 becomes thermodynamically unstable relative to the semiconducting oP20 structure. The GGA band gap of oP20-CaB_4 (0.1 eV) is smaller than MgB_4 at 30 GPa (0.6 eV). The conduction bands of MgB_4 are dominated by boron whilst the conduction bands of CaB_4 at dominated by calcium. The valence bands of both structures are dominated contributions from boron p_z and p_x orbitals. The metastable polymorphs hR10 and mP20 are semiconductors with GGA band gaps around 0.8 eV (Figure 3.35).. All high pressure CaB_4 structures have similar contributions from Ca and

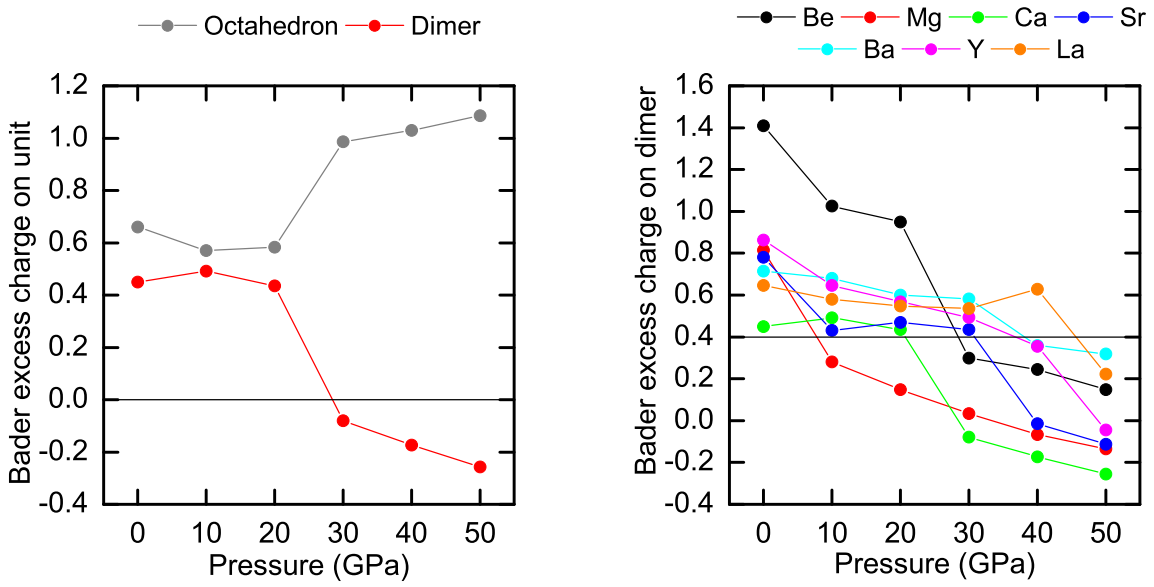


Figure 3.34: The excess charge on the octahedron and dimer as calculated relative to 3 electrons per boron atom for the tP20-CaB_4 structure with pressure. Right: The excess charge on the dimer as calculated relative to 3 electrons per boron atom for the tP20-MB_4 structure with pressure, where M - alkaline earth metals, ytrium and lanthanum.

B around the Fermi level.

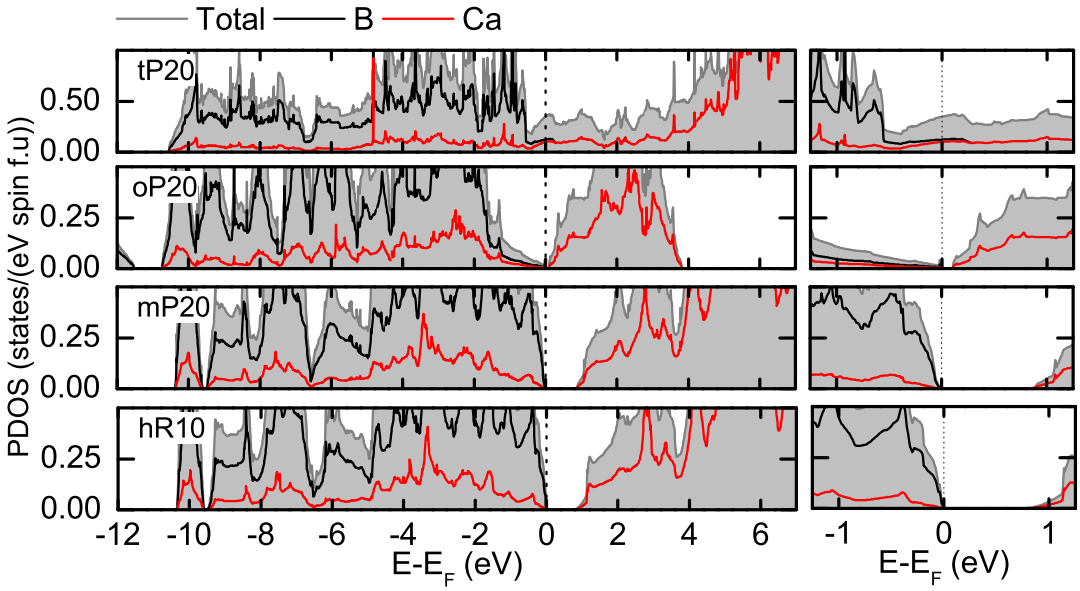


Figure 3.35: Projected electronic density of states of tP20, oP20, mP20 and hR10 CaB_4 structures relaxed to 30 GPa. PDOS is stated in units of states per eV per spin per formula unit (f.u.) against the energy relative to the Fermi energy (E_F). To the right is a zoomed in portion of the DOS close to the Fermi level.

3.3.3 Superconducting properties of CaB_4

Whilst tP20-CaB_4 is metallic, it is not expected to be superconducting. λ calculated using a mesh of q-points is found to be very low (0.23) and its ω_{log} of 532 cm^{-1} is much lower than for the superconducting CaB_6 derivative compound. The relatively low density of states at the Fermi level also do not make it ideal for observing superconductivity. The Eliashberg function in Figure 3.36 shows that around 1/3 of total lambda for CaB_4 is due to the calcium modes close to 190 cm^{-1}. This strengthens the hypothesis that calcium vibrational and electronic states are the main reason for superconductivity in the calcium-borides. The other 2/3 of lambda comes from the boron modes at higher frequencies.

If we think about how to make CaB_4 superconducting, we could say that it would be desirable to have calcium phonon modes at higher frequencies. One could suggest tP20-MgB_4 for example could have a higher lambda as the phonon modes from the lighter magnesium atom would be at higher frequencies. Unfortunately as described in previous sections, MgB_4 is more stable as another structure, emphasising the main conclusion of this whole chapter that stability and a high T_c are inversely related.

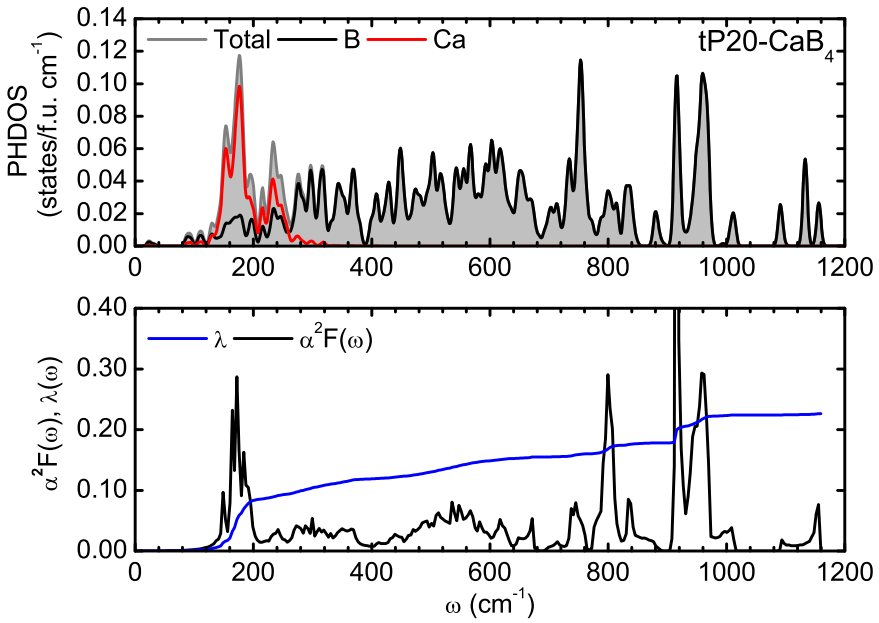


Figure 3.36: Top: Total and projected phonon density of states (PHDOS), bottom: Eliashberg function and the strength of the electron-phonon coupling (λ) of tP20-CaB_4 at 0 GPa.

3.4 Calcium diboride

The diborides are the most studied boride composition after the discovery of superconductivity in MgB_2 [44], though amongst the alkaline earths, only magnesium diboride is stable at ambient pressure. As described in Subsection 1.1.4, calcium diboride has been examined by many as a possible MgB_2 type superconductor. In terms of possessing properties desirable for a good BCS superconductor, the hexagonal form of CaB_2 could be thought of as being ideal. It is composed of light elements and relative to MgB_2, it has a higher DOS at the Fermi level and vibrational phonon softening of the in-plane boron mode [214]. A recent study on the hypothetical hP3-CaB_2 (Pearson notation) structure indeed predicted it to be a superconductor with a T_c of 50 K [111]. Unfortunately this AlB_2 type structure lies 187 meV/atom higher than the fcc-Ca$\leftrightarrow$tP20-CaB_4 tie-line.

The related BeB_2 has been studied with a stable ambient pressure state of BeB_2 being proposed [215, 216]. Experiments however were not able to fully characterize the structure. Our calculations actually indicate that the F$\bar{4}$3m theoretically proposed structure [215] is thermodynamically unstable by 84 meV/atom relative to buckled hexagonal sheets of boron with a double layer of metal ions (See Table 5.9). We are not suggesting that this structure is the ground state as a full evolutionary search was not carried out but shows that structures proposed in the literature still need to be fully investigated. Similarly a CaB_2 structure of linear boron chains [217] was recently predicted to stabilise at ambient pressure. This structure was actually previously proposed (δ-CaB_2) and found to be highly unstable against phase separation into CaB_6 and fcc-Ca by 144 meV/atom due to the large ionic size of calcium [218].

At high pressure, MgB_2 is known to be stable in the AlB_2 (hP3) configuration up to

57 GPa [219]. It has been suggested that CaB_2 also has an hP3 ground state above 8 GPa [217]. Our calculations indicate that at 30 GPa, hP3-CaB_2 lies 56 meV/atom above the CaB_4-Ca tie-line (Figure 3.38. In this document we propose a lower energy, stable state of oI12-CaB_2. Stabilising above 8 GPa, the structure is a poor superconductor and consists of ABA stacking of B-Ca layers with 4-8 membered rings of boron. At higher pressures (32 GPa) a monoclinic structure (mS12) of joined-up step-like boron hexagons layers becomes thermodynamically more stable.

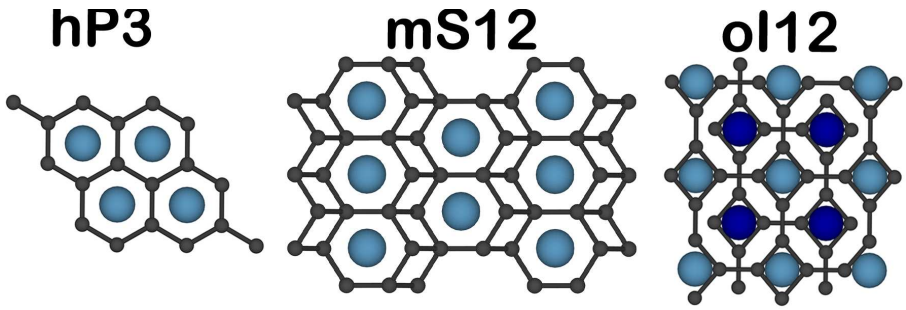


Figure 3.37: The layered structures of considered CaB_2 ground states at 30 GPa, the AlB_2 type hP3 structure and proposed oI12 and mS12 structures. The dark blue in oI12 represents the calcium atom in the shifted layer.

3.4.1 Structural properties of CaB_2

To investigate if this composition has a stable ground state at higher pressures we have run an evolutionary search for the following unit cells: 2:4, 3:6, 4:8 and 6:12. We find that the AlB_2 type structure becomes dramatically more stable with pressure (Figure 3.38), however it is not the ground state. Our proposed ground state structure (oI12-CaB_2), which is composed of an ABA stacking of B-Ca layers with 4-8 membered rings of boron was found using a Ca_4B_8 unit cell. The AlB_2 type structure is the lowest enthalpy structure from the searches using smaller unit cells. At 50 GPa, the oI12 structure rearranges into a base centered monoclinic unit cell (mS12 in Figure 3.37). This is composed of hexagons of boron joined via rhombi, forming a buckled sheet. Metal atoms sit above and

below the centre of the hexagon.

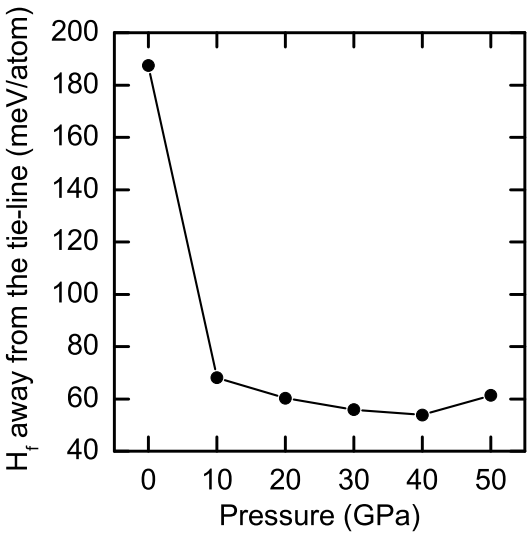


Figure 3.38: How far the formation enthalpy (H_F) of the AlB_2 type structure of CaB_2 is away from the tie line at increasing pressures.

hP3-CaB_2 is unstable at ambient pressure as metal ions are too close together in the plane. The in plane distance (lattice vector a) is much closer than the distance perpendicular to the plane (lattice vector c) so it has a greater effect on stability. The hP3 structure is stable if the normalised distance [(2 x ionic radius)/a] between metal ions is between 0.45 and 0.69 (Figure. 3.39). All known AlB_2 type structures lie within this boundary. Like CaB_2, LaB_2 is unstable as hP3 at all pressures up to 50 GPa as its metal ions lie too close together within the plane.

At 0 GPa, the predicted 4-8 membered boron ring structure of CaB_2 (oI12) is 82 meV/atom lower in enthalpy than hP3-CaB_2. Even though the metal ions are slightly closer in oI12 than hP3, they are layered up, so parallel to the boron layer, the metal ions are in fact further apart at 0 GPa. At 8 GPa, oI12 becomes thermodynamically stable relative to CaB_4 and Ca. Figure 3.39 shows our examination of all the MB_2 structures in our database. At 30 GPa we find that the formation enthalpy of CaB_2 structures is dependent on the shortest metal-boron distance (M-B) within the structure, optimized

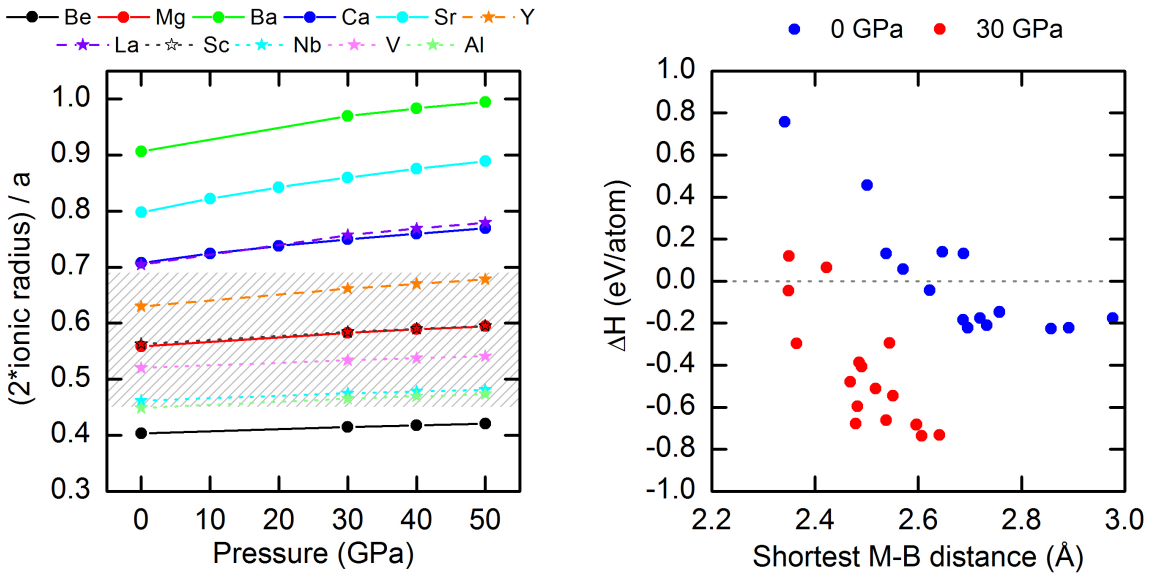


Figure 3.39: Left: The normalised in plane M-M distance [(2 x ionic radius)/a] for hP3 metal diborides with pressure, where M = Be, Mg, Ba, Ca, Sr, Y, La, Sc, Nb, V, Al. Right: The shortest M-B distance in all CaB_2 structures against their formation enthalpy.

at 2.61Å. Similarly, SrB_2 has an optimal M-B at 30 GPa of 2.78Å and MgB_2 of 2.3Å. The optimal M-B (largest of all structures considered) for CaB_2 is achieved in oI12-CaB_2 through the formation of an 8-membered boron ring which forces the metal ion to sit above the centre of a large ring.

3.4.2 Electronic properties of CaB_2

Figure 3.40 is the electronic DOS of the predicted ground states of oI12 and mS12 CaB_2 and hypothetical hP3. All the structures are metallic which is a good starting point for proposing superconductors. The DOS at the Fermi level for hP3-CaB_2 is around double the DOS of the ground states, showing that whilst the high density of states is desirable for high T_c, it results in an unstable structure. All three structures have relatively high contributions from the metal atom at the Fermi level comparing with MgB_2 which has mainly boron states. The hP3 and oI12 structures have equal contributions from both

boron and calcium atoms at the Fermi level, whilst the mS12 structure has a slightly higher contribution from the calcium atom. In oI12-CaB_2, the boron states are mainly from p_y and p_z orbitals which lie perpendicular and parallel to the boron plane. Calcium states are mainly from d_{xy} and d_{xz} orbitals.

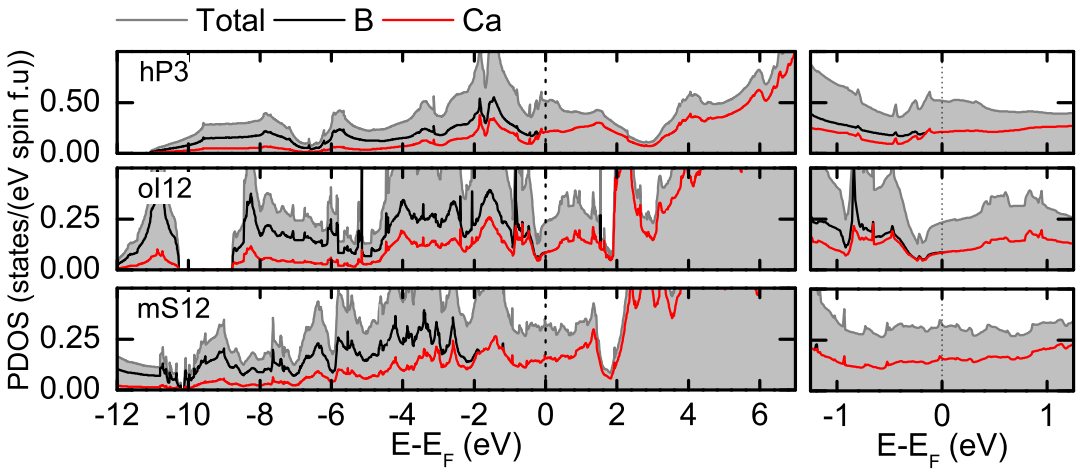


Figure 3.40: Projected density of states of three structures of CaB_2 relaxed to 30 GPa. The scale for hP3 is double that for oI12 and mS12. PDOS is stated in units of states per eV per spin per formula unit (f.u.) against the energy relative to the Fermi energy (E_F). To the right is a zoomed in portion of the DOS close to the Fermi level.

3.4.3 Superconducting properties of CaB_2

Through calculating the electron-phonon coupling of oI12-CaB_2 at 30 GPa and mS12-CaB_2 at 50 GPa, we predict that both structures are poor superconductors with a T_c of 0.8 and 1.0 K respectively. The shape of the Eliashberg function and the phonon density of states indicates that almost 70 % of the the total λ is due to phonon modes below 500 cm^{-1} (Figure 3.42). These are mixed modes with contributions from both boron and calcium movement. The higher frequency modes providing the other 30 % of the the total λ are mainly due to in plane and out of plane movement of boron atoms. $\langle\omega_{ln}\rangle$ for this structure is 495 cm^{-1}.

Mixed boron and calcium modes (130 - 405 cm^{-1}) contribute to just over half of

the total lambda for the mS12 structure at 50 GPa. The slightly higher T_c in mS12 compared with oI12 can be attributed to the phonon modes being shifted to slightly higher frequencies. Also the calcium modes cover a larger frequency range. High frequency boron modes contribute very little to the total lambda.

Evolutionary searches using a unit cell of Sr_4B_8 indicated that oI12-SrB_2 is also a ground state at 30 GPa, predicted to be superconducting with a T_c of 0.7 K. The λ values and thus the electron-phonon coupling strength of SrB_2 and CaB_2 are similar. A decomposition of the phonon density of states shows that SrB_2 has a narrower range of the mixed B and M modes, which are below 250 cm^{-1}. The main difference between SrB_2 and CaB_2 is that for SrB_2 60% of the total λ is due to pure boron modes. Despite strontium having a larger mass than calcium, therefore lowering its $\langle\omega_{ln}\rangle$, the structure has a similar predicted T_c.

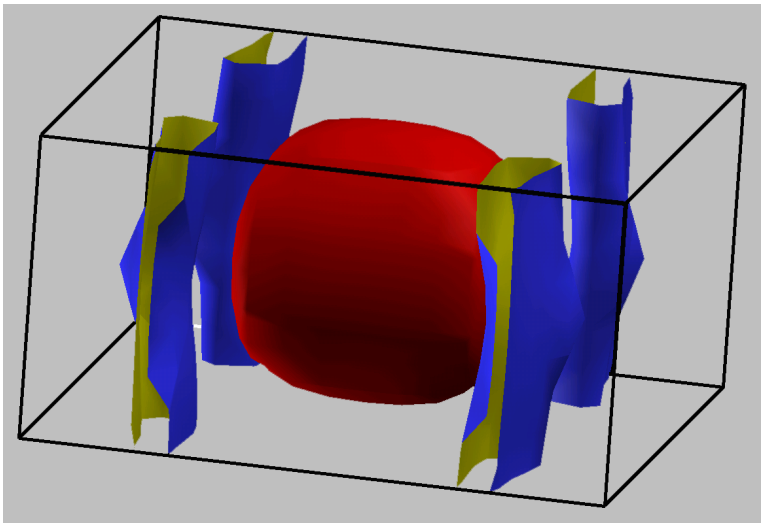


Figure 3.41: Fermi surface of oI12-CaB_2 relaxed to 30 GPa.

The Fermi surface of oI12-CaB_2 given in Figure 3.41 shows one folded sheet at the corners with a spherical portion in the middle of the Brillouin zone.

Convergence tests on superconducting properties with respect to k-mesh and q-mesh have been performed. Gamma point phonon frequencies were converged to within 12

cm^{-1} as shown in Table 5.8. A q-mesh of 3 x 3 x 3 and 4 x 4 x 4 with two different k-meshes were used to calculate the Eliashberg function. It is clear from table 3.4 that the T_c was not converged with the lower meshes as there was a dramatic reduction in the T_c from 9 to 1 K. A larger k- and q- mesh was not used to confirm the convergence of the T_c as the T_c is so low that the extra computational cost would not add any value to the original conclusion.

	oI12		mS12
q-mesh	3 x 3 x 3	4 x 4 x 4	4 x 2 x 4
no. q-points	8	18	14
k-mesh (ph)	12 x 12 x 12	16 x 16 x 16	12 x 6 x 12
k-mesh (e-ph)	24 x 24 x 24	32 x 32 x 32	12 x 6 x 12
$\langle\omega_{ln}\rangle$ (cm^{-1})	340.6	495.2	563.8
λ	0.691	0.376	0.384
T_c (K)	9.6	0.8	1.0

Table 3.4: The superconducting properties of oI12-CaB_2 at 30 GPa and mS12-CaB_2 at 50 GPa for all k- and q-meshes used for the calculations.

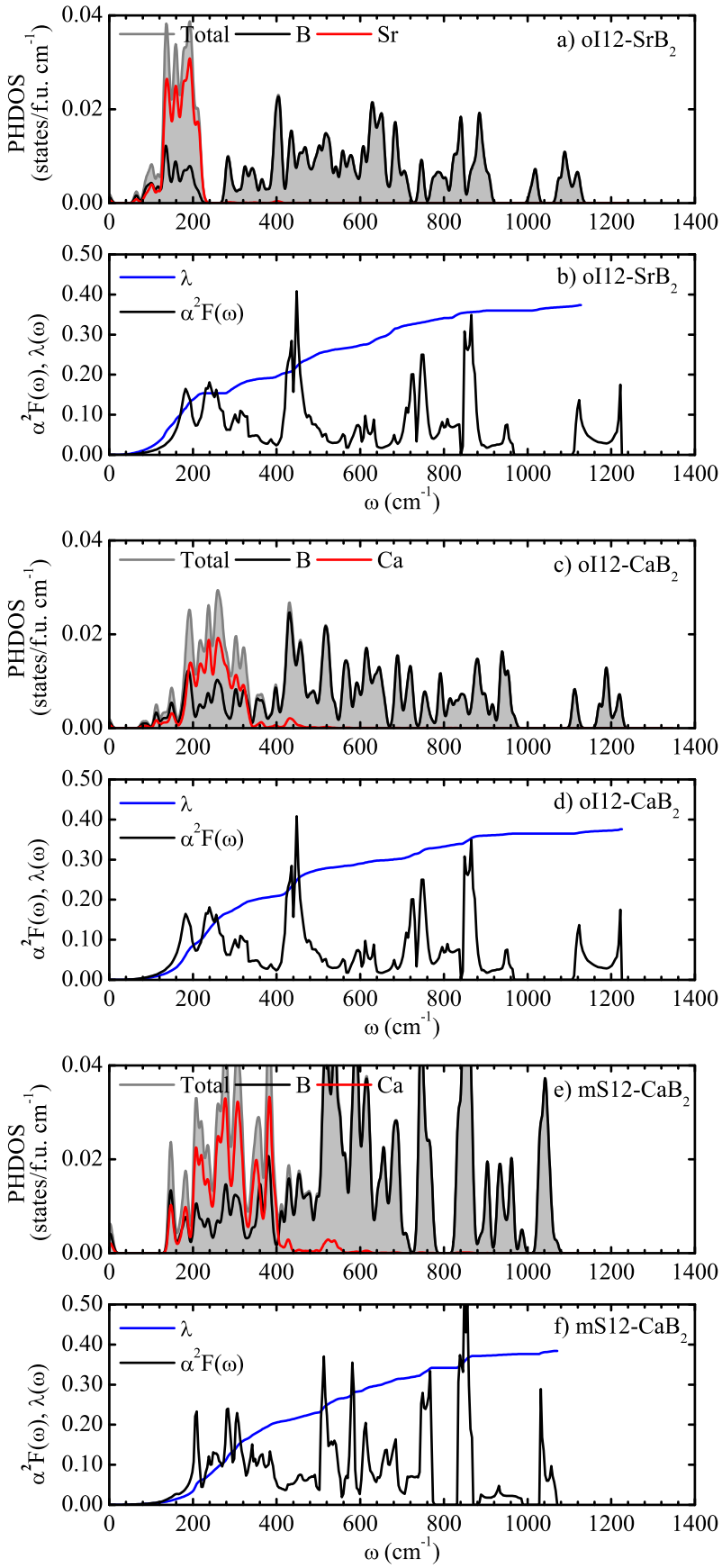


Figure 3.42: Plots a, c and e are the total and projected phonon density of states in oI12-SrB_2 (30 GPa), oI12-CaB_2 (30 GPa) and mS12-CaB_2 (50 GPa). Plots b, d and f show $\alpha^2F(\omega)$ and λ for these listed diboride structures.

3.5 Calcium monoboride: CaB

Monoboride structures are unknown amongst the alkaline earth metals at both ambient and high pressure due to the suboptimal number of electrons in the compound. In this section we will show that a metallic form of CaB stabilises at high pressure and is superconducting at 5 K.

3.5.1 Structural properties of CaB

There are several known monoboride structures of the transition metals such as FeB, and MoB, both of which are highly unstable for CaB at high pressure. A structure search was therefore run to find a lower energy form of CaB at 30 GPa. Unit cells of 3:3, 5:5, 4:4, 6:6 and 8:8 of Ca:B were used for the search but with only one boron atom per metal atom there are limited configurations that a covalent boron network can form [220]. All structures involve individual chains as a slightly higher concentration of boron is required to form double chains (as in Cr_3B_4) and a slightly lower concentration is required for branched chains (as in $Ru_{11}B_8$) [220]. The structure search revealed three low energy types of boron chains that we have compared: oP8 - linear, mS16 - snake-like and oI8 - zig-zag (Figure 3.43). oI8-CaB is an ABA layered structure with calcium atoms sitting in the bends of the chains and it was revealed in the 4:4 unit cell search.

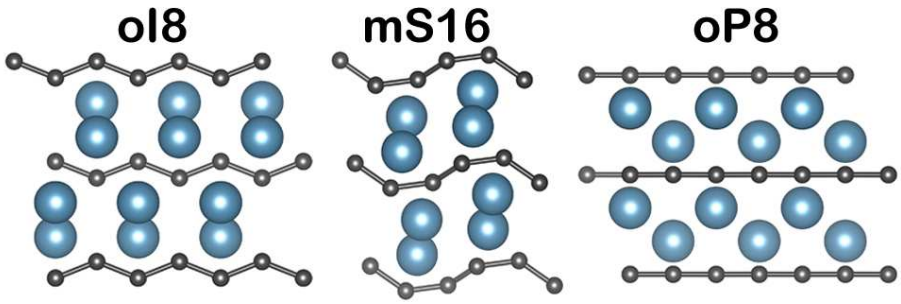


Figure 3.43: The structures of proposed high pressure ground states of CaB (oI8 and mS16) compared with a linear chained structure oP8. Boron atoms are represented by dark grey spheres and calcium, blue spheres.

At 30 GPa, linear chained oP8 is 53 meV/atom higher in enthalpy than the zig-zagged oI8 and snake-like mS16 is 2 meV/atom higher in enthalpy, showing that the boron chains like to fit themselves around the group II metal ions. In the zig-zag structure we find that the B-B-B bond angle is greater for larger metal ions (Fig. 3.44). Applying pressure to the oI8-MB structure decreases the bond angle, with a large reduction occurring for the two smallest ions (Be and Mg) between 10 and 20 GPa. The relaxed bond angle in both structures of BeB and MgB at ambient pressure is also much below 180^o.

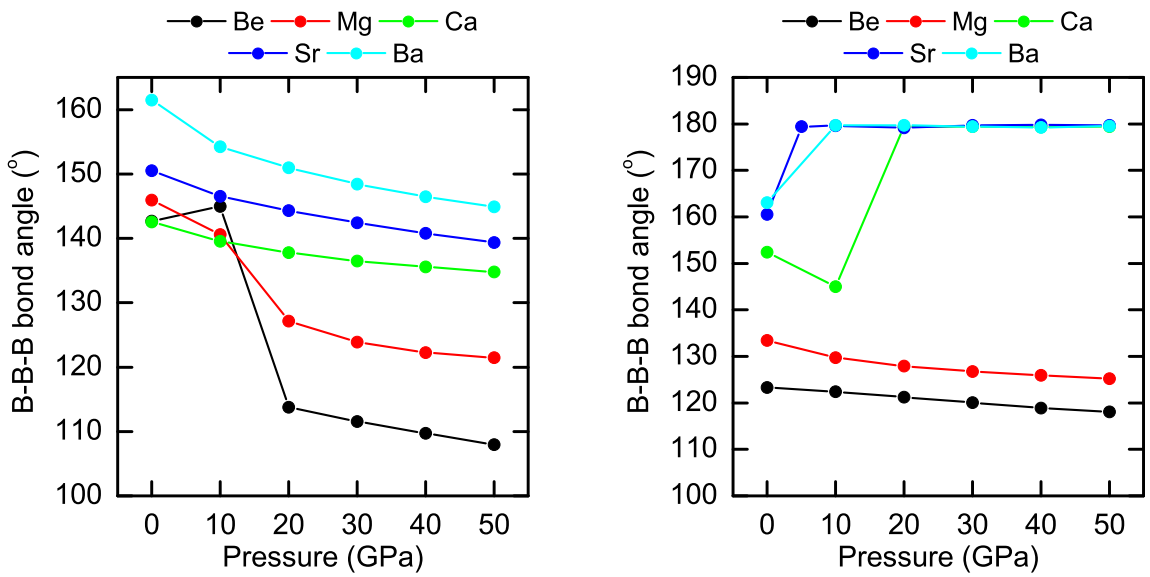


Figure 3.44: B-B-B bond angle in oI8 and oP8 MB structures with pressure for M = alkaline earth metal.

Studying the linear chains (oP8) we find that the smallest ions (Be and Mg) relax away from linear chains and back to zig-zag chains (oI8). oP8-CaB relaxes as linear chains only when 20 GPa of pressure is applied, below which it is zig-zagged. A much lower pressure (∼5 GPa) is required to straighten up the boron chains of the much larger metallic ion of strontium. It is expected that hundreds of gigapascals of pressure would be required to relax Be and Mg boride as linear chains.

At ambient pressure, as one goes down the alkaline earths, the metal ion gets closer to

the boron layer for both the oP8 and oI8 structures, with little difference between the two structures. At 30 GPa, the oI8 structure is more stable for Ca because the metal ions are further away from the boron layer than in oP8, minimising repulsion. One could say that the same is true for SrB, which has a metastable, oI8 structure, lying 6 meV/atom higher in enthalpy than its ground state, the mS16 structure that has been determined using an evolutionary search with a unit cell of Sr_4B_4. A full mesh of q-points have not been used to calculate the phonon dispersion of mS16-SrB but the gamma point frequencies are all positive, giving preliminary indication that the structure is dynamically stable. The berilium ion is so small and far away from the boron layer that at 30 GPa the oP8 structure is 367 meV/atom lower in enthalpy than the oI8 structure. This shows that the most stable structure at high pressure is one with the optimal metal to boron distance.

From the discussion given in this subsection, it is evident that the stability of a particular structure of calcium monoboride is mainly due to the effect of the size of the metal ion and its repulsion with the boron layer.

3.5.2 Electronic properties of CaB

The electronic density of states (Figure 3.46) shows all considered CaB structures are metallic. The DOS at Fermi level of oI8 and oP8 are 0.45 and 0.65 states/(eV spin f.u.) respectively, coming mainly from the calcium atom, in particular Ca ($d_{x^2-y^2}$) which lies along the line of the boron chains and between the layers. Boron p_y and p_z orbitals which lie in the zig-zag plane contribute most to boron states at the Fermi level. The mS16 structure has a much lower DOS at E_F (0.20 states/(eV spin f.u.)), possibly resulting from a higher contribution (50%) to the total DOS from the boron.

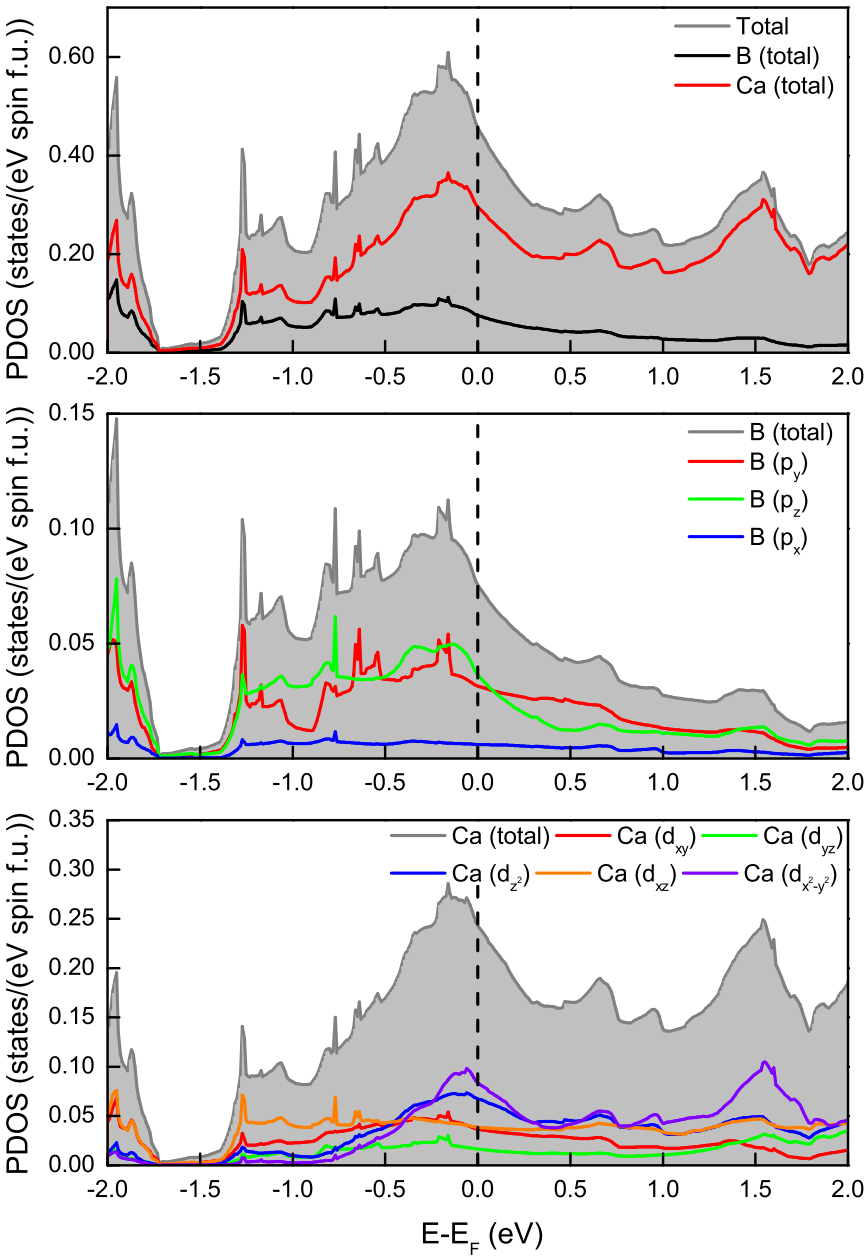


Figure 3.45: The projected density of states for oI8-CaB relaxed to 30 GPa. Top: projections on the calcium and boron atoms. Middle: Projection on the boron p orbitals. Bottom: Projection on the calcium d orbitals.

The DOS at the Fermi level of oP8 is similar to that in oI8 with a major contribution from calcium with a slightly higher DOS of 0.65 states/(eV spin f.u.). The peak of the DOS 0.06 eV above E_F is 0.86 states/(eV spin f.u.). This electron doped hypothetical structure would be approximately 50 meV/atom higher in enthalpy. This demostrates

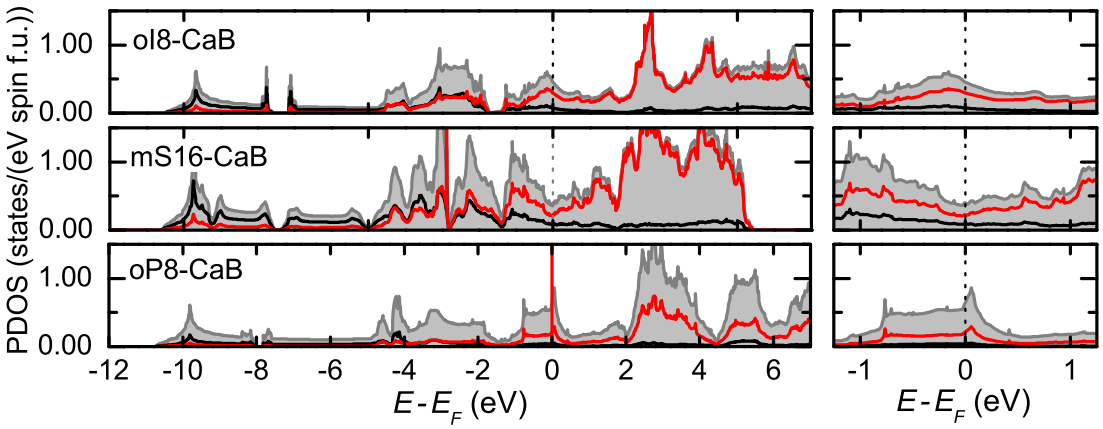


Figure 3.46: The projected density of states (PDOS) of the 3 lowest enthalpy structures (oI8, mS16 and oP8) of CaB found using the evolutionary search. PDOS is stated in units of states per eV per spin per formula unit (f.u.) against the energy relative to the Fermi energy (E_F). On the right there is a close up of the states around the Fermi level.

that the desireable property for superconductivity of a high DOS at E_F does not always go hand in hand with a thermodynamically stable structure. The mS16 structure has a much lower DOS at E_F (0.20 states/(eV spin f.u.)), possibly resulting from a higher contribution (50%) to the total DOS from the boron.

Close to the Fermi level, the small contributions from the boron in the oI8 structure come from p_y and p_z which lie perpendicular to the line of the zig-zag. B p_y hybridises with Ca $d_{x^2-y^2}$.

The electronic structure of the oI8 structure can be compared to a predicted LiB structure [221] which also contains of linear boron chains. We find that unlike CaB, the DOS at the Fermi level has a major contribution from the boron, with little from the lithium atom.

The electronic properties described in this section show that for calcium borides the boron is not as important as the calcium in contributing electronic states which result in superconductivity. Comparing just oI8 and mS16 CaB it is clear to see that the higher

the contribution of calcium states to the Fermi level, the higher the predicted T_c is.

3.5.3 Superconducting properties of CaB

Figure 3.47 shows the the Eliashberg spectral function $\alpha^2F(\omega)$ and the electron-phonon coupling strength λ for both structures. We predict that oI8-CaB will be superconducting at 30 GPa with a T_c of 5.5K, total lambda of 0.58, ω_{log} of 330.15 and use a value of 0.12 for μ^*. 68% of the total lambda results from modes below 360 cm^{-1}, which are mainly movements of calcium atoms. The decomposition of the phonon density of states into contributions from the atoms (Figure. 3.47) also shows that the in-plane movement of boron atoms (phonons with frequency around 500 cm^{-1}) have a negligible contribution to the electron-phonon coupling in this compound. A phonon dispersion calculation indicates this sructure is dynamically unstable at ambient pressure.

3.5.4 Comparison of CaB with isoelectronic LiC

oI8-CaB can be compared with the isoelectronic oS8-LiC linear chain structure, recently predicted to form under pressure [222]. Our calculations show that although this structure has a favourable covalent bonding network, its density of states at the Fermi level (0.25 states /(eV spin f.u.)) is not high enough for the structure to be superconducting above ~ 1 K.

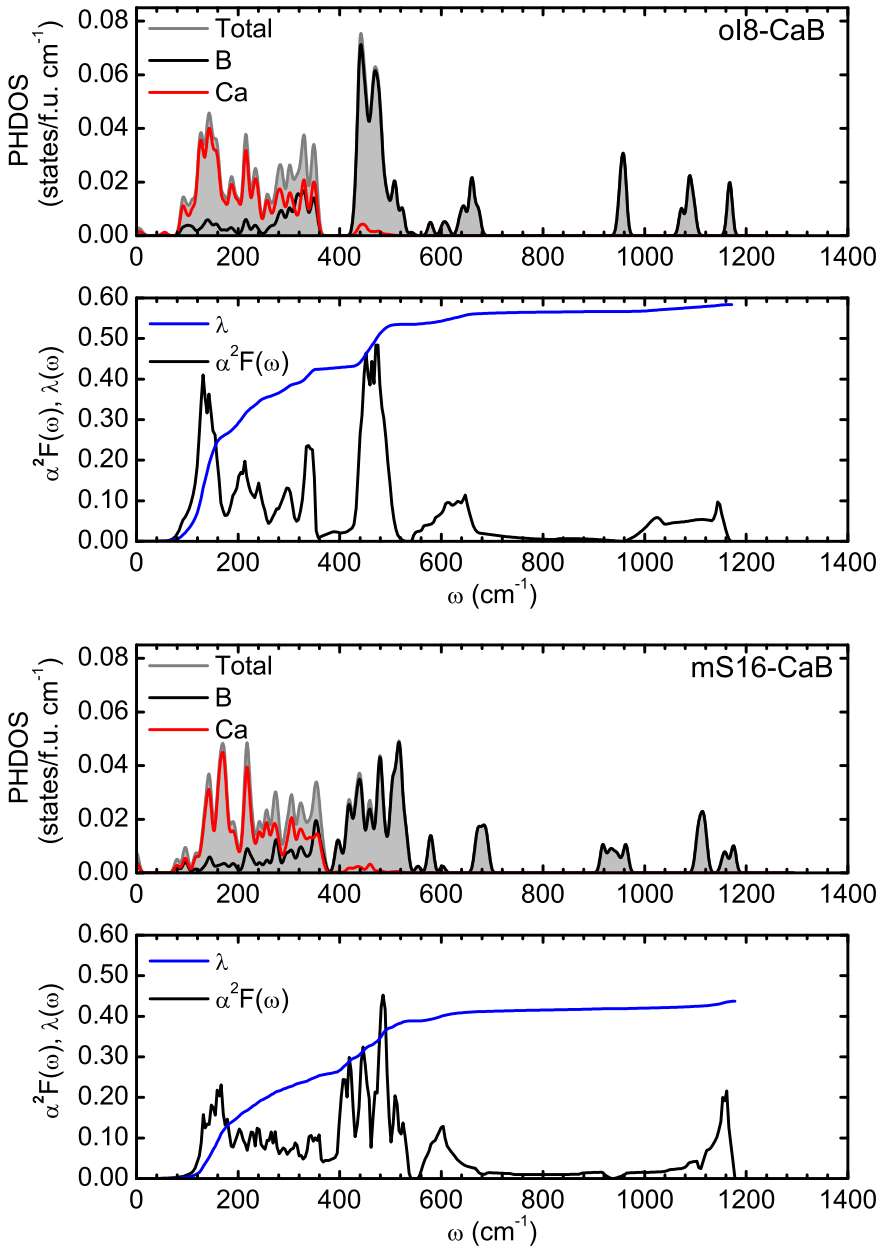


Figure 3.47: Top: total and projected phonon density of states (PHDOS), bottom: Eliashberg function and the strength of the electron-phonon coupling (λ) of oI8-CaB and mS16-CaB at 30 GPa.

3.6 LiC superconductivity calculations

We have used the linear response theory with fine k- and q-meshes to calculate the phonon density of states, Eliashberg function and λ. This has revealed that the structure may superconducting with a T_c of $\approx$ 1K. It has however been difficult to find a suitable

pseudopotential for lithium that accurately calculates phonon properties for the ground state structures of elemental lithium therefore it not possible to conclusively predict the T_c. The calculations that we have done and the problems associated with them are described here.

Quantum ESPRESSO [154] provides a large database of reliable pseudopotentials for many elements in the periodic table. With ultrasoft pseudopotentials, one can calculate the electron-phonon interaction faster than norm-conserving pseudopotentials and therefore we started with these. Li.pbe-n-van.UPF is an ultrasoft pseudopotential that does not treat the 1s electrons as valence electrons which should be done to accurately describe electronic properties in lithium. Li.pbe-s-van_ak.UPF is an ultrasoft pseudopotential that does however treat 1s electrons as valence but has been reported [154] to give seriously wrong results when calculating forces and phonon frequencies. We have used this pseudopotential to calculate the phonon dispersion for bcc-Li at 0 GPa with a converged k-mesh and converged cutoff of 80 and 640 Ry for the wave functions and charge density, respectively. The three acoustic modes were calculated to have frequencies of 190 cm^{-1}. Our attempts at constructing an ultrasoft pseudopotential with all electrons counted as valence was unsuccessful as the phonon dispersion for the bcc-Li structure indicated that it was dynamically unstable.

Norm-conserving pseudpotentials are more reliable for calculating phonon properties but require a higher cutoff energy for convergence. There were however large discrepancies between pseudpotentials and with the phonon dispersions in the LiC paper. Chen *et.al.* [222] used Perdew Zunger pseudopotentials for their calculations: Li.pz-n-vbc.UPF and C.pz-vbc.UPF. Our calculations indicate that using these pseudopotentials the T_c of oI8-LiC at 30 GPa is $\approx$ 1K. Approximately 60 % of the total lambda comes from mixed

vibrational modes between 400 and 700 cm^{-1}. 2/3 of these modes are from movement of the lithium atoms parallel to the zig-zag chains of carbon. There is negligible contribution from the pure carbon high frequency modes above 1060 cm^{-1}. This structure is predicted to form at pressures above 5 GPa. Our calculations indicated that the calculated T_c was highly dependent on the mesh off q-points used. A 2x2x2 mesh calculated a T_c of 14K. This dependence leads us to the conclusion that if a reliable ultrasoft pseudopotential for lithium is found then a larger mesh of q-points must be used before any conclusions can be made on the reliability of the T_c.

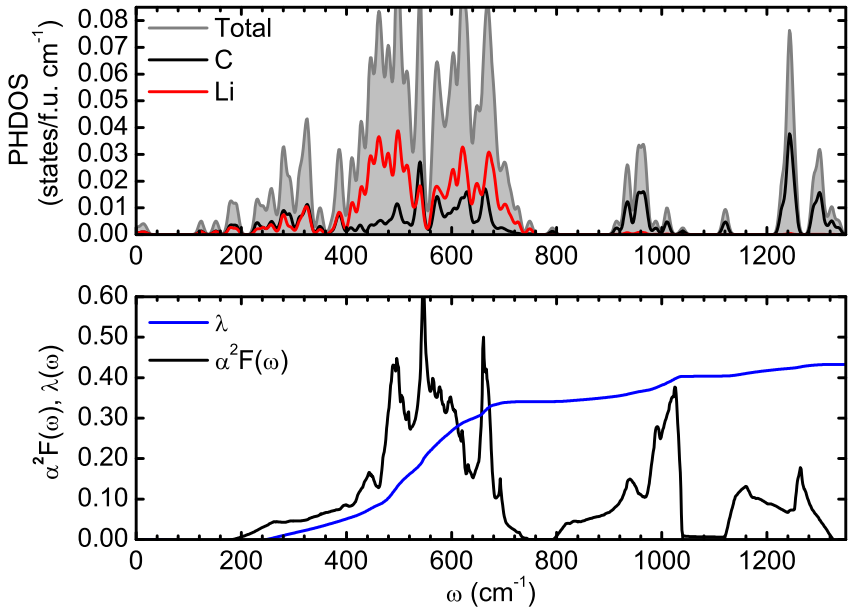


Figure 3.48: The phonon density of states (PHDOS), Eliashberg function (α^2F) and the strength of the electron-phonon coupling ($\lambda(\omega)$) for oS8-LiC at 30 GPa. Calculated using the Perdew and Zunger functional and a q-mesh of 4 x 4 x 4 and k-mesh of 14 x 14 x 14.

3.7 Other Ca-B compositions considered

Other Ca:B compositions which were considered but did not have high pressure ground states are described in this section. When proposing stable structures it is important to make sure that they will not decompose into structures at other compositions. On the boron rich side, the only known alkaline earth metal boride is MgB_{12}. Hagg found that boron rich compounds would not be expected (English description in [223]). Therefore we did not expect to discover any ground states here. A preliminary search of CaB_{12} was run using a unit cell of 1:12, Ca:B at 30 GPa. A structure was found that is a rearranged form of MgB_{12} containing the B_{12} icosahedra. The structure is 7 meV/atom more stable than the MgB_{12} type and becomes more stable with applied pressure but still lies 323 meV/atom above the tie-line at 30 GPa.

Due to the existence of MgB_7 at ambient pressure, we have used a unit cell of 2:14, Ca:B for an evolutionary search of CaB_7 at 30 GPa. The MgB_7 type CaB_7 is the most stable structure but lies 70 meV/atom above the CaB_6-B tie-line.

Unit cells of 2:6, 3:9 and 4:12 have been used to investigate CaB_3. The lowest enthalpy structure from this search is 114 meV/atom above the tie-line and is composed of twisted octahedra, based on the Li_2B_6 structure [167]. This structure was only found with the two larger unit cells.

On the metal rich side of the phase diagram, no alkaline-earth metal borides are known. Thought to be because of the M/B radius ratio as described by Hagg (English description in [223]). Ca_2B_3 has been studied using a unit cell of 2:3 and 6:9, Ca:B. This produced structures which were hundreds of meV/atom above the tie-line. hP10-Ru_2B_3 structure type lies 300 meV/atom above the tie-line. The proposed existence of Be_2B gave

impetus to the study of Ca_2B, using unit cells of 4:2, 8:4 and 12:6 of Ca:B. The lowest enthalpy structure at this composition lied 44 meV/atom above the tie-line at 30 GPa. The structure is similar to oI8-CaB but with a double layer of metallic ions in between the boron zig-zag chain layers. Due to the existence of Be_4B, an initial search of Ca_4B was run with a unit cell of 8:4, Ca:B. A stable structure was not found. At 0 GPa, The Be_4B structure type lies 375 meV/atom above the tie-line and gets more unstable with applied pressure.

To confirm that the 1:1 CaB structure would not collapse to nearby structures, we investigated the calcium deficient Ca_5B_6 using a 5:6 unit cell of Ca:B. The lowest enthalpy structure at this composition lied 153 meV/atom above the tie-line.

4 Conclusions and Outlook

Our study of the metal-borides was motivated by magnesium diboride being the highest T_c BCS superconductor. MgB_2 is superconducting because of its unique covalent boron network resulting in optimised electronic states at the Fermi level for superconductivity. Replicating the situation in other borides is difficult. In the two cases described in this thesis however, the metal atom is found to play a greater role in the electronic and phonon states involved in superconductivity.

We have shown that thermodynamically stable structures do not have very high superconducting critical temperatures. The two sets of compounds studied here show that the search for higher T_c BCS superconductors should continue with a focus on materials which are close to some form of instability. The first case, FeB_4, is expected to be a good superconductor because of its high electronic density of states at the Fermi level but at a cost to the structure being possibly close to instability. In the calcium borides, all the structures were shown to be highly stable but as a result their electronic density of states were low at the Fermi level, unfavourable for superconductivity.

Key conclusions of iron and calcium borides will be described below, with ideas to aid the design of BCS superconductors.

Iron tetraboride

Iron tetraboride is proposed as one of the few rare iron-based BCS-type superconductors, with a T_c of 15-20 K. In addition, a brand new crystal structure (oP10-FeB_4) which is stable at ambient pressure has been proposed in the well studied binary system of Fe-B.

FeB_4 displays features beneficial for superconductivity such as its high electronic density of states at the Fermi level of FeB_4. Unusual for a superconducting boride, we find that 2/3 of these electronic states originate from the d orbitals of the iron atom. These electronic states interact with a mixture of iron and boron phonon modes which result in a surprisingly large lambda of 0.80. No one would have expected BCS-type superconductivity in FeB_4 because of the presence of a magnetic element. We have run a series of theoretical tests that show that the structure is neither ferro- nor antiferromagnetic. The analysis involves a novel method of expanding the lattice to see where magnetism is induced, showing that the FeB_4 structure would need to be vastly distorted before it becomes magnetic. The structure for related CrB_4 was experimentally determined decades ago but our phonon dispersion calculation found it to be dynamically unstable. We showed that CrB_4 adopts the same oP10 crystal structure as FeB_4 and may have originally been incorrectly characterised as the two structures have similar X-ray diffraction patterns. CrB_4 is not superconducting as it has a very low density of states at the Fermi level.

The combination of a magnetic element with boron has resulted in superconductivity. It would be interesting to explore other magnetic transition metals (Ni, Co, Cr, Mn) combined with boron using an evolutionary algorithm at ambient and high pressure. We may be able to determine new boron structures which suppress the magnetic nature of the elements and could be close to a phase instability which would be good for a high T_c. Confirmation of the prediction of the new FeB_4 crystal structure and its superconducting properties is naturally the next step. Two articles have recently been published in a preprint archive describing the synthesis of Fe-B compounds [172, 173]. One article showed that the oP10-FeB_4 structure has been observed and it is superconducting at around 3 K [172]. The other article observed superconductivity of an iron-boron film but the

composition and structure was unknown. The observations are likely to attract further experimental interest [173].

Calcium boride

We have used an evolutionary structure search to propose high pressure ground states of Ca_xB_{1-x}. At 30 GPa, three new structures of CaB_6, CaB_2 and CaB stabilise and CaB_4 stabilises as the known MgB_4 structure type. At higher pressure, a new predicted parent structure of CaB_6 has been experimentally confirmed. For all compositions we have found that the stability of a particular structure is highly dependent on the size of the metal ion, shaping the boron framework around it.

A variety of stable superconducting calcium boride compounds are predicted but have low T_c's, exemplifying the inverse correlation between stability and superconducting T_c. Stable superconductors are only found for medium calcium concentrations where x = 0.33 - 0.5. The superconducting properties are attributed to the high contribution of calcium electronic states at the Fermi level combined with relatively high calcium phonon frequencies.

In general, basing superconductor searches on element compositions is an appropriate approach because we find some superconductors in the calcium borides but they are just not as good as MgB_2. Here are the key structural stability and superconducting features for each of the stable Ca-B compositions.

CaB_6 - The known semi-conducting cubic structure (cP7), adopted by a variety of metals, was shown to becomes dynamically unstable around 25 GPa. At 13 GPa, a metallic orthorhombic structure (oS56) stabilises, formed from cP7 through the opening up of half of the octahedra and them fusing to form a strip. oS56 is shown to be more stable when

the boron bond between octahedra is longer than in cP7 and this rule can be applied to explain the stability of other alkaline earth hexaborides. oS56-CaB_6 is not superconducting because its calcium phonon modes are at lower frequencies than the proposed superconducting calcium borides. At higher pressures (32 GPa), a B_{24} unit made from fusing four octahdra in cP7, becomes more stable than oS56. This parent tI56 structure was experimentally confirmed using powder X-ray diffraction experiments. The addition of a small amount of boron to tI56 results in a slightly more stable structure of tP57-$CaB_{6.125}$ which is expected to be superconducting. Whilst it is possible to apply pressure to a semiconductor resulting in a phase transition to a metal, the features favourable for superconductivity were not found in calcium hexaboride.

CaB_4 - The ThB_4 type structure (tP20) was previously thought to be unstable because insufficient electrons were transferred from the metal atom to the boron framework. We demonstrated that the structure is thermodynamically stable at ambient pressure because the calcium ion is of a suitable size for the boron framework. At 19 GPa, tP20 destabilises relative to the MgB_4 type structure because the boron framework becomes too small to hold the calcium ion. A general rule for the space filling of the metal ion in the tP20 boron network has been developed and applied to most metals in the periodic table. Atoms with ionic radii of 0.99-1.18 Å will form tP20-MB_4 at ambient pressure. tP20 may be metallic but its density of states at the Fermi level is too low for it to be superconducting. Applying pressure to tP20 results in a semiconducting structure which cannot be superconducting. The metastable high pressure structures of hR10 and mP20 are also semiconducting.

CaB_2 - This composition is not stable at ambient pressure but forms a 4 and 8-membered boron ring layered metallic structure (oI12) under 8 GPa of pressure. oI12-CaB_2 and its

SrB_2 analog are superconducting at ~ 1 K. Above 32 GPa, a poorly superconducting monoclinic step-like hexagon structure becomes thermodynamically more stable. All proposed structures are stable as they have a long metal-boron distance.

CaB - No alkaline earth monoborides are known at ambient pressure. Above 8 GPa a superconducting zig-zag chained structure of oI8-CaB stabilises with a predicted T_c of 5.5 K. The most stable form of calcium monoboride contains zig-zagged boron chains as they fit themselves around the metal ion. A DOS of around 0.5 states/(eV spin f.u.) was sufficient for superconductivity in this compound. Compared with FeB_4 which has a DOS around 1, it seems that the minimum DOS required for superconductivity above 4.3 K (temperature of liquid He) is around 0.5. Screening for compounds with this minimum DOS at the Fermi level could be a way to search for new superconductors.

Our experimental study of calcium hexaboride is still incomplete. Whilst we were able to identify the tI56 parent structure, oS56 was not observed at all. As there is negligible difference between the XRD patterns of boron doped and undoped tI56 it was unclear which product was formed. Resistance and magnetic measurements of the high pressure phase could be used to see if the compound is superconducting. As mentioned in the FeB_4 conclusions, the next step would be to attempt synthesis of the CaB_2 and CaB superconductors.

For theoretical superconductor prediction one could study other calcium compounds looking out for those with both high frequency calcium phonon modes around 400 cm^{-1} and a high proportion of electronic calcium states at the Fermi level. An example would be Ca-C compounds at ambient and high pressure. C_6Ca is already known to be superconducting at 11.5 K but other compounds such as CaC_2 are insulating so high pressure

could induce a phase transition.

Future ab-initio design of superconductors would involve the use of maximally-localized Wannier functions to calculate the electron-phonon coupling on much larger grids than those used in this thesis [224]. More specifically, the electron-phonon interaction will no longer be assumed to be isotropic within the Brillouin zone and therefore provide a more accurate prediction of the T_c.

Overall, the two case studies have shown that using an evolutionary crystal structure search to discover new materials is a viable option. Numerous experimental studies have been performed on iron boride but all missed the existence of iron tetraboride. Also, our crystal structure search of calcium hexaboride was able to identify the high pressure polymorph, something that was almost impossible using the experimental XRD patterns alone. The evolutionary crystal structure search method is thus a nice complement to experiment. Our search of FeB_4 also led us to investigate the structure of CrB_4. We were able to find a lower energy form of CrB_4 and this has since been confirmed with experiments.

BCS superconductor design is difficult as we want to predict the most stable crystal structures so that they can be synthesised but these often do not possess properties considered necessary for a high T_c. The unexpected discovery of superconductivity in FeB_4 however, shows that there is still scope to find compounds which are superconducting at ambient pressure.

5 Appendix

5.1 FeB_4 appendix

	Quantum ESPRESSO pseudopotentials		
	B.pbe-n-van.UPF Fe.pbe-sp-van_ak.UPF	B.pbe-n-van.UPF Fe.pbe-sp-van.UPF	B.pbe-n-van.UPF Fe.pbe-sp-van_mit.UPF
	Orbital occupancies		
3s	2.0	2.0	2.0
3p	6.0	6.0	6.0
3d	6.5	6.0	5.5
4s	1.0	2.0	0.4
4p	0.0	0.0	0.1
	Phonon frequencies (cm^{-1})		
	-89.4	-88.2	-72.1
	306.2	300.1	304.0
	307.5	306.2	305.3
	309.7	309.0	306.7
	423.1	423.0	423.2
	433.8	433.8	435.1
	529.9	528.8	527.3
	539.8	539.5	533.3
	555.1	555.0	551.9
	623.9	623.4	624.1
	647.0	647.2	645.1
	667.5	667.5	665.1
	691.6	690.5	686.0
	922.9	923.1	920.8
	966.8	966.6	964.1

Table 5.1: Phonon frequencies with varying Fe pseudopotential for a primitive unit cell of oI10-FeB_4.

12	16	20	24	28	32
13.2	13.6	13.5	13.9	13.8	13.8
14.3	14.7	14.7	15.0	14.9	14.9
14.8	15.2	15.1	15.5	15.4	15.4
391.4	391.5	391.5	391.5	391.5	391.5
419.7	420.1	420.1	420.1	420.0	420.0
433.8	433.9	434.0	434.0	434.0	434.0
439.6	440.8	441.0	441.0	441.0	441.0
441.1	441.1	441.1	441.1	441.0	441.0
608.2	608.5	608.6	608.6	608.6	608.6
630.4	630.7	630.8	630.8	630.7	630.7
651.7	652.9	653.3	653.4	653.4	653.4
707.0	707.7	707.9	707.9	707.8	707.8
716.9	717.2	717.4	717.5	717.5	717.5
921.7	921.7	921.7	921.7	921.7	921.7
960.3	963.1	963.6	963.6	963.6	963.5

Table 5.2: Gamma point phonon frequencies with varying k-mesh of N x N x N where N = 12, 16, 20, 24, 28 and 32 for the primitive unit cell of oI10-FeB_4.

12	16	20	24	28
-89.4	-88.3	-87.5	-87.3	-87.3
306.2	309.2	307.5	306.9	307.0
307.5	309.7	308.2	308.0	308.0
309.7	311.3	310.1	309.8	309.8
423.1	423.1	423.2	423.1	423.1
433.8	434.0	434.0	434.0	434.0
529.9	530.2	530.3	530.3	530.3
539.8	539.8	539.8	539.8	539.8
555.1	555.2	555.2	555.2	555.2
623.9	624.1	624.1	624.1	624.1
647.0	647.4	647.4	647.5	647.4
667.5	667.9	667.9	667.9	667.9
691.6	691.7	691.6	691.6	691.6
922.9	923.0	923.0	922.9	922.9
966.8	967.2	967.2	967.3	967.3

Table 5.3: Phonon frequencies for imaginary frequency q-point with varying k-mesh of N x N x N where N = 12, 16, 20, 24 and 28 for the primitive unit cell of oI10-FeB_4.

	a	b	c
B	0.26	-0.24	0.00
B	-0.26	0.24	0.00
B	-0.26	0.24	0.00
B	0.26	-0.24	0.00
B	-0.26	-0.24	0.00
B	0.26	0.24	0.00
B	0.26	0.24	0.00
B	-0.26	-0.24	0.00
B	0.00	0.00	0.00
Fe	0.00	0.00	0.00

Table 5.4: Eigenvector for the imaginary mode of gamma point frequency -208cm^{-1} for oI10-FeB_4. The vector is in direct coordinates.

	Space group	a (Å)	b (Å)	c (Å)	Wyckoff positions B		Fe	
oI10	71	4.518	5.287	3.052	$8n$	(0.2121, 0.3407, 0)	$2a$	(0 , 0 , 0)
oP10	58	4.521	5.284	3.006	$4g$	(0.1606, 0.1267, 0)	$2c$	(0 , 1/2 , 0)

Table 5.5: Space groups, lattice parameters, and Wyckoff-positions of fully relaxed FeB_4 structures.

5.2 Ca-B appendix

Compound	k-mesh	q-mesh
tI56-CaB_6	6x6x6	3x3x3
tP57-$CaB_{6.125}$	6x6x4	Γ only
oI12-CaB_2	16x16x16	4x4x4
mS12-CaB_2	12x6x12	4x2x4
oI8-CaB	32x32x32*	4x4x4
oI12-SrB_2	16x16x16	4x4x4
oI8-SrB	24x24x24	4x4x4

Table 5.6: List of k and q-meshes used for calculating the electron-phonon interaction when a superconducting T_c has been quoted. *Electron-phonon properties of two low symmetry q-points were calculated using a k-mesh of 24x24x24.

e_1^R			
B	0.0	0.0	0.0
B	0.0	0.0	0.0
B	0.0	0.5	0.0
B	0.0	-0.5	0.0
B	0.0	0.0	-0.5
B	0.0	0.0	0.5
Ca	0.0	0.0	0.0

e_2^R			
B	0.0	-0.5	0.0
B	0.0	0.5	0.0
B	0.0	0.0	0.0
B	0.0	0.0	0.0
B	0.5	0.0	0.0
B	-0.5	0.0	0.0
Ca	0.0	0.0	0.0

e_3^R			
B	0.0	0.0	0.5
B	0.0	0.0	-0.5
B	-0.5	0.0	0.0
B	0.5	0.0	0.0
B	0.0	0.0	0.0
B	0.0	0.0	0.0
Ca	0.0	0.0	0.0

e_1^M			
B	0.0	0.0	0.0
B	0.0	0.0	0.0
B	0.0	0.5	0.0
B	0.0	-0.5	0.0
B	0.0	0.0	-0.5
B	0.0	0.0	0.5
Ca	0.0	0.0	0.0

Table 5.7: Three degenerate R and one M imaginary phonon eigenvectors.

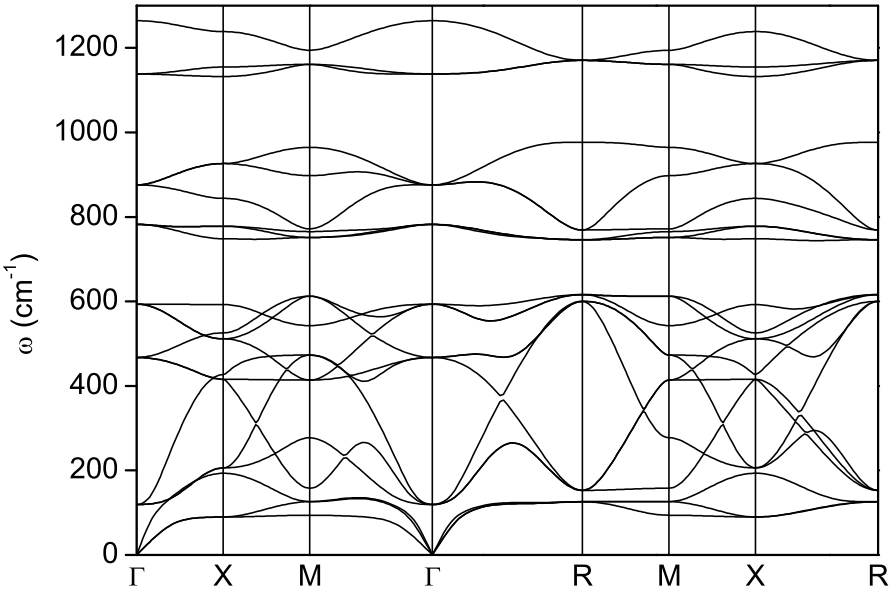


Figure 5.1: Phonon dispersion of cP7-CaB_6 relaxed to 0 GPa. A q-mesh of 2 x 2 x 2 and k-mesh of 12 x 12 x 12 has been applied. The high symmetry k-points are taken from Reference [198].

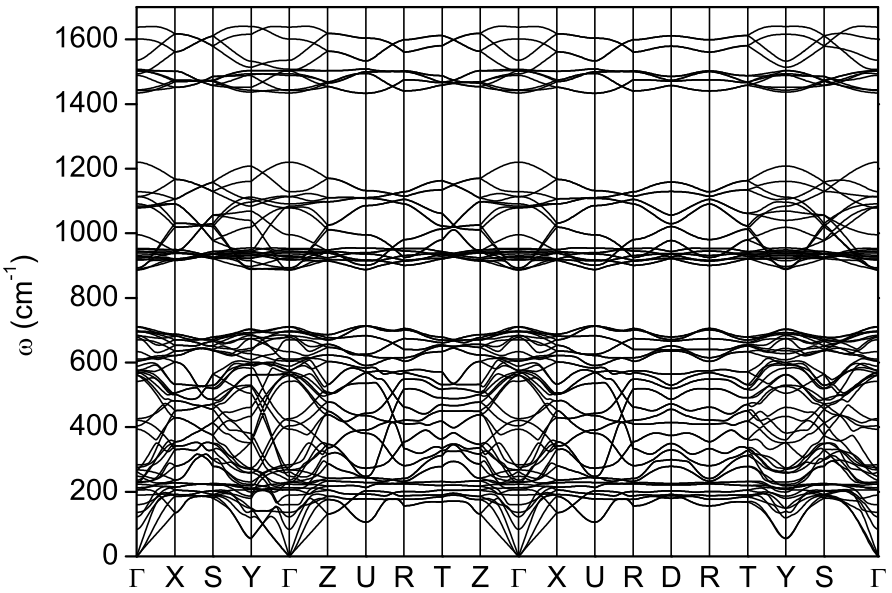


Figure 5.2: Phonon dispersion of oP28-CaB_6 relaxed to 50 GPa. A q-mesh of 4 x 3 x 4 and k-mesh of 8 x 6 x 8 has been applied. The k-path is taken from Reference [200].

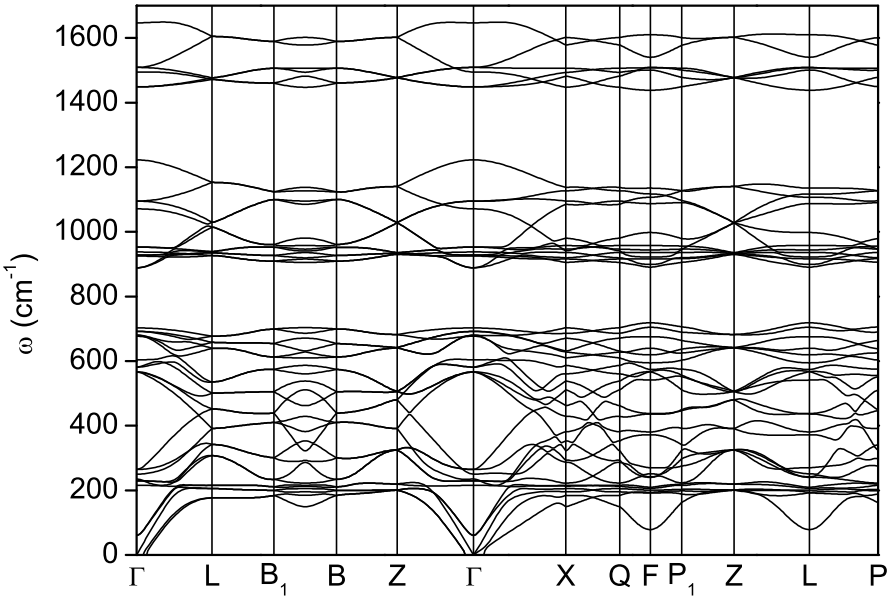


Figure 5.3: Phonon dispersion of hR42-CaB_6 relaxed to 50 GPa. A q-mesh of 4 x 4 x 4 and k-mesh of 8 x 8 x 8 has been applied. The k-path is taken from Reference [200].

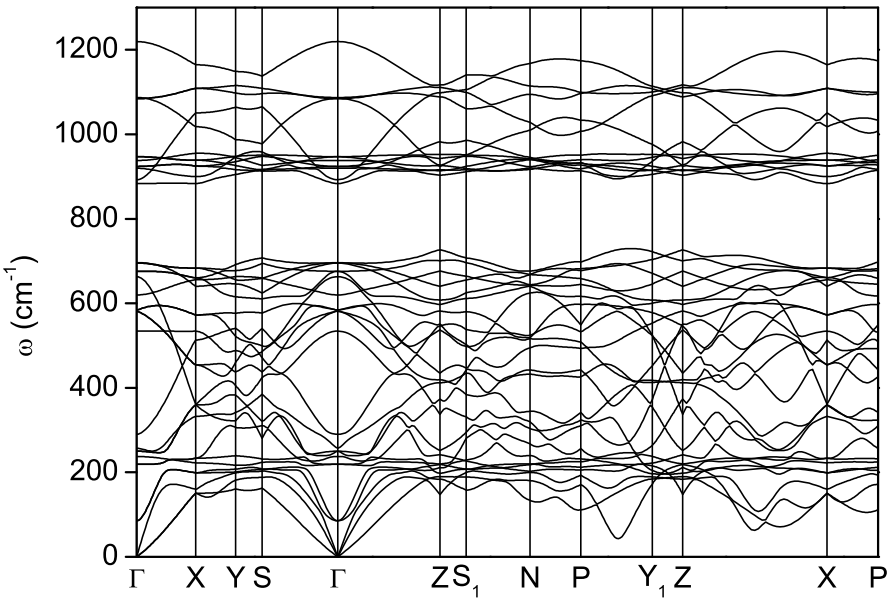


Figure 5.4: Phonon dispersion of tI28-CaB_6 relaxed to 50 GPa. A q-mesh of 4 x 4 x 4 and k-mesh of 8 x 8 x 8 has been applied. The k-path is taken from Reference [200].

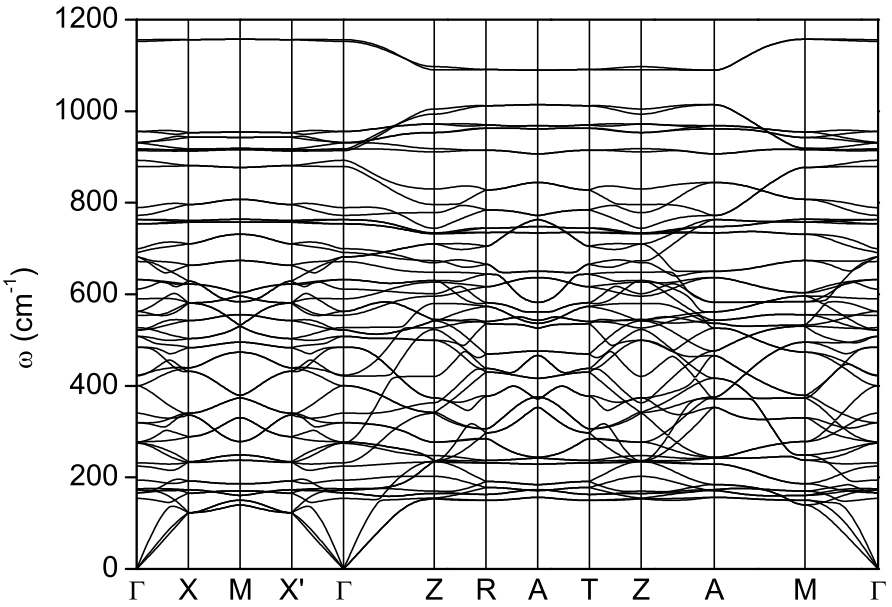


Figure 5.5: Phonon dispersion of tP20-CaB_6 relaxed to 0 GPa. A q-mesh of 3 x 3 x 4 and k-mesh of 6 x 6 x 12 has been applied. The k-path is taken from Reference [200].

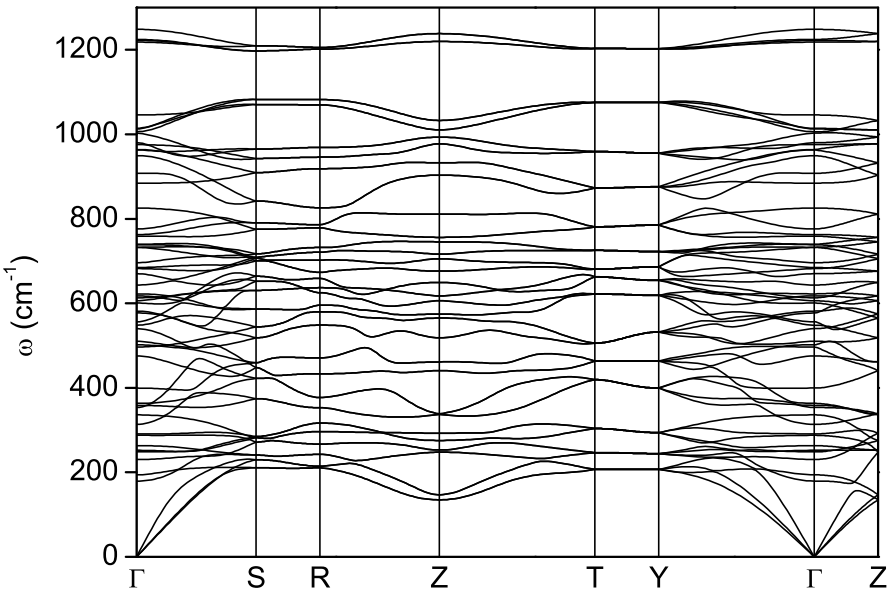


Figure 5.6: Phonon dispersion of oP20-CaB_6 relaxed to 30 GPa. A q-mesh of 4 x 4 x 2 and k-mesh of 12 x 12 x 6 has been applied. The k-path is taken from Reference [200].

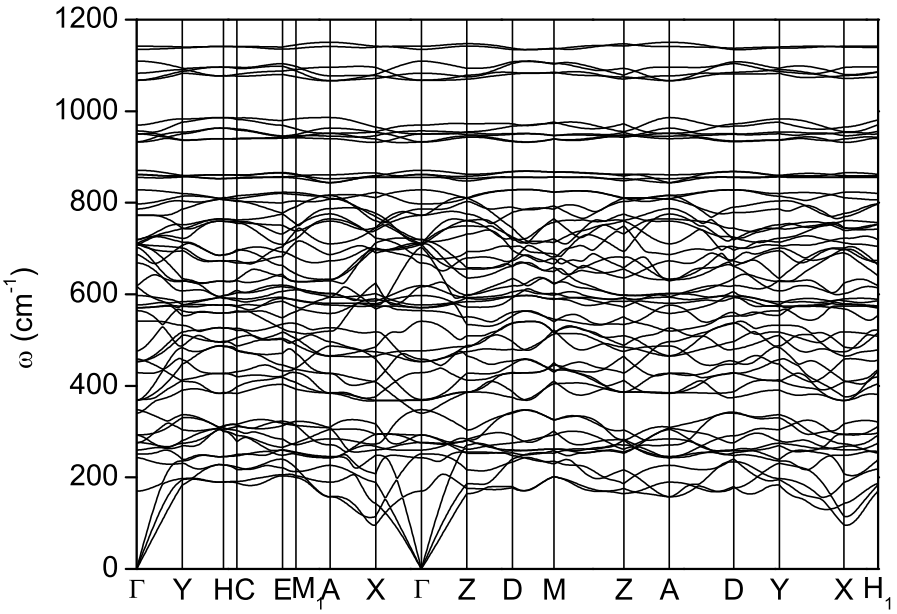


Figure 5.7: Phonon dispersion of mP20-CaB_6 relaxed to 30 GPa. A q-mesh of 2 x 2 x 2 and k-mesh of 8 x 8 x 8 has been applied. The k-path is taken from Reference [200].

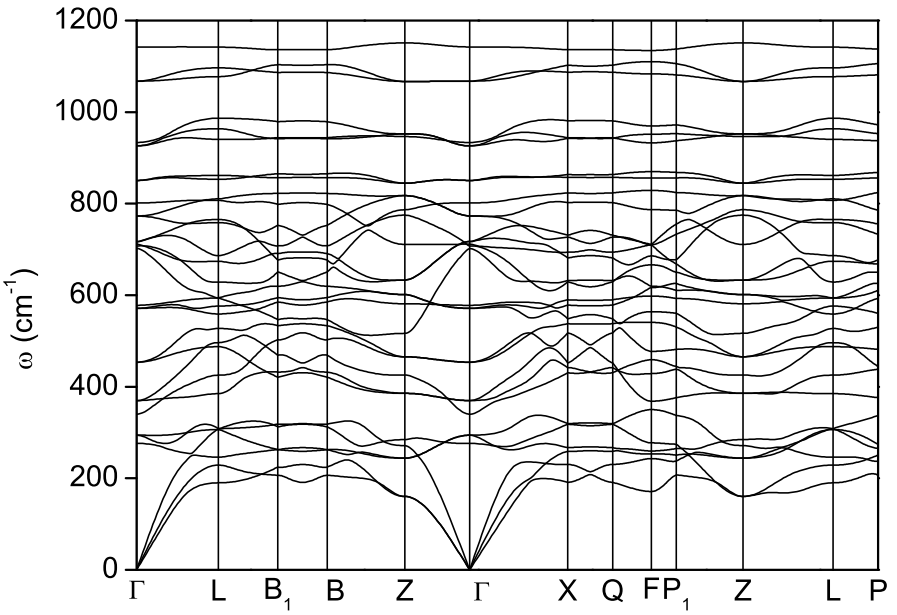


Figure 5.8: Phonon dispersion of hR10-CaB_6 relaxed to 30 GPa. A q-mesh of 4 x 4 x 4 and k-mesh of 10 x 10 x 10 has been applied. The k-path is taken from Reference [200].

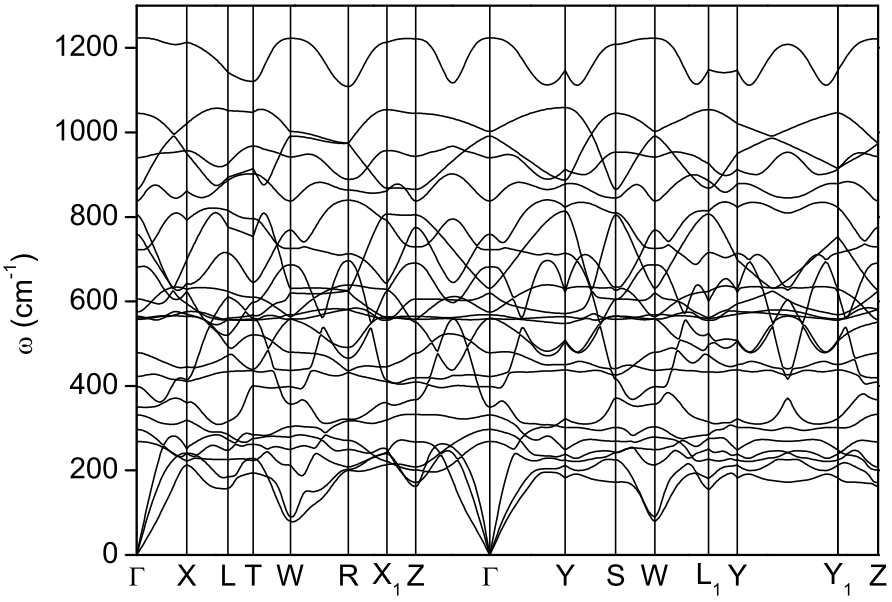


Figure 5.9: Phonon dispersion of oI12-CaB_2 relaxed to 30 GPa. A q-mesh of 4 x 4 x 4 and k-mesh of 16 x 16 x 16 has been applied. The k-path is taken from Reference [200].

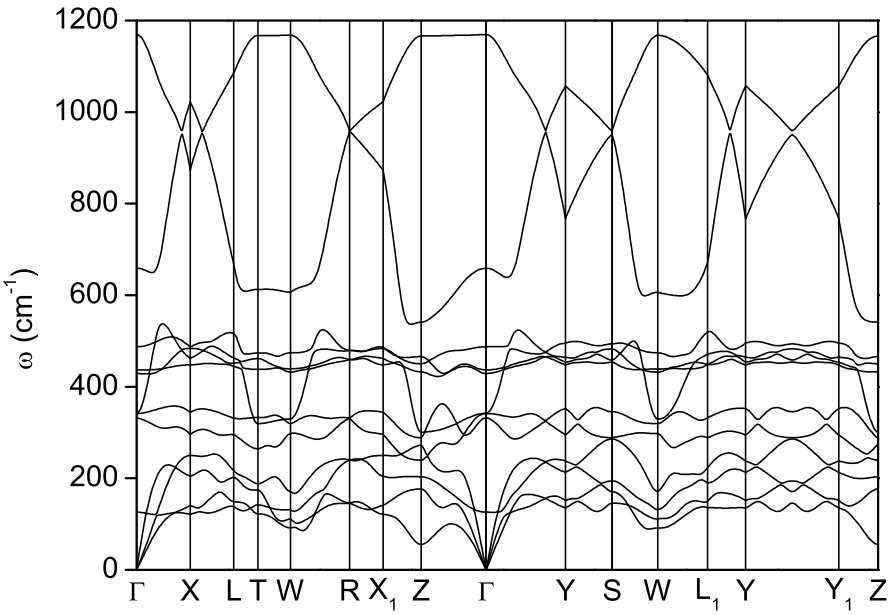


Figure 5.10: Phonon dispersion of oI8-CaB relaxed to 30 GPa. A q-mesh of 4 x 4 x 4 and k-mesh of 32 x 32 x 32 has been applied (see Table 5.6 for details). The k-path is taken from Reference [200].

The phonon frequencies for mS12-CaB_2 and mS16-CaB have been calculated on a dense mesh of q-points and no imaginary modes were found.

12 x 12 x 12	16 x 16 x 16	24 x 24 x 24	32 x 32 x 32
-12.5	-13.2	-13.3	-13.3
-11.2	-12.0	-12.1	-12.1
-4.9	-6.4	-6.4	-6.4
267.0	267.9	268.6	268.5
296.2	296.6	296.7	296.7
332.5	331.2	331.7	331.6
349.5	349.6	349.8	349.8
398.7	398.5	398.6	398.5
423.9	422.6	423.1	423.0
472.0	478.7	478.3	478.3
559.2	560.5	560.9	560.8
573.7	575.0	575.6	575.5
671.3	681.7	683.0	682.7
718.2	723.0	724.1	723.8
761.6	758.8	771.1	767.9
836.6	837.8	837.6	837.6
941.1	940.0	940.4	940.3
1227.2	1223.5	1226.7	1225.9

Table 5.8: The gamma point calculated phonon frequencies in cm^{-1} for a primitive unit cell of oI12-CaB_2 relaxed to 30 GPa for increasing k-meshes.

Structure	Space group	a (Å)	b (Å)	c (Å)	Wyckoff positions B		Ca	
oP12-BeB_2	581 (Pnnm)	6.044	5.132	2.970	4g	(0.7285, 0.0911, 0.0000)	4g	(0.5884, 0.7521, 0.0000)
					4g	(0.2726, 0.5875, 0.0000)		

Table 5.9: Pearson symbols, space groups, lattice parameters, Wyckoff-positions and stability pressure ranges of BeB_2 0 GPa.

Structure	Space group	a (Å)	b (Å)	c (Å)	Wyckoff positions B		Ca	
cP7-CaB_6	221 (Pm-3m)	4.148			6f	(0.1993, $\frac{1}{2}$, $\frac{1}{2}$)	1a	(0.0000, 0.0000, 0.0000)
tP20-CaB_4	(I4/mmm)	6.839		8.986	16l	(-0.3071, 0.1251, 0.0000)	4e	(0.0000, 0.0000, $\frac{1}{4}$)
					16m	(-0.2253, -0.2253, 0.3393)	4d	(0.0000, $\frac{1}{2}$, $\frac{1}{4}$)
					16n	(0.0000, -0.2042, 0.4104)		

Table 5.10: Pearson symbols, space groups, lattice parameters, Wyckoff-positions and stability pressure ranges of fully relaxed Ca_xB_{1-x} structures at 0 GPa.

Structure	Space group	a (Å)	b (Å)	c (Å)	Wyckoff positions B		Ca	
oS56-CaB_6	63 (Cmcm)	8.378	10.185	5.303	8g	(0.1450, 0.1401, $\frac{1}{4}$)	8g	(-0.2945,0.3575, $\frac{1}{4}$)
					8g	(-0.3315, 0.0868, $\frac{1}{4}$)		
					8e	(0.4012, 0.0000, 0.0000)		
					8f	(0.0000, 0.3571, -0.0864)		
					8f	(0.0000, 0.0599, 0.4059)		
					8f	(0.0000, -0.2264, 0.4092)		
oP20-CaB_4	62 (Pnma)	3.905	4.174	7.558	4c	(0.2374, $\frac{1}{4}$, -0.3196)	4c	(0.4184, $\frac{1}{4}$, 0.3682)
					4c	(0.3936, $\frac{1}{4}$, -0.1274)		
					8d	(-0.3855, -0.4429, -0.0749)		
oI12-CaB_2	71 (Immm)	7.558	4.174	3.905	4g	(0.0000, 0.1914, 0.0000)	4f	(0.3126, $\frac{1}{2}$, 0.0000)
					4j	($\frac{1}{2}$, 0.0000, 0.2181)		
oI8-CaB	74 (Imna)	3.036	4.270	7.353	4e	($\frac{1}{2}$,$\frac{1}{4}$, 0.2912)	4el	($\frac{1}{2}$,$\frac{1}{4}$,-0.0865)

Table 5.11: Pearson symbols, space groups, lattice parameters, Wyckoff-positions and stability pressure ranges of fully relaxed Ca_xB_{1-x} structures at 30 GPa.

Structure	Space group	a (Å)	b (Å)	c (Å)	β	Wyckoff positions B		Ca	
tI56-CaB_6	139 (I4/mmm)	6.691		8.808		16l	(-0.3090, 0.1249, 0.0000)	4e	(0.0000, 0.0000, $\frac{1}{4}$)
						16m	(-0.2264, -0.2264, 0.3392)	4d	(0.0000, $\frac{1}{2}$, $\frac{1}{4}$)
						16n	(0.0000, -0.2026, 0.4096)		
hR10-CaB_4	166 (R-3m)	4.361				6c	(0.0000, 0.0000, -0.4371)	6c	(0.0000, 0.0000, 0.2160)
						18h	(0.7991, 0.2009, 0.3811)		
mP20-CaB_4	11 ($P2_1/m$)	5.305	4.362	6.868	104.5	2e	(0.2871, $\frac{1}{4}$, 0.4302)	2e	(0.6823, $\frac{1}{4}$, 0.0341)
						2e	(0.1241, $\frac{1}{4}$, 0.8129)	2e	(0.8182, $\frac{1}{4}$, 0.4660)

Table 5.12: Pearson symbols, space groups, lattice parameters, Wyckoff-positions and stability pressure ranges of fully relaxed Ca_xB_{1-x} structures at 50 GPa.

Bibliography

[1] "Basic research needs for superconductivity, report on the basic energy sciences workshop," *The, United States Department of Energy*, 2006.

[2] L. Rossi, "The Large Hadron Collider and the role of superconductivity in one of the largest scientific enterprises," *IEEE Transactions on Applied Superconductivity*, vol. 17, no. 2, pp. 1005–1014, 2007.

[3] N. A. of Sciences, "Selling the nation's helium reserve," 2010.

[4] www.bnl.gov/magnets/Cryo/facility.asp.

[5] J. Bardeen, "Theory of superconductivity," *Physical Review*, vol. 108, no. 5, p. 1175, 1957.

[6] A. Migdal, "Interaction between electrons and the lattice vibrations in a normal metal," *Journal Name: Zhur. Eksptl'. i Teoret. Fiz.*, vol. 34, pp. 1438–46, 1958.

[7] Eliashberg, "Interactions between electrons and lattice vibrations in a superconductor," *Journal Name: Sov. Phys. - JETP (Engl. Transl.); (United States); Journal Volume: 11:3*, pp. 696–702, 1960.

[8] W. Koch and H. M. C., *A Chemist's Guide to Density Functional Theory*. Wiley-VCH, 2nd ed., 2000.

[9] C. Buzea and K. Robbie, "Assembling the puzzle of superconducting elements: A review," *Superconductor Science and Technology*, vol. 18, no. 1, 2004.

[10] B. T. Matthias, "Empirical relation between superconductivity and the number of valence electrons per atom," *Physical Review*, vol. 97, no. 1, p. 74, 1955.

[11] Y. Akahama, M. Kobayashi, and H. Kawamura, "Pressure effect on superconductivity of V and V-Cr alloys up to 50 Gpa," *Journal of the Physical Society of Japan*, vol. 64, no. 10, pp. 4049–4050, 1995.

[12] M. Ishizuka, M. Iketani, and S. Endo, "Pressure effect on superconductivity of vanadium at megabar pressures," *Physical Review B*, vol. 61, pp. R3823–R3825, Feb 2000.

[13] H. Fujihisa, Y. Nakamoto, M. Sakata, K. Shimizu, T. Matsuoka, Y. Ohishi, H. Yamawaki, S. Takeya, and Y. Gotoh, "Ca-vii: A chain ordered host-guest structure of calcium above 210 gpa," *Phys. Rev. Lett.*, vol. 110, p. 235501, 2013.

[14] W. Fan, Y. L. Li, J. L. Wang, L. J. Zou, and Z. Zeng, "Tc map and superconductivity of simple metals at high pressure," *Physica C: Superconductivity*, vol. 470, no. 17-18, pp. 696–702, 2010.

[15] T. Matsuoka and K. Shimizu, "Direct observation of a pressure-induced metal-to-semiconductor transition in lithium," *Nature*, vol. 458, no. 7235, pp. 186–189, 2009.

[16] N. W. Ashcroft, "Metallic hydrogen: A high-temperature superconductor?," *Physical Review Letters*, vol. 21, no. 26, p. 1748, 1968.

[17] W. E and H. H. B, "On the possibility of a metallic modification of hydrogen," *Journal of Chemical Physics*, vol. 3, no. 764, 1935.

[18] I. F. Silvera and J. W. Cole, "Metallic hydrogen: The most powerful rocket fuel yet to exist," *Journal of Physics: Conference Series*, vol. 215, no. 1, p. 012194, 2010.

[19] I. Silvera, "The insulator-metal transition in hydrogen," *Proceedings of the National Academy of Sciences*, vol. 107, no. 29, pp. 12743–12744, 2010.

[20] M. I. Eremets and I. A. Troyan, "Conductive dense hydrogen," *Nature Materials*, vol. 10, no. 12, pp. 927–931, 2011.

[21] J. G. Bednorz, "Possible high Tc superconductivity in the Ba-La-Cu-O system," *Zeitschrift fr Physik. C, Particles and fields*, vol. 64, p. 189, 1986.

[22] http://tfy.tkk.fi/nanospin/facilities/pld/basics/supercond.php.

[23] I. I. Mazin, "Superconductivity gets an iron boost," *Nature*, vol. 464, no. 7286, pp. 183–186, 2010.

[24] W. Buckel and R. Kleiner, *Superconductivity, Fundamentals and Applications*. Wiley-VCH, 2nd ed., 2004.

[25] S. Graser, P. J. Hirschfeld, T. Kopp, R. Gutser, B. M. Andersen, and J. Mannhart, "How grain boundaries limit supercurrents in high-temperature superconductors," *Nature Physics*, vol. 6, no. 8, pp. 609–614, 2010.

[26] www.superconductors.org.

[27] Y. Kamihara, T. Watanabe, M. Hirano, and H. Hosono, "Iron-based layered superconductor $La[O_{1-x}F_x]FeAs$ (x = 0.0-0.12) with $T_c = 26$ K," *Journal of the American Chemical Society*, vol. 130, no. 11, pp. 3296–3297, 2008.

[28] J. Paglione and R. L. Greene, "High-temperature superconductivity in iron-based materials," *Nature Physics*, vol. 6, no. 9, pp. 645–658, 2010.

[29] L. Boeri, O. V. Dolgov, and A. A. Golubov, "Is $LaFeAsO_{1-x}F_x$ an electron-phonon superconductor?," *Physical Review letters*, vol. 101, no. 2, p. 026403, 2008.

[30] M. Capone, M. Fabrizio, C. Castellani, and E. Tosatti, "Colloquium: Modeling the unconventional superconducting properties of expanded A_3C_{60} fullerides," *Reviews of Modern Physics*, vol. 81, pp. 943–958, Jun 2009.

[31] M. J. Rosseinsky and K. Prassides, "Materials science: Hydrocarbon superconductors," *Nature*, vol. 464, no. 7285, pp. 39–41, 2010.

[32] R. Mitsuhashi, Y. Suzuki, Y. Yamanari, H. Mitamura, T. Kambe, N. Ikeda, H. Okamoto, A. Fujiwara, M. Yamaji, N. Kawasaki, Y. Maniwa, and Y. Kubozono, "Superconductivity in alkali-metal-doped picene," *Nature*, vol. 464, no. 7285, pp. 76–79, 2010.

[33] A. Y. Ganin, Y. Takabayashi, Y. Z. Khimyak, S. Margadonna, A. Tamai, M. J. Rosseinsky, and K. Prassides, "Bulk superconductivity at 38 K in a molecular system," *Nature Materials*, vol. 7, no. 5, pp. 367–371, 2008.

[34] Y. Takabayashi, A. Y. Ganin, P. Jeglic, D. Arcon, T. Takano, Y. Iwasa, Y. Ohishi, M. Takata, N. Takeshita, K. Prassides, and M. J. Rosseinsky, "The disorder-free non-bcs superconductor Cs_3C_{60} emerges from an antiferromagnetic insulator parent state," *Science*, vol. 323, no. 5921, pp. 1585–1590, 2009.

[35] T. E. Weller, M. Ellerby, S. S. Saxena, R. P. Smith, and N. T. Skipper, "Superconductivity in the intercalated graphite compounds C_6Yb and C_6Ca," *Nature Physics*, vol. 1, no. 1, pp. 39–41, 2005.

[36] A. Y. Liu and I. I. Mazin, "Combining the advantages of superconducting mgb_2 and cac_6 in one material: Suggestions from first-principles calculations," *Physical Review B*, vol. 75, no. 6, p. 064510, 2007.

[37] M. Calandra and F. Mauri, "Theoretical explanation of superconductivity in C_6Ca," *Physical Review letters*, vol. 95, no. 23, p. 237002, 2005.

[38] I. I. Mazin, L. Boeri, O. V. Dolgov, A. A. Golubov, G. B. Bachelet, M. Giantomassi, and O. K. Andersen, "Unresolved problems in superconductivity of CaC_6," *Physica C: Superconductivity*, vol. 460-462, no. Part 1, pp. 116–120, 2007.

[39] J. S. Kim, L. Boeri, R. K. Kremer, and F. S. Razavi, "Effect of pressure on superconducting Ca-intercalated graphite CaC_6," *Physical Review B*, vol. 74, no. 21, p. 214513, 2006.

[40] P. S. Gennady and L. I. Alexander, "The chemical bonding and electronic properties of metal borides," *Russian Chemical Reviews*, vol. 63, no. 9, p. 711, 1994.

[41] B. Albert and H. Hillebrecht, "Boron: Elementary challenge for experimenters and theoreticians," *Angewandte Chemie International Edition*, vol. 48, no. 46, pp. 8640–8668, 2009.

[42] M. E. Jones and R. E. Marsh, "The preparation and structure of magnesium boride, MgB_2," *Journal of the American Chemical Society*, vol. 76, no. 5, pp. 1434–1436, 1954.

[43] J. Nagamatsu, N. Nakagawa, T. Muranaka, Y. Zenitani, and J. Akimitsu, "Superconductivity at 39 K in magnesium diboride," *Nature*, vol. 410, no. 6824, pp. 63–64, 2001.

[44] C. Buzea and T. Yamashita, "Review of the superconducting properties of MgB_2," *Superconductor Science and Technology*, vol. 14, no. 11, pp. R115–R146, 2001. 0953-2048.

[45] J. M. An and W. E. Pickett, "Superconductivity of MgB_2: Covalent bonds driven metallic," *Physical Review Letters*, vol. 86, no. 19, p. 4366, 2001.

[46] J. Kortus, I. I. Mazin, K. D. Belashchenko, V. P. Antropov, and L. L. Boyer, "Superconductivity of metallic boron in MgB_2," *Physical Review Letters*, vol. 86, no. 20, p. 4656, 2001.

[47] I. I. Mazin and V. P. Antropov, "Electronic structure, electron-phonon coupling, and multiband effects in MgB_2," *Physica C: Superconductivity*, vol. 385, no. 1-2, pp. 49–65, 2003.

[48] Y. Wang, J. Lv, Y. Ma, T. Cui, and G. Zou, "Superconductivity of MgB_2 under ultrahigh pressure: A first-principles study," *Physical Review B*, vol. 80, no. 9, p. 092505, 2009.

[49] B. Lorenz, R. L. Meng, and C. W. Chu, "High-pressure study on MgB_2," *Physical Review B*, vol. 64, no. 1, p. 012507, 2001.

[50] J. S. Slusky, N. Rogado, K. A. Regan, M. A. Hayward, P. Khalifah, T. He, K. Inumaru, S. M. Loureiro, M. K. Haas, H. W. Zandbergen, and R. J. Cava, "Loss of superconductivity with the addition of Al to MgB_2 and a structural transition in $Mg_{1-x}Al_xB_2$," *Nature*, vol. 410, no. 6826, pp. 343–345, 2001.

[51] R. H. T. Wilke, S. L. Bud'ko, P. C. Canfield, D. K. Finnemore, R. J. Suplinskas, and S. T. Hannahs, "Systematic effects of carbon doping on the superconducting properties of $Mg(B_{1-x}C_x)_2$," *Physical Review Letters*, vol. 92, p. 217003, May 2004.

[52] M. R. Cimberle and et al., "Magnetic characterization of sintered MgB_2 samples: effect of substitution or 'doping' with Li, Al and Si," *Superconductor Science and Technology*, vol. 15, no. 1, p. 43, 2002.

[53] S. Agrestini, C. Metallo, M. Filippi, G. Campi, C. Sanipoli, S. De Negri, M. Giovannini, A. Saccone, A. Latini, and A. Bianconi, "Sc doping of MgB_2: the structural and electronic properties of $Mg_{1-x}Sc_xB_2$," *Journal of Physics and Chemistry of Solids*, vol. 65, no. 8-9, pp. 1479–1484, 2004.

[54] T. M. Shen, G. Li, C. H. Cheng, and Y. Zhao, "Doping effects of carbon and titanium on the critical current density of MgB_2," *Superconductor Science and Technology*, vol. 19, no. 11, p. 1219, 2006.

[55] A. Tampieri, G. Celotti, S. Sprio, D. Rinaldi, G. Barucca, and R. Caciuffo, "Effects of copper doping in MgB_2 superconductor," *Solid State Communications*, vol. 121, no. 9-10, pp. 497–500, 2002.

[56] N. Hörhager, M. Eisterer, H. W. Weber, T. Prikhna, T. Tajima, and V. F. Nesterenko, "Ti and Zr doped MgB_2 bulk superconductors," *Journal of Physics: Conference Series*, vol. 43, no. 1, p. 500, 2006.

[57] X. L. Xu, J. D. Guo, Y. Z. Wang, and X. Wang, "Au-doping effects in the $Mg_{1-x}Au_xB_2$ series," *Materials Letters*, vol. 58, no. 1-2, pp. 142–145, 2004.

[58] C. Shekhar, R. Giri, R. S. Tiwari, D. S. Rana, S. K. Malik, and O. N. Srivastava, "Effect of La doping on microstructure and critical current density of MgB_2," *Superconductor Science and Technology*, vol. 18, no. 9, p. 1210, 2005.

[59] R. J. Cava, H. W. Zandbergen, and K. Inumaru, "The substitutional chemistry of MgB_2," *Physica C: Superconductivity*, vol. 385, no. 1-2, pp. 8–15, 2003. 0921-4534.

[60] N. I. Medvedeva, A. L. Ivanovskii, J. E. Medvedeva, and A. J. Freeman, "Electronic structure of superconducting MgB_2 and related binary and ternary borides," *Physical Review B*, vol. 64, no. 2, p. 020502, 2001.

[61] F. Bernardini and S. Massidda, "Anomalous effect of Li-Al codoping in MgB_2 : A simple explanation," *Physical Review B*, vol. 74, no. 1, p. 014513, 2006.

[62] H. L. Li, K. Q. Ruan, S. Y. Li, Y. Yu, C. Y. Wang, and L. Z. Cao, "Upper critical field and the effect of Li doping on the activation energy in MgB_2," *Physica C: Superconductivity*, vol. 386, pp. 560–564, 2003.

[63] I. Pallecchi and et al., "Investigation of Li-doped MgB_2," *Superconductor Science and Technology*, vol. 22, no. 9, p. 095014, 2009.

[64] Y. Sun, D. Yu, Z. Liu, J. He, X. Zhang, Y. Tian, J. Xiang, and D. Zheng, "Decrease of T_c and persistent two gaps upon enhancement of the Ca doping in MgB_2 superconductor," *Applied Physics Letters*, vol. 90, no. 5, pp. 052507–3, 2007.

[65] A. S. Cooper, "Superconductivity: the transition temperature peak below four electrons per atom," *Proceedings of the National Academy of Sciences of the United States of America*, vol. 67, no. 1, p. 313, 1970. 0027-8424.

[66] L. Leyarovska and E. Leyarovski, "A search for superconductivity below 1 K in transition metal borides," *Journal of the Less Common Metals*, vol. 67, no. 1, pp. 249–255, 1979.

[67] Y. G. Naidyuk, O. E. Kvitnitskaya, I. K. Yanson, S. L. Drechsler, G. Behr, and S. Otani, "Electron-phonon interaction in transition-metal diborides TB_2 (T = Zr, Nb, Ta) studied by point-contact spectroscopy," *Physical Review B*, vol. 66, no. 14, p. 140301, 2002.

[68] P. P. Singh, "Electron-phonon interaction in NbB_2: a comparison with MgB_2," *Solid State Communications*, vol. 125, no. 6, pp. 323–326, 2003. 0038-1098.

[69] R. Heid, "Lattice dynamics and electron-phonon coupling in transition-metal diborides," *Physical Review B*, vol. 67, p. 180510, 2003.

[70] I. Shein, N. Medvedeva, and A. Ivanovskii, "Effect of metal vacancies on the band structure of Nb, Zr, and Y diborides," *Physics of the Solid State*, vol. 45, no. 9, pp. 1617–1621, 2003.

[71] H. Takagiwa, E. Nishibori, N. Okada, M. Takata, M. Sakata, and J. Akimitsu, "Relationship between superconductivity and crystal structure in NbB_{2+x}," *Science and Technology of Advanced Materials*, vol. 7, no. 1, pp. 22–25, 2006. 1468-6996.

[72] A. K. M. A. Islam, A. S. Sikder, and F. N. Islam, "NbB_2: a density functional study," *Physics Letters A*, vol. 350, no. 3-4, pp. 288–292, 2006.

[73] M. Mudgel, V. P. S. Awana, H. Kishan, I. Felner, D. G. A. Alvarez, and G. L. Bhalla, "Superconductivity of various borides: The role of stretched c-parameter," *Journal of Applied Physics*, vol. 105, no. 7, pp. 07E313–3, 2009.

[74] D. Kaczorowski, A. J. Zaleski, O. J. Zogal, and J. Klamut, "Incipient superconductivity in TaB_2," *arXiv:cond-mat/0103571v2*, 2001.

[75] V. Gasparov, N. Sidorov, I. Zver'kova, and M. Kulakov, "Electron transport in diborides: Observation of superconductivity in ZrB_2," *JETP Letters*, vol. 73, no. 10, pp. 532–535, 2001.

[76] H. Rosner, W. E. Pickett, S. L. Drechsler, A. Handstein, G. Behr, G. Fuchs, K. Nenkov, K. H. Müller, and H. Eschrig, "Electronic structure and weak electron-phonon coupling in TaB_2," *Physical Review B*, vol. 64, no. 14, p. 144516, 2001.

[77] A. Yamamoto, C. Takao, T. Masui, M. Izumi, and S. Tajima, "High-pressure synthesis of superconducting $Nb_{1-x}B_2$ (x=0-0.48) with the maximum T_c = 9.2 K," *Physica C: Superconductivity*, vol. 383, no. 3, pp. 197–206, 2002.

[78] P. P. Singh, "Theoretical study of electron-phonon interaction in ZrB_2 and TaB_2," *Physical Review B*, vol. 69, no. 9, p. 094519, 2004.

[79] M. Sigrist, D. F. Agterberg, P. A. Frigeri, N. Hayashi, R. P. Koga, I. Milat, and W. K., "Unconventional superconductivity in non-centrosymmetric materials," in *Effective models for low-dimensional strongly correlated systems* (G. G. Batrouni and D. Poilblanc, eds.), Springer, 2006.

[80] E. Bauer, G. Hilscher, H. Michor, C. Paul, E. W. Scheidt, A. Gribanov, Y. Seropegin, H. Noël, M. Sigrist, and P. Rogl, "Heavy fermion superconductivity and magnetic order in noncentrosymmetric $CePt_3Si$," *Physical Review letters*, vol. 92, no. 2, p. 027003, 2004.

[81] K. Togano, P. Badica, Y. Nakamori, S. Orimo, H. Takeya, and K. Hirata, "Superconductivity in the metal rich Li-Pd-B ternary boride," *Physical Review Letters*, vol. 93, no. 24, p. 247004, 2004.

[82] P. Badica, T. Kondo, and K. Togano, "Superconductivity in a new pseudo-binary $Li_2B(Pd_{1-x}Pt_x)_3$ (x = 0-1) boride system," *Journal of the Physical Society of Japan*, vol. 74, no. 3, p. 1014, 2005.

[83] B. Lee and L.-W. Wang, "Electronic structure of calcium hexaborides," *Applied Physics Letters*, vol. 87, no. 26, pp. 262509–3, 2005.

[84] S. K. Bose and E. S. Zijlstra, "Electronic structure, electron-phonon coupling and superconductivity of isotypic noncentrosymmetric crystals Li_2Pd_3B and Li_2Pt_3B," *Physica C: Superconductivity*, vol. 432, no. 3-4, pp. 173–181, 2005.

[85] A. Mani, T. Geetha Kumary, A. Bharathi, S. Kalavathi, V. Sankara Sastry, and Y. Hariharan, "Study of the effect of Ni substitution and external pressure in Li_2Pd_3B superconductor," *Physica C: Superconductivity*, vol. 433, no. 1-2, pp. 139–145, 2005.

[86] S. Tsuda, T. Yokoya, T. Kiss, T. Shimojima, K. Ishizaka, S. Shin, T. Togashi, S. Watanabe, C. Zhang, C. Chen, I. Hase, H. Takeya, K. Hirata, and K. Togano, "Strong-coupling superconductivity in noncentrosymmetric superconductor Li_2Pd_3B by sub-meV photoemission spectroscopy," *Journal of the Physical Society of Japan*, vol. 78, no. 3, p. 034711, 2009.

[87] C. F. Miclea, A. C. Mota, M. Sigrist, F. Steglich, T. A. Sayles, B. J. Taylor, C. A. McElroy, and M. B. Maple, "Vortex avalanches in the noncentrosymmetric superconductor Li_2Pt_3B," *Physical Review B*, vol. 80, no. 13, p. 132502, 2009.

[88] L. Fang, H. Yang, X. Zhu, G. Mu, Z.-S. Wang, L. Shan, C. Ren, and H.-H. Wen, "Physical properties of the noncentrosymmetric superconductor Ru_7B_3," *Physical Review B*, vol. 79, no. 14, p. 144509, 2009.

[89] T. Klimczuk, Q. Xu, E. Morosan, J. D. Thompson, H. W. Zandbergen, and R. J. Cava, "Superconductivity in noncentrosymmetric $Mg_{10}Ir_{19}B_{16}$," *Physical Review B*, vol. 74, no. 22, p. 220502, 2006.

[90] R. M. Wentzcovitch, M. L. Cohen, S. G. Louie, and D. Tomnek, "σ-states contribution to the conductivity of BC_3," *Solid State Communications*, vol. 67, no. 5, pp. 515–518, 1988.

[91] D. Tomanek, R. M. Wentzcovitch, S. G. Louie, and M. L. Cohen, "Calculation of electronic and structural properties of BC_3," *Physical Review B*, vol. 37, no. 6, p. 3134, 1988.

[92] F. J. Ribeiro and M. L. Cohen, "Possible superconductivity in hole-doped BC_3," *Physical Review B*, vol. 69, no. 21, p. 212507, 2004.

[93] M. M. Ali, A. A. Islam, M. Aftabuzzaman, and F. Parvin, "Superconductivity in diamond-like BC_3 phase," *Journal of Scientific Research*, vol. 2, no. 2, p. 203, 2010.

[94] A. Bharathi, S. Jemima Balaselvi, M. Premila, T. N. Sairam, G. L. N. Reddy, C. S. Sundar, and Y. Hariharan, "Synthesis and search for superconductivity in LiBC," *Solid State Communications*, vol. 124, no. 10-11, pp. 423–428, 2002.

[95] K. Kobayashi and M. Arai, "LiBC and related compounds under high pressure," *Physica C: Superconductivity*, vol. 388-389, pp. 201–202, 2003.

[96] K. Kobayashi and M. Arai, "Lattice anomaly of LiBC and related compounds under anisotropic compression," *Journal of the Physical Society of Japan*, vol. 72, no. 2, pp. 217–220, 2003.

[97] L. Zhao, P. Klavins, and K. Liu, "Synthesis and properties of hole-doped $Li_{1-x}BC$," *Journal of Applied Physics*, vol. 93, no. 10, pp. 8653 –8655, 2003.

[98] D. Souptel, Z. Hossain, G. Behr, W. Lser, and C. Geibel, "Synthesis and physical properties of LiBC intermetallics," *Solid State Communications*, vol. 125, no. 1, pp. 17–21, 2003.

[99] A. V. Pronin, K. Pucher, P. Lunkenheimer, A. Krimmel, and A. Loidl, "Electronic and optical properties of LiBC," *Physical Review B*, vol. 67, no. 13, p. 132502, 2003.

[100] Y. Nakamori and S.-i. Orimo, "Synthesis and characterization of single phase Li_xBC (x=0.5 and 1.0), using Li hydride as a starting material," *Journal of Alloys and Compounds*, vol. 370, no. 1-2, pp. L7–L9, 2004.

[101] P. F. Karimov, N. A. Skorikov, E. Z. Kurmaev, L. D. Finkelstein, S. Leitch, J. MacNaughton, A. Moewes, and T. Mori, "Resonant inelastic soft x-ray scattering and electronic structure of LiBC," *Journal of Physics: Condensed Matter*, vol. 16, no. 28, p. 5137, 2004.

[102] H. Rosner, A. Kitaigorodsky, and W. E. Pickett, "Prediction of high t_c superconductivity in hole-doped LiBC," *Physical Review letters*, vol. 88, no. 12, p. 127001, 2002.

[103] J. K. Dewhurst, S. Sharma, C. Ambrosch-Draxl, and B. Johansson, "First-principles calculation of superconductivity in hole-doped LiBC: $T_c = 65$ K," *Physical Review B*, vol. 68, no. 2, p. 020504, 2003.

[104] P. P. Singh, "Hole-doped, high-temperature superconductors Li_xBC, Na_xBC and C_x: a coherent-potential-based prediction," *Solid State Communications*, vol. 124, no. 1-2, pp. 25–28, 2002.

[105] A. Lazicki, C. S. Yoo, H. Cynn, W. J. Evans, W. E. Pickett, J. Olamit, K. Liu, and Y. Ohishi, "Search for superconductivity in LiBC at high pressure: Diamond anvil cell experiments and first-principles calculations," *Physical Review B*, vol. 75, no. 5, p. 054507, 2007.

[106] P. Ravindran, "Detailed electronic structure studies on superconducting MgB_2 and related compounds," *Physical Review B*, vol. 64, no. 22, p. 224509, 2001.

[107] N. Medvedeva, J. Medvedeva, A. Ivanovskii, V. Zubkov, and A. Freeman, "Band structure of the superconducting MgB_2 compound and modeling of related ternary systems," *JETP Letters*, vol. 73, no. 7, pp. 336–340, 2001.

[108] S. Okatov, A. Ivanovskii, Y. Medvedeva, and N. Medvedeva, "The electronic band structures of superconducting MgB_2 and related borides CaB_2, MgB_6 and CaB_6," *Physica Status Solidi (b)*, vol. 225, no. 1, pp. R3–R5, 2001.

[109] T. Oguchi, "Cohesion in AlB_2-type diborides: A first-principles study," *Journal of The Physical Society of Japan*, vol. 71, no. 6, p. 1495, 2002. 0031-9015.

[110] G. Satta, G. Profeta, F. Bernardini, A. Continenza, and S. Massidda, "Electronic and structural properties of superconducting MgB_2, $CaSi_2$, and related compounds," *Physical Review B*, vol. 64, no. 10, p. 104507, 2001.

[111] H. J. Choi, S. G. Louie, and M. L. Cohen, "Prediction of superconducting properties of CaB_2 using anisotropic eliashberg theory," *Physical Review B*, vol. 80, no. 6, p. 064503, 2009.

[112] E. Schrödinger, "An undulatory theory of the mechanics of atoms and molecules," *Phys. Rev.*, vol. 28, no. 6, pp. 1049–1070, 1926.

[113] R. P. Feynman, N. Metropolis, and E. Teller, "Equations of state of elements based on the generalized Fermi-Thomas theory," *Physical Review*, vol. 75, no. 10, pp. 1561–1573, 1949.

[114] E. Teller, "On the stability of molecules in the Thomas-Fermi theory," *Reviews of Modern Physics*, vol. 34, no. 4, pp. 627–631, 1962.

[115] P. Hohenberg and W. Kohn, "Inhomogeneous electron gas," *Physical Review*, vol. 136, no. 3B, p. B864, 1964.

[116] W. Kohn and L. J. Sham, "Self-consistent equations including exchange and correlation effects," *Physical Review*, vol. 140, no. 4A, p. A1133, 1965.

[117] J. P. Perdew and Y. Wang, "Accurate and simple analytic representation of the electron-gas correlation energy," *Physical Review B*, vol. 45, no. 23, p. 13244, 1992.

[118] L. Hedin and U. von Barth, "A local exchange-correlation potential for the spin polarized case. i," *Journal of Physics C: Solid State Physics*, vol. 5, no. 13, p. 1629, 1972. 0022-3719.

[119] S. H. Vosko and L. Wilk, "Influence of an improved local-spin-density correlation-energy functional on the cohesive energy of alkali metals," *Physical Review B*, vol. 22, pp. 3812–3815, Oct 1980.

[120] A. Kolmogorov, "www.maise-guide.org,"

[121] A. R. Oganov and C. W. Glass, "Crystal structure prediction using ab initio evolutionary techniques: Principles and applications," *The Journal of Chemical Physics*, vol. 124, no. 24, pp. 244704–15, 2006.

[122] Y. Wang, J. Lv, L. Zhu, and Y. Ma, "Crystal structure prediction via particle-swarm optimization," *Physical Review B*, vol. 82, p. 094116, Sep 2010.

[123] C. J. Pickard and R. J. Needs, "High-pressure phases of silane," *Physical Review Letters*, vol. 97, p. 045504, Jul 2006.

[124] S. Goedecker, "Minima hopping: An efficient search method for the global minimum of the potential energy surface of complex molecular systems," *The Journal of Chemical Physics*, vol. 120, no. 21, pp. 9911–9917, 2004.

[125] A. N. Kolmogorov, S. Shah, E. R. Margine, A. F. Bialon, T. Hammerschmidt, and R. Drautz, "New superconducting and semiconducting Fe-B compounds predicted with an ab initio evolutionary search," *Physical Review letters*, vol. 105, no. 21, p. 217003, 2010.

[126] Y. Xie, A. R. Oganov, and Y. Ma, "Novel high pressure structures and superconductivity of $CaLi_2$," *Physical Review letters*, vol. 104, no. 17, p. 177005, 2010.

[127] L. Xu, Z. Zhao, Q. Wang, L.-M. Wang, B. Xu, J. He, and Y. Tian, "Prediction of a superconductive superhard material: Diamond-like BC_7," *Journal of Applied Physics*, vol. 110, no. 1, pp. 013501–5, 2011.

[128] D. Y. Kim, R. H. Scheicher, C. J. Pickard, R. J. Needs, and R. Ahuja, "Predicted formation of superconducting platinum-hydride crystals under pressure in the presence of molecular hydrogen," *Physical Review Letters*, vol. 107, p. 117002, Sep 2011.

[129] J. A. Flores-Livas, M. Amsler, T. J. Lenosky, L. Lehtovaara, S. Botti, M. A. L. Marques, and S. Goedecker, "High-pressure structures of disilane and their superconducting properties," *Physical Review Letters*, vol. 108, p. 117004, Mar 2012.

[130] S. M. Woodley and R. Catlow, "Crystal structure prediction from first principles," *Nature Materials*, vol. 7, pp. 937–946, 2008.

[131] H. K. Onnes, "Further experiments with liquid helium," *Commun. Phys. Lab. Univ. Leiden*, vol. 180b, 1925.

[132] J. Schmalian, "Failed theories of superconductivity," *arXiv:1008.0447*, 2010.

[133] W. Meissner and R. Ochsenfeld, "Ein neuer effekt bei eintritt der supraleitfhigkeit," *Naturwissenschaften*, vol. 21, no. 44, pp. 787–788, 1933.

[134] A. M. Forrest, "Meissner and Ochsenfeld revisited," *European Journal of Physics*, vol. 4, no. 2, p. 117, 1983.

[135] http://en.wikipedia.org/wiki/Meissner_effect.

[136] F. London and H. London, "The electromagnetic equations of the supraconductor," *Proceedings of the Royal Society of London. Series A, Mathematical and Physical Sciences*, vol. 149, no. 866, pp. 71–88, 1935.

[137] J. P. Carbotte, "Properties of boson-exchange superconductors," *Reviews of Modern Physics*, vol. 62, p. 1027, 1990.

[138] F. Marsiglio and J. P. Carbotte, "Electron-phonon superconductivity," in *Superconductivity, Conventional and Unconventional Superconductors* (K. H. Bennemann and J. B. Ketterson, eds.), vol. 1, Springer, 2008.

[139] C. A. Reynolds, B. Serin, W. H. Wright, and L. B. Nesbitt, "Superconductivity of isotopes of mercury," *Physical Review*, vol. 78, no. 4, p. 487, 1950.

[140] E. Maxwell, "Isotope effect in the superconductivity of mercury," *Physical Review*, vol. 78, no. 4, p. 477, 1950.

[141] H. Förhlich, "Theory of the superconducting state. I. the ground state at the absolute zero of temperature," *Physical Review*, vol. 79, no. 5, p. 845, 1950.

[142] L. N. Cooper, "Bound electron pairs in a degenerate Fermi gas," *Physical Review*, vol. 104, no. 4, p. 1189, 1956.

[143] M. Tinkham, *Introduction to Superconductivity*. Dover Publications Inc., New York, 2004.

[144] A. A. Abrikosov, L. P. Gorkov, and I. E. Dzyaloshinski, *Methods of Quantum Field Theory in Statistical Physics*. Dover Publications Inc. New York, 1963.

[145] L. D. Landau and E. M. Lifshitz, *Statistical physics. Part 2, Theory of the condensed state*. Oxford: Oxford : Pergamon, 1986.

[146] G. Grimvall, *The Electron-Phonon Interaction in Metals*. North-Holland Pub. Co., 1981.

[147] S. V. Vonsovsky, Y. A. Izyumov, and E. Z. Kurmaev, *Superconductivity of transition metals : their alloys and compounds*. Berlin; New York: Springer-Verlag, 1982.

[148] P. Allen and B. Mitrović̀h, "Theory of superconducting T_c," in *Solid State Physics* (F. Seitz, D. Turnbull, and H. Ehrenreich, eds.), vol. 37, pp. 1–92, Academic, New York, 1982.

[149] D. J. Scalapino, J. R. Schrieffer, and J. W. Wilkins, "Strong-coupling superconductivity. I," *Physical Review*, vol. 148, no. 1, p. 263, 1966.

[150] W. L. McMillan, "Transition temperature of strong-coupled superconductors," *Physical Review*, vol. 167, no. 2, p. 331, 1968.

[151] P. Morel and P. W. Anderson, "Calculation of the superconducting state parameters with retarded electron-phonon interaction," *Physical Review*, vol. 125, pp. 1263–1271, Feb 1962.

[152] S. Baroni, S. de Gironcoli, A. Dal Corso, and P. Giannozzi, "Phonons and related crystal properties from density-functional perturbation theory," *Reviews of Modern Physics*, vol. 73, pp. 515–562, Jul 2001.

[153] J. Noffsinger, F. Giustino, B. D. Malone, C.-H. Park, S. G. Louie, and M. L. Cohen, "EPW: A program for calculating the electron-phonon coupling using maximally localized Wannier functions," *Computer Physics Communications*, vol. 181, no. 12, pp. 2140 – 2148, 2010.

[154] P. Giannozzi and et al., "QUANTUM ESPRESSO: a modular and open-source software project for quantum simulations of materials," *Journal of Physics: Condensed Matter*, vol. 21, no. 39, p. 395502, 2009. 0953-8984.

[155] G. Kresse and J. Furthmüller, "Efficient iterative schemes for ab initio total-energy calculations using a plane-wave basis set," *Physical Review B*, vol. 54, no. 16, p. 11169, 1996.

[156] P. E. Blöchl, "Projector augmented-wave method," *Physical Review B*, vol. 50, no. 24, p. 17953, 1994.

[157] H. J. Monkhorst and J. D. Pack, "Special points for Brillouin-zone integrations," *Physical Review B*, vol. 13, no. 12, p. 5188, 1976.

[158] J. D. Pack and H. J. Monkhorst, "Special points for Brillouin-zone integrations" a reply," *Physical Review B*, vol. 16, no. 4, p. 1748, 1977.

[159] J. P. Perdew, K. Burke, and M. Ernzerhof, "Generalized gradient approximation made simple," *Physical Review Letters*, vol. 77, no. 18, p. 3865, 1996. PRL.

[160] Momma and Izumi, "VESTA 3 for three-dimensional visualization of crystal, volumetric and morphology data," *Journal of Applied Crystallography*, vol. 44, no. 6, pp. 1272–1276, 2011.

[161] A. Kokalj, "XCrySDen a new program for displaying crystalline structures and electron densities," *Journal of Molecular Graphics and Modelling*, vol. 17, no. 34, pp. 176 – 179, 1999.

[162] W. Pearson, *A Handbook of Lattice Spacings and Structures of Metals and Alloys*, vol. 2. Pergamon Press, Oxford, 1967.

[163] K. H. Mller and V. N. Narozhnyi, "Interaction of superconductivity and magnetism in borocarbide superconductors," *Reports on Progress in Physics*, vol. 64, no. 8, p. 943, 2001.

[164] J. Smith, J. Lashley, H. Volz, R. Fisher, and P. Riseborough, "Thermodynamics and superconductivity of the th7(fe, ru, os, co, rh, ir)3 system," *Philosophical Magazine*, vol. 88, no. 18-20, pp. 2847–2850, 2008.

[165] Y. Nakai, K. Ishida, D. Kikuchi, H. Sugawara, and H. Sato, "Evidence for *s*-wave superconductivity with antiferromagnetic fluctuations in filled skutterudite $lafe_4p_{12}$: ^{139}la and ^{31}p-nmr studies," *Journal of the Physical Society of Japan*, vol. 74, no. 12, pp. 3370–3374, 2005.

[166] A. F. Bialon, T. Hammerschmidt, R. Drautz, S. Shah, E. R. Margine, and A. N. Kolmogorov, "Possible routes for synthesis of new boron-rich Fe-B and $Fe_{1-x}Cr_xB_4$ compounds," *Applied Physics Letters*, vol. 98, no. 8, p. 081901, 2011.

[167] G. Bergerhoff and I. Brown, *Crystallographic Databases*. International Union of Crystallography, 1987.

[168] S. L. Bud'ko, G. Lapertot, C. Petrovic, C. E. Cunningham, N. Anderson, and P. C. Canfield, "Boron isotope effect in superconducting MgB_2," *Physical Review Letters*, vol. 86, pp. 1877–1880, 2001.

[169] R. Zeller, "Spin-polarized dft calculations and magnetism," in *Computational Nanoscience: Do It Yourself!* (J. Grotendorst, S. Blugel, and D. Marx, eds.), vol. 31, John von Neumann Institute for Computing, Julich,, 2006.

[170] H. Niu, J. Wang, X.-Q. Chen, D. Li, Y. Li, P. Lazar, R. Podloucky, and A. N. Kolmogorov, "Structure, bonding, and possible superhardness of CrB_4," *Physical Review B*, vol. 85, p. 144116, Apr 2012.

[171] A. Knappschneider, C. Litterscheid, D. Dzivenko, J. A. Kurzman, R. Seshadri, N. Wagner, J. Beck, R. Riedel, and B. Albert, "Possible superhardness of CrB_4," *Inorganic Chemistry*, vol. 52, no. 2, pp. 540–542, 2013.

[172] H. Gou, N. Dubrovinskaia, E. Bykova, A. A. Tsirlin, D. Kasinathan, A. Richter, M. Merlini, M. Hanfland, A. M. Abakumov, D. Batuk, G. V. Tendeloo, Y. Nakajima, A. N. Kolmogorov, and L. Dubrovinsky, "Discovery of a superhard iron tetraboride superconductor," *arXiv:1304.5106 [cond-mat.mtrl-sci]*, 2013.

[173] K. Jin, R. Suchoski, S. Fackler, Y. Zhang, X. Pan, R. L. Greene, and I. Takeuchi, "Combinatorial search of superconductivity in fe-b composition spreads," *arXiv:1306.3024 [cond-mat.supr-con]*, 2013.

[174] T. Yabuuchi, T. Matsuoka, Y. Nakamoto, and K. Shimizu, "Superconductivity of Ca exceeding 25 K at megabar pressures," *Journal of the Physical Society of Japan*, vol. 75, no. 8, p. 083703, 2006.

[175] M. Sakata, Y. Nakamoto, K. Shimizu, T. Matsuoka, and Y. Ohishi, "Superconducting state of Ca-VII below a critical temperature of 29 K at a pressure of 216 GPa," *Physical Review B*, vol. 83, no. 22, p. 220512, 2011.

[176] T. Ogitsu, E. Schwegler, and G. Galli, "β-rhombohedral boron: At the crossroads of the chemistry of boron and the physics of frustration," *Chemical Reviews*, 2013.

[177] A. N. Kolmogorov, S. Shah, E. R. Margine, A. K. Kleppe, and A. P. Jephcoat, "Pressure-driven evolution of the covalent network in CaB_6," *Physical Review Letters*, vol. 109, p. 075501, Aug 2012.

[178] S. Shah and A. N. Kolmogorov, "Stability and superconductivity of ca-b phases at ambient and high pressure," *Physical Review B*, vol. X, p. XXX, July 2013.

[179] Rodgers and Villars, "Statistical studies of intermetallics stressing the validity of three principles," *Journal of Alloys and Compounds*, vol. 197, no. 2, pp. 167–176, 1993.

[180] H. Moissan and P. Williams, *Sur la préparation et les propriétés des borures de calcium, de strontium et de baryum.* Gauthier-Villars, 1897.

[181] M. Stackelberg and F. Neumann, "Die kristallstruktur der boride der zusammensetzung MeB_6," *Z. Phys. Chem. B*, vol. 19, pp. 314–20, 1932.

[182] D. P. Young, D. Hall, M. E. Torelli, Z. Fisk, J. L. Sarrao, J. D. Thompson, H. R. Ott, S. B. Oseroff, R. G. Goodrich, and R. Zysler, "High-temperature weak ferromagnetism in a low-density free-electron gas," *Nature*, vol. 397, no. 6718, pp. 412–414, 1999.

[183] Z. Wu, D. J. Singh, and R. E. Cohen, "Electronic structure of calcium hexaboride within the weighted density approximation," *Physical Review B*, vol. 69, no. 19, p. 193105, 2004.

[184] J.-S. Rhyee and B. K. Cho, "The effect of boron purity on electric and magnetic properties of CaB_6," *Journal of Applied Physics*, vol. 95, no. 11, pp. 6675–6677, 2004.

[185] L.-H. Li, L. Chen, J.-Q. Li, and L.-M. Wu, "The first-principles study of bulk CaB_6 and the field emission of CaB_6 nanowires using the hcth functional," *The Journal of Physical Chemistry C*, vol. 113, no. 34, pp. 15384–15389, 2009.

[186] J. Matsushita and S. Komarneni, "High temperature oxidation behavior of CaB_6 sintered body," *Journal of Materials Science*, vol. 34, no. 13, pp. 3043–3046, 1999. 0022-2461.

[187] X. H. Ji, Q. Y. Zhang, J. Q. Xu, and Y. M. Zhao, "Rare-earth hexaborides nanostructures: Recent advances in materials, characterization and investigations of physical properties," *Progress in Solid State Chemistry*, vol. 39, no. 2, pp. 51–69, 2011.

[188] H. C. Longuet-Higgins and D. V. Roberts, "The electronic structure of the borides mb_6," *Proceedings of the Royal Society of London. Series A. Mathematical and Physical Sciences*, vol. 224, no. 1158, pp. 336–347, 1954. 10.1098/rspa.1954.0162.

[189] Li, Yang, Li, Wang, Liang, and Gao, "Pressure-induced phase transitions in CaB6 by means of XRD and resistance measurement," *Physica B: Condensed Matter*, vol. 406, no. 1, pp. 59–62, 2011.

[190] Y. Li, J. Yang, X. Cui, T. Hu, C. Liu, Y. Tian, H. Liu, Y. Han, and C. Gao, "Electrical properties of polycrystalline CaB_6 under high pressure and low temperature," *Physica Status Solidi (b)*, vol. 248, no. 5, pp. 1162–1165, 2011.

[191] Y.-K. Wei, J.-X. Yu, Z.-G. Li, Y. Cheng, and G.-F. Ji, "Elastic and thermodynamic properties of CaB6 under pressure from first principles," *Physica B: Condensed Matter*, vol. 406, no. 23, pp. 4476–4482, 2011.

[192] P. Teredesai, D. V. S. Muthu, N. Chandrabhas, S. Meenakshi, V. Vijayakumar, P. Modak, R. S. Rao, B. K. Godwal, S. K. Sikka, and A. K. Sood, "High pressure phase transition in metallic LaB_6: Raman and x-ray diffraction studies," *Solid State Communications*, vol. 129, no. 12, pp. 791–796, 2004.

[193] Godwal, Petruska, Speziale, Yan, Clark, Kruger, and Jeanloz, "High-pressure raman and x-ray diffraction studies on LaB_6," *Physical Review B*, vol. 80, no. 17, p. 172104, 2009.

[194] B. T. Matthias, T. H. Geballe, K. Andres, E. Corenzwit, G. W. Hull, and J. P. Maita, "Superconductivity and antiferromagnetism in boron-rich lattices," *Science*, vol. 159, no. 3814, p. 530, 1968.

[195] Y. Xu, L. Zhang, T. Cui, Y. Li, Y. Xie, W. Yu, Y. Ma, and G. Zou, "First-principles study of the lattice dynamics, thermodynamic properties and electron-phonon coupling of YB_6," *Physical Review B*, vol. 76, p. 214103, 2007.

[196] E. L. Muetterties, *The Chemistry of Boron and its Compounds*. John Wiley & Sons, Inc., 1967.

[197] I. Popov, N. Baadji, and S. Sanvito, "Magnetism and antiferroelectricity in MgB_6," *Physical Review Letters*, vol. 108, no. 10, p. 107205, 2012.

[198] M. I. Aroyo, J. M. Perez-Mato, C. Capillas, E. Kroumova, S. Ivantchev, G. Madariaga, A. Kirov, and H. Wondratschek, "Bilbao crystallographic server: I. databases and crystallographic computing programs," *Zeitschrift fur Kristallographie*, vol. 221, no. 1 2006, pp. 15–27, 2006.

[199] M. I. Aroyo, A. Kirov, C. Capillas, J. M. Perez-Mato, and H. Wondratschek, "Bilbao crystallographic server. II. Representations of crystallographic point groups and space groups," *Acta Crystallographica Section A*, vol. 62, no. 2, pp. 115–128, 2006.

[200] W. Setyawan, R. M. Gaume, S. Lam, R. S. Feigelson, and S. Curtarolo, "High-throughput combinatorial database of electronic band structures for inorganic scintillator materials," *ACS Combinatorial Science*, vol. 13, no. 4, pp. 382–390, 2011.

[201] A. Zalkin and D. H. Templeton, "The crystal structures of CeB_4 ThB_4 and UB_4," *Acta Crystallographica*, vol. 6, no. 3, pp. 269–272, 1953.

[202] J. M. Lafferty, "Boride cathodes," *Journal of Applied Physics*, vol. 22, no. 3, pp. 299–309, 1951.

[203] R. W. Johnson and A. H. Daane, "The lanthanum-boron system," *The Journal of Physical Chemistry*, vol. 65, no. 6, pp. 909–915, 1961.

[204] R. Schmitt, B. Blaschkowski, K. Eichele, and H. J. Meyer, "Calcium tetraboride-does it exist? Synthesis and properties of a carbon-doped calcium tetraboride that is isotypic with the known rare earth tetraborides," *Inorganic Chemistry*, vol. 45, no. 7, pp. 3067–3073, 2006.

[205] M. B. Yahia, O. Reckeweg, R. Gautier, J. Bauer, T. Schleid, J.-F. Halet, and J.-Y. Saillard, "Can undoped calcium tetraborides exist? An answer from the comparison of its density functional theory electronic structure with that of rare-earth metal tetraboride," *Inorganic Chemistry*, vol. 47, no. 14, pp. 6137–6143, 2008.

[206] Z. P. Yin and W. E. Pickett, "Rare-earth boron bonding and 4f state trends in RB_4 tetraborides," *Physical Review B*, vol. 77, no. 3, p. 035135, 2008.

[207] Z. Liu, X. Han, D. Yu, Y. Sun, B. Xu, X.-F. Zhou, J. He, H.-T. Wang, and Y. Tian, "Formation, structure, and electric property of CaB_4 single crystal synthesized under high pressure," *Applied Physics Letters*, vol. 96, no. 3, p. 031903, 2010.

[208] W. N. Lipscomb and D. Britton, "Valence structure of the higher borides," *The Journal of Chemical Physics*, vol. 33, no. 1, pp. 275–280, 1960.

[209] J. K. Burdett and E. Canadell, "Cheminform abstract: Fused and linked deltahedral clusters in the chemistry of the group 13 elements," *ChemInform*, vol. 22, no. 1, pp. 7207–7217, 1991.

[210] R. Shannon, "Revised effective ionic radii and systematic studies of interatomic distances in halides and chalcogenides," *Acta Crystallographica Section A*, vol. 32, no. 5, pp. 751–767, 1976.

[211] J. C. Slater, "Atomic radii in crystals," *The Journal of Chemical Physics*, vol. 41, no. 10, pp. 3199–3204, 1964.

[212] M. R. Naslain, A. Guette, and M. Barret, "Sur le diborure et le tétraborure de magnésium. considrations cristallochimiques sur les tétraborures," *Journal of Solid State Chemistry*, vol. 8, no. 1, pp. 68 – 85, 1973.

[213] R. F. Zhang, D. Legut, Z. J. Lin, Y. S. Zhao, H. K. Mao, and S. Veprek, "Stability and strength of transition-metal tetraborides and triborides," *Physical Review Letters*, vol. 108, p. 255502, 2012.

[214] A. N. Kolmogorov, M. Calandra, and S. Curtarolo, "Thermodynamic stabilities of ternary metal borides: An ab initio guide for synthesizing layered superconductors," *Physical Review B*, vol. 78, no. 9, p. 094520, 2008.

[215] A. Hermann, N. W. Ashcroft, and R. Hoffmann, "Making sense of boron-rich binary Be-B phases," *Inorganic Chemistry*, vol. 51, no. 16, pp. 9066–9075, 2012.

[216] D. E. Sands, C. F. Cline, A. Zalkin, and C. L. Hoenig, "The beryllium-boron system," *Acta Crystallographica*, vol. 14, no. 3, pp. 309–310, 1961.

[217] P. Vajeeston, P. Ravindran, and H. Fjellvaå, "Prediction of structural, lattice dynamical, and mechanical properties of CaB_2," *RSC Advances*, vol. 2, pp. 11687–11694, 2012.

[218] A. N. Kolmogorov and S. Curtarolo, "Theoretical study of metal borides stability," *Physical Review B*, vol. 74, p. 224507, Dec 2006.

[219] A. Goncharov and V. Struzhkin, "Pressure dependence of the raman spectrum, lattice parameters and superconducting critical temperature of MgB_2: evidence for pressure-driven phonon-assisted electronic topological transition," *Physica C: Superconductivity*, vol. 385, no. 1-2, pp. 117 – 130, 2003.

[220] J. Etourneau and P. Hagenmuller, "Structure and physical features of the rare-earth borides," *Philosophical Magazine Part B*, vol. 52, no. 3, pp. 589–610, 1985.

[221] A. N. Kolmogorov, R. Drautz, and D. G. Pettifor, "*Ab initio* modeling of Li-B-H boron-chain alloys for hydrogen storage applications," *Physical Review B*, vol. 76, p. 184102, Nov 2007.

[222] C. Xing-Qiu, C. L. Fu, and C. Franchini, "Polymeric forms of carbon in dense lithium carbide," *Journal of Physics: Condensed Matter*, vol. 22, no. 29, p. 292201, 2010.

[223] G. Samsonov and T. Serebryakova, "Classification of borides," *Soviet Powder Metallurgy and Metal Ceramics*, vol. 17, no. 2, pp. 116–120, 1978.

[224] E. R. Margine and F. Giustino, "Anisotropic Migdal-Eliashberg theory using Wannier functions," *Physical Review B*, vol. 87, p. 024505, 2013.